



# City Research Online

## City, University of London Institutional Repository

---

**Citation:** Naseri, Homa (2019). Modelling of nozzle cavitation in newtonian and viscoelastic fluids. (Unpublished Doctoral thesis, City, University of London)

This is the accepted version of the paper.

This version of the publication may differ from the final published version.

---

**Permanent repository link:** <http://openaccess.city.ac.uk/id/eprint/23279/>

**Link to published version:**

**Copyright and reuse:** City Research Online aims to make research outputs of City, University of London available to a wider audience. Copyright and Moral Rights remain with the author(s) and/or copyright holders. URLs from City Research Online may be freely distributed and linked to.

---

City Research Online:

<http://openaccess.city.ac.uk/>

[publications@city.ac.uk](mailto:publications@city.ac.uk)

---

---

# MODELLING OF NOZZLE CAVITATION IN NEWTONIAN AND VISCOELASTIC FLUIDS

---

By Homa Naseri



Thesis Submitted in Partial Fulfillment for

Degree of Doctor of Philosophy

City, University of London, UK

Department of Mechanical Engineering

and Aeronautics

MAY 9, 2019



*I, Homa Naseri confirm that the work presented in this thesis is my own. Where information has been derived from other sources, I confirm that this has been indicated in the thesis.*

*Homa Naseri  
London, 2019*

... To my mother & Daye

# Abstract

Cavitation is the abrupt process of vapour formation due to pressure drop in liquid flows, which may occur in various equipment and hydraulic machinery such as propellers, bearings or fuel injectors. In fuel injector nozzles, cavitation formation may be either beneficial or detrimental to the engine performance, depending on the location and type of the vaporous structures. Cavitation can enhance the turbulence levels inside the nozzle and therefore improve the spray atomisation, moreover large vortex cavities known as string cavitation, can increase the spray cone angle. However, cavitation bubbles collapsing near the internal surfaces result in erosion and ultimately failure of the injector parts. Furthermore, excessive vapour formation inside the nozzle significantly reduces the nozzle discharge coefficient and may eventually result in choked flow conditions. Therefore, understanding the cavitation dynamics and cavitation control is vital for injector design and an active topic in fluid dynamics research.

Newly developed deposit control fuel additives have the potential to reduce the in-nozzle cavitation and enhance the flowrate even in clean injectors due to their non-Newtonian properties. This research aims to provide an understanding about the association between viscoelastic detergent additives and turbulent cavitating nozzle flows using computational fluid dynamics.

An accurate framework for modelling the in-nozzle cavitation is developed. Performance of several RANS and LES models is assessed in predicting incipient and developed cavitation regimes. The Reboud et al. eddy viscosity correction is utilized to compensate the effect of mixture compressibility on turbulent viscosity in  $k-\varepsilon$  RNG and  $k-\omega$  SST models. WALE LES results are validated against the velocity and rms of turbulent velocity measurements in a step nozzle. A homogeneous equilibrium cavitation model based on Wallis speed of sound formula is utilised to study the effect of vapour-liquid mass transfer rate compared to Zwart-Gerber-Belamri (ZGB) and Schnerr-Sauer (SS) cavitation models. Cavitation vapour fraction values are validated against X-ray CT measurements.

The Phan-Thien-Tanner (PTT) fluid model is implemented to simulate the shear-induced viscoelastic behaviour of Quaternary Ammonium Salt (QAS) surfactants in the additised fuel. The model is validated against analytical solution for channel flow and experimental measurements of corner vortex in a square contraction geometry. The effect of liquid viscosity on cavitation development is presented using LES simulations. Finally, the effect of viscoelasticity on different cavitation regimes, namely cloud cavitation inside a step nozzle and string cavitation in a realistic injector geometry is investigated using LES. The physical flow characteristics are investigated and the effect of the additive on cavitation inside the nozzle is presented. The numerical findings are found to be in agreement with experimental studies of additised fuel.

# Acknowledgments

Firstly, I would like to thank my supervisor Prof Manolis Gavaises, for creating the opportunity to conduct this research and for believing in me throughout my journey from an undergraduate student to becoming a PhD. Completing this work would not have been possible without his vision, experience and scientific and financial support. I feel fortunate for the chance to get involved in the work of our research group and to get the opportunity to interact with ambitious researchers in cavitation research.

Secondly, I must thank Dr Ilias Malgarinos for assisting me during the implementation of the CFD code. His help is especially valuable to me as it was during some of the hardest days of my PhD and he supported me with an unbiased attitude and a professional approach.

Furthermore, I would like to thank my advisor Dr Phoevos Koukouvinis for his help in conducting the simulations, sharing his CFD knowledge and experience in processing and publishing the research outcomes. Moreover, the support of my second supervisor Dr Ioannis Karathanassis and our productive discussions on various fluid dynamics topics is also recognised.

Thanks are due to the Lubrizol Corporation, especially Dr Robert Barbour, Dr Kieran Trickett and Dr Eugene Pashkovski, for sharing their knowledge of fuels and additives chemistry, that allowed combining the additive properties in CFD investigations.

I would like to thank all the members of the International Institute for Cavitation Research group at City, University of London. In no particular order, my thanks are to Prof George Bergeles, Prof Jamshid Nouri, Dr Konstantinos Papadopolous, Mr Nikos Chatziarsenis, Dr Hesamaldin Jadidbonab, Dr Nikos Kyriazis, Dr Andreas Papoutsakis, Dr Yves Paquette, Dr Carlos Rodriguez, Ms Georgia Nykteri, Mr Milad Heidari Koochi, Mr Akis Stavropoulos, Mr Alvaro Vidal, Mr Murali-Girija Mithun, Mr Maxwell Brunhart, Mr Thodoris Lyras and Mr Konstantinos Kolovos. I have learnt from each and every person in our group and I am grateful for the nice memories we shared.

I would also like to thank my friends and family for supporting me and being by my side in both sad days and happy days. Thanks to Georgia for being kind and for the precious times that we got to spend together in London and around the university. I also thank Andreea and Khush for growing up with me during our friendship of 7 years, and I thank Soroush, Naimeh, Shahandeh and Magda for being supportive and encouraging throughout my studies.

Special thanks are due to my mother, Dr Saadat Molanaei. I want to thank her for being my inspiration, my best friend in all times and my biggest supporter. Finally, I am grateful to my grandmother, Daye, for her big heart that always had a secure place for me. Without their continuous support and love, I could never reach where I am today or understand the meaning of humanity.





# Present Contribution

The simulations performed in this thesis provide the following insights:

- **Mechanism for “power gain” in additised fuels proposed:** This thesis explains the improved volumetric efficiency of fuel injectors enriched with the newly developed deposit control additives containing quaternary ammonium salts. The interaction between viscoelasticity and flow turbulence and cavitation is found to be responsible for the additive effect and the findings are currently employed by the project’s industrial partner, Lubrizol, for developing a new range of additives for enhanced fuel delivery and limiting the pressure losses.
- **Flow physics in turbulent and cavitating viscoelastic fluids presented:** The Phan-Thien-Tanner model that can simulate the effect of entanglement of surfactant aggregates is implemented in a Navier-Stokes equations flow solver. Instantaneous and time-averaged flow field predictions are analysed to distinguish between the effect of the viscoelastic additives in cloud cavitation and string cavitation in a step nozzle and an injector nozzle. The vapour structures and cavitation cloud shedding dynamics in Newtonian and viscoelastic fluids are compared. To the best of the author’s knowledge, these studies have not been reported in the past.
- **Findings consistent with parallel X-ray studies on cavitating flows:** The numerical simulations were developed in a close collaboration with experimental studies to identify the additive effect. The conclusions reached regarding the effect of the viscoelasticity on various cavitation regimes are compared with the experiments and the findings are in line with the numerical results.
- **Quantitative validation of cavitation vapour fraction:** Extent of cavitation predicted in the simulations is validated in detail against X-ray CT measurements of in-nozzle vapour fraction. Quantitative validations for in-nozzle cavitation are scarce in the literature due to the complexity of experimental measurements. The effect of turbulence modelling in cavitation simulation is presented using 2-equation RANS models, RSM model and WALE LES model in a range of cavitation regimes. LES performance in incipient cavitation condition and cloud shedding is validated against experimental data. Effect of mass transfer rate on simulation of turbulent nozzle flow is identified with two-phase mass transfer rate models and the barotropic model.



# Contents

<b>1. Introduction.....</b>	<b>1</b>
1.1. Cavitation in nozzle flow .....	2
1.2. Viscoelastic fluids .....	6
1.3. Detergents and surfactant micelles .....	9
1.4. Current investigation.....	13
1.4.1. Surfactant aggregation properties of the deposit control additive.....	14
1.4.2. Fuel flowrate measurements .....	15
1.4.3. Cavitation volume fraction measurements using X-ray micro-CT .....	16
1.4.4. High-flux X-ray phase-contrast measurements.....	17
1.4.5. Hypothesis.....	20
1.4.6. Aims and Outline of the Thesis.....	22
<b>2. Literature Review .....</b>	<b>24</b>
2.1. Cavitation studies .....	24
2.1.1. Cavitation in nozzle flow .....	25
2.1.2. Modelling of cavitation.....	31
2.2. Turbulence in cavitating flows.....	36
2.3. Turbulent drag reduction by viscoelastic additives.....	38
2.4. Literature gap: Cavitation and viscoelasticity .....	41
2.4.1. Bubble dynamics in viscoelastic fluids .....	41
2.4.2. Vortex cavitation suppression by polymer injection.....	42
<b>3. Computational Methodology .....</b>	<b>43</b>
3.1. Governing equations .....	43
3.2. Turbulence modelling .....	44
3.2.1. RANS models .....	47
3.2.2. LES model .....	51
3.3. Cavitation modelling.....	51
3.3.1. Mechanical cavitation models.....	51
3.3.2. Thermodynamic cavitation model.....	54
3.4. Viscoelastic model .....	56
3.4.1. Viscoelastic model implementation .....	57
3.4.2. Viscoelastic model verification and validation .....	58
3.5. Test cases, boundary conditions and solution methods .....	65
3.5.1. Axisymmetric nozzle .....	65
3.5.2. Asymmetric nozzle .....	67

3.5.3.	Step nozzle .....	70
3.5.4.	Injector nozzle .....	72
<b>4.</b>	<b>Turbulence and Cavitation Models for Cavitation Simulation .....</b>	<b>75</b>
4.1.	Preliminary studies: Cavitation modelling validation .....	75
4.1.1.	Axisymmetric nozzle .....	76
4.1.2.	Asymmetric nozzle .....	84
4.2.	Turbulence modelling .....	88
4.2.1.	RANS Simulations .....	91
4.2.2.	Modifications of RANS models .....	93
4.2.3.	LES Simulations .....	95
4.3.	Cavitation Models .....	98
4.4.	Chapter summary .....	101
<b>5.</b>	<b>Cavitation in Viscoelastic Fluids.....</b>	<b>103</b>
5.1.	Step Nozzle .....	103
5.1.1.	Effect of fluid viscosity .....	104
5.1.2.	Effect of viscoelasticity on flow and cavitation .....	105
5.2.	Injector Nozzle .....	118
5.2.1.	Cloud cavitation and string cavitation.....	119
5.3.	Chapter summary .....	126
<b>6.</b>	<b>Conclusions and Future Work.....</b>	<b>128</b>
6.1.	Future work .....	129
	<b>Appendix A .....</b>	<b>132</b>
	<b>Appendix B .....</b>	<b>137</b>
	<b>Bibliography .....</b>	<b>139</b>

# List of figures

Figure 1-1. Microbubble in a liquid at rest .....	3
Figure 1-2. (a) Schematic of nozzle flow and the separated shear layer (b) incipient cavitation (c) developed cavitation (shadowgraphy images (Mauger, Méès, Michard, Azouzi, & Valette, 2012) dark regions indicate the cavitation vapours and grey is the liquid flow).....	5
Figure 1-3. Flow structures and cavitation vapours in a nozzle, flow structures are presented by means of second invariant of the velocity gradient which identifies the vortex cores (blue translucent iso-surfaces), cavitation structures are presented by the black iso-surface showing regions with 50% liquid and 50% vapour, (1) cavitation inception in the core of microvortices, (2) development of the re-entrant jet instability, (3) shedding of detached cavity cloud .....	6
Figure 1-4. Polyisobutylene polymer made from isobutylene monomers .....	6
Figure 1-5. Flow in a contraction/expansion geometry for (a) Newtonian and (b) viscoelastic fluids at $Re \approx 6$ (Campo-Deaño & Galindo-Rosales, 2011) .....	7
Figure 1-6. Cross flow geometry and the PIV measurement plane passing through the spiral vortex forming at the junction of the incoming streams (top), Streamlines and PIV measurements of the dimensionless vorticity for (a) water, (b) aqueous solutions of 0.001wt% and (c) 0.003 wt% polyethylene oxide (Burshtein et al., 2017) .....	8
Figure 1-7. Initially, reverse spherical micelles form, the micelles become cylindrical when salt is introduced in the additive composition and the electrostatic repulsion between the head groups is reduced, cylindrical micelles can entangle and form network microstructures when the fluid is subjected to shear stress (shear induced structures or SIS).....	10
Figure 1-8. Direct observation of formation of entangled micellar networks (c) from spherical micelles (a) by gradually increasing the shear stress (Keller et al., 1998).....	11
Figure 1-9. The intensity of scattered neutrons versus the scattering vector for the QAS additive blend at different concentrations (symbols) along with the model fits (continuous lines), spherical micelles start forming at concentrations as low as 10 ppm and they start to become elongated at 50 ppm (courtesy of Dr K. Trickett (Naseri et al., 2018)).....	14
Figure 1-10. Percentage change of discharge coefficient by addition of the QAS additive at different injection pressures and durations (courtesy of Dr N. Mitroglou (Naseri et al., 2018)).....	16
Figure 1-11. 3D view of the iso-surface of 50% liquid volume fraction in diesel with 1000 ppm QAS additive (transparent grey colour) and iso-surface of regions with 10% increased liquid volume fraction ( $\alpha_{Difference} = 0.1$ , blue colour) (courtesy of Dr N. Mitroglou (Naseri et al., 2018)) .....	17
Figure 1-12. (a) High speed X-ray phase contrast imaging of the cavitation vortex (string) forming under the injector needle,(b) FFT of the string radius fluctuations in base and additised fuels (courtesy of Dr I. Karathanassis (Naseri et al., 2018)) .....	18
Figure 1-13. Appearance of both cloud and string cavitation at higher cavitation number in the XCPI device, (a) the contour of time-averaged probability of vapour presence, (b) Mean cavity surface area	

along the nozzle for the base and the additised fuels, values calculated from the projected vapour area in the mid-plane (image courtesy of Dr I. Karathanassis) .....	19
Figure 2-1: Pressure difference versus mass flow rate for transition of non-cavitating flow to choked flow, CS refers to start of cavitation and CC is the critical cavitation point (Winklhofer et al., 2001) 25	25
Figure 2-2: Process of cavity shedding, from formation of the re-entrant motion to collapse of the separated bubbles (Sato & Saito, 2002) .....	28
Figure 2-3. Cavitation mechanisms inside a diesel injector nozzle .....	29
Figure 2-4 (a) Cavitation structures in cylindrical (top) and tapered (bottom) injector nozzles; in the cylindrical nozzle a cavity cloud covers the orifice surface area whereas in the tapered nozzle only string cavitation is visible (Gavaises et al., 2009), (b) enhancement of the spray cone angle due to string cavitation presence (Mitroglou et al., 2011) .....	30
Figure 2-5. Shadowgraph of cavitation structures appearing inside an injector replica (left) and X-ray reconstruction of the time-averaged cavitation volume fraction (right) (Mitroglou et al., 2016) .....	31
Figure 2-6. Dynamic behaviour of a string cavitation forming under the needle of an injector replica, white lines show the cavitation interface and images are taken with $1.5 \times 10^{-5}$ s intervals (I. Karathanassis, Koukouvinis, Kontolatis, et al., 2017) .....	31
Figure 3-1. Comparison of the standard and the modified eddy viscosity multipliers as a function of density .....	50
Figure 3-2. Graph showing the behaviour of the barotropic EoS and the speed of sound variation as a function of liquid density .....	55
Figure 3-3. Schematic presentation of the velocity profile inside the 2D channel flow .....	58
Figure 3-4. Comparison of the CFD code and the analytical solution for the PTT model; non-dimensionalized values for (a) the streamwise velocity, (b) normal viscoelastic stresses and (c) tangential viscoelastic stresses are presented in the channel at different viscosity ratios ( $\beta = \mu_s/\mu_0$ , where $\mu_0$ is the total viscosity $\mu_p + \mu_s$ ) for $\varepsilon = 0.25$ and $De = \lambda U/H = 1$ .....	61
Figure 3-5. (a) Schematic representation of the flow in the contraction, (b) streak line photography images showing the corner vortices and the flow path and (c) the computational grid with near-wall refinement for the simulations .....	62
Figure 3-6. Comparison of flow streamline images from the experimental study (green) and the PTT model predictions (grey) for CR 2.4 at different $De$ .....	64
Figure 3-7. Dimensionless corner vortex length at different Deborah numbers for contraction ratios of 2.4 and 4, the results are measured in the centre plane of the contraction geometry .....	64
Figure 3-8. Schematic of the axisymmetric nozzle test section with the main dimensions (all in mm), the flow path is shown using blue arrows .....	66
Figure 3-9. The computational domain and the grid used for the axisymmetric nozzle. (a) the geometry and flow path (blue arrows), the inlet tubes separated by $120^\circ$ are demonstrated in the inset, (b) magnified image shows the grid cross-section in more detail .....	66

Figure 3-10. Schematic of the asymmetric nozzle geometry and the flow direction (blue arrows), the main dimensions of the nozzle are presented (in mm), for full details of the test section geometry see (Koukouvini et al., 2017) .....	68
Figure 3-11. (a) The computational domain and the grid used for the asymmetric nozzle, (b) magnified image shows the grid cross-section in more details.....	69
Figure 3-12. (a) Geometry of the step nozzle and the relevant dimensions in mm, inlet boundary (red color) and outlet boundary (blue color) surfaces are shown; all the other surfaces are no-slip walls (gray color). (b) Computational grid with additional refinement inside the nozzle.....	70
Figure 3-13. (a) Simulation domain for the injector test case. The boundary conditions are indicated by coloured surfaces; inlet and outlet boundaries are coloured in red and blue, respectively, and the green surface shows the periodic boundary (another periodic boundary with the same cross section is located on the opposite side of the geometry); all the other surfaces are no-slip walls (grey colour), (b) The computational grid for the injector; the domain is partitioned using blocking and it is hex-dominant except from an unstructured tetrahedral section in the sac volume .....	73
Figure 4-1. Photography image of the cavitation cloud forming inside the nozzle for (a) incipient cavitation regime $CN = 0.95$ and (b) developed cavitation regime $CN = 1.5$ (Bauer et al., 2012).....	76
Figure 4-2. Effect of successive grid refinement on pressure distribution inside the cavitating nozzle, the area-averaged pressure values are calculated in several slices along the nozzle .....	76
Figure 4-3. (b) Pressure (b) and streamwise velocity distribution inside the nozzle predicted by the k- $\epsilon$ RNG model .....	77
Figure 4-4. Iso-surface of 70% vapour volume fraction artificially introduced at the nozzle inlet (a), cavitation vapours diminish after $\sim 1$ ms (b) (results predicted by the k- $\epsilon$ RNG model) .....	78
Figure 4-5. Time variations of the liquid fraction (solid line) and the turbulence kinetic energy dissipation rate (dashed line) at the nozzle entrance.....	78
Figure 4-6. Iso-surfaces of 70% vapour volume fraction at the nozzle inlet, cavitation vapours diminish after $\sim 10$ ms (results predicted by the k- $\omega$ SST model).....	79
Figure 4-7. Comparison of cavitation distribution inside the nozzle as shown by the experimental image and iso-surfaces of liquid fraction predicted by CFD for the $CN = 1.5$ condition. In the simulation results, five translucent iso-surfaces show regions of 5%, 30%, 50%, 70% and 90% liquid fraction.....	80
Figure 4-8. Cross sectional liquid fraction measurement locations along the nozzle are indicated at (a) 4.25 mm, (b) 19.25 mm, (c) 40.25 mm, (d) 59.75 mm, (e) 80.75 mm and (f) 94.25 mm downstream the nozzle entrance, the experimental and numerical values for the liquid fraction are compared side by side. Liquid fraction values higher than 100 represent the solid walls made of Perspex (all values are time-averaged) .....	81
Figure 4-9. (a) Pressure tapping measurements (experiment) and CFD predictions of pressure along the cavitating nozzle length, (b) spatially averaged liquid fraction measured using the X-ray CT and the corresponding predictions by CFD simulations.....	82
Figure 4-10. Distribution of TKE inside the nozzle and the experiment image of the cavitating flow	83

Figure 4-11. (a) Shadowgraphy image of the cavitation cloud (Koukouvinis et al., 2017) and (b) translucent iso-surfaces of liquid fraction ranging from 10% to 90%. .....	84
Figure 4-12. Time-averaged contours of liquid fraction in four slices along the nozzle (a) as measured by the X-ray CT experiment and (b) as predicted by RANS simulation .....	85
Figure 4-13. Average liquid fraction values in the nozzle, the experimental X-ray measurements are compared to the numerical predictions and the values are calculated in several slices along the nozzle .....	85
Figure 4-14. (a) Shadowgraphy images of the cavity cloud (b) and iso-surfaces of vapour fraction from the simulations, iso-surface values ranging from 10%-90% at 0.1 ms intervals, green circles in the shadowgraphy images indicate the bubbly cloud regions at the nozzle inlet with a foamy appearance and red circles show the small-scale vortices shedding from the cloud.....	86
Figure 4-15. Schematic demonstrating the unsteady cavitation cloud structures inside the nozzle (blue colour), the bubbly cloud at the entrance and the small-scale micro-cavities are the major source of discrepancy between the experiments and the CFD results .....	87
Figure 4-16. Effect of grid refinement on streamwise velocity profile predictions at $X = 1.5$ mm downstream the nozzle entrance (nozzle geometry and measurement location is shown in the inset). 90	90
Figure 4-17. Streamwise velocity and RMS of turbulent velocity at three locations downstream the nozzle inlet, experimental data are compared to the standard RANS models .....	92
Figure 4-18. Iso-surface of 50% vapour volume fraction predicted by the modified $k-\omega$ SST model, the cavitation vapours completely shed after a few cycles at $\sim 100 \mu\text{s}$ and the eventually only the liquid phase remains.....	93
Figure 4-19. Iso-surface of 50% vapour volume fraction (left) and contours of TKE in the nozzle midplane (right) as predicted by the modified $k-\omega$ SST model, results presented at the beginning of the simulation (a) and after $\sim 200 \mu\text{s}$ (b), black lines show regions below vapour pressure .....	94
Figure 4-20. Streamwise velocity and RMS of turbulent velocity at three locations downstream the nozzle inlet, Experimental data are compared the modified RANS models .....	95
Figure 4-21. Streamwise velocity and RMS of turbulent velocity at three locations downstream the nozzle inlet, results presented for LES simulations with different cavitation models .....	97
Figure 4-22. Indicative (a) pressure and (b) density contours in the nozzle midplane, (c) three instances of shadowgraphy images showing the in-nozzle vapour distribution in the experimental study (Sou et al., 2014). Black iso-lines in the pressure contour (a) indicate regions where the pressure drops below the saturation pressure and iso-surfaces of 75% liquid fraction are added to the density contours in (b).....	98
Figure 4-23. Contours of liquid fraction in the midplane of the nozzle predicted by the two-phase models (SS, ZGB and the modified ZGB) and the barotropic model.....	99
Figure 4-24. Instantaneous density contours for (a) standard ZGB model and (b) modified ZGB model at 0.1 ms intervals .....	100
Figure 5-1. Contours of time-averaged velocity (left) and liquid volume fraction (right) in the midplane, data presented for the standard viscosity fluid, reduced viscosity fluids (by factors of $\times 0.25$	



and x0.5) and increased viscosity fluids (by factors x2 and x4), the black iso-lines indicate regions with velocities higher than 18 m/s .....	105
Figure 5-2. Nozzle geometry and cavitation in the shear layer (top), contours of the velocity magnitude for the Newtonian and the viscoelastic fluid in the mid-plane of the nozzle, the black iso-lines show regions with pressures below the vapour pressure (bottom) .....	106
Figure 5-3. (a) Iso-surface of the second invariant of the velocity gradient with the value $1 \times 10^9 \text{ s}^{-2}$ coloured with the streamwise velocity,(b) 3D view of the iso-surface of the second invariant of the velocity gradient at $3 \times 10^9 \text{ s}^{-2}$ coloured with the streamwise velocity along with iso-surface of 50% vapour volume fraction (grey colour) .....	107
Figure 5-4. (a) Density variations inside the nozzle during three cavitation cycles, (b) magnitude of the streamwise vorticity, mean values are calculated in several planes along the nozzle length, (c) contour plots of streamwise vorticity inside the nozzle .....	108
Figure 5-5. Energy spectra inside the step nozzle for the Newtonian and the viscoelastic fluid, dashed lines (- - - - and - - - -) show indicative examples of the spectra and continuous lines (— and —) show the mean value of the spectra for the Newtonian and viscoelastic fluid.....	109
Figure 5-6. Comparison of time-averaged values of the streamwise velocity, RMS of streamwise velocity, RMS of wall-normal velocity and Reynolds stress ( $-u'v'$ ) in the Newtonian and the viscoelastic fluid, data are presented in the mid-plane of the step nozzle at four different X locations along the nozzle .....	110
Figure 5-7. Cavitation development inside the step nozzle presented by means of iso-surfaces of 50 % vapour volume fraction, data are presented every 0.1 ms. Small microcavities shedding from the cloud (blue circle 1) are not present in the viscoelastic fluid, cavitation vapours can initially shrink before growing (red circle 2) and elongated streamwise vortices appear between the detached cloud and the cavitation cloud (red circle 3 and 4).....	112
Figure 5-8. FFT of mass flowrate fluctuations at the outlet of the step nozzle for the Newtonian and the viscoelastic fluid, the dominant frequency corresponds to frequency of mass flowrate fluctuations induced by cyclic growth and shedding of large cavity clouds .....	113
Figure 5-9. Maximum pressures recorded for the Newtonian (top row) and the viscoelastic fluid (bottom row), images show from the side view (left) and in a 3D view (right) .....	115
Figure 5-10. Time-averaged data for pressure and vapour volume fraction inside the nozzles.....	116
Figure 5-11. (a) Average liquid volume fraction ( $1-\alpha$ ) in the step nozzle mid-plane along with iso-surfaces of 75%, 80% and 85% average liquid volume fraction in the Newtonian and the viscoelastic fluid, (b) Average liquid volume fraction ( $1-\alpha$ ) inside the cavitation cloud for the Newtonian and the viscoelastic fluid, values taken along 4 lines passing through the cavitation cloud in the nozzle mid-plane.....	117
Figure 5-12. Pressure spectrum inside the nozzle for the Newtonian and the viscoelastic fluid showing the additive can either increase or decrease the local pressure, depending on the flow scale (a) Probability of cavitation inception at $X = 2 \text{ mm}$ for the Newtonian and the viscoelastic fluid (b).....	118

Figure 5-13. (a) Two distinct cavitation regions forming inside the injector nozzle, cavitation vapours are presented using 5 translucent vapour volume fraction iso-surfaces ranging from 0.1 to 1, cavitating vortex is presented by streamlines coloured with pressure, (b) Indicative cavitation structures inside the nozzle at 20  $\mu\text{s}$  intervals ( $0.1 < \alpha < 1$ ) showing a larger string cavity in the viscoelastic fluid. .... 119

Figure 5-14. (a) Separated vapour volume fraction regions inside the injector nozzle showing the cloud cavitation and the string cavitation in term of iso-surfaces of 80% vapour volume fraction, (b) Development of the string cavitation (dotted lines  $\bullet\bullet\bullet\bullet\bullet$  and  $\bullet\bullet\bullet\bullet\bullet$ ), the cloud cavitation (dashed lines  $-\ -$  and  $-\ -$ ) and the total vapour volume fraction (continuous lines  $-\ -$  and  $-\ -$ ) inside the injector nozzle for the Newtonian and the viscoelastic fluid calculated in several slices along the nozzle axis using area weighted averages, error bars indicate the overlap of the vapour volume fraction in the string and cloud region in  $\pm 40\mu\text{m}$  in the vicinity of the nozzle axis, (c) Normalized helicity ( $H_n$ ) contours in four slices inside the injector nozzle (at  $X = 0.2\text{ mm}, 0.5\text{ mm}, 0.8\text{ mm}$  and  $1.1\text{ mm}$ ), the black iso-lines show the regions of  $H_n = 0.95$  and  $H_n \rightarrow 1$  in vortex cores..... 120

Figure 5-15. (a) and (b) evaporation and condensations rates computed by the mass transfer rate cavitation model in the cloud and the string cavitation region of the Newtonian and the viscoelastic fluid, (c) vortical flow structures in the vicinity of the injector nozzle entrance plotted using the contours of second invariant of the velocity gradient (Q-criterion) in the nozzle mid-plane and translucent iso-surfaces of Q-criterion at  $5E+12\text{ s}^{-2}$ ..... 122

Figure 5-16. (a) Vortex structures inside the sac volume visualized using the iso-surface of second invariant of the velocity gradient at  $4E+12\text{ s}^{-2}$ , (b) velocity fluctuations inside the nozzle plotted in terms of RMS of X,Y and Z velocities, values obtained from surface-averaged data calculated in slices along the nozzle ..... 124

Figure 5-17. Schematic representation of the additive effect on the cavitating vortices, black arrows indicate the cavitating vortices and the red arrow shows the axis of rotation of the vortices, cavitation is presented by the blue clouds and the micelles are presented by yellow worms. (a) Cavitating vortices in the recirculation region in the Newtonian fluid (top) and the viscoelastic fluid (bottom), micelles align with the flow and suppress vortices rotating out of the nozzle cross sectional plane, (b) Vortex (string) cavitation under the needle in the Newtonian fluid (top) and the viscoelastic fluid (bottom), perturbations by the turbulent eddies can decay the string coherence and breakup the cavitating vortex, micelles can reduce the flow turbulence and contribute to development of a more stable longitudinal vortex and cavity core. .... 125

## List of tables

Table 3-1. Thermodynamic properties used for water and diesel in two-phase models..... 54

Table 3-2. Thermodynamic properties used for water in barotropic model..... 55

Table 3-3. Test case conditions and the non-dimensional vortex length values measured experimentally and numerically for contraction ratios 2.4 and 4. Deborah number is defined based on velocity and channel length inside the contraction  $De = \lambda U_2/H_2$ ..... 63

Table 3-4. Static pressure values used at the inlet and outlet boundaries for the simulations ..... 74

Table 4-1. Grid parameters and their effect on inlet pressure convergence..... 90

# Glossary of terms

## Symbols and abbreviations

B	Liquid bulk modulus (Pa)
C	Speed of sound (Pa.Kg/m <sup>3</sup> )
CFD	Computational fluid dynamics
CFL	Courant–Friedrichs–Lewy
CN	Cavitation number
CR	Contraction ratio
DCA	Deposit control additive
De	Deborah number
EoS	Equation of state
FFT	Fast Fourier transform
H <sub>n</sub>	Normalized helicity
k	Turbulent kinetic energy (m <sup>2</sup> /s <sup>2</sup> )
LDV	Laser Doppler velocimetry
LES	Large eddy simulation
PISO	Pressure implicit with splitting of operator
PTT	Phan-Thien-Tanner
P <sub>v</sub>	Vapor pressure (Pa)
P <sub>sat</sub>	Saturation pressure (Pa)
QAS	Quaternary ammonium salt
QUICK	Quadratic upstream interpolation for convective kinetics
R	Mass transfer rate (Kg/m <sup>3</sup> .s)
ℜ <sub>B</sub>	Bubble radius (m)
RANS	Reynolds-averaged Navier–Stokes
Re	Reynolds number
RMS	Root mean square
RNG	Renormalization group
RSM	Reynolds stress model
S	Surface tension (N/m)
SIMPLE	Semi-implicit method for pressure-linked equations
SS	Schnerr-Sauer

SST	Shear stress transport
St	Strouhal number
T	Time (s)
tr	Tensor trace
UDF	User defined function
URANS	Unsteady
$u_\tau$	Friction velocity (m/s)
ZGB	Zwart-Gerber-Belamri
WALE	Wall-adapting local eddy-viscosity
$Y^+$	Dimensionless wall distance

### Greek Symbols

$\Pi_a$	Second invariant of the velocity gradient tensor ( $1/s^2$ )
$\alpha$	Vapour volume fraction
$\beta$	Viscosity ratio
$\delta_{ij}$	Kronecker delta
$\dot{\gamma}$	Shear rate ( $1/s$ )
$\lambda$	Polymer relaxation time (s)
$\lambda_g$	Taylor length scale (m)
$\varepsilon$	Dissipation rate ( $m^2/s^3$ )
$\varphi$	Probability
$\mu$	Dynamic viscosity (Pa.s)
$\mu_p$	Polymer viscosity ( $m^2/s$ )
$\mu_s$	Solvent viscosity ( $m^2/s$ )
$\mu_t$	Turbulent viscosity ( $m^2/s$ )
$\rho$	Density ( $kg/m^3$ )
$\rho_l$	Liquid density ( $kg/m^3$ )
$\rho_v$	Vapour density ( $kg/m^3$ )
$\tau$	Stress (Pa)
$\tau_v$	Viscoelastic stress (Pa)
$\tau_w$	Wall shear stress (Pa.s)
$\nu$	Kinematic viscosity ( $m^2/s$ )
$\omega$	Specific dissipation rate ( $1/s$ )



# 1.Introduction

---

Advances in fuel injection equipment represent a key technology for meeting forthcoming emission regulations and mitigating the environmental impacts by improving fuel economy. As energy demand increases to meet the growing society needs associated with the expansion of urbanisation, population growth and increased car ownership, particularly in developing economies, the CO<sub>2</sub> and soot emissions will also escalate. Increasing the fuel injection pressure can reduce the soot emissions; however, it will also increase the amount of cavitation, which can induce material erosion due to bubble collapse inside the injector. In addition, pressurisation of fuel to such extreme levels absorbs a non-negligible amount of useful work produced by the engine. Thus, even small improvements to the rheological characteristics of the fuel can lead to significant energy savings.

Moreover, impurities in the fuel composition may lead to formation of deposit layers on injector parts, altering its internal geometry and significantly blocking the fuel flow. Such effects degrade the injector's performance, reduce atomisation quality and result in excess and uncontrollable emissions, regardless of the legislation limits the engine met when new (Barker, Richards, Snape, & Meredith, 2011). Injector fouling problems become even more pronounced by large variations of diesel and biodiesel fuel blends. Thus, the use of additives to keep injectors deposit-free is essential for today's engines. However, due to their proprietary nature, the mechanisms by which the additives affect the injector flow and cavitation are largely missing from the literature.

The current investigation was initiated when it was discovered that some compositions of deposit control additives containing quaternary ammonium salts (R Barbour, 2011) have the ability to increase the volumetric efficiency of clean diesel/biodiesel fuel injectors by up to 5% (Robert Barbour, Quigley, & Panesar, 2014). Further investigations revealed that the main difference between this additive and traditional deposit control additives is formation of elongated micelles which can induce viscoelasticity properties in this fuel composition (I. K. Karathanassis et al., 2018; Naseri et al., 2018).

In this chapter, a brief background regarding the physical characteristics of cavitating nozzle flows and viscoelastic fluids is presented. Furthermore, diesel fuel additives and the role of detergents in the fuel injection systems is discussed. Finally, the research question leading to the current study is presented in the context of previous flow measurements and further X-ray and SANS measurements that were conducted concurrently during this research project.

## **1.1. Cavitation in nozzle flow**

Cavitation is the phenomenon of vapour formation in flow regions where the local pressure drops below the saturated vapour pressure. The pressure in a liquid flow can drop due to different mechanisms such as flow acceleration, recirculation or pressure oscillations (Brennen, 2013). Phase change can be best described in the context of phase diagrams covering the thermodynamic properties of solid, liquid and gaseous phases. Vapour and liquid can coexist in the dome shaped mixture region between the vapour and the liquid saturation curves. If no nucleation sites are present in the liquid phase (i.e. pure liquid) vapour structures do not form when the fluid is depressurized. At this stage, liquid is under “tension”, where it can withstand negative pressures without phase change and can stay for a certain time in this “metastable” condition. However, in engineering systems, nuclei is always present and phase change occurs at the weak solid-liquid interface. While negative pressures have been found in delicate experiments in liquids (for example see (Brennen, 2013), (Caupin & Stroock, 2013) and (Franc & Michel, 2005)), the existence of such cases in industrial scales is questionable and for water in cavitation tunnels, evidence suggests that pressure in the cavity region matches the saturation pressure (Washio, 2014).

Cavitation can begin from pre-existing microbubbles inside the liquid that grow as the pressure drops. If a microbubble is in equilibrium with the surrounding liquid at rest, pressure inside the

bubble is higher than the surrounding pressure due to the effect of surface tension. Hence, the pressure balance for equilibrium of the interface can be written as:

$$P_g + P_v = P_\infty + \frac{2S}{R} \quad \text{Equation 1.1}$$

where  $P_g$  and  $P_v$  are pressures of the gas and vapour inside the bubble,  $P_\infty$  is the surrounding liquid pressure,  $S$  is the surface tension and  $R$  is the bubble equilibrium radius. Figure 1-1 shows the schematic of a microbubble inside a liquid and the corresponding pressures.

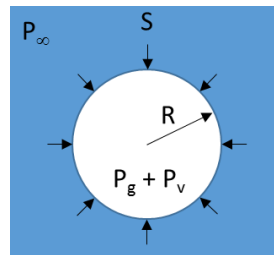


Figure 1-1. Microbubble in a liquid at rest

As the pressure in the surrounding liquid is reduced, the microbubble expands and the oscillations of the bubble radius are governed by Rayleigh-Plesset equation for bubble dynamics (Plesset, 1949; Rayleigh, 1917):

$$R \frac{d^2R}{dt^2} + \frac{3}{2} \left( \frac{dR}{dt} \right)^2 + \frac{4\mu_L}{R} \frac{dR}{dt} + \frac{2S}{\rho_L R} + \frac{\Delta P(t)}{\rho_L} = 0 \quad \text{Equation 1.2}$$

where  $\mu_L$  is the liquid viscosity and  $\rho_L$  is the liquid density.

Cavitation in a liquid flow occurs when the total stress (pressure plus the deviatoric stress) falls below the vapour pressure (Joseph, 1995). This criterion suggested by Joseph, indicates that cavitation occurs at any point that tension exceeds a threshold, regardless of the values of other principal stresses. Therefore, unlike a liquid at rest where pressure must definitely be below the vapour pressure for cavitation to occur, in a flowing liquid cavitation can happen due to shear stress even when pressure values are above the vapour pressure.

Classical scaling theory implies that the flow regime remains the same when the conditions are scaled up. However due to “scale effects” which arise from changes in the velocity, size, fluid properties and bubbles distribution, this theory does not apply to cavitating flows (Stinebring,



Billet, Lindau, & Kunz, 2001). Scale effects can be divided into two groups; “viscous effects” and “bubble dynamics effects” (Martynov, 2005). Viscous effects make changes in the local pressure field of the liquid surrounding the cavitation bubbles. These include the effects of turbulent pressure fluctuations and geometry imperfections due to surface roughness and manufacturing errors. Bubble dynamics effects have an impact on the behaviour of bubbles formation, growth and collapse. Temperature variations, surface tension, effect of non-condensable gases and micro bubbles in the flow are some of the factors that can affect the bubble dynamics.

Studies of cavitation and bubble dynamics have been the subject of research for more than a century with applications that span across areas such as pumps and turbines, fuel systems and lubricants and biomedical applications. Inside a fuel injector nozzle, cavitation vapours can significantly block the flow passage area and hence reduce the nozzle discharge coefficient. One of the first studies that investigated in-nozzle flow cavitation was carried out by Bergwerk (Bergwerk, 1959) in diesel injector nozzles. This study shows that in non-cavitating flow regimes, the discharge coefficient is mostly a function of the Reynolds number ( $Re = UD/\nu$ , where  $U$  and  $D$  are the characteristic velocity and length scale of the flow respectively and  $\nu$  is the kinematic viscosity). However, in cavitating flow conditions, the cavitation number effect becomes more dominant and therefore cavitating flows are better described by means of cavitation number (see also (D. P. Schmidt, Rutland, & Corradini, 1999b)).

Various formulations are used in the literature to classify cavitation regimes, in the current study, the cavitation number based of the definition proposed by Bergwerk for nozzle flows (Bergwerk, 1959) will be employed:

$$CN = \frac{P_1 - P_2}{P_2 - P_v} \quad \text{Equation 1.3}$$

where  $P_1$  and  $P_2$  are the pressure upstream and downstream of the nozzle and  $P_v$  is the vapour pressure.

As the flow enters the nozzle, a strong streamline curvature forms due to the sharp turn in the flow direction. This results in the separation of the boundary layer and formation of a recirculation zone at the nozzle entrance, which reduces the cross sectional area for the main flow passage as demonstrated in Figure 1-2. Furthermore, due to the velocity difference

between the recirculating flow and the main flow ( $V_R$  and  $V_M$ ) a shear layer forms between these two regions that induces further flow instabilities. Cavitation can be induced in the core of microvortices that are produced by the shear layer instability and as the cavitation number is increased, small vapour pockets merge to form larger cavity clouds.

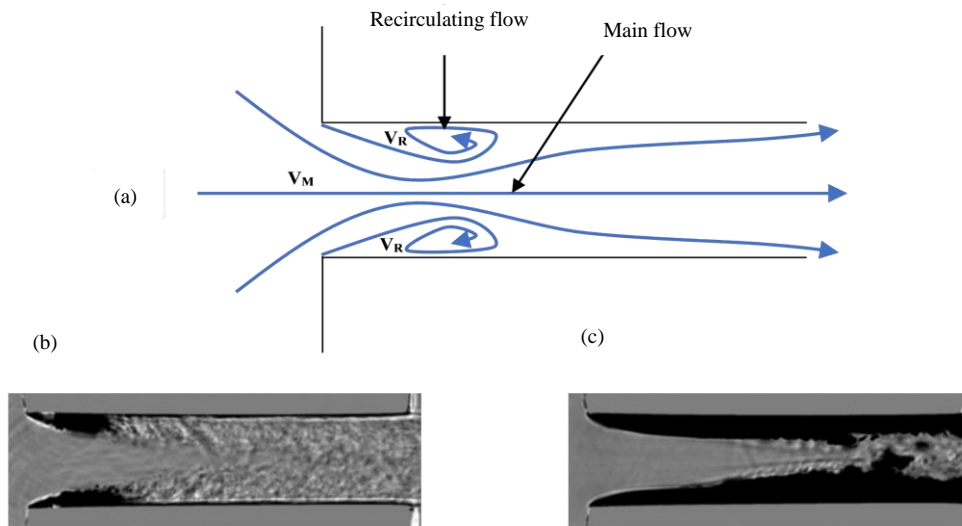


Figure 1-2. (a) Schematic of nozzle flow and the separated shear layer (b) incipient cavitation (c) developed cavitation (shadowgraphy images (Mauger, Méès, Michard, Azouzi, & Valette, 2012), dark regions indicate the cavitation vapours and grey is the liquid flow)

The mass flowrate through the nozzle is a function of the difference between the upstream and downstream pressure ( $P_1 - P_2$ ) such that the mass flowrate is enhanced as  $\Delta P$  is increased. As the cavitation number is increased, vapour structures cover a large area of the nozzle and fill the lower and upper nozzle surfaces. At this point, the mass flowrate reaches a maximum value and it remains constants as  $\Delta P$  is further increased (choked flow condition) (Mauger et al., 2012; Nurick, 1976).

Formation and evolution of cavitation cloud structures is described by a schematic using a simulation instance in Figure 1-3 which shows cavitation development in a step nozzle. Initially, small-scale microcavities appear in the core of the shear layer vortices emerging in the separated flow between the recirculating flow region and the main flow passing through the nozzle (label 1). As these vortices grow and the pressure drops in their core, the size of the cavitation vapours increases and they are convected downstream the nozzle. A re-entrant jet instability (label 2) forms before the cavity closure region due to the adverse pressure gradient in the recirculation region (Callenaere, Franc, Michel, & Riondet, 2001). The re-entrant jet travels upstream toward the nozzle entrance and cuts the liquid/vapour interface, forming a

detached cavity cloud. The detached cloud (label 3) is convected towards the nozzle exit by the motion of larger eddies in a turbulent flow region containing a combination of streamwise, spanwise and hairpin vortices (Altimira & Fuchs, 2015). The re-entrant jet instability has a periodic motion that results in cyclic growth and shedding of the cavity cloud. The Strouhal number ( $St = fL/U$ , where  $f$  is the cloud shedding frequency,  $L$  is the cavity length and  $U$  is the re-entrant jet velocity) is in the range of 0.2-0.4, irrespective of the operating conditions and the cavity length (Callenaere et al., 2001).

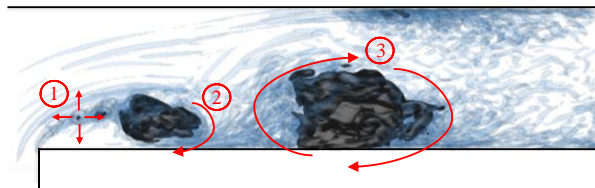


Figure 1-3. Flow structures and cavitation vapours in a nozzle, flow structures are presented by means of second invariant of the velocity gradient which identifies the vortex cores (blue translucent iso-surfaces), cavitation structures are presented by the black iso-surface showing regions with 50% liquid and 50% vapour, (1) cavitation inception in the core of microvortices, (2) development of the re-entrant jet instability, (3) shedding of detached cavity cloud

More recently, X-ray densitometry of cavitation void fraction in a cavity cloud identified that in addition to the re-entrant jet motion, bubbly shock propagation due to reduction of speed of sound in the liquid/vapour mixture region is also responsible for the shedding of the cavity cloud (Ganesh, Makiharju, & Ceccio, 2016).

## 1.2. Viscoelastic fluids

Polymers are large molecules made of smaller structural units called monomers. For example, a class of detergents commonly used as fuel additives is amines with a polyisobutylene tail, and polyisobutylene is made from isobutylene monomers:

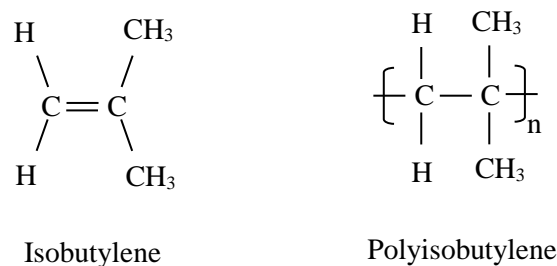


Figure 1-4. Polyisobutylene polymer made from isobutylene monomers

The configuration of a polymer can change as it is stretched due to stress or thermal effects and the time scale associated with these changes is known as the “relaxation time”. It is then possible to say that the polymer has a “fading memory” due to the relaxation time required for the polymer to get back to its equilibrium configuration. In Newtonian fluids however, equilibrium state is reached as soon as the stress disappears and the flow is stopped. Polymeric solutions are non-Newtonian and therefore, the shear rate is not linearly proportional to the shear stress. The Non-Newtonian property of viscoelastic fluids is attributed to structural changes or the orientation of particles in the fluid flow. A property of polymeric solutions is that on top of the Newtonian shear stress, they add an extra stress component along the streamline (Bird, Armstrong, Hassager, & Curtiss, 1977). The extra stress is usually measured by means of the “first normal stress difference”, that is the difference between the streamwise stress and the wall-normal stress. The “second normal stress difference” is the difference between the wall-normal and spanwise stresses which has a magnitude much smaller than the first normal stress difference.

In order to characterise the properties of polymeric solutions, various rheological parameters such as storage modulus  $G'$ , loss modulus  $G''$ , shear viscosity  $\mu$ , dynamic viscosity  $\eta'$ , polymer viscosity  $\mu_p$  and polymer relaxation time  $\lambda$  should be measured at a range of strain rates. Due to the complex behaviour of viscoelastic fluids, it is difficult to define general rheological relations to describe their properties and usually experimental measurements are conducted to define the properties of individual solutions. Extensional viscosity is usually used to define the resistance of viscoelastic fluids when they are subjected to pure extensional (normal) stress and usually polymers with higher molecular weight have higher extensional viscosities and relaxation times.

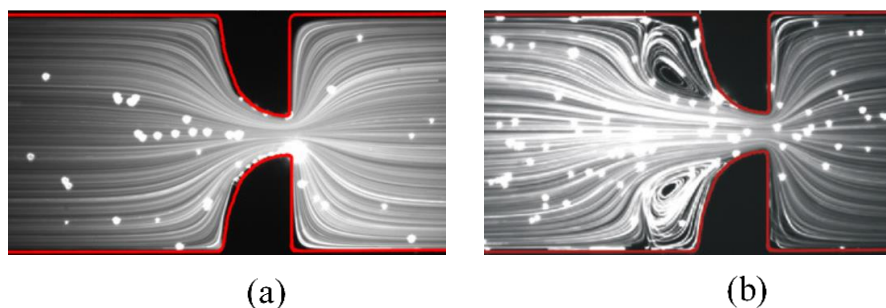


Figure 1-5. Flow in a contraction/expansion geometry for (a) Newtonian and (b) viscoelastic fluids at  $Re \approx 6$  (Campo-Deaño & Galindo-Rosales, 2011)

The viscoelastic stress effect is observed in many benchmark flow configurations such as the flow around a sphere, rotating disk-cylinder, rising bubble and jet breakup and whether it causes flow stabilization or destabilization largely depends on the specific flow configuration.

An example of the additional viscoelastic stresses can be demonstrated in flow near a sudden contraction at low Reynolds numbers ( $Re \approx 6$ ) in Figure 1-5. In case of the Newtonian fluid, all the flow upstream of the contraction enters the small tube without forming any recirculation zone before the entrance due to the low Reynolds number. However, in the polymeric solution a large recirculation region forms before the entrance. At higher Reynolds numbers corner vortices develop in the Newtonian fluid after the expansion, however in the viscoelastic fluid these corner vortices are completely suppressed. (Campo-Deaño & Galindo-Rosales, 2011). This is because in contraction flows, vortex growth is inhibited by increasing the Reynolds number, but the situation is reversed in expansion flows where inertial effects stimulate the vortex growth, likewise the polymer extensional viscosity affects each flow region differently.

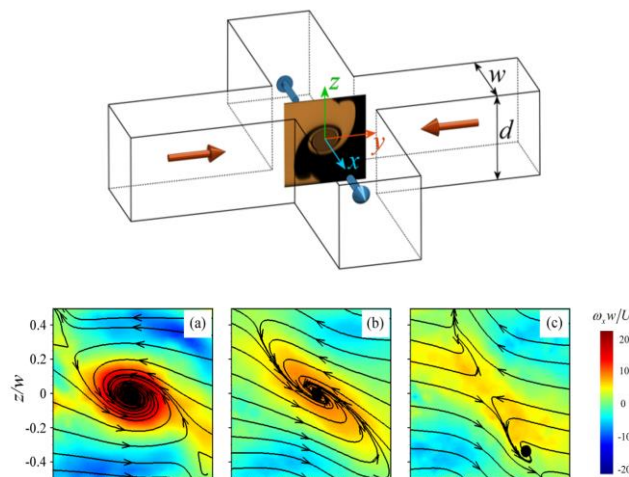


Figure 1-6. Cross flow geometry and the PIV measurement plane passing through the spiral vortex forming at the junction of the incoming streams (top), Streamlines and PIV measurements of the dimensionless vorticity for (a) water, (b) aqueous solutions of 0.001wt% and (c) 0.003 wt% polyethylene oxide (Burshtein, Zografos, Shen, Poole, & Haward, 2017)

The flow in a pair of cross-slots channels can demonstrate the ability of polymers in suppressing the instabilities (Burshtein et al., 2017). The two incoming streams of fluids move in the opposite directions form a spiral vortex core as the flow exists from adjacent channels positioned at  $90^\circ$  with respect to the inlet channels. In Figure 1-6 the flow configuration, streamlines and PIV measurements of vorticity are presented for water and viscoelastic solutions of water and polyethylene oxide. It is evident that by adding polymers and increasing the polymer concentration, the vorticity in the core of the vortex is significantly reduced while

the vortex formation is inhibited. These results indicate that even by adding a very small concentration of high molecular weight polymers to a fluid, the flow instabilities can be suppressed by the action of the polymer torque.

It is known that addition of minute amounts of high molecular weight polymers to a solution can reduce the turbulent drag in the flow passing through a pipe. Turbulent drag reduction (DR) by viscoelastic additives is referred to as Toms effect after the first scientist who discovered this property (Toms, 1948). Since then, DR by additives has been studied extensively numerically and experimentally and the knowledge is applied in oil delivery pipelines or district heating/cooling systems to reduce the turbulent drag, heat losses and the pumping costs.

### **1.3. Detergents and surfactant micelles**

Fuel injectors operate at high injection pressures (>2000 bar) and they have small hole diameters (<0.2 mm) in order to achieve optimum fuel atomization, improve fuel and combustion efficiency and eventually reduce emissions. However, at high temperatures unstable components of the fuel can oxidise and form deposit layers that alter the internal geometry of the injector. Because of the small size of nozzle holes, deposits can significantly block the fuel flow in the injector and reduce the engine efficiency. Additives are blended with diesel fuel in order to improve its properties, they can enhance the performance of the fuel and engine in several ways including:

- Improving the combustion process and reduce emissions
- Improving the fuel flow and lubricity
- Removing deposits in the fuel injection system and help engine cleanliness

Diesel fuel injectors are carefully designed, as the injector cleanliness is critical to fuel atomization, mixture formation and subsequently improving combustion efficiency and reduction of fuel consumption and emissions. Deposits formed in tubes of the exhaust gas recirculation system can result in engine knocking and increase NO<sub>x</sub> emissions and deposit build-up-inside the injector nozzles, results in power loss due to reduction of the fuel flow.

Deposit control additives (DCAs or detergents) are usually made of polyalkenyl-succinic-acid derivatives, Mannich bases and ashless polymeric compounds and have a polar head group and a nonpolar tail. The polar head attaches to the deposit precursor and prevents deposit formation

while neutralizing acid activities (dispersant effect/keep-clean effect). A thin layer of additive film covers the metal parts and prevents the formation of new deposit (protective effect). Moreover, the polar head of detergent molecules attaches to deposit layers and removes them from the metal surfaces (clean-up effect). In multifunctional additive packages, deposit control additives are combined with other additives such as antioxidants, antifoam additives, metal deactivators, corrosion inhibitors and cetane improvers (Srivastava & Hancsok, 2014).

As mentioned earlier, polymeric solutions are known for their turbulence suppression properties. Adding small quantities of certain polymers to Newtonian fluids (in some cases as low as a few ppm) induces viscoelastic properties and generally such effects intensify as the polymer concentration increases. For instance, low concentrations of high molecular weight Polyisobutylene (PIB) in oil pipelines are used as drag reducers in treat rates of 10-20 ppm (Mowla & Naderi, 2006). Addition of polymers can alter the dynamics of flow such as laminar to turbulent transition, formation and shedding of vortices and transport of mass, momentum and energy in the flow. Increasing the ratio of counter-ions to surfactants can induce high extensional viscosity, overshoot in normal and shear stress and increase the drag reduction property of viscoelastic fluids. Moreover, viscoelastic surfactant additives are also used in enhanced oil recovery applications to decrease the interfacial surface tension.

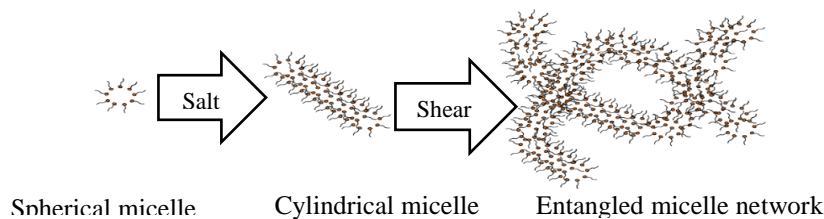


*Figure 1-7. Initially, reverse spherical micelles form, the micelles become cylindrical when salt is introduced in the additive composition and the electrostatic repulsion between the head groups is reduced, cylindrical micelles can entangle and form network microstructures when the fluid is subjected to shear stress (shear induced structures or SIS)*

Lurizol<sup>®</sup> diesel fuel deposit control additive compositions can increase the mass flowrate through clean (deposit-free) injection systems, resulting in power gains up to 5% depending on the type of engine (R Barbour, 2011; Robert Barbour et al., 2014). The main novelty of the aforementioned additive is introduction of quaternary ammonium salts to the traditional Polyisobutylene Succinimide (PIBSI) detergent formulation. The flow enhancement effect is attributed to formation of cylindrical micelles by addition of QAS counter-ions to the additive, which can induce viscoelastic properties in the fuel composition.

urfactant molecules can form spherical micelles as the hydrophobic tail dissolves in the non-polar fuel and the hydrophilic head groups of the surfactant gather in the centre of the micelle (see Figure 1-7). In presence of added salt or electrolytes, surfactant micelles can cluster to form long rodlike micelles that can entangle under shear stress and form network structures. The salt acts by screening the electrostatic repulsion between the charged particles, thus increasing the ionic strength and allowing surfactant molecules to join. When the length of the rodlike micelles increases, they bend and form wormlike micelles (J. Yang, 2002). Figure 1-7 demonstrates the transition of initially spherical micelles to rod-like micelles and finally to entangled networks by addition of salt and shear stress. These network structures are known as shear induced structures (SIS) and can be directly visualised by freeze-fracture electron microscopy (Keller, Boltenhagen, Pine, & Zasadzinski, 1998).

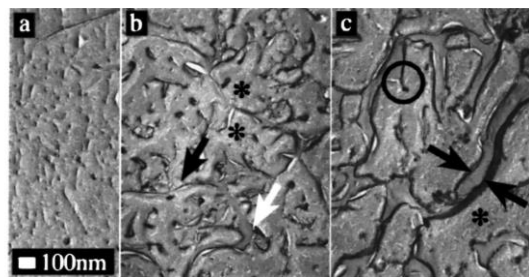


*Figure 1-8. Direct observation of formation of entangled micellar networks (c) from spherical micelles (a) by gradually increasing the shear stress (Keller et al., 1998)*

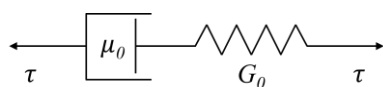
Figure 1-8 shows the transition from spherical/rodlike micelle to wormlike micelles and finally entangled micelle networks in a solution of TTAA (tris (2-hydroxyethyl) tallowalkyl ammonium acetate) and NaCl (Keller et al., 1998). Viscoelastic properties can also be present in surfactant solutions where only long rod-like micelles form (i.e. without any evidence of network structures under shear stress).

Due to formation of the rodlike micelles in the fluid, the shear modulus increases and this effect is intensified as the salt concentration increases (Cates & Candau, 1990). However, above a critical micelle concentration, spherical micelles can form again and the viscoelasticity effect is diminished. In linear viscoelastic fluids, either the viscosity or the elasticity property may be dominant depending on the time scale of the experimental measurements. Typically when the experiment time is short and measurements are taken at a fast pace, the elasticity effect becomes more dominant, whereas in longer experimental time scales the viscosity effect can be more significant (Fischer & Rehage, 1997).



Long-chain polymer additives can break under strong shear stress or in high temperatures without returning to their original structure after destruction, and so they lose their viscoelasticity and drag reduction effect. On the other hand, entangled micelle networks in surfactant additives have a more dynamic nature. The main difference in the microstructure between the polymer additives and surfactant additives is that the latter can recombine after breaking, i.e. the surfactant solutions can restore their viscoelastic properties even after breaking. The surfactant networks are in thermodynamic equilibrium with surfactant monomers and molecules are constantly exchanged between the solution and the network, which makes the breaking mechanism reversible. The ability of surfactant additives to self-assemble after breaking renders them beneficial for applications such as fuel injector where the fuel undergoes a lot of shear stress while passing through various parts of the fuel injection equipment and before reaching the injector holes. The high temperatures in diesel injectors can have an adverse effect on the additive effect and reduce the viscoelasticity of the fuel composition. Nonetheless, entangled micelle networks can also demonstrate thermo-thickening properties, i.e. some low viscous micellar solutions become highly viscoelastic by increasing the temperature (Feng, Chu, & Dreiss, 2015), therefore it is necessary to investigate the thermal response of individual solutions to determine their response at high temperatures.

The viscoelastic behaviour of surfactant solutions fits approximately with a Maxwellian fluid model where a damper and a spring in series are used to model the viscoelastic stress. Therefore, the Maxwell fluid model consists of a viscous stress and an elastic stress part:



The diagram shows a mechanical model of a Maxwell fluid. It consists of a damper (represented by a rectangle with a vertical line) and a spring (represented by a zigzag line) connected in series. A horizontal line passes through both, with arrows pointing outwards from each end, labeled with the Greek letter tau (τ). The damper is labeled with mu\_0 (μ₀) and the spring is labeled with G\_0 (G₀).

$$\tau + \lambda \frac{\partial \tau}{\partial t} = \mu_0 \dot{\gamma} \quad \text{Equation 1.4}$$

where  $\tau$  is the shear stress,  $\mu_0$  is the zero shear viscosity,  $\lambda$  is the polymer relaxation time and  $\dot{\gamma}$  is the shear rate. The relaxation time is defined as the ratio of viscosity and the shear modulus  $G_0$  ( $\lambda = \mu_0 / G_0$ ) (Bird et al., 1977).

However at regions of high shear in entangled polymers, flow properties become non-linear and constitutive equations like Giesekus model (Giesekus, 1982) or Phan-Tien-Tanner model (Thien & Tanner, 1977) are required to describe the flow dynamics. These models are able to predict stress overshoots, non-vanishing second normal stress difference and limiting shear stress at high velocity gradient regions (Fischer & Rehage, 1997).

## 1.4. Current investigation

The current investigation was triggered when some compositions of deposit control additives demonstrated the ability to increase the engine power output above the baseline power, even in clean (deposit-free) injectors (Robert Barbour et al., 2014). Traditional DCAs can clean-up the injector deposits and ideally, return the engine power to the initial value of a deposit-free injector. However the new Lubrizol DCA containing quaternary ammonium salts, can increase the power above the baseline level up to 5% in various engine tests (Robert Barbour et al., 2014), an effect referred to as “*power gain*” in the original study. The change in the fuel flow was simultaneously measured, indicating that the specific fuel consumption remained unchanged during the tests. Further investigations that are presented in this section confirm that the increase of power is due to increase of flowrate in the fuel injection system. However, the underlying mechanism for this phenomenon is not understood and describing the *power gain* mechanism is challenging as the additive does not significantly alter the physical properties of the fuel such a density and viscosity. Quaternary ammonium surfactants with appropriate counter-ions can be very effective in reducing the turbulent drag in aqueous solutions (Lu et al., 1998), however, less is known about the effect of such surfactants in oil-based solvents or in cavitating flow conditions.

Studies about the interaction of viscoelasticity and cavitating flows are scarce in the literature. A study on tip vortex cavitation in propellers showed that addition of small amounts of high molecular weight polymers in water can delay cavitation inception (Chahine, Frederick, & Bateman, 1993). The effect of viscoelasticity on single bubble dynamics has also been studied experimentally and numerically (E. A. Brujan, Ohl, Lauterborn, & Philipp, 1996a; E A Brujan, 1999; E A Brujan, Ikeda, & Matsumoto, 2004; Dollet, Marmottant, & Garbin, 2018; Fogler & Goddard, 1970; Tanasawa & Yang, 1970; W. Yang & Lawson, 1974). However, there are no studies in the literature investigating the effect of viscoelasticity on turbulent cavitating flows, such as those realised in high-pressure fuel injectors.

This thesis investigates the effect of viscoelasticity on injector flows in a numerical framework and the relevant experimental studies conducted simultaneously by collaborators in the project are also presented in this section. The concurrent studies include small angle neutron scattering (SANS) for investigation of micelles self-assembly in the additive, injector flowrate measurement in tapered and cylindrical nozzles, X-ray micro computed tomography (micro-CT) and high-flux X-ray phase contrast imaging (XPCI) in nozzle replicas to identify the

additive effect in various cavitation regimes. Finally, a hypothesis regarding the effect of the additive on cavitating vortices is developed based on the experimental observations, which will be presented at the end of this section.

### 1.4.1. Surfactant aggregation properties of the deposit control additive

SANS studies conducted by Lubrizol provide evidence for the viscoelastic property of the QAS additive (Naseri et al., 2018). The time-of-flight instruments LOQ and SANS2D at the ISIS spallation source located at the Rutherford Appleton Laboratory, UK were used for the SANS experiments.

During spallation,  $H^-$  ions are accelerated and then stripped of their electrons by a thin aluminium oxide film, producing high energy  $H^+$  ions. These ions are further accelerated using a circular synchrotron and then used to bombard a heavy-metal target producing pulses of neutrons which are directed to the sample for the SANS measurements. The observed scattering is dependent on both the wavelength of the incoming radiation and the scattering angle, which can be used to plot the intensity of the scattered neutrons ( $I(Q)$ ) versus the scattering vector ( $Q$ ).

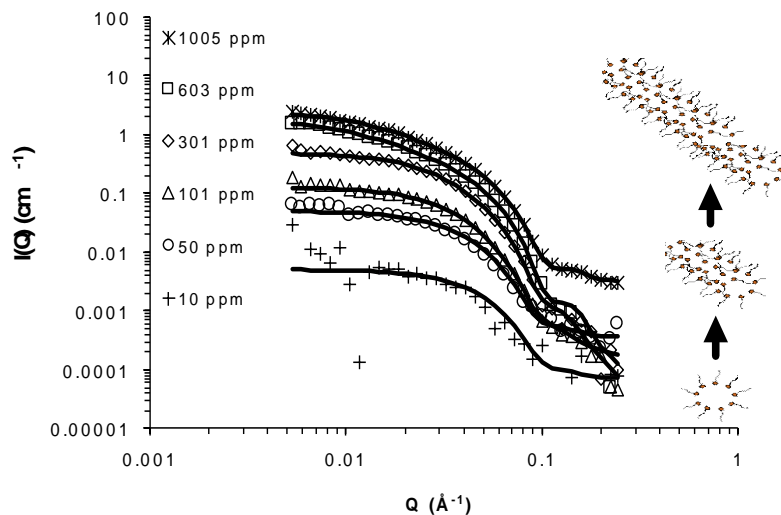


Figure 1-9. The intensity of scattered neutrons versus the scattering vector for the QAS additive blend at different concentrations (symbols) along with the model fits (continuous lines), spherical micelles start forming at concentrations as low as 10 ppm and they start to become elongated at 50 ppm (courtesy of Dr K. Trickett (Naseri et al., 2018))

The SANS patterns obtained for the PIBSI additive (traditional DCA) fit with a spherical micelle profile with a core radii of 3.5 nm and the shape of the micelles is not concentration dependent; i.e. spherical micelles form in the range of 100 ppm to 14,000 ppm. However, any attempts to fit the QAS additive data with a spherical model is unsuccessful and a cylinder model is used to fit the dataset as shown in Figure 1-9. The QAS additive micelle shape is studied for a wide range of concentrations and it is observed that cylindrical micelles exist in concentrations between 50 ppm to 1,005 ppm. Viscoelasticity has been reported for micelle rod lengths of around 10-40 nm (Ohlendorf, Interthal, & Hoffmann, 1986) and rod lengths of 25-250 nm in concentrations of 100-2,000 ppm (Gyr & Bewersdorff, 2013). The lower end values quoted here are similar to those observed with the QAS additives. It is common for QAS surfactant systems to form highly viscoelastic solutions by forming entangled micelles (Berret, Gamez-Corrales, Séréro, Molino, & Lindner, 2001; In, Bec, Aguerre-Chariol, & Zana, 1999; Oda, Panizza, Schmutz, & Lequeux, 1997) and the viscoelasticity in these solutions is found to be due to formation of three-dimensional dynamic surfactant networks. Likewise, the effectiveness of the additive performance in the highly turbulent and cavitating flow conditions of the injector at such dilute concentrations can be attributed to formation of shear-induced-structures. In fact, a recent Holtzer plot analysis of the additised fuel composition established that the micelles present the morphological characteristics required to form complex network aggregates (I. K. Karathanassis et al., 2018).

#### **1.4.2. Fuel flowrate measurements**

Both experimental and computational studies performed in enlarged nozzle replicas (Andriotis, Gavaises, & Arcoumanis, 2008; Gavaises, 2008) have established that nozzles with tapered holes (converging towards the nozzle exit) can suppress or eliminate cavitation, although at the highest (>3000 bar) injection pressures, even tapered nozzles are likely to suffer from cavitation. On the other hand, in nozzles with cylindrical holes there is a high level of cavitation and the nozzle discharge coefficient is significantly reduced due to the blockage of the holes by cavitation bubbles (Gavaises, 2008).

The fuel flowrate in cylindrical and tapered injector nozzles in fuel injection equipment is compared in order to determine whether the flow enhancement property of the QAS additive is related to the injector geometry and the amount of in-nozzle cavitation (Naseri et al., 2018). The fuel flowrate is measured by collecting and weighing the injected fuel after 1000 successive injections. The percentage change in the discharge coefficient is calculated from the

difference in the injector flowrate using the base diesel and diesel treated with 1000 ppm of the QAS additive.

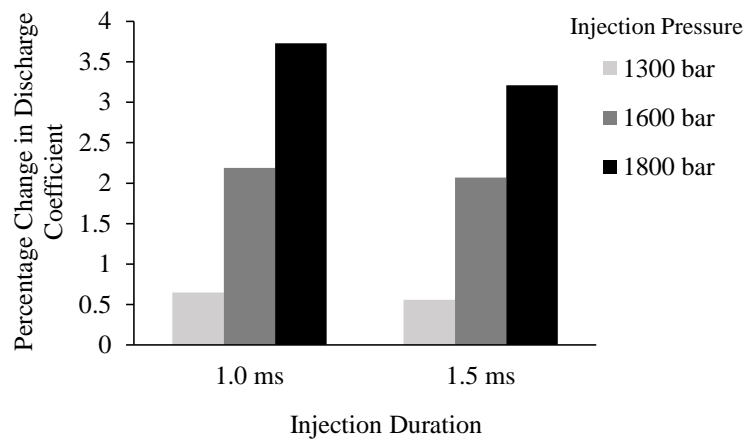


Figure 1-10. Percentage change of discharge coefficient by addition of the QAS additive at different injection pressures and durations (courtesy of Dr N. Mitroglou (Naseri et al., 2018))

It is noted that the additive does not alter the fuel flowrate when tapered injector nozzles are used (only small variations below 0.5% observed in injection pressures from 1300bar to 1800 bar). However, its effect becomes significant in cylindrical nozzles where the flow is more turbulent and prone to cavitation. In cylindrical nozzles, as the injection pressure is increased from 1300 bar to 1800 bar, the discharge coefficient enhancement is also increased from 0.65% to 3.73% for the 1 ms injection duration and from 0.56% to 3.21% for the 1.5 ms injection duration. This observation confirms that the additive is effective in maintaining its flow enhancement property even after passing through the fuel pump, filters and the common rail, providing further evidence about the dynamic nature of the surfactants viscoelasticity. Furthermore, it is demonstrated that the flow enhancement effect is in fact observed in cavitating flow conditions. Moreover, as the injection pressure is increased and so the flow becomes more turbulent and cavitation is enhanced, the additive effect is also improved

### 1.4.3. Cavitation volume fraction measurements using X-ray micro-CT

Flow measurement and visualization studies such as shadowgraphy can only provide qualitative information about cavitation. More recently, application of micro-CT (Bauer, Chaves, & Arcoumanis, 2012) and high energy X-rays (Duke et al., 2014; Sun, Jiang, Strzalka, Ocola, & Wang, 2012) have allowed for quantification of cavitation volume fraction. In order to quantify the additive effect on cavitation, a device designed (Mitroglou, Lorenzi, Santini, &

Gavaises, 2016) for measuring vapour fraction in cavitating flow conditions similar to the fuel flow in a diesel injector orifice is used. X-ray micro-CT is employed to detect regions of pure liquid or vapour or mixtures of the two. The cavitating nozzle makes a 360° rotation in front of the X-ray source, providing time-averaged data for the in-nozzle liquid volume fraction. This test case is discussed in more details in the methodology and results sections of this thesis, but for the purpose of this chapter, Figure 1-11 shows the effect of the QAS additive on the vapour volume fraction inside the nozzle. The additive effect on the amount of cavitation is defined in terms of  $\alpha_{\text{Difference}} = \alpha_{\text{Additised diesel}} - \alpha_{\text{Base diesel}}$ , where  $\alpha$  is the liquid volume fraction.

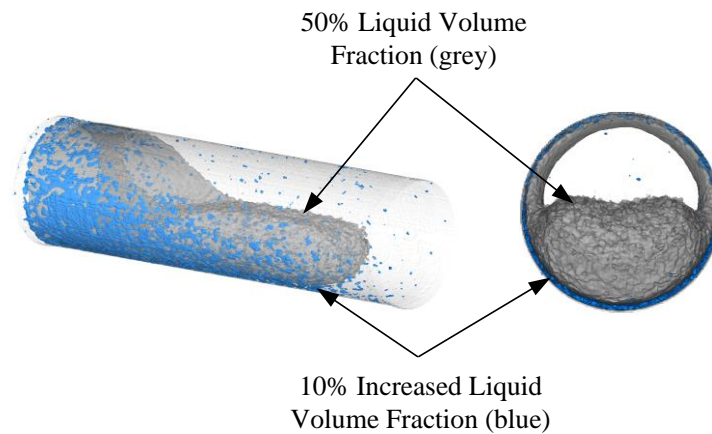


*Figure 1-11. 3D view of the iso-surface of 50% liquid volume fraction in diesel with 1000 ppm QAS additive (transparent grey colour) and iso-surface of regions with 10% increased liquid volume fraction ( $\alpha_{\text{Difference}} = 0.1$ , blue colour) (courtesy of Dr N. Mitroglou (Naseri et al., 2018))*

The liquid volume fraction for the base diesel fuel and the additised fuels (one with 1000 ppm of the traditional PIBSI additive and the other one with 1000 ppm of the QAS additive) are measured and averaged over 2 hour. The results indicate that the liquid volume fraction inside the orifice is not significantly altered by the PIBSI additive (less than 1% visible differences), whereas the QAS additive is able to suppress the cavitation at regions close to the nozzle wall by more than 10% in the cavitation cloud. The specific volume of the liquid phase is negligible to the specific volume of the vapour, therefore suppression of a seemingly small amount of vapour inside the nozzle can significantly contribute to the mass flowrate through the injector.

#### 1.4.4. High-flux X-ray phase-contrast measurements

Further to the X-ray micro-CT measurements, temporally-resolved X-ray phase-contrast imaging (XPCI) of a cavitating vortex flow within an enlarged-injector replica was conducted. In this case, cavitation in the injector hole emerges in the form of a vortical structure (string)

of fluctuating and irregular shape with an interface of high morphological variance. The string attaches to and then detaches from the needle tip in a fluctuating manner. The flow region exactly downstream of the needle tip is expected to be highly turbulent with longitudinal vortices (see also (Koukouvinis, Mitroglou, Gavaises, Lorenzi, & Santini, 2017)) setting in at the hole entrance due to the effect of the upstream geometrical constriction.

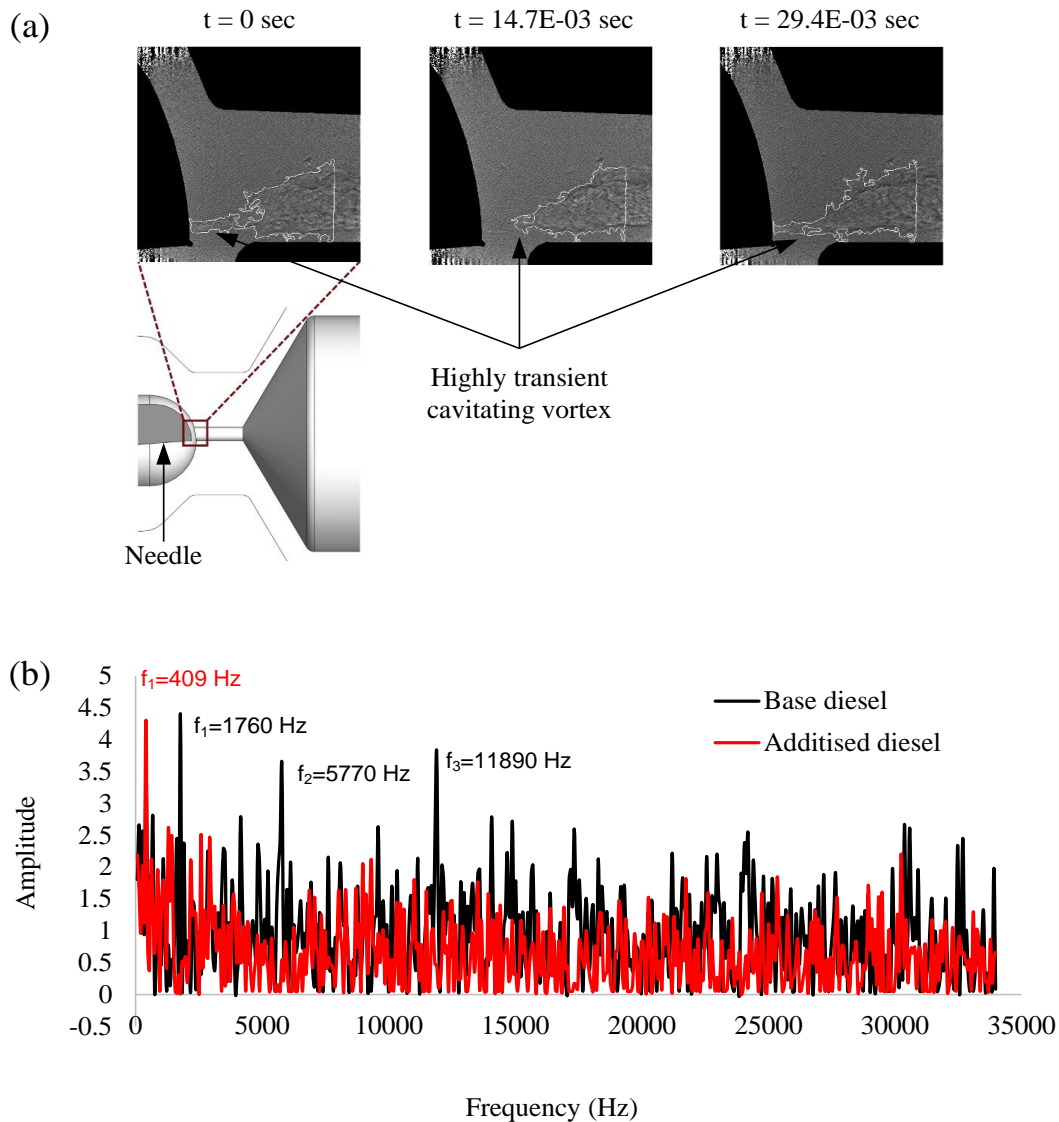


Figure 1-12. (a) High speed X-ray phase contrast imaging of the cavitation vortex (string) forming under the injector needle, (b) FFT of the string radius fluctuations in base and additised fuels (courtesy of Dr I. Karathanassis (Naseri et al., 2018))

It is known that the lifetime of a vortex cavity is strongly affected by flow turbulence and viscous dissipation can reduce the vortex lifetime (Franc & Michel, 2005). The underlying cause for formation of the string cavity is the presence of a coherent longitudinal vortex emanating due to the flow path constriction, as verified in the experimental studies of the

authors' research group (I. Karathanassis, Koukouvinis, Kontolatis, et al., 2017; I. Karathanassis, Koukouvinis, Lorenzi, et al., 2017). Therefore, the string lifetime is directly related to the interaction and evolution of the vortical motions. The interaction of small scale vortices with the larger cavitating vortex, disrupts the coherent motion of the vortex and leads to collapse of the vaporous core.

The probability of the string lifetime, i.e. the time period for which a vaporous structure exists in the vicinity of the injector hole, is measured in a comparative manner for base diesel and for diesel additised with 1000 ppm of the QAS additive. Referring to the base diesel, it is demonstrated that the string is short-lived with the cumulative probability for lifetimes less than  $5 \times 10^{-5}$ s being equal to 32%. On the contrary, the string lifetime for the additised fuel exhibits relatively even probabilities up to a lifetime of  $2 \times 10^{-4}$ s, with the average probability shifted to higher values.

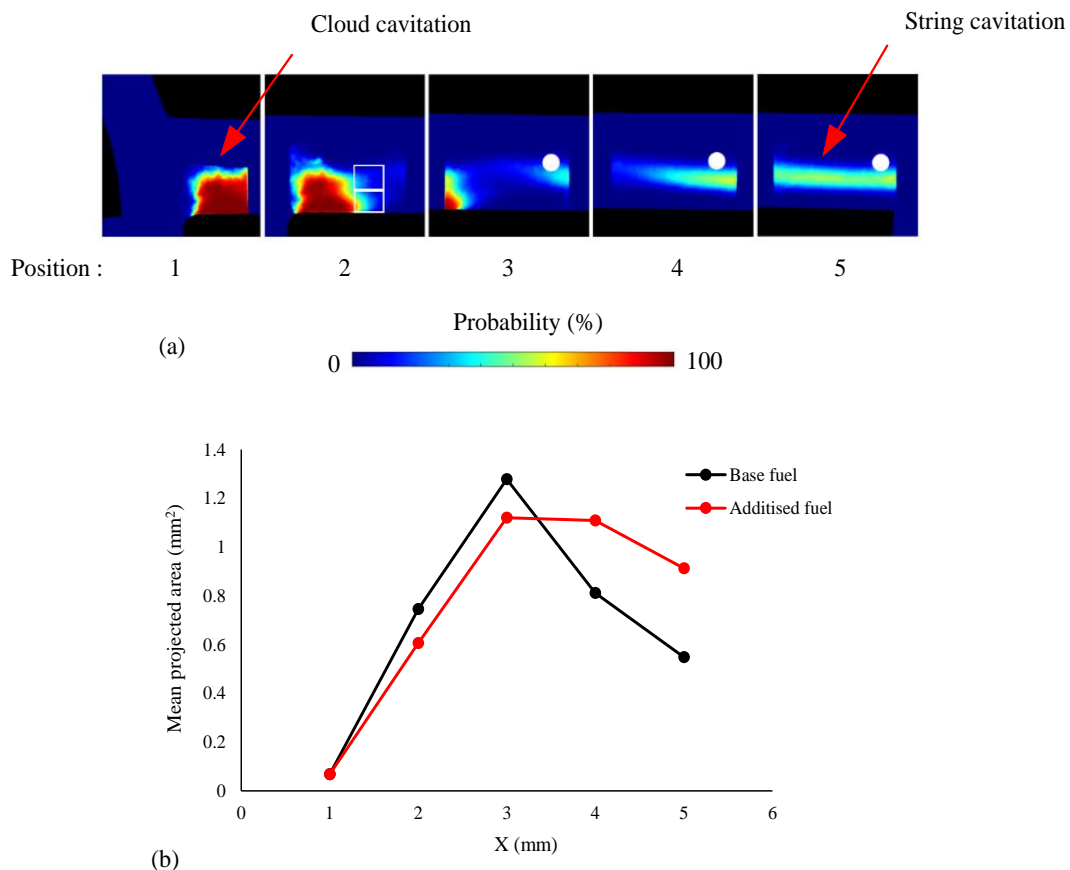


Figure 1-13. Appearance of both cloud and string cavitation at higher cavitation number in the XCPI device, (a) the contour of time-averaged probability of vapour presence, (b) Mean cavity surface area along the nozzle for the base and the additised fuels, values calculated from the projected vapour area in the mid-plane (image courtesy of Dr I. Karathanassis)



The string dynamic behaviour suggests that the perturbations leading to the decay of the string coherence are suppressed in this region, thus the probability of vortex breakup is reduced and the string lifetime is increased. An increased string lifetime is indicative of reduced interaction between large and small scale vortices and thus, a decreased level of turbulence. Similar behaviour, for a viscoelastic fluid has been observed in a DNS study (Pereira, Mompean, Thais, & Soares, 2017) referring to a Couette flow. It was established that for high values of drag reduction, the small-scale vortices initially present in the flow have decayed completely, while large-scale vortices aligned to the main flow direction are enhanced.

Moreover, the Fourier analysis of prevailing frequencies of the string radius downstream of the entrance is also investigated in Figure 1-12 (b). In this location, the string is well-established and exhibits a relatively smooth topology. A clear prevailing frequency of 409 Hz can be identified for the additised diesel, whereas the temporal evolutions of the string radius are highly chaotic for the base fuel with at least three peak frequencies of 1760, 5770 and 11890 Hz. Once again, the single peak observed for the additised diesel and the lower frequency of the string radius fluctuations are indications of a more stable flow field compared to the base fuel.

At higher cavitation numbers, both cloud and string cavitation structures appear inside the nozzle as shown in Figure 1-13 (a). The time-averaged probability of cavitation presence can be obtained by calculating the mean contour of ~16000 radiographs in each location. The mean cavity surface area in 5 positions along the nozzle is presented in Figure 1-13 (b) for base and additised fuels. It is evident that in the first 3 locations, corresponding to cloud cavitation regime, the additive suppresses the vapour fraction. However, in locations 4 and 5 where mainly the string cavity prevails, the additive effect is reversed and string vapour fraction is enhanced.

#### **1.4.5. Hypothesis**

The findings from SANS experiments, nozzle flow measurements and X-ray studies alongside the knowledge established in the literature regarding the effect of viscoelasticity on flow turbulence can form a basis for a hypothesis regarding the additive effect on cavitation.

Introduction of quaternary ammonium salts to the traditional PIBSI additive chemistry provides counter-ions that help to screen the electrostatic repulsions between the surfactant head groups, allowing the formation of larger elongated structures and inducing viscoelastic

properties in the additised fuel composition. Flowrate measurements with cylindrical and tapered injector tips indicate that the increase of flowrate in fact depends on the injector geometry and hence on the level of flow turbulence and cavitation inside the injector holes. These results indicate that the increase of flowrate by the additive is mainly seen in cylindrical nozzle injectors which are prone to cavitation and operate at more turbulent flow conditions compared to tapered nozzle injectors. Enhancement of the additive performance at higher shear rates and morphological analysis of the micellar structures suggests the formation of shear-induced structures in the additised fuel compositions.

X-ray micro-CT measurements of the liquid volume fraction inside the cavitating orifice show that when the QAS additive is used, the liquid volume fraction near the walls of the channel is increased by more than 10% in the cavitation cloud. X-ray phase contrast imaging measurements that provide information regarding the temporal dynamics of a fluctuating cavitating vortex, show that the vortex breakup events are less probable and the string radius fluctuates at a lower frequency when the fuel is enriched with the QAS additive. This indicates that the additive can locally stabilize the flow and reduce turbulence perturbations leading to the vortex breakup. At higher cavitation numbers, when both cloud and string cavitation structures are present, the dual effect of the additive on vapour structures is identified. In the cloud cavitation region, the additive has a suppressive influence on vapour formation, a finding in line with the X-ray micro-CT study. However, the vapour fraction is strongly enhanced in string cavitation regions due to the presence of the QAS additive.

The findings of the above studies suggest that the micelles formed in fuels enriched with QAS additives can make the additised fuel composition viscoelastic. Wormlike micelles entangle in shear flow conditions and form transient shear-induced-structures that locally induce significant viscoelastic properties in the fluid. The state of the art on turbulent viscoelastic fluids demonstrates that viscoelastic forces acts against the vortices and turbulence eddies developing in the crossflow direction, while promoting the streamwise vortices.

Therefore, the effect of the additive on cavitating vortices depends on the type of cavitation regime. In the cloud cavitation region where vapours form in the shear layer, the development of the cavitation vortices in the spanwise direction is hindered as the micellar structures align in the main flow direction. Furthermore, in vortex cavitation region with streamwise vortices, turbulent perturbations can breakdown the vortex that forms under the needle. Therefore

turbulence suppression by the viscoelastic additive in this regime, leads to a more stable cavity core and longer cavitation lifetimes.

In fuel injector conditions, the in nozzle cavitation is mainly in the form of cloud cavitation while the vortex cavity has a more intermittent appearance. Therefore, the cumulative effect of the additive on the injector flow is the reduction of vapour volume inside the nozzle. The combined effect of cavitation suppression and turbulence reduction by the viscoelastic additive results in overall reduction of the flow resistance and flow enhancement in the injection system.

#### **1.4.6. Aims and Outline of the Thesis**

The aim of this work is to provide an understanding about the effect of viscoelastic deposit control additives on fuel injection systems, in particular, on the flow and cavitation inside injector nozzles. Addition of quaternary ammonium salt surfactants can significantly alter the complex turbulent and multiphase flow of the fuel injectors, such that the engine output power is increased. However, these effects are not well understood and numerical simulations provide new insights into the physical mechanisms involved in this type of flow, as well as explaining the experimental observations regarding the fuel flowrate, turbulence levels and the amount of in-nozzle cavitation.

The main work in this thesis is organized in chapters 2 to 6 and an overview of each chapter is described below:

Chapter 2 reviews the existing body of literature and the topics covered in this chapter are experimental and numerical studies of in-nozzle cavitation, turbulence effects in cavitating flows and turbulence drag reduction in viscoelastic fluids. Finally, the literature gap is identified, and the current knowledge in viscoelastic fluids in bubble dynamics studies and tip vortex cavitation in propellers is presented.

Chapter 3 presents the computational methodology including different RANS and LES turbulence models and two-phase and barotropic cavitation models. Furthermore, the PTT viscoelastic model equations, implementation and validation cases in 2D and 3D are presented. Finally, the flow conditions and setup for four different cavitating flow test cases with incipient, film-like, cloud and string cavitation regimes are documented.

Chapter 4 evaluates the performance of RANS and LES turbulence models in predicting cavitation in different flow regimes. Moreover, performance of two-phase and barotropic cavitation models is also compared. The results are validated against the available experimental data for the vapour volume fraction, the velocity and the RMS of turbulent velocity.

Chapter 5 presents the simulation results for viscoelastic cavitating flows. Initially, simulations of Newtonian and viscoelastic fluids in a step nozzle test case with cloud cavitation are presented and the main flow features are analysed. Finally, the effect of the viscoelastic additive in a realistic diesel fuel injector geometry is investigated and the additive effect on string cavitation and cloud cavitation is differentiated.

Chapter 6 outlines the main research findings related to the thesis objectives and summarises the conclusions drawn from comparing the numerical and the experimental studies.

## 2. Literature Review

---

Viscoelastic additives can change the fluid properties, therefore altering the cavitation and turbulence levels inside the injector nozzle. The relevant body of literature mainly fall in two different categories, studies about in-nozzle cavitation and studies about the interaction of viscoelasticity and turbulence. In this chapter, a review of the most relevant studies about in-nozzle cavitation and different approaches for modelling cavitation is presented. Afterwards, the relation between flow turbulence and cavitation is discussed and the mechanisms of turbulence suppression by viscoelastic additives is explained. A few studies also focus on the interaction of viscoelasticity and cavitation; these are discussed in the last section of this chapter to identify the gap in the literature.

### 2.1. Cavitation studies

Cavitation can appear in engineering devices such as propellers, gear pumps, fuel injectors and heart valves as well as in the nature for instance in pistol shrimp's snapping claws and in the xylem of vascular plants. Therefore, there is an increasing interest in the scientific community as well as in industries to understand and control cavitation. Cavitation formation and development mechanisms depend on the specific flow configuration, nevertheless there is a general consensus that vapour production and transport is closely related to the strength and frequency of formation vortical structures in the flow. Flow recirculation and large scale vortices appear frequently inside an injector nozzle, due to its complex geometry and the

movement of the needle. In order to understand the cavitation mechanisms in nozzle flows, many pioneering studies were carried out in simplified nozzle replicas and those findings have been cross-linked with observations in more realistic nozzle geometries.

### 2.1.1. Cavitation in nozzle flow

Early experimental investigations established that the diesel spray is influenced by cavitation development inside the injector nozzle (Bergwerk, 1959) The initial perturbations on the spray interface intensify by cavitation formation and the nozzle discharge coefficient is reduced as cavitation bubbles block the effective fuel passage area. Cavitation development can be inhibited by increasing the corner radius at the nozzle entrance, which in turn results in an increased flowrate and higher momentum at the nozzle exit (Bergwerk, 1959; D. Schmidt, Rutland, & Corradini, 1997).

By increasing the pressure difference across a nozzle, cavitation volume can grow such that vapour fills the nozzle cross section, a condition known as choked flow condition (Winklhofer, Kull, Kelz, & Morozov, 2001). Initially, the mass flowrate through the nozzle increases as the pressure difference is increased and cavitation develops. However as cavitation approaches the nozzle exit and enters the choked flow condition, there is no further increase in the mass flowrate with the pressure difference. This transition is termed “Critical Cavitation” (CC). As the flow approaches the CC condition, the liquid flow line along the nozzle disappears and near the exit the flow is mainly vaporous.

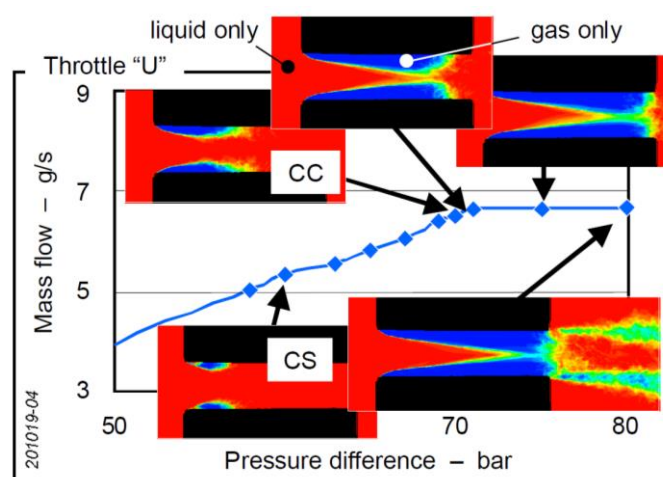


Figure 2-1: Pressure difference versus mass flow rate for transition of non-cavitating flow to choked flow, CS refers to start of cavitation and CC is the critical cavitation point (Winklhofer et al., 2001)

Experiments on nozzles with different length to width ratios (L/W) are useful to gain insight into the effect of geometry on cavitation and spray characteristics of diesel injectors (H. Suh & Lee, 2008). Cavitation has a significant effect on spray characteristics and as long as it has not reached the hydraulic flip condition, where cavitating bubbles extend outside the nozzle, it can improve the spray shape. By increasing the injection pressure, cavitation intensifies and consequently the spray widens. Nozzles with higher L/W have a smaller spray angle, but the effect of cavitation is similar in both nozzles. However, at higher L/W, cavitation inception and therefore hydraulic flip occur at higher injection pressures.

The amount of cavitation in nozzle varies if biodiesel is used instead on diesel (H. K. Suh, Park, & Lee, 2008). Characteristics of cavitating flows in tapered and rectangular nozzles with diesel and biodiesel fuels is investigated in the above-mentioned study. It is observed that generally biodiesel cavitates less than diesel fuel and for the same amount of cavitation inside the nozzle, biodiesel must have a higher injection pressure. This was contributed to lower viscosity of diesel, i.e. less viscous stress is required to rupture the liquid. In fact, Joseph (Joseph, 1995) proposed that cavitation threshold for a flowing liquid is inversely proportional to its viscosity; as the total stress ( $\tau$ ) consists of the pressure and the shear stress:

$$\tau = -P + 2\mu \frac{\partial u}{\partial x} \quad \text{Equation 2.1}$$

and the liquid ruptures when the total stress exceeds the vapour pressure ( $\tau \geq P_v$ ). Therefore, the cavitation threshold is defined by the critical rate of strain ( $\dot{s} = \frac{\partial u}{\partial x}$ ):

$$\dot{s} > \frac{P - P_v}{2\mu} \quad \text{Equation 2.2}$$

Flow rotation and recirculation regions regularly appear in practical flow conditions where pre-existing bubbles and nuclei are convected into areas of low pressure. In swirling flow conditions, cavitation inception can happen in the low pressure core of large scale vortices forming in regions of high vorticity. This phase change mechanism is known as “vortex cavitation”(Brennen, 2013) and it can appear in propellers, turbines and hydrofoils as well as inside the fuel injector nozzles where it is referred to as “string cavitation” (Andriotis et al., 2008; Gavaises, Andriotis, Papoulias, Mitroglou, & Theodorakakos, 2009). Geometric constrictions such as sharp turns at a nozzle entrance (Giannadakis, Gavaises, & Arcoumanis,

2008) or a venturi throat (Dittakavi, Chunekar, & Frankel, 2010), generate flow instabilities that produce clouds of vapour. “Cloud cavitation” regions are characterized by a re-entrant jet motion and the periodic growth and shedding of the vapour clouds (Callenaere et al., 2001).

Cavitation bubbles downstream of the inception region expand and form a cavity cloud that breaks off by the re-entrant jet motion, which subsequently leads to shedding of the cavity cloud. The cavitation cloud shedding process increases the flow turbulence and fluctuations, resulting in enhanced spray atomization. (Ganippa, Bark, Andersson, & Chomiak, 2001). The energy released during the breakup of cavitation vapours is identified as a dominant factor for enhancement of fuel atomization and reduction of the Sauter mean diameter (SMD) value (H. Suh & Lee, 2008). Furthermore, bubble collapse events near the liquid-gas interface also promote the primary jet breakup (Örley et al., 2015).

In case of cavitation vapours forming in shear layer vortices, vapour production delays the vortex roll-up process, resulting in suppression of velocity fluctuations due to turbulence. (Koukouvinis et al., 2017). On the other hand, collapse of cavitation vapours in the closure region of the cavity cloud increases turbulence, momentum and displacement thickness (Gopalan & Katz, 2000). The impulsive pressures generated during the collapse of cavitation bubbles, result in reduction of vortex-stretching and increased vorticity generation (Dittakavi et al., 2010). The vorticity enhancement by cavitation collapse events is also responsible for increased vortex-induced vibrations in hydrofoils (Ausoni, Farhat, Escaler, Egusquiza, & Avellan, 2007).

The re-entrant jet mechanism and condensation shocks are the two dominant instability mechanisms in partial cavities (Budich, Schmidt, & Adams, 2018; Callenaere et al., 2001; Ganesh et al., 2016). However, the adverse pressure gradient due to the sudden contraction may itself be enough to induce a shock front if cavitation cloud collapse occurs at a distance location from the inception point (Budich et al., 2018).

Fully developed cavitation clouds are dominated by a condensation shock-induced shedding mechanism, whereas in incipient cavitation conditions, the re-entrant jet motion is mainly responsible for shedding of the cavity cloud due to small size of the cavity cloud and the subsequent condensation shocks (Ganesh et al., 2016).



The shedding behaviour of the cloud-like cavities due to the re-entrant jet motion can be described in the following order (Sato & Saito, 2002):

- A re-entrant jet motion is formed below the leading edge cavity after the shedding of cloud-like cavity.
- The jet has a higher velocity than the convection velocity of the vortex cavities and it causes the break-off and shedding of the attached cavity.
- As the re-entrant motion reaches the leading edge of the orifice, attached cavity partially disappears and micro-vortex cavities are formed in the leading edge and the shear layer
- Micro vortex cavities move downstream the orifice, as a new cavity grows at the entrance of the orifice. These cavities coalesces and grow while pairing, rolling up and glowing.

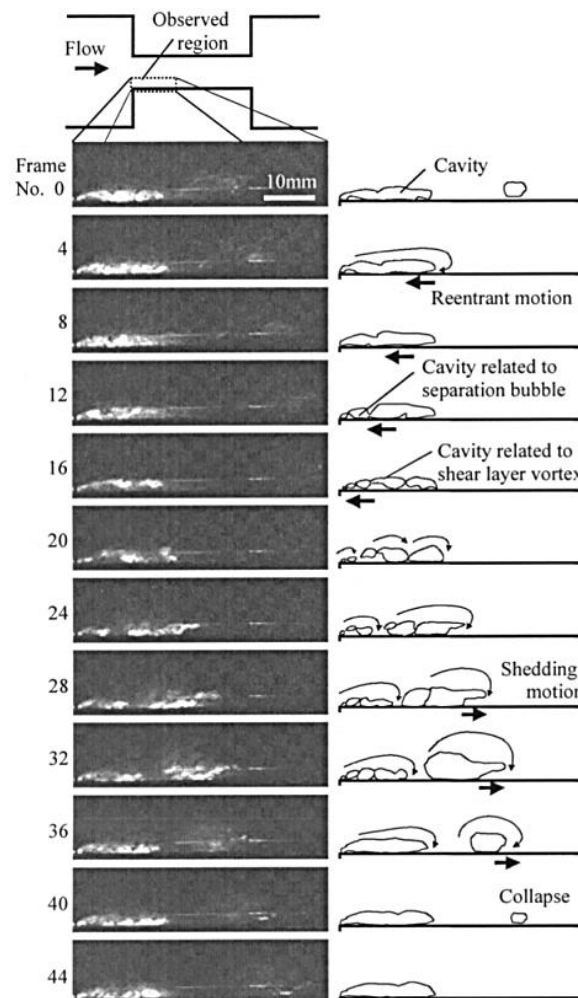


Figure 2-2: Process of cavity shedding, from formation of the re-entrant motion to collapse of the separated bubbles (Sato & Saito, 2002)

The time period  $T_c$  for all the above processes, i.e. from the start of re-entrant motion to the shedding of the cloud-like cavity can be estimated from:

$$T_c = \frac{L_o}{U_r} + \frac{L_o}{U_v} \quad \text{Equation 2.3}$$

where  $L_o$  is the cavity length,  $U_r$  is re-entrant motion velocity and  $U_v$  is the convection velocity of the vortex cavity.  $U_r$  is estimated as the mean throat velocity and  $U_v$  is almost half  $U_r$ . The inverse of the time period  $T_c$  is the frequency of vortex shedding  $F$ , and hence the Strouhal number based on the mean liquid velocity inside the nozzle ( $U$ ), can be defined in Equation 2.4:

$$St = \frac{F L_o}{U} = \frac{1}{\left(\frac{U}{U_r} + \frac{U}{U_v}\right)} \quad \text{Equation 2.4}$$

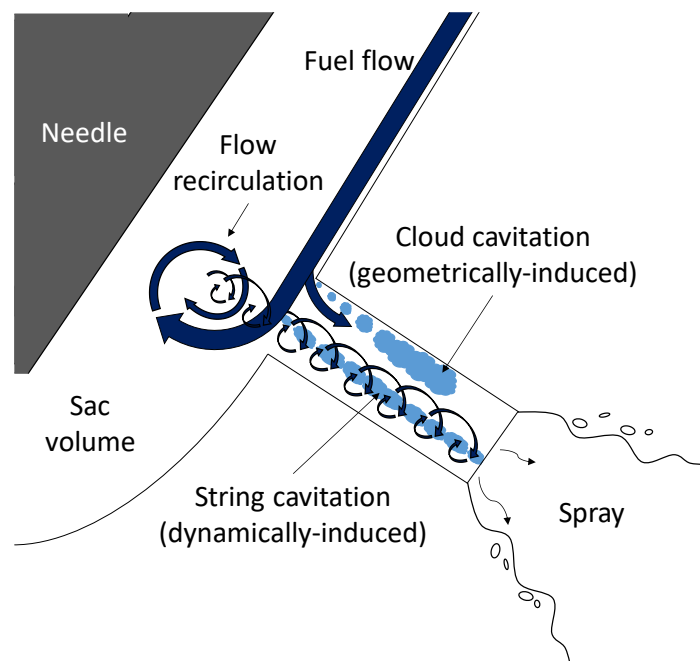


Figure 2-3. Cavitation mechanisms inside a diesel injector nozzle

In diesel injectors, cavitation can exhibit two distinctive topologies, namely cloud cavitation and string cavitation (Figure 2-3). Cloud cavitation, also referred to as “geometrically-induced cavitation”, occurs at the sharp entrance of the nozzle hole and has similar characteristics to the flows previously discussed in this section. String cavitation, also referred to as “dynamically-induced cavitation”, appears in form of a transient vaporous core in vortical flow structures originating from the sac volume (Arcoumanis, Gavaises, Flora, & Roth, 2001).

String cavitation vortices can either act as carriers of gas from the pre-existing cavitation sites or the downstream air, or they can develop low pressure cores that form cavitation vapours (Andriotis et al., 2008).

In converging tapered nozzles, the pressure distribution at the nozzle entrance is modified such that it has a smaller gradient and therefore, formation of the cloud cavitation can be completely suppressed. However, string cavitation dominates the flow in tapered nozzles and it can induce hole-to-hole variations as the string has an intermittent nature and vortices in adjacent nozzle holes can join and form large voids inside the sac volume (Gavaises et al., 2009; Reid et al., 2014). Formation of string cavitation is also linked with increased spray instabilities and widening of the spray cone angle (Mitroglou, Gavaises, Nouri, & Arcoumanis, 2011).

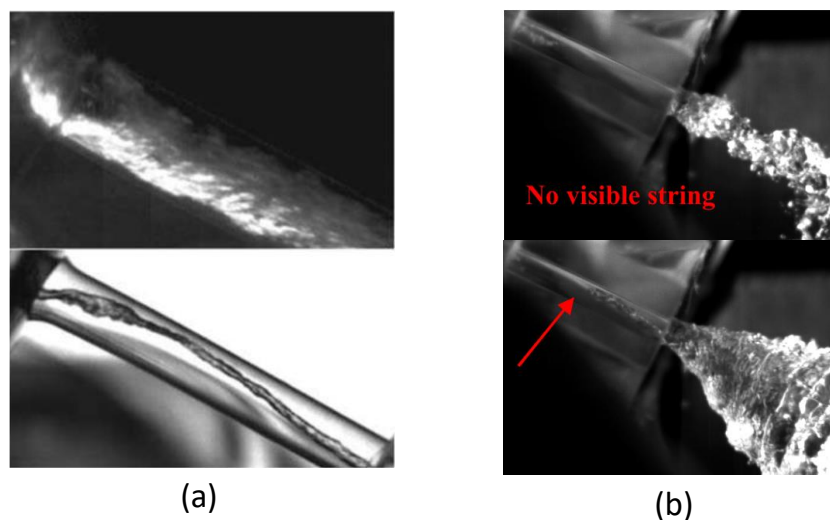


Figure 2-4 (a) Cavitation structures in cylindrical (top) and tapered (bottom) injector nozzles; in the cylindrical nozzle a cavity cloud covers the orifice surface area whereas in the tapered nozzle only string cavitation is visible (Gavaises et al., 2009), (b) enhancement of the spray cone angle due to string cavitation presence (Mitroglou et al., 2011)

More recently, X-ray phase contrast imaging and X-ray computed tomography techniques have enabled researchers to quantitatively study the nozzle flow cavitation. A recent study using the X-ray micro-CT technique (Mitroglou et al., 2016) demonstrates the capability of this method by reconstructing the 3D vapour volume fraction map inside a single hole cavitating nozzle that resembles the flow field inside an injector nozzle. In this method, the nozzle makes 360° rotations in front of the X-ray source for a long exposure time (~2 hours) while the detector records the density variations inside the nozzle (using the X-ray attenuation data), which allows for reconstruction of the time averaged density map as shown in Figure 2-5.

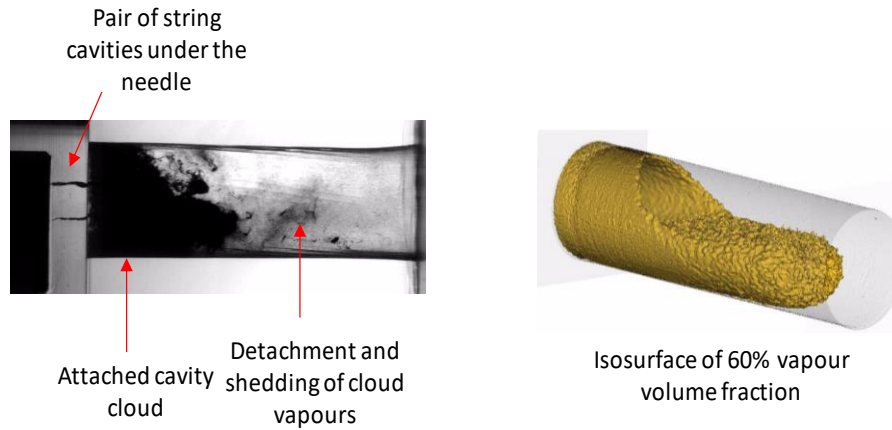


Figure 2-5. Shadowgraph of cavitation structures appearing inside an injector replica (left) and X-ray reconstruction of the time-averaged cavitation volume fraction (right) (Mitroglou et al., 2016)

String cavitation is susceptible to deformation and collapse due to perturbations produced by the local flow turbulence, therefore it has a dynamic nature and temporal data are required to describe its behaviour. Time-resolved X-ray phase contrast imaging technique can provide the information to describe the interface topology and the periodicity of cavitating vortices. This technique was recently used to describe the morphology and dynamics of a string cavity and calculate the local velocity, vorticity and turbulence intensity (I. Karathanassis, Koukouvini, Kontolatis, et al., 2017).

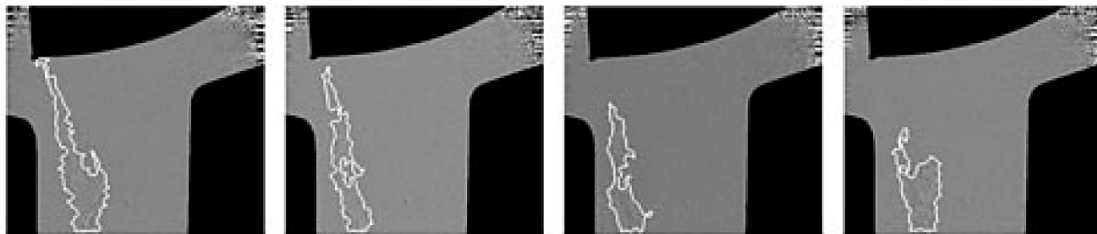


Figure 2-6. Dynamic behaviour of a string cavitation forming under the needle of an injector replica, white lines show the cavitation interface and images are taken with  $1.5 \times 10^{-5}$  s intervals (I. Karathanassis, Koukouvini, Kontolatis, et al., 2017)

### 2.1.2. Modelling of cavitation

Cavitation dynamics can generally be described in two approaches, mechanical models and thermodynamic models (Giannadakis, 2005). In mechanical models, the driving force for cavitation is pressure difference and equations based on bubble dynamics are used to describe the evolution of the cavity volume. In thermodynamic models, cavitation is defined in the context of thermodynamic properties of the fluids and/or the energy equation.

### 2.1.2.1. Mechanical (two-phase) cavitation models

A number of cavitation models employ the Rayleigh-Plesset equation to prescribe a mass transfer rate between the phases. An advection equation for the vapour volume fraction is solved, assuming pre-existing bubble nuclei and a bubble number density. Lord Rayleigh (Rayleigh, 1917) developed one of the first models to describe the collapse of a single bubble using a potential flow approximation. This model was further developed to include the effect of surface tension (Plesset, 1949). The resulting equations can be solved to determine the dynamics of a spherical bubble with radius  $R$ :

$$\frac{3}{2}\dot{R}^2 + R\ddot{R} = \frac{P(R) - P_\infty}{\rho} \quad \text{Equation 2.5}$$

$$P(R) = P_v - \frac{2S}{R} \quad \text{Equation 2.6}$$

where  $\dot{R} = \frac{dR}{dt}$  and  $\ddot{R} = \frac{d^2R}{dt^2}$ ,  $S$  is the surface tension and  $P_v$  is the vapour pressure.

Considering the viscous terms in Equation 2.5, the generalized Rayleigh-Plesset equation for spherical bubble dynamics can be written as (Brennen, 2013):

$$\frac{P(R) - P_\infty}{\rho} = \frac{3}{2}\dot{R}^2 + R\ddot{R} + \frac{4\nu}{R}\dot{R} + \frac{2S}{\rho R} \quad \text{Equation 2.7}$$

In this section, the main concepts behind some of the well-known cavitation models based on formulation of mass transfer rate between the phases is briefly discussed. One of the early cavitation models is the Bubble Two Phase Model (BTM) developed to macroscopically model cavitating flows (Kubota, Kato, & Yamaguchi, 1990). The BTM uses the mixture multiphase framework and a modified Rayleigh model that includes a velocity potential from the interaction of bubbles. Another cavitation model similar to the BTM (Chen & Heister, 1995) assumes a constant bubble number density per unit mass of cavitation mixture instead of a constant bubble number density everywhere. This modification means the bubble number density decreases as the cavitation region grows.

In the Schnerr-Sauer (SS) cavitation model (Schnerr & Sauer, 2001) a more realistic bubble number density formulation is achieved by assuming a constant bubble number density in the local liquid phase only. Evaporation and condensation rates are defined from the bubble number density and rate of change of nuclei bubble mass. The mass transfer rate function of

this model has a unique property that it is zero when the vapour volume fraction is 0 or 1, and it reaches a maximum between 0 and 1.

The “full cavitation model” (Singhal, Athavale, Li, & Jiang, 2002) accounts for first order effects in cavitation, i.e. the formation and transport of vapour by pressure and velocity fluctuations due to turbulence and the effect of non-condensable gases as well as the surface tension. As in the previous models, transport of vapour is modelled in the vapour volume fraction advection equation, with a source term for the net rate of mass transfer based on Rayleigh-Plesset equation, relating the vapour volume fraction to the local bubble radius and the bubble number density. In order to account for the effect of turbulence, the vapour pressure is raised to saturation pressure plus turbulent pressure fluctuation. The non-condensable gas effect is considered in the mixture formulation and calculation of the liquid volume fraction.

In the ZGB cavitation model (Zwart, Gerber, & Belamri, 2004) the mass transfer rate is proportional to vapour density only. In addition to omission of surface tension effects, this is the main difference between the mass transfer rate of Singhal *et al.* and the ZGB model. In order to account for the reduction of the nucleation site density with increasing the vapour volume fraction, the evaporation rate is proportional to  $\alpha_{nuc}(1 - \alpha_v)$ , where  $\alpha_{nuc}$  is the nucleation site volume fraction (constant) and  $\alpha_v$  is the vapour volume fraction.

In another approach (Giannadakis, Gavaises, & Roth, 2004) an Eulerian-Lagrangian method is used to model cavitation as discrete bubbles and a probability density function is used to describe the nuclei density distribution. Bubble momentum due to drag, lift, added mass force and pressure gradient is calculated. The two-way coupling of Eulerian and Lagrangian phases is by adding bubble momentum due to effect of contact forces to the momentum source term. A dispersion model is used to model the effect of turbulence on bubbles motion. Bubble breakup is modelled by considering the local turbulence and the shear force due to relative velocity of the bubble and the liquid phase. This model is one of the most comprehensive and advanced models of cavitation and therefore it has a high computational cost.

Cavitation can also be predicted by assuming that pre-existing gas nuclei is always present in the flow field (C. Hsiao & Chahine, 2004). In this model, the bubble nucleus is released upstream the cavitation region and Navier-Stokes and bubble dynamics equations are separately solved for this bubble. The flow on the bubble boundary is calculated using a moving

chimera grid, where two sets of grid are assumed; one for the flow and one for the bubble and the communication between these two sets of data is by interpolation for the overlapping points.

More recently a model is developed based on the diffuse interface method to capture the sharp density jumps of the vapour and liquid phase (Petitpas, Massoni, & Saurel, 2009). Four sets of equations (mass, momentum, specific internal energy and volume fraction conservation equations) are solved for each phase. All phases are compressible and an equation of state (EoS) is used for the mixture based on mixture energy conservation and pressure equilibrium between the phases. A stiffened gas equation of state is used for pure liquid and pure vapour and the entropy equation is used to close the set of equations. The diffuse interface model is based on a relaxation parameter which is set to zero at non-metastable states and is infinity in the liquid-vapour interface in metastable state. This model enforces thermodynamic equilibrium at the liquid/vapour interfaces that are under metastable conditions.

In addition to the aforementioned models which use second order differential equations based on Rayleigh-Plesset equation, some cavitation models use the simpler Rayleigh relation or a linear approximation based on local pressure difference to calculate the vapour fraction. These models are less computationally expensive and they are efficient in prediction of certain cavitating flows, such as those occurring in hydrofoil applications. (Ahuja, Hosangadi, & Arunajatesan, 2001; Dittakavi et al., 2010; Kunz et al., 2000; Lindau, Kunz, Venkateswaran, & Boger, 2001; Senocak & Shyy, 2004)).

#### **2.1.2.2. Thermodynamic cavitation models**

One of the earliest models in this category is based on an empirical barotropic law defining density as a function of pressure (Dellanooy & Kueny, 1990). The mixture properties are calculated from the speed of sound in liquid/vapour mixture. The viscosity effect are neglected and Euler equation is solved for a single fluid. The advantage of this group of models is that no extra equation is needed for the volume fraction, hence they are known as “one fluid” cavitation models. However, the main difficulty in this approach is to define the mixture properties. One approach to address this matter, is a numerical method based on tabulated thermodynamic properties for vapour and liquid and the mixture (Ventikos & Tzabiras, 2000).

In a more recent study, the cavitation model of Dellanooy and Kueny was combined with a stiffened gas equation of state for the mixture phase for solution of inviscid Euler equations

(Goncalves & Patella, 2009). Equations are solved with an implicit preconditioned RANS solver and the effect of mixture equation of state on the accuracy of the cavitation prediction is investigated. One of the earliest barotropic models similar to the model of Dellanoy and Kueny was developed with the main difference in the mixture speed of sound formulation (D. P. Schmidt, Rutland, & Corradini, 1999a) and (D. Schmidt et al., 1997)). The homogenous equilibrium model (HEM) based on Wallis speed of sound (Wallis, 1969) is used to model the mixture and both liquid and vapour phases are fully compressible. The authors applied a third-order Runge-Kutta scheme for temporal discretization and a third-order shock-capturing scheme for the continuity equation. The model is applied to simulate a single bubble collapse and results are in good agreement compared to experimental data. The model is also able to accurately predict the centreline velocity and discharge coefficient of in a cavitating nozzle.

Another model similar to the HEM is developed more recently based on the Riemann problem (S. Schmidt, Sezal, & Schnerr, 2006). Mass, momentum and energy conservation equations are solved. Tait's law is used for liquid equations of state, with a modification to increase the accuracy by using temperature dependant saturation values. Ideal gas law is used for the vapour phase equation of state. Mixture properties are defined assuming thermodynamic equilibrium and mixture speed of sound is defined by Wallis (Wallis, 1969).

More recently, a cavitation model was developed that defines the density of liquid and vapour phases as a function of the thermal and calorific equations of state (Sezal, Schmidt, & Schnerr, 2009). The model was developed and validated with Euler equations, although inclusion of viscous effects is also possible with the same methodology. The energy equation that includes the vapour volume fraction in the formulation is solved. For the liquid phase, a modified Tait equation of state is used which defines the density as a function of temperature and pressure. For the vapour phase an ideal gas law is used. In order to account for the decoupling of pressure and velocity at low Mach numbers, the authors have proposed a modified pressure flux calculation scheme. The model was developed with the main aim to capture the shock dynamics inside high pressure injectors which induce acoustic cavitation.

In a recent study, direct numerical simulation (DNS) of bubble collapse near a rigid wall in water and large eddy simulation of cavitation in a simple nozzle are reported (Hickel, 2015). In the DNS study of the bubble, a 3D Cartesian grid is used and both phases are compressible. Ideal gas equation of state is used for the vapour phase and Tait's equation is used for the liquid phase. A level-set method is used to track the liquid-vapour interface. Mass transfer at the



interface, i.e. evaporation and condensation, is modelled with a non-equilibrium mass transfer rate model based on the liquid and vapour temperature at vapour pressure in the interface (Schrage, 1953). Also an interface interaction term is used to couple the vapour and liquid mass, momentum and energy. In the LES study, cavitation in a micro-channel at two different operating pressures corresponding to incipient and fully developed cavitation. Fully compressible Navier-Stokes equations are solved with thermodynamic data obtained from tabulated barotropic equations for diesel. The methodology is capable of predicting the incipient cavitation due to shear layer instability as well as the fully developed cavitation condition.

## 2.2. Turbulence in cavitating flows

Inception and development of cavitation consists of a two-way interaction problem between the vapour structures and the flow. This interaction is enhanced by the fact that most practical flows are turbulent. Under such flow conditions, the scales of fluid motion underlying in the flow field in the form of vortices can contribute and even become the dominant mechanism cavitation formation, leading to structures termed as cavitating vortices (Franc & Michel, 2005). Formation of vapour in the core of vortices is an additional mechanism for generation of vorticity, hence it modifies the dynamics of turbulence (Arndt, 1981). Production of vorticity is due to density variations which are not aligned with pressure variations and create a baroclinic torque (the source term  $e_{ijk} \frac{\partial \rho}{\partial x_j} \frac{\partial P}{\partial x_k} / \rho^2$  appearing in the vorticity transport equation) (Pozrikidis, 2009). Experimental studies on stationary hydrofoils show that baroclinic torques contribute to vorticity generation especially in regions of cavity collapse (Laberteaux & Ceccio, 2001). Investigation of vorticity generation transport equation shows that vortex stretching, dilatation and baroclinic torque due to density gradients in cavitating flows are major sources of vorticity generation (Bin, Lou, Peng, & Wu, 2013).

Cavitating vortices are especially important in erosion studies since they can be very destructive and cause significant damage as they collapse (Franc & Michel, 2005). Erosive vortex rings have been used in industrial applications for cutting rock and underwater cleaning. Numerical comparison of erosive power of a cavitating vortex ring and a spherical bubble indicate that the collapse of cavitating bubble ring is much more erosive than the collapse of a spherical bubble (Chahine & Genoux, 1983).

Vortices are also formed in the shear layer, for example in turbulent wake of bluff bodies, mixing layers of liquid jets or between the flow recirculation region and the bulk flow in separated flows. In a forward-facing-step nozzle, vortices can cavitate and they constantly pair-up forming larger clouds downstream. Shear layer vortices can have small length and time scales and contribute to viscous dissipation (Simpson, 1989). Precise prediction of the coherent structures of shear flow requires resolving the flowfield down to the inertial subrange.

Pressure fluctuations in shear flows have a higher intensity than pressure fluctuations in an ideal isotropic turbulence (Arndt, 1981). In separated flows, cavitation is initiated in the turbulent shear layer but instantaneous minimum pressure probes near the solid surface do not specify this event, indicating that cavitation inception does not occur near the walls. Instead cavitation starts to appear as microscopic bubbles in the shear layer upstream the reattachment location of the separated flow (Katz, 1984).

The two-way interaction between cavitation and turbulence is investigated with DNS, with the main interest on the development of shear layer instabilities (Okabayashi & Kajishima, 2009). It is reported that turbulence is modulated by cavitation. This modulation can form a basis for a Sub Grid Scale (SGS) model for cavitation modelling in LES. Reynolds Averaged Navier-Stokes models are computationally less expensive than LES but they can have significant shortcomings in modelling of turbulent cavitating flows. It is shown that traditional RANS/URANS models may overestimate turbulent viscosity in cavitation zones, preventing the development of a cavity shedding pattern and yielding unnatural results (Coutier-Delgosha, Fortes-Patella, & Reboud, 2003; Coutier-Delgosha, Reboud, & Dellanoy, 2003; Dular & Coutier-Delgosha, 2008). Eventually, a correction (Reboud, Stutz, & Coutier-Delgosha, 1998) was applied in order to modify the turbulent kinetic energy term in two-equation RANS model closure and with this term it was possible to replicate the experimental shedding pattern with CFD simulations. The importance of accurately capturing the turbulence-induced pressure fluctuations in cavitating flows is highlighted in a study with the main focus on throttles and constrictions appearing in fuel injection system (Edelbauer, Strucl, & Morozov, 2014). They have compared RANS and LES simulations of a cavitating throttle flow. Despite the fact that they employed a rather specialized variant of the  $v_2$ - $f$  turbulence model, they were unable to get good results in any of the examined cases, showing the situational applicability of the RANS model. They conclude that RANS can predict cavitation with a reasonably acceptable accuracy in operating conditions with high upstream-downstream pressure difference, whereas

it fails to predict cavitation at lower pressure difference values. Other researchers (Andriotis et al., 2008; Giannadakis, 2005; Singhal et al., 2002) tried to compensate for the turbulent effect on cavitation inception through the inclusion of an additional semi-empirical pressure fluctuation term to the saturation pressure.

Fluid properties and compressibility effects, also affect the in-nozzle flow by modifying the flow turbulence and cavitation. This is because formation and collapse of cavitation vapours is subject to pressure fluctuations due to local flow instabilities and a two-way interaction exists between cavitation and turbulence. Moreover, as mentioned earlier, collapse of cavitation bubbles is a primary mechanism for vorticity production and enhancement of streamwise velocity fluctuations (Aeschlimann, Barre, & Djeridi, 2011; Dittakavi et al., 2010; Gopalan & Katz, 2000; Iyer & Ceccio, 2002). Compression and expansion of cavitation vapours results in misalignment of the density gradients and the pressure gradients, resulting in baroclinic torque and vorticity production (Dittakavi et al., 2010; Iyer & Ceccio, 2002).

In addition to compressibility effects, cavitation also modifies the size and shape of the vortical structures in the flow and hence the interaction between the small and large scales. Experimental analysis using PIV-LIF in a cavitating mixing layer shows a reduction in the size of the coherent vortices as cavitation intensifies (Aeschlimann et al., 2011). Turbulence anisotropy is increased as cavitation enhances the diffusivity in the streamwise direction while damping the cross-stream diffusivity (Aeschlimann et al., 2011). Moreover, bubbles in vortex rings can distort and elongate an initially circular vortex core, as the bubble volume forces (pressure gradient, viscous and buoyancy forces) change the momentum in the liquid phase (Sridhar & Katz, 1999).

### **2.3. Turbulent drag reduction by viscoelastic additives**

Turbulent drag contributes to flow losses in fluid machinery and an extensive body of research is dedicated to provide innovative techniques to reduce the turbulent drag. These include passive methods such as polymer and surfactant additives, microbubble injection, and particle addition or active methods such as sensor/suction and fluid injection. Using viscoelastic additives in injectors is the most practical option among the drag reduction methods and an overview of the drag reduction mechanism is described in this section.

Turbulent drag reduction by viscoelastic additives was first discovered by Toms (Toms, 1948) in 1948, since then it has been numerically and experimentally studied extensively (Bewersdorff & Ohlendon, 1988; C. D. Dimitropoulos, Sureshkumar, & Beris, 1998; C. Dimitropoulos, Dubief, Shaqfeh, Moin, & Lele, 2005; Dubief et al., 2004; Graham, 2014; Japper-Jaafar, Escudier, & Poole, 2010; F. Li, Kawaguchi, & Hishida, 2004; Luchik & Tiederman, 1988; Ohlendorf et al., 1986; Owolabi, Dennis, & Poole, 2017; Procaccia, L'vov, & Benzi, 2008; Virk, 1971, 1975; White & Mungal, 2008; Xi & Graham, 2010). Modification of fluid properties and flow turbulence is achieved using even very dilute solutions of high molecular weight polymers (C. Li, Sureshkumar, & Khomami, 2006) or surfactant systems (Rose & Foster, 1989). This knowledge is applied in oil delivery pipelines or district heating/cooling systems to reduce the turbulent drag, heat losses and the pumping costs (Zakin, Lu, & Bewersdorff, 1998).

The drag reduction mechanism in viscoelastic fluids is related to the interaction between the polymers and turbulence. Polymer viscosity as well as polymer elasticity, measured in terms of relaxation time, are both shown to be effective in this mechanism; however viscosity and elasticity effects form the basis for two theories describing drag reduction (White & Mungal, 2008). In the theory based on polymer viscosity, stretching of the polymers increases the total viscosity, suppressing the Reynolds stresses in the buffer layer region. As a result, the thickness of the viscous sub-layer is increased and the turbulent drag is reduced (L'vov, Pomyalov, Procaccia, & Tiberkevich, 2004; Lumley, 1973; Ryskin, 1987; White & Mungal, 2008). In the elastic theory, the onset of drag reduction is when the elastic energy in the polymers becomes comparable to the Reynolds stresses in the buffer layer at length scales larger than the Kolmogorov scale. Consequently the energy cascade is truncated as the small-scales are suppressed and the viscous sublayer is thickened, resulting in drag reduction (Tabor & de Gennes, 1986; White & Mungal, 2008). Numerical and experimental studies verify that in a drag-reduced flows, thickness of the viscous sublayer is increased (Luchik & Tiederman, 1988; Min, Yoo, Choi, & Joseph, 2003; Virk, 1971). It is shown that drag reduction happens only when the polymer relaxation time is above a certain limit and the percentage of drag reduction does not exceed a maximum value (Virk, 1971). The criterion for onset of drag reduction is that the polymer relaxation time must be larger than the time scale of near wall turbulence (Berman, 1977):

$$\lambda > \frac{\nu}{u_\tau^2} \quad \text{Equation 2.8}$$

where  $\nu$  is the kinematic viscosity and  $u_\tau$  is the friction velocity define by  $u_\tau = \sqrt{\frac{\tau_w}{\rho}}$ .

This criterion also points to the fact that drag reduction is not only due to the effect of the elongational viscosity, but also the elastic property of the fluid plays a significant role in this mechanism. When measuring the total shear stress in a drag-reduced flow, it is noted that the sum of viscous shear stress and the Reynolds stress ( $\rho \overline{u'v'}$ ) is smaller than the total shear stress, this is known as the “stress deficit” and the missing stress in this calculation is the polymeric stress induced by the extended polymers (Den Toonder, Hulslen, Kuiken, & Nieuwstadt, 1997):

$$\tau_{total} = \mu \frac{d\bar{u}}{dy} - \rho \overline{u'v'} + \tau_p \quad \text{Equation 2.9}$$

Investigations on the effect of polymer on turbulent characteristics of drag-reduced flows, show that the rms of streamwise velocity fluctuations is reduced in the viscous region near the wall and increased in rest of the flow. However, the spanwise and wall-normal values of rms of turbulent velocity fluctuation are constantly reduced by polymer additives (Harder, Tiederman, & Hardert, 1991; Min et al., 2003; Warholic, Heist, Katcher, & Hanratty, 2001; Wei & Willmarth, 1992). This means that the polymers reduce the near-wall turbulence and transport the turbulence kinetic energy to the buffer layer and the log layer. When the relaxation time of the viscoelastic fluid is too short for drag-reduction to happen, the energy extracted from the near wall turbulence does not reach the buffer layer and is instead released near the wall, forming an equilibrium state of energy exchange in the viscous layer, which does not have an effect on the drag. Reynolds stresses and vorticity fluctuations are reduced in in the drag-reduced flow and on average location of the vortex cores moves away from the wall, making the skin friction due to vortex motion less effective (Min et al., 2003).

It is worth mentioning that friction drag can be reduced and increased at the same time by viscoelastic additives. Reduction of drag is by the mechanism mentioned earlier, i.e. transport of near wall turbulence energy outside the viscous sublayer. Enhancement of drag is due to the additional viscoelastic stress by the polymer strands, however in drag-reduced flows the amount of added viscous stress is much smaller than drag reduction, so the overall effect is reduction of the friction drag (Yu, Li, & Kawaguchi, 2004).

Moreover, in polymeric drag-reduced flows, the spacing of the streamwise streaks is increased and the streaks become less frequent (C. D. Dimitropoulos et al., 1998; Luchik & Tiederman, 1988). It has also been noted that turbulent vortical structures and deforming microstructures of the polymers are asynchronous as the location of high polymer extension in the flow and vortex structure do not coincide (C. Dimitropoulos et al., 2005).

## **2.4. Literature gap: Cavitation and viscoelasticity**

The existing body of literature related to the interaction of viscoelasticity and cavitation is limited and it is mainly focused on dynamics of single bubbles in a viscoelastic medium due to their applications in biomedicine and rheology. A few studies have focused on active polymer injection for suppression of tip vortex cavitation in hydrofoils for naval applications, which are presented in the following section.

### **2.4.1. Bubble dynamics in viscoelastic fluids**

Literature studies that correlate viscoelasticity and cavitation mainly focus on bubble dynamics in viscoelastic tissue-like medium. Microbubbles can act as powerful tools for ultrasound contrast agents (Goldberg, Liu, & Forsberg, 1994; Sijl et al., 2010) or as rheological probes (Jamburidze, De Corato, Huerre, Pommella, & Garbin, 2017) and bubble cluster collapse events can be used to destroy kidney stones (lithotripsy) (Roberts et al., 2006) and malignant tissue (histotripsy) (Roberts et al., 2006). Viscoelasticity can inhibit the high velocity liquid jet formed during the bubble collapse (E. A. Brujan, Ohl, Lauterborn, & Philipp, 1996b; E A Brujan et al., 2004; Chahine & Fruman, 1979; Lind & Phillips, 2012, 2013) and reduces the pressure amplitudes of acoustic emissions in ultrasound induced cavitation (E A Brujan et al., 2004; Emil Alexandru Brujan, 2008). Viscous effects inhibit large bubble deformations and prevent incoherent bubble oscillations (Lind & Phillips, 2012). In a viscoelastic fluid, bubble oscillations can be damped by viscosity and compressibility effects, however at large elasticity values, viscous damping becomes almost negligible and mainly compressibility effects are important (Hua & Johnsen, 2013). When elasticity effects are small, viscous damping is more dominant but compressibility can also have a substantial contribution to the damping mechanism (Hua & Johnsen, 2013) and should be accounted for in strong collapse events (Warnez & Johnsen, 2015).

Bubble oscillations are enhanced when the relaxation time of the viscoelastic media is increased (Hua & Johnsen, 2013; Jiménez-Fernández & Crespo, 2005; Warnez & Johnsen, 2015). At high relaxation times, bubble motion is more violent and less damped, resulting in higher bubble growth rates (Warnez & Johnsen, 2015). This is because when elasticity is high, the surrounding fluid behaves like an inviscid medium, whereas for low relaxation times (negligible elasticity) the behaviour of the surrounding fluid is Newtonian (Warnez & Johnsen, 2015). More specifically, when the relaxation time of the surrounding fluid is larger than the flow forcing period, stress can build up during each oscillation cycle, resulting in a highly chaotic bubble behaviour (Dollet et al., 2018).

#### **2.4.2. Vortex cavitation suppression by polymer injection**

Polymer injection can suppress the inception of vortex cavitation by increasing the pressure along the vortex core (C. T. Hsiao, Zhang, Wu, & Chahine, 2010). The experimental test rig in the aforementioned study consists of a vortex chamber, where flow enters the chamber tangentially forming a vortex at the centre of the chamber. If vorticity at the core of the vortex is high enough, the pressure at the vortex core will drop below the saturation pressure of the liquid, forming a vaporous core. Injection of polymer above a critical injection rate from a nozzle upstream of the chamber can effectively suppress the formation of the vortex cavitation. Numerical simulations of Newtonian and viscoelastic fluid shows that in the polymeric solution, pressure at a vortex core is increased compared to the Newtonian solution. It was shown that the polymeric stress increases in the vicinity of the vortex and reaches a maximum at the vortex core (C. T. Hsiao et al., 2010).

Mass and polymer injection into the core of the trailing vortex in hydrofoils can also suppress the tip vortex cavitation (Chang, Ganesh, Yakushiji, & Ceccio, 2011). In a set of experiments, water and polymer are injected from a hole in the tip of the hydrofoil where the cavitation inception takes place. Both water and polymer can suppress cavitation, however injection of the polymer is more effective in delaying the cavitation inception. Two mechanisms are identified for the tip vortex cavitation suppression; suppression of the flow unsteadiness and intensification of the mass and momentum flux. PIV measurements indicated that by injection of water or polymer into the vortex core, the pressure fluctuations in the core, which lead to cavitation inception, are reduced. Moreover, mass injection (water or polymer) leads to a larger vortex core size while maintaining the circulation level, resulting in the increased pressure in the vortex core.

## 3. Computational Methodology

---

In this chapter, the governing equations and numerical methods used to simulate the test cases are described. In order to fully describe the dynamics of cavitating flows, turbulence and cavitation models are solved in addition to continuity equation and Navier-Stokes equations for momentum conservation. Furthermore, a constitutive equation based on the Phan-Thien-Tanner model is solved to find the viscoelastic stresses in the polymeric solutions. All simulations are performed in ANSYS FLUENT<sup>®</sup> V17 using either pre-existing implemented models or with programmed modifications through user defined functions.

### 3.1. Governing equations

Compression or expansion of a fluid element causes a divergence in the velocity field  $\mathbf{U}$  (u,v,w), and the total rate of change of the density  $\rho$  can be described by the mass conservation equation:

$$\frac{\partial \rho}{\partial t} + \nabla \cdot (\rho \mathbf{U}) = 0 \quad \text{Equation 3-1}$$

The Navier-Stokes (N-S) equations are momentum conservation equations for viscous fluids. The equations represents the balance between body and surface forces. Body forces act directly on the mass of the fluid element such as gravity and surface forces arise from the distribution



of forces through direct contact with the fluid surface such as pressure. The conservative form of N-S equations are:

$$\frac{\partial(\rho U)}{\partial t} + \nabla \cdot (\rho U U) = -\nabla P + \nabla \cdot \boldsymbol{\tau} + \rho \mathbf{g} + \mathbf{F} \quad \text{Equation 3-2}$$

where  $P$  is the pressure force,  $\boldsymbol{\tau}$  is the stress tensor,  $\mathbf{g}$  is the gravitational acceleration and  $\mathbf{F}$  is any external force. The stress tensor is defined as the combination of viscous stress and the stress due to volume dilatation:

$$\boldsymbol{\tau} = \mu \left[ (\nabla \mathbf{U} + (\nabla \mathbf{U})^T) - \frac{2}{3} (\nabla \cdot \mathbf{U}) \mathbf{I} \right] \quad \text{Equation 3-3}$$

where  $\mu$  is the fluid viscosity and  $\mathbf{I}$  is the identity tensor.

The N-S partial differential equations should be discretized in order to be solved. In Finite Volume (FV) method, the computational domain is divided into a set of control volume cells and the governing equations are integrated over the control volume  $V$ . The integral form of the transport equation for a scalar  $\phi$  can be written as:

$$\int_V \frac{\partial(\rho \phi)}{\partial t} dV + \oint \rho \phi \mathbf{U} \cdot d\mathbf{A} = \oint \Gamma_\phi \nabla \phi \cdot d\mathbf{A} + \int_V S_\phi dV \quad \text{Equation 3-4}$$

where  $\mathbf{A}$  is the surface area vector,  $\Gamma_\phi$  is the diffusion coefficient and  $S_\phi$  is the scalar source. Note that in order to convert the volume integral terms to surface integral, the Gauss divergence theorem is applied to Equation 3-4. The discretized form of the equation produces:

$$\frac{\partial(\rho \phi)}{\partial t} V + \sum_f^{N_{faces}} \rho_f \phi_f \mathbf{U}_f \cdot \mathbf{A}_f = \sum_f^{N_{faces}} \Gamma_\phi \nabla \phi_f \cdot \mathbf{A}_f + S_\phi V \quad \text{Equation 3-5}$$

where the subscript  $f$  represents the face values and  $N_{faces}$  is the number of cells closing a cell volume. The resulting set of algebraic equations are then solved using discretization schemes mentioned separately for each test case.

## 3.2. Turbulence modelling

Turbulence occurs when adjacent layers of fluid moving at different velocities start mixing above a certain Reynolds number. Turbulent flows are characterized by chaotic and random

fluid motion resulting in enhancement of the momentum exchange. Moreover, the flow consists of large scale eddies which are inertia-dominated down to small scale dissipative eddies. Largest eddies extract the flow energy by means of vortex stretching and subsequently stretch the smaller eddies. This process results in the transfer of energy from the largest to the smallest eddies through an “energy cascade”. The Reynolds number at the smallest scales known as the Kolmogorov microscales is equal to unity, which implies that the inertial and viscous effects are of the same order. The inertial energy of eddies in the Kolmogorov subrange is dissipated as heat which results in higher energy losses associated with turbulent flows. (Pope, 2000; Versteeg & Malalasekera, 2007).

Based on Reynolds decomposition, the velocity vector in a turbulent flow can be defined by the sum of the mean velocity  $\bar{\mathbf{U}}$  and the fluctuating velocity component:  $\mathbf{U}'$ :  $\mathbf{U} = \bar{\mathbf{U}} + \mathbf{U}'$ . RANS models use the Reynolds decomposition definition of the variables and apply ensemble averaging to the governing equations to solve for the mean velocity  $\bar{\mathbf{U}}$ . The density-weighted (Favre-averaged) form of the equations are solved when the compressibility effects become significant. The governing equations for Reynolds averaged compressible flows are: ( $\tilde{\mathbf{U}}$  stands for mass-averaged velocity):

$$\frac{\partial \bar{\rho}}{\partial t} + \nabla \cdot (\bar{\rho} \tilde{\mathbf{U}}) = 0 \quad \text{Equation 3-6}$$

$$\frac{\partial (\bar{\rho} \tilde{\mathbf{U}})}{\partial t} + \nabla \cdot (\bar{\rho} \tilde{\mathbf{U}} \tilde{\mathbf{U}}) = -\frac{\partial \bar{P}}{\partial x} + \nabla \cdot (\mu \nabla \tilde{\mathbf{U}}) + \left[ -\frac{\partial (\overline{\bar{\rho} u'^2})}{\partial x} - \frac{\partial (\overline{\bar{\rho} u' v'})}{\partial y} - \frac{\partial (\overline{\bar{\rho} u' w'})}{\partial z} \right] \quad \text{Equation 3-7}$$

$$\frac{\partial (\bar{\rho} \tilde{V})}{\partial t} + \nabla \cdot (\bar{\rho} \tilde{V} \tilde{\mathbf{U}}) = -\frac{\partial \bar{P}}{\partial y} + \nabla \cdot (\mu \nabla \tilde{V}) + \left[ -\frac{\partial (\overline{\bar{\rho} u' v'})}{\partial x} - \frac{\partial (\overline{\bar{\rho} v'^2})}{\partial y} - \frac{\partial (\overline{\bar{\rho} v' w'})}{\partial z} \right] \quad \text{Equation 3-8}$$

$$\frac{\partial (\bar{\rho} \tilde{W})}{\partial t} + \nabla \cdot (\bar{\rho} \tilde{W} \tilde{\mathbf{U}}) = -\frac{\partial \bar{P}}{\partial z} + \nabla \cdot (\mu \nabla \tilde{W}) + \left[ -\frac{\partial (\overline{\bar{\rho} u' w'})}{\partial x} - \frac{\partial (\overline{\bar{\rho} v' w'})}{\partial y} - \frac{\partial (\overline{\bar{\rho} w'^2})}{\partial z} \right] \quad \text{Equation 3-9}$$

Averaging the momentum equations introduces new terms known as Reynolds stresses, which require modelling:

$$\text{Reynolds stresses (normal):} \quad \tau_{xx} = \overline{\bar{\rho} u'^2} \quad \tau_{yy} = \overline{\bar{\rho} v'^2} \quad \tau_{zz} = \overline{\bar{\rho} w'^2}$$

$$\text{Reynolds stresses (shear):} \quad \tau_{xy} = \tau_{yx} = \overline{\bar{\rho} u' v'} \quad \tau_{xz} = \tau_{zx} = \overline{\bar{\rho} u' w'} \quad \tau_{yz} = \tau_{zy} = \overline{\bar{\rho} v' w'}$$

The closure models for Reynolds stresses generally rely on the assumption of isotropic turbulence. In two equation models (k- $\epsilon$  and k- $\omega$  family), Boussinesq eddy viscosity hypothesis

is employed, which assumes Reynolds stresses are proportional to the mean strain rate. The index notation as defined below will be used where appropriate:

$$\mathbf{x} = (x_i) = (x_1, x_2, x_3) = (x, y, z)$$

$$\mathbf{U} = (U_i) = (u_1, u_2, u_3) = (u, v, w)$$

Using the index notation the eddy viscosity hypothesis defines the Reynolds stress as:

$$-\overline{\rho u'_i u'_j} = \mu_t \left( \frac{\partial U_i}{\partial x_j} + \frac{\partial U_j}{\partial x_i} \right) - \frac{2}{3} \rho k \delta_{ij} \quad \text{Equation 3-10}$$

where  $k$  is the turbulent kinetic energy ( $k = 0.5(\overline{u'^2} + \overline{v'^2} + \overline{w'^2})$ ) and  $\mu_t$  is the turbulent viscosity and  $\delta_{ij}$  is the Kronecker delta. In Reynolds Stress Model (RSM) turbulence anisotropy is considered by calculating each component of the Reynolds stress tensor separately, adding 6 extra transport equations.

Large eddy simulation is based on resolving the large scale transient eddies and modelling the smaller eddies which have a more universal behaviour. A filtering function is applied to all the flow variables, which passes the low frequency scales to be solved directly while filtering the high frequency scales. A spatially filtered variable  $\widehat{\phi}(x)$  by means of a filter function  $G(x, x')$  in a fluid domain  $D$  is:

$$\widehat{\phi}(x) = \int_D \phi(x') G(x, x') dx', \quad x' \in D \quad \text{Equation 3-11}$$

In ANSYS FLUENT a top-hat type filtering operator is applied and the filtering is implicitly provided by the finite volume method:

$$G(x, x') = \begin{cases} 1/V & x' \in v \\ 0 & x' \text{ otherwise} \end{cases} \quad \text{Equation 3-12}$$

so

$$\widehat{\phi}(x) = \frac{1}{V} \int_v \phi(x') dx', \quad x' \in v \quad \text{Equation 3-13}$$

where  $V$  is the cell volume. In a similar manner to RANS equations, filtering operation in LES results in additional terms in the momentum equations that require modelling.

$$\frac{\partial \rho}{\partial t} + \nabla \cdot (\rho \hat{\mathbf{U}}) = 0 \quad \text{Equation 3-14}$$

$$\frac{\partial(\rho \hat{U})}{\partial t} + \nabla \cdot (\rho \hat{U} \hat{\mathbf{U}}) = -\frac{\partial \hat{P}}{\partial x} + \nabla \cdot (\mu \nabla \hat{U}) + \left[ -\frac{\partial(\rho \widehat{u'^2})}{\partial x} - \frac{\partial(\rho \widehat{u'v'})}{\partial y} - \frac{\partial(\rho \widehat{u'w'})}{\partial z} \right] \quad \text{Equation 3-15}$$

$$\frac{\partial(\rho \hat{V})}{\partial t} + \nabla \cdot (\rho \hat{V} \hat{\mathbf{U}}) = -\frac{\partial \hat{P}}{\partial y} + \nabla \cdot (\mu \nabla \hat{V}) + \left[ -\frac{\partial(\rho \widehat{u'v'})}{\partial x} - \frac{\partial(\rho \widehat{v'^2})}{\partial y} - \frac{\partial(\rho \widehat{v'w'})}{\partial z} \right] \quad \text{Equation 3-16}$$

$$\frac{\partial(\rho \hat{W})}{\partial t} + \nabla \cdot (\rho \hat{W} \hat{\mathbf{U}}) = -\frac{\partial \hat{P}}{\partial z} + \nabla \cdot (\mu \nabla \hat{W}) + \left[ -\frac{\partial(\rho \widehat{u'w'})}{\partial x} - \frac{\partial(\rho \widehat{v'w'})}{\partial y} - \frac{\partial(\rho \widehat{w'^2})}{\partial z} \right] \quad \text{Equation 3-17}$$

Hybrid RANS/LES models don't have the strict grid and time step requirement of LES models and at the same time they provide more details than RANS models, hence they can be a better alternative to LES simulations in cases where the computational domain is large compared to relevant flow length scales.

### 3.2.1. RANS models

Cavitating flows are associated with flow conditions such as adverse pressure gradient, flow separation and recirculation and therefore, default RANS models are not the most suitable option. Therefore, instead the RNG  $k-\varepsilon$  model, the Realizable  $k-\varepsilon$  model, the SST  $k-\omega$  model and the Reynolds stress model that are more accurate in predicting flows with rapid strain and strong streamline curvature are employed.

#### 3.2.1.1. RANS $k-\varepsilon$ models

This group of RANS models solve two additional transport equations; one for the turbulence kinetic energy  $k$ , and one for its dissipation rate  $\varepsilon$ . This is based on Prandtl's mixing length model that describes the eddy viscosity from a one velocity scale  $\vartheta$  and one length scale  $\ell$ :

$$\mu_t = C_\rho \vartheta \ell \quad \text{Equation 3-18}$$

After applying dimensional analysis, the eddy viscosity can be expressed in terms of  $k$  and  $\varepsilon$  as:

$$\mu_t = \rho C_\mu \frac{k^2}{\varepsilon} \quad \text{Equation 3-19}$$

where  $C_\mu$  is a dimensionless constant. The main deficiency of this model is in calculation of turbulence kinetic energy in regions of flow separation and stagnation points. To overcome the

shortcomings of the standard  $k$ - $\varepsilon$  model in conditions with flow separation and recirculation, two of the more advanced variants of this model have been used for the purpose of the current study:

- Renormalization Group (RNG)  $k$ - $\varepsilon$  model: This model provides an improved description for swirling flows and can account for the low Reynolds number effects in the effective viscosity formulation (Yakhot & Orszag, 1992). The transport equations for  $k$  and  $\varepsilon$  are analytically derived from the N-S equations using the statistical RNG method to represent the effects of small scale turbulence in terms of eddy viscosity and larger scale motions:

$$\frac{\partial(\rho k)}{\partial t} + \nabla \cdot (\rho k \mathbf{U}) = \nabla \cdot (\alpha_k \mu_{eff} \nabla k) + 2\mu_t S_{ij} \cdot S_{ij} - \rho \varepsilon \quad \text{Equation 3-20}$$

$$\frac{\partial(\rho \varepsilon)}{\partial t} + \nabla \cdot (\rho \varepsilon \mathbf{U}) = \nabla \cdot (\alpha_\varepsilon \mu_{eff} \nabla \varepsilon) + C_{1\varepsilon} \frac{\varepsilon}{k} \tau_{ij} \cdot S_{ij} - C_{2\varepsilon} \rho \frac{\varepsilon^2}{k} \quad \text{Equation 3-21}$$

where  $\mu_{eff} = \mu + \mu_t$  and the constant  $C_\mu = 0.0845$  is used for calculation of the eddy viscosity. More specific details regarding the terms used in this equation can be found in (FLUENT, 2017)

- Realizable  $k$ - $\varepsilon$  model: In formulation of the eddy viscosity, a constraint is put on the normal stress to remain positive even at regions of very high strain rate. This is achieved by making  $C_\mu$  a function of the mean flow and the turbulence. Another key difference in equations of the Realizable  $k$ - $\varepsilon$  model and the standard  $k$ - $\varepsilon$  model is in the  $\varepsilon$  equation, which is derived from the transport equation of vorticity fluctuations (Shih, Liou, Shabbir, Yang, & Zhu, 1995). The  $k$  and  $\varepsilon$  transport equations are:

$$\frac{\partial(\rho k)}{\partial t} + \nabla \cdot (\rho k \mathbf{U}) = \nabla \cdot \left( \left( \mu + \frac{\mu_t}{\sigma_k} \right) \nabla k \right) + 2\mu_t S_{ij} \cdot S_{ij} - \rho \varepsilon \quad \text{Equation 3-22}$$

$$\frac{\partial(\rho \varepsilon)}{\partial t} + \nabla \cdot (\rho \varepsilon \mathbf{U}) = \nabla \cdot \left( \left( \mu + \frac{\mu_t}{\sigma_\varepsilon} \right) \nabla \varepsilon \right) + \rho C_1 S \varepsilon - \rho C_2 \frac{\varepsilon^2}{k + \sqrt{\nu \varepsilon}} \quad \text{Equation 3-23}$$

### 3.2.1.2. RANS $k$ - $\omega$ models

Similar to  $k$ - $\varepsilon$  models, this group of turbulence models also solve two additional transport equations, one for the turbulence kinetic energy  $k$ , and one for the specific dissipation rate  $\omega$ .

The unit for  $\omega$  is hertz and it is defined from the inverse of the kinetic energy dissipation time scale ( $\omega = \varepsilon/k$ ). This model accounts for low Reynolds number effects and is best suited for modelling the near wall turbulence (DC Wilcox, 1988). The eddy viscosity using  $\omega$  is given by:

$$\mu_t = \rho \frac{k}{\omega} \quad \text{Equation 3-24}$$

The standard  $k$ - $\omega$  model is sensitive to the freestream value of  $\omega$  and some modifications are proposed to overcome this shortcoming:

- Shear Stress Transport (SST)  $k$ - $\omega$  model: The SST model offers the best of both the  $k$ - $\varepsilon$  and  $k$ - $\omega$  models, blending the freestream independency of the  $k$ - $\varepsilon$  model with the accurate near wall prediction of the  $k$ - $\omega$  model. The set of equations are (Menter, 1993, 1994):

$$\frac{\partial(\rho k)}{\partial t} + \nabla \cdot (\rho k \mathbf{U}) = \nabla \cdot \left( \left( \mu + \frac{\mu_t}{\sigma_k} \right) \nabla k \right) + \tilde{G}_k - Y_k \quad \text{Equation 3-25}$$

$$\frac{\partial(\rho \omega)}{\partial t} + \nabla \cdot (\rho \omega \mathbf{U}) = \nabla \cdot \left( \left( \mu + \frac{\mu_t}{\sigma_{\omega,1}} \right) \nabla \omega \right) + G_w - Y_\omega \quad \text{Equation 3-26}$$

where G and Y terms respectively represent the generation and dissipation of  $k$  or  $\omega$ . More specific details regarding the terms used in this equation can be found in (FLUENT, 2017).

### 3.2.1.3. Reynolds stress model (RSM)

The Reynolds Stress Model is the most general and elaborate form of RANS models. It disregards the assumption of turbulence isotropy and the eddy viscosity hypothesis and instead solves a transport equation for Reynolds stresses in each direction. Solving a transport equation for each component adds a significant amount of computational cost (6 extra equations). This model is most appropriate for highly anisotropic flows such as swirling flows and flows with rotating boundaries (Launder, Reece, & Rodi, 1975; Speziale, Sarkar, & Gatski, 1991).

### 3.2.1.4. RANS models modifications

The Reboud *et al.* modification is proposed to account for reduction of eddy viscosity in the two-phase mixture region, allowing the development of stronger shear flows. These

modifications can be applied to unsteady simulations. A function  $f(\rho)$ , is introduced to replace the density in the eddy viscosity formulation (Coutier-Delgosha, Fortes-Patella, & Reboud, 2002; Reboud et al., 1998):

$$f(\rho) = \rho_v + (1 - \alpha)^n(\rho_l - \rho_v) \quad n \gg 1 \quad \text{Equation 3-27}$$

where  $\rho_v$  is the vapour density,  $\rho_l$  is the liquid density and  $n$  is the exponent, which is set to 10 for the present study.

The eddy viscosity correction for  $k-\varepsilon$  RNG model is:

$$\mu_t = \frac{f(\rho)C_\mu k^2}{\varepsilon} \quad C_\mu = 0.845 \quad \text{Equation 3-28}$$

and for the  $k-\omega$  SST model:

$$\mu_t = f(\rho) \frac{\alpha_1 k}{\max(\alpha_1 \omega, SF_2)} \quad \text{Equation 3-29}$$

where  $\alpha_1=5/9$ ,  $S$  is the magnitude of the strain rate tensor and  $F_2$  is the blending function (D. Wilcox, 2006). The DEFINE\_TURBULENT\_VISCOSITY UDF functionality of FLUENT is used to implement the new eddy viscosity models. In Figure 3-1, the density multiplier in the eddy viscosity formulation for the standard and the modified models for water is compared.

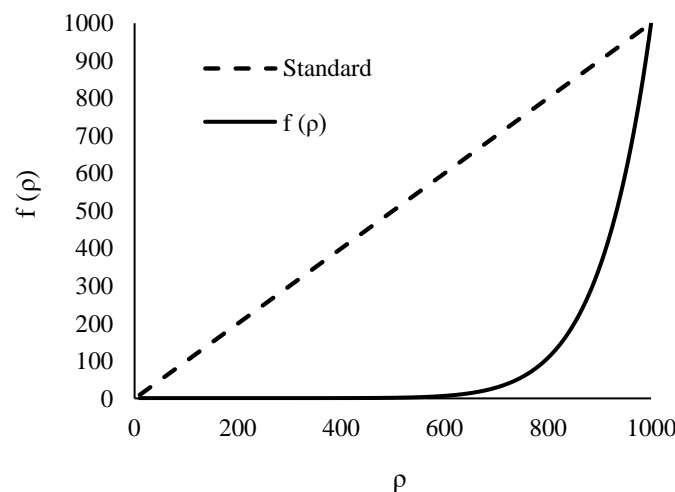


Figure 3-1. Comparison of the standard and the modified eddy viscosity multipliers as a function of density

### 3.2.2. LES model

The wall-adapting local eddy viscosity (WALE) model is used to model the flow turbulence in the LES framework (Nicoud & Ducros, 1999). The eddy viscosity in this model is based on the square of velocity gradient tensor, and it has the property that both local strain and rotation rates are included in the formulation. Also in order to accurately model the laminar and near wall flow regimes, eddy viscosity in pure shear and near wall is zero, this is an advantage over the Smagorinsky-Lilly model:

$$\mu_t = \rho L_s^2 \frac{(\mathbf{S}_{ij}^d \mathbf{S}_{ij}^d)^{3/2}}{(\mathbf{S}_{ij} \mathbf{S}_{ij})^{5/2} + (\mathbf{S}_{ij}^d \mathbf{S}_{ij}^d)^{5/4}} \quad \text{Equation 3-30}$$

where the spatial operator  $L_s = \min(d, C_w U^{1/3})$  is defined based on the distance from the wall  $d$ , and  $C_w = 0.325$ , the eddy viscosity predicts the correct  $y^3$  near wall asymptote and naturally goes to zero at the wall.  $\mathbf{S}_{ij}$  is the strain rate tensor and  $\mathbf{S}_{ij}^d$  is the symmetric traceless part of the strain rate tensor:

$$\mathbf{S}_{ij}^d = \frac{1}{2} \left[ \left( \frac{\partial u_i}{\partial x_j} \right)^2 + \left( \frac{\partial u_j}{\partial x_i} \right)^2 \right] - \frac{1}{3} \text{tr} \left[ \left( \frac{\partial u_i}{\partial x_j} \right)^2 \right] \delta_{ij} \quad \text{Equation 3-31}$$

## 3.3. Cavitation modelling

The performance of the two-phase cavitation models is compared with the barotropic cavitation model and the model equations are explained in this section. The fundamental difference between the two models is that the former is based on the assumption of mechanical equilibrium between the phases whereas the latter is based on the thermodynamic equilibrium assumption.

### 3.3.1. Mechanical cavitation models

The cavitation models of Zwart-Gerber-Belamri (Zwart et al., 2004) and Schnerr-Sauer (Schnerr & Sauer, 2001) are employed. In both of the models, a transport equation for the vapour volume fraction  $\alpha$  is solved:

$$\frac{\partial}{\partial t} (\alpha \rho_v) + \nabla \cdot (\alpha \rho_v \bar{\mathbf{U}}) = R_e - R_c \quad \text{Equation 3-32}$$



where  $\rho_v$  is the vapour density,  $R_e$  is the evaporation rate and  $R_c$  is the condensation rate. A homogenous mixture model is used to describe the two-phase fluid. It is important to mention that even if the liquid and gas phase are assumed to be incompressible, the mixture is compressible because of the effect of mass transfer, in fact the mixture compressibility is directly proportional to the rate of mass transfer rate (Franc & Michel, 2005). By solving Equation 3-32, the vapour volume fraction value is used to calculate the mixture density:

$$\rho = \alpha\rho_v + (1 - \alpha)\rho_l \quad \text{Equation 3-33}$$

Therefore, the mass and momentum conservation equations are solved for the mixture phase only. Fluid properties used for these models are presented in Table 3-1 and the mass transfer rate formulation specific to each model is described below.

- Zwart-Gerber-Belamri Model:

The ZGB model proposes that the evaporation/condensation rates in a unit volume of fluid can be described by the mass change rate of the bubbles inside the fluid element. Effectively, the mass transfer rate  $R$  is defined in terms on the bubble number density ( $n$ ) and the rate of mass change of a single bubble based on the Rayleigh-Plesset equation:

$$R = n \times \left( \rho_v \times 4\pi\mathfrak{R}_B^2 \frac{D\mathfrak{R}_B}{Dt} \right) \quad \text{Equation 3-34}$$

where :

$$\frac{D\mathfrak{R}_B}{Dt} \approx \sqrt{\frac{2 P_v - P}{3 \rho_l}} \quad \text{Equation 3-35}$$

and the vapour volume fraction  $\alpha$  can be defined in terms of the bubble number density  $n$ :

$$\alpha = n \times \left( \frac{4}{3} \pi \mathfrak{R}_B^3 \right) \quad \text{Equation 3-36}$$

The mass transfer rate can now be expressed in terms of the pressure of the fluid element ( $P$ ) and the vapour volume fraction. When the local pressure is above the fluid saturation pressure, the condensation rate equation is used:

$$R_c = F_{cond} \frac{3\alpha\rho_v}{\mathfrak{R}_B} \sqrt{\frac{2P - P_v}{3\rho_l}} \quad \text{Equation 3-37}$$

and the evaporation rate is calculated from the following equation:

$$R_e = F_{vap} \frac{3\alpha_{nuc}(1 - \alpha)\rho_v}{\mathfrak{R}_B} \sqrt{\frac{2P_v - P}{3\rho_l}} \quad \text{Equation 3-38}$$

Note that the evaporation rate is proportional to  $\alpha_{nuc}(1 - \alpha)$  in order to consider the reduction of nucleation site vapour volume fraction ( $\alpha_{nuc}$ ) as the vapour volume fraction grows.  $F_{vap}$  and  $F_{cond}$  are empirical evaporation and condensation coefficients and  $\mathfrak{R}_B$  is the bubble radius. The following constants are used for this study:

$$\alpha_{nuc} = 5 \times 10^{-4} \quad F_{vap} = 50 \quad F_{cond} = 0.001 \quad \mathfrak{R}_B = 10^{-6}m$$

- Schnerr and Sauer Model:

The mass transfer rate in the SS model is proportional to  $\frac{\rho_v\rho_l}{\rho}\alpha(1 - \alpha)$  which means that in pure liquid and pure vapour phases, evaporation and condensation rates approach zero. This property of the model takes into account that the evaporation process stops when all the liquid has evaporated ( $\alpha = 1$ ), moreover, no evaporation process is modelled in the case of pure liquid substances ( $\alpha = 0$ ). The evaporation and condensation rates in the SS are defined as:

$$R_e = \frac{\rho_v\rho_l}{\rho}\alpha(1 - \alpha) \frac{3}{\mathfrak{R}_B} \sqrt{\frac{2P_v - P}{3\rho_l}} \quad \text{Equation 3-39}$$

$$R_c = \frac{\rho_v\rho_l}{\rho}\alpha(1 - \alpha) \frac{3}{\mathfrak{R}_B} \sqrt{\frac{2P - P_v}{3\rho_l}} \quad \text{Equation 3-40}$$

The fluid property values used in all the test cases with the ZGB and the SS cavitation models are summarized in Table 3-1. In the fuel injector test case, the pressure levels change significantly because of the high injection pressure, so the subsequent changes in the diesel fuel properties should be considered. Therefore, the density and the viscosity of the fuel are calculated as a function of pressure. The density is calculated using the Tait equation of state to represent the weak compressibility of the liquid diesel:

$$P = B \left[ \left( \frac{\rho}{\rho_{sat,L}} \right)^n - 1 \right] + P_{sat} \quad \text{Equation 3-41}$$

where the bulk modulus  $B$  is 110 MPa, the material exponent  $n$  is 7.15, and  $\rho_{sat,L}$  and  $P_{sat}$  are the liquid saturation density and saturation pressure, respectively. The liquid viscosity is calculated based on the correlation proposed by Kolev (Kolev, 2005):

$$\log_{10} \left( \frac{10^6 \mu_L}{\rho} \right) = 0.035065275 - \frac{0.000234373P}{10^5} \quad \text{Equation 3-42}$$

	Liquid Properties				Vapour Properties		
	Water	Diesel			Water	Diesel	
$\rho_{sat,l}$	998.16	747.65	kg/m <sup>3</sup>	$\rho_{sat,v}$	0.0171	6.56	kg/m <sup>3</sup>
$\mu_l$	10 <sup>-3</sup>	Equation 3-42	Pa.s	$\mu_v$	9.75×10 <sup>-7</sup>	7.50×10 <sup>-6</sup>	Pa.s
$P_{sat,l}$	2340	130000	Pa				

Table 3-1. Thermodynamic properties used for water and diesel in two-phase models

### 3.3.2. Thermodynamic cavitation model

A homogenous equilibrium model (HEM) similar to cavitation model of Schmidt (David P Schmidt, 1997) is used which solves for one fluid only with a variable density (Koukouvinis & Gavaises, 2015). The model is implemented in FLUENT using UDF functionalities and the density of the fluid is modelled using a barotropic EoS (Koukouvinis, Naseri, et al., 2016). The liquid region is described by Tait EoS and the vaporous region is described by the isentropic gas EoS. Regions of vapour/liquid mixture can be described using Wallis speed of sound formula:

$$\frac{1}{c_m^2 \rho_m} = \frac{\alpha_l}{c_l^2 \rho_l} + \frac{\alpha_v}{c_v^2 \rho_v} \quad \text{Equation 3-43}$$

where  $\alpha$  is the volume fraction and  $c$  is the speed of sound, subscripts  $m$ ,  $l$  and  $v$  refer to mixture, liquid and vapour phases respectively.

The isentropic fluid speed of sound formula is (Koop, 2008):

$$c^2 = \left( \frac{\partial P}{\partial \rho} \right)_s \quad \text{Equation 3-44}$$

Integrating the above relation with respect to mixture density, and using the liquid, vapour and mixture EoS, we can get the complete set of equation of state for the fluid:

$$P(\rho) = \begin{cases} B \left[ \left( \frac{\rho}{\rho_l} \right)^n - 1 \right] + P_{sat,l} & \rho \geq \rho_l \\ \frac{c_v^2 c_l^2 \rho_l \rho_v (\rho_v - \rho_l)}{c_v^2 \rho_v^2 - c_l^2 \rho_l^2} \ln \left( \frac{\rho}{c_l^2 \rho_l (\rho_l - \rho) + c_v^2 \rho_v (\rho - \rho_v)} \right) + P_{ref} & \rho_v \leq \rho < \rho_l \\ C \rho^\gamma & \rho < \rho_v \end{cases} \quad \text{Equation 3-45}$$

where  $B$  is the bulk modulus of the liquid and  $n$  is the stiffness of the liquid set to 7.15 for weakly compressible liquids (Ivings, Causon, & Toro, 1998).  $C$  is the isentropic process constant and  $\gamma$  is the heat capacity ratio.  $P_{sat,l}$  and  $P_{ref}$  are added to mixture and liquid pressure curves to have a continuous pressure function. The properties are listed in Table 3-2.

Liquid Properties			Vapour Properties		
	Water			Water	
$B$	307.1 $10^6$	Pa	$C$	27234.7	Pa
$n$	7.15	-	$\gamma$	1.33	-
$\rho_{sat,l}$	998.16	kg/m <sup>3</sup>	$\rho_{sat,v}$	0.0171	kg/m <sup>3</sup>
$c_{sat,l}$	1483	m/s	$c_{sat,v}$	97.9	m/s
$P_{sat,l}$	4664.4	Pa	$P_{sat,v}$	125	Pa
$\mu_l$	$10^{-3}$	Pa.s	$\mu_v$	$9.75 \cdot 10^{-6}$	Pa.s

Table 3-2. Thermodynamic properties used for water in barotropic model

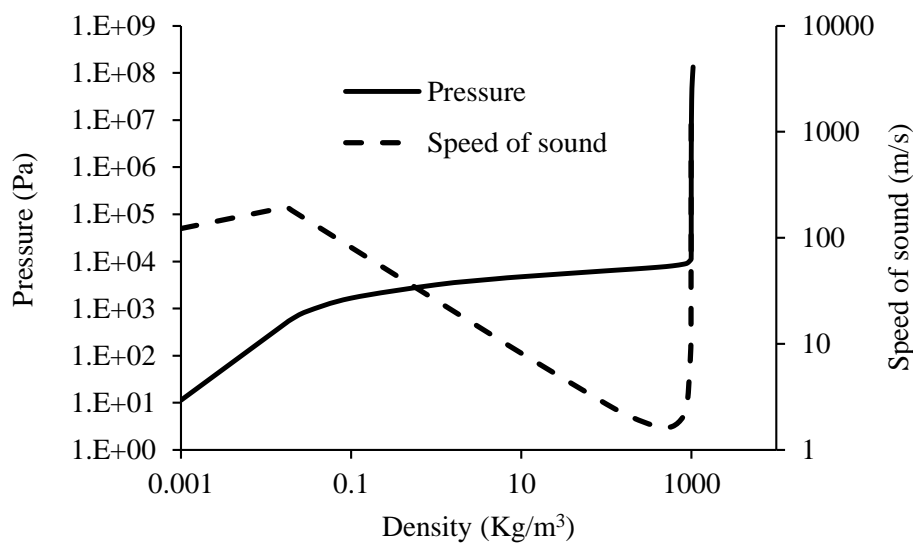


Figure 3-2. Graph showing the behaviour of the barotropic EoS and the speed of sound variation as a function of liquid density

### 3.4. Viscoelastic model

The Phan-Thien-Tanner model (Thien & Tanner, 1977) is used to model the viscoelastic fluid, which provides a constitutive equation taking into account the polymers' microstructure. This model is based on a Lodge-Yamamoto network theory (Lodge, 1968; Yamamoto, 1956) and assumes that polymer junctions constantly break and reform, so unlike the models that consider the polymers to act as elastic beads and spring dumbbells, the PTT polymer network has a dynamic nature.

The PTT constitutive model assumes that the fluid element contains several polymer junctions which can be moved by polymer extension and relaxation and the rate of "creation and destruction" of the junctions is determined from the strain rate tensor:

$$f(tr(\boldsymbol{\tau}_v)) \cdot \boldsymbol{\tau}_v + \lambda \overset{\nabla}{\boldsymbol{\tau}}_v = \mu_p (\nabla \mathbf{U} + \nabla \mathbf{U}^T) \quad \text{Equation 3-46}$$

where  $\boldsymbol{\tau}_v$  is the viscoelastic stress,  $\mu_p$  is the polymer viscosity, and the linear form of  $f(tr(\boldsymbol{\tau}_v))$  is given by:

$$f(tr(\boldsymbol{\tau}_v)) = 1 + \varepsilon \frac{\lambda}{\mu_p} tr(\boldsymbol{\tau}_v) \quad \text{Equation 3-47}$$

where  $\lambda$  is the polymer relaxation time and the extensibility factor  $\varepsilon$  is 0.02 for dilute solutions (Sibley, 2010; Thien & Tanner, 1977). For  $\lambda \rightarrow 0$ , the Oldroyd-B model is recovered and both of these models have been widely used in the literature to fit the experimental data for a range of viscoelastic fluids.  $\overset{\nabla}{\boldsymbol{\tau}}_v$  is the Oldroyd upper convected derivative, defined as:

$$\overset{\nabla}{\boldsymbol{\tau}}_v = \frac{D\boldsymbol{\tau}_v}{Dt} - [\nabla \mathbf{U} \cdot \boldsymbol{\tau}_v + \boldsymbol{\tau}_v \cdot \nabla \mathbf{U}^T] \quad \text{Equation 3-48}$$

Rearranging Equation 3-46, the final form of the constitutive model for PTT fluids is written as:

$$\lambda \frac{D\boldsymbol{\tau}_v}{Dt} = \mu_p (\nabla \mathbf{U} + \nabla \mathbf{U}^T) + \lambda [\nabla \mathbf{U} \cdot \boldsymbol{\tau}_v + \boldsymbol{\tau}_v \cdot \nabla \mathbf{U}^T] - f(tr(\boldsymbol{\tau}_v)) \cdot \boldsymbol{\tau}_v + \lambda k \nabla^2 \boldsymbol{\tau}_v \quad \text{Equation 3-49}$$

The last term is an artificial diffusion term and  $k$  is the artificial diffusivity. At the end of each iteration, the values of the velocity gradient tensor are used to calculate the viscoelastic stress terms. The viscoelastic stress source term ( $\nabla \cdot \boldsymbol{\tau}_v$ ) is then added to the momentum equations in the subsequent iteration:

$$\frac{\partial(\rho U)}{\partial t} + \nabla \cdot (\rho U U) = -\nabla P + \nabla \cdot \boldsymbol{\tau} + \nabla \cdot \boldsymbol{\tau}_v \quad \text{Equation 3-50}$$

Subgrid scale viscoelastic effects are neglected in calculations since, to the best of our knowledge, no such models have been developed for PTT fluids as this requires direct numerical simulation and experimental data for validation.

### 3.4.1. Viscoelastic model implementation

The left hand side of Equation 3-49 is the total derivative of the viscoelastic stress and the right hand side is the scalar source term (note that the transport equation is multiplied by  $\lambda$ ). The viscoelastic stress tensor has 9 components; however, since the matrix is symmetric, 6 transport equations are solved to get the full solution for  $\tau_{v11}, \tau_{v12} = \tau_{v21}, \tau_{v22}, \tau_{v13} = \tau_{v31}, \tau_{v23} = \tau_{v32}$  and  $\tau_{v33}$ . FLUENT can solve for arbitrary transport equations using the user-defined scalar (UDF) solver capability. The viscoelastic stress source term in expanded form is:

$$\begin{aligned} & \text{Source term (RHS)} \quad \text{Equation 3-51} \\ & = \mu_p \begin{bmatrix} 2 \frac{\partial u}{\partial x} & \frac{\partial u}{\partial y} + \frac{\partial v}{\partial x} & \frac{\partial u}{\partial z} + \frac{\partial w}{\partial x} \\ \frac{\partial u}{\partial y} + \frac{\partial v}{\partial x} & 2 \frac{\partial v}{\partial y} & \frac{\partial v}{\partial z} + \frac{\partial w}{\partial y} \\ \frac{\partial u}{\partial z} + \frac{\partial w}{\partial x} & \frac{\partial v}{\partial z} + \frac{\partial w}{\partial y} & 2 \frac{\partial w}{\partial z} \end{bmatrix} \\ & + \lambda \begin{bmatrix} \frac{\partial u}{\partial x} \tau_{v11} + \frac{\partial u}{\partial y} \tau_{v21} + \frac{\partial u}{\partial z} \tau_{v31} & \frac{\partial u}{\partial x} \tau_{v12} + \frac{\partial u}{\partial y} \tau_{v22} + \frac{\partial u}{\partial z} \tau_{v32} & \frac{\partial u}{\partial x} \tau_{v13} + \frac{\partial u}{\partial y} \tau_{v23} + \frac{\partial u}{\partial z} \tau_{v33} \\ \frac{\partial v}{\partial x} \tau_{v11} + \frac{\partial v}{\partial y} \tau_{v21} + \frac{\partial v}{\partial z} \tau_{v31} & \frac{\partial v}{\partial x} \tau_{v12} + \frac{\partial v}{\partial y} \tau_{v22} + \frac{\partial v}{\partial z} \tau_{v32} & \frac{\partial v}{\partial x} \tau_{v13} + \frac{\partial v}{\partial y} \tau_{v23} + \frac{\partial v}{\partial z} \tau_{v33} \\ \frac{\partial w}{\partial x} \tau_{v11} + \frac{\partial w}{\partial y} \tau_{v21} + \frac{\partial w}{\partial z} \tau_{v31} & \frac{\partial w}{\partial x} \tau_{v12} + \frac{\partial w}{\partial y} \tau_{v22} + \frac{\partial w}{\partial z} \tau_{v32} & \frac{\partial w}{\partial x} \tau_{v13} + \frac{\partial w}{\partial y} \tau_{v23} + \frac{\partial w}{\partial z} \tau_{v33} \end{bmatrix} \\ & + \lambda \begin{bmatrix} \frac{\partial u}{\partial x} \tau_{v11} + \frac{\partial u}{\partial y} \tau_{v12} + \frac{\partial u}{\partial z} \tau_{v13} & \frac{\partial v}{\partial x} \tau_{v11} + \frac{\partial v}{\partial y} \tau_{v12} + \frac{\partial v}{\partial z} \tau_{v13} & \frac{\partial w}{\partial x} \tau_{v11} + \frac{\partial w}{\partial y} \tau_{v12} + \frac{\partial w}{\partial z} \tau_{v13} \\ \frac{\partial u}{\partial x} \tau_{v21} + \frac{\partial u}{\partial y} \tau_{v22} + \frac{\partial u}{\partial z} \tau_{v23} & \frac{\partial v}{\partial x} \tau_{v21} + \frac{\partial v}{\partial y} \tau_{v22} + \frac{\partial v}{\partial z} \tau_{v23} & \frac{\partial w}{\partial x} \tau_{v21} + \frac{\partial w}{\partial y} \tau_{v22} + \frac{\partial w}{\partial z} \tau_{v23} \\ \frac{\partial u}{\partial x} \tau_{v31} + \frac{\partial u}{\partial y} \tau_{v32} + \frac{\partial u}{\partial z} \tau_{v33} & \frac{\partial v}{\partial x} \tau_{v31} + \frac{\partial v}{\partial y} \tau_{v32} + \frac{\partial v}{\partial z} \tau_{v33} & \frac{\partial w}{\partial x} \tau_{v31} + \frac{\partial w}{\partial y} \tau_{v32} + \frac{\partial w}{\partial z} \tau_{v33} \end{bmatrix} \\ & - f(\text{tr}(\boldsymbol{\tau}_v)) \begin{bmatrix} \tau_{v11} & \tau_{v12} & \tau_{v13} \\ \tau_{v21} & \tau_{v22} & \tau_{v23} \\ \tau_{v31} & \tau_{v32} & \tau_{v33} \end{bmatrix} \end{aligned}$$

The unsteady and convective flux parts of the transport equation are defined by default, however the source term has to be implemented into the solver. The DEFINE\_SOURCE macro can be used to specify the source term for each component of the viscoelastic stress tensor. The expanded form of the viscoelastic stress added to the momentum equations is:

$$\nabla \cdot \boldsymbol{\tau}_v = \begin{bmatrix} \frac{\partial \tau_{v11}}{\partial x} + \frac{\partial \tau_{v21}}{\partial y} + \frac{\partial \tau_{v31}}{\partial z} \\ \frac{\partial \tau_{v12}}{\partial x} + \frac{\partial \tau_{v22}}{\partial y} + \frac{\partial \tau_{v32}}{\partial z} \\ \frac{\partial \tau_{v13}}{\partial x} + \frac{\partial \tau_{v23}}{\partial y} + \frac{\partial \tau_{v33}}{\partial z} \end{bmatrix} \quad \text{Equation 3-52}$$

Furthermore, an artificial diffusion term is added to the viscoelastic stress transport equations, such that the dimensionless artificial diffusivity ( $D=k/u_\tau H$ , where  $k$  is the constant artificial diffusivity,  $u_\tau$  is the friction velocity, and  $H$  is the nozzle width) is kept below 0.1, this is necessary in order to achieve a stable solution by smoothing the sharp gradients in the viscoelastic stress terms (Sureshkumar & Beris, 1995). For details about the model implementation UDF see appendix A.

### 3.4.2. Viscoelastic model verification and validation

The model implementation is verified against the analytical solution for channel flow in viscoelastic fluids (solution by (Cruz, Pinho, & Oliveira, 2005)). This problem involves the fully developed laminar flow in a 2D channel:

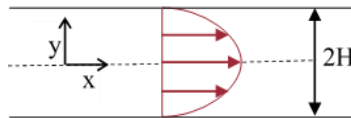


Figure 3-3. Schematic presentation of the velocity profile inside the 2D channel flow

For a fully developed steady channel flow the momentum equation is reduced to (the subscript  $v$  is excluded from  $\tau_v$  for convenience and  $\tau$  represents the viscoelastic stress values):

$$0 = -\frac{\partial P}{\partial x} + \mu_s \frac{d^2 u}{dy^2} + \frac{d\tau_{xy}}{dy} \quad \text{Equation 3-53}$$

Integrating once with respect to y we get (pressure gradient  $p_x$  is a constant):

$$\frac{du}{dy} = \frac{p_x y}{\mu_s} - \frac{\tau_{xy}}{\mu_s} \quad \text{Equation 3-54}$$

In the conservation equation for the viscoelastic stress (Equation 3-49) we note that  $\frac{D\tau}{Dt} = 0$ , so the expanded equations in 2D can now be written as:

$$\begin{aligned} & \mu_p \begin{bmatrix} \frac{\partial u}{\partial x} & \frac{\partial u}{\partial y} + \frac{\partial v}{\partial x} \\ \frac{\partial u}{\partial y} + \frac{\partial v}{\partial x} & \frac{\partial v}{\partial y} \end{bmatrix} & \text{Equation 3-55} \\ & + \lambda \begin{bmatrix} \frac{\partial u}{\partial x} \tau_{xx} + \frac{\partial u}{\partial y} \tau_{yx} & \frac{\partial u}{\partial x} \tau_{xy} + \frac{\partial u}{\partial y} \tau_{yy} \\ \frac{\partial v}{\partial x} \tau_{xx} + \frac{\partial v}{\partial y} \tau_{yx} & \frac{\partial v}{\partial x} \tau_{xy} + \frac{\partial v}{\partial y} \tau_{yy} \end{bmatrix} \\ & + \lambda \begin{bmatrix} \tau_{xx} \frac{\partial u}{\partial x} + \tau_{xy} \frac{\partial u}{\partial y} & \tau_{xx} \frac{\partial v}{\partial x} + \tau_{xy} \frac{\partial v}{\partial y} \\ \tau_{yx} \frac{\partial u}{\partial x} + \tau_{yy} \frac{\partial u}{\partial y} & \tau_{yx} \frac{\partial v}{\partial x} + \tau_{yy} \frac{\partial v}{\partial y} \end{bmatrix} \\ & - f(tr(\tau)) \begin{bmatrix} \tau_{xx} & \tau_{xy} \\ \tau_{yx} & \tau_{yy} \end{bmatrix} = 0 \end{aligned}$$

so the set of equations for the viscoelastic stress is reduced to:

$$2\lambda \frac{du}{dy} \tau_{xy} - f(tr(\tau)) \tau_{xx} = 0 \quad \text{Equation 3-56}$$

$$\mu_p \frac{du}{dy} - f(tr(\tau)) \tau_{xy} = 0$$

therefore:

$$\tau_{xx} = \frac{2\lambda}{\mu_p} \tau_{xy}^2 \quad \text{Equation 3-57}$$



$$f(tr(\tau)) = 1 + \varepsilon \frac{\lambda \tau_{xx}}{\mu_p}$$

combining Equation 3-54 and Equation 3-57 we get:

$$\left(1 + \varepsilon \frac{\lambda}{\mu_p} \frac{2\lambda}{\mu_p} \tau_{xy}^2\right) \tau_{xy} = \mu_p \left(\frac{p_x y}{\mu_s} - \frac{\tau_{xy}}{\mu_s}\right) \quad \text{Equation 3-58}$$

which can be solved as a cubic equation, taking  $\tau_{xy}$  as the unknown:

$$\tau_{xy} = \sqrt[3]{B + \sqrt{A^3 + B^2}} + \sqrt[3]{B - \sqrt{A^3 + B^2}}$$

$$A = \frac{\mu_p^2}{6\varepsilon\lambda^2} \left(1 + \frac{\mu_p}{\mu_s}\right) \quad \text{Equation 3-59}$$

$$B = \left(\frac{\mu_p^2}{4\varepsilon\lambda^2} \frac{\mu_p}{\mu_s} p_x\right) y$$

Using Equation 3-59 one can get the full solution for the viscoelastic stresses inside the channel flow. A velocity scale  $U_N$  is defined for non-dimensionalization of the velocity profile as  $U_N = \frac{p_x H^2}{8\mu_0}$ , where H is the channel half length. Moreover, the viscoelastic stresses are non-dimensionalized using the stress scale  $\mu_p U_N / H$ . The values predicted by the PTT code for velocity (U(y)), normal viscoelastic stress ( $\tau_{xx}$ ) and tangential viscoelastic stress ( $\tau_{xy}$ ) are compared against the analytical solution in Figure 3-4. A steady state pressure based solver is used, where the pressure-velocity coupling is according to the SIMPLE algorithm, second order upwind discretization is used for the momentum equations while the constitutive equations are solved using a first order upwind scheme.

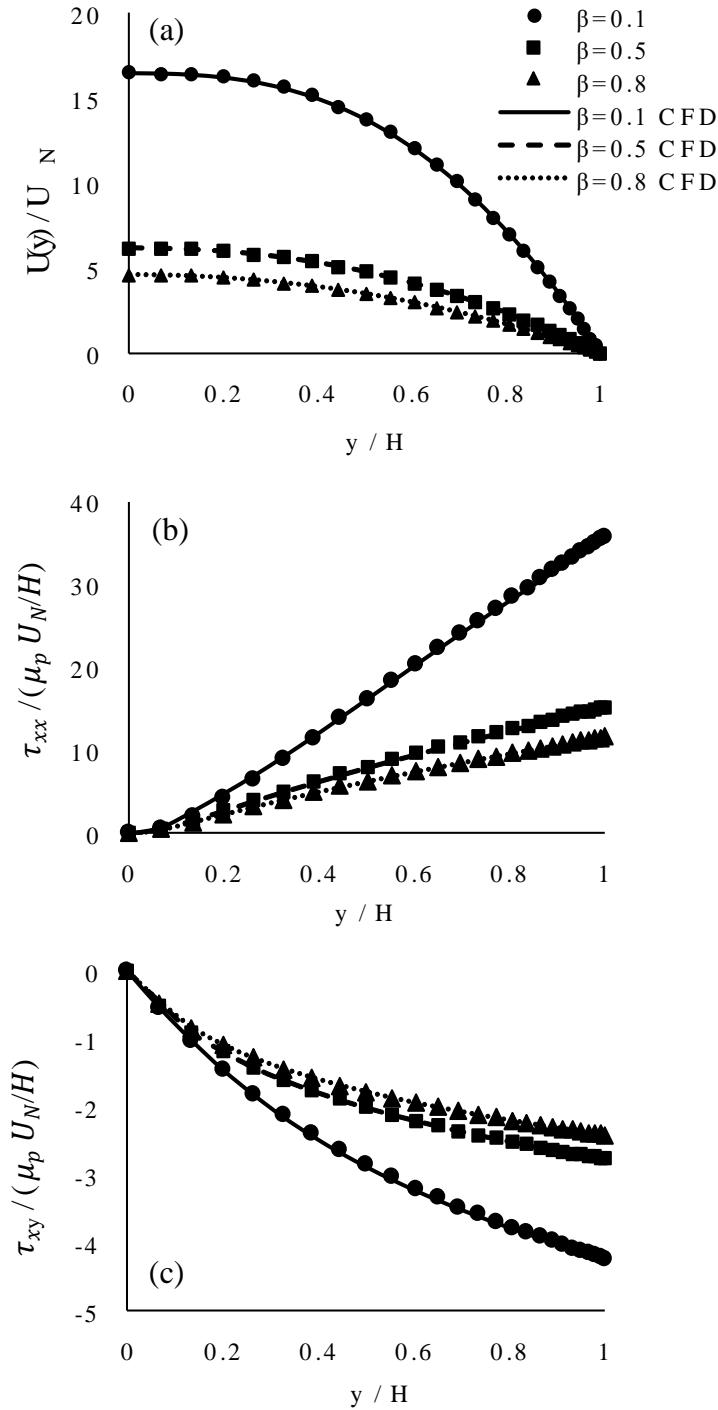


Figure 3-4. Comparison of the CFD code and the analytical solution for the PTT model; non-dimensionalized values for (a) the streamwise velocity, (b) normal viscoelastic stresses and (c) tangential viscoelastic stresses are presented in the channel at different viscosity ratios ( $\beta = \mu_s/\mu_0$ , where  $\mu_0$  is the total viscosity  $\mu_p + \mu_s$ ) for  $\varepsilon = 0.25$  and  $De = \lambda U/H = 1$ .

Finally, the physical accuracy of the viscoelastic model predictions is validated against the experimental measurements of a corner vortex developing inside a square contraction geometry (Sousa, Coelho, Oliveira, & Alves, 2011). In low Reynolds number flows of Newtonian fluids, the size of the corner vortex is decreased as the Reynolds number is increased. However, in

viscoelastic fluids this effect is reversed, i.e. the corner vortex increases in size as the Reynolds number increases, an effect known as “vortex enhancement”. The size of the corner vortex predicted by the viscoelastic code (in 3D) is measured for two different contraction ratios (CR2.4 and CR4) in different Reynolds numbers and compared to the experimental measurements for the same conditions.

The geometry and flow streamlines are demonstrated in Figure 3-5 along with the computational grid for the validation study. The computational domain consists of purely hexahedral cells and the upstream and downstream boundaries are positioned at  $10H_1$  and  $10H_2$  distance from the contraction respectively to achieve a steady velocity profile. Based on a grid dependency study performed in (Sousa et al., 2011), 80 cells are used along the upstream channel width ( $2H_1$ ) and the near wall cells are refined such that the ratio of the smallest cell size to the channel length ( $\Delta x_{\min}/2H_1$ ) remains below 0.01.

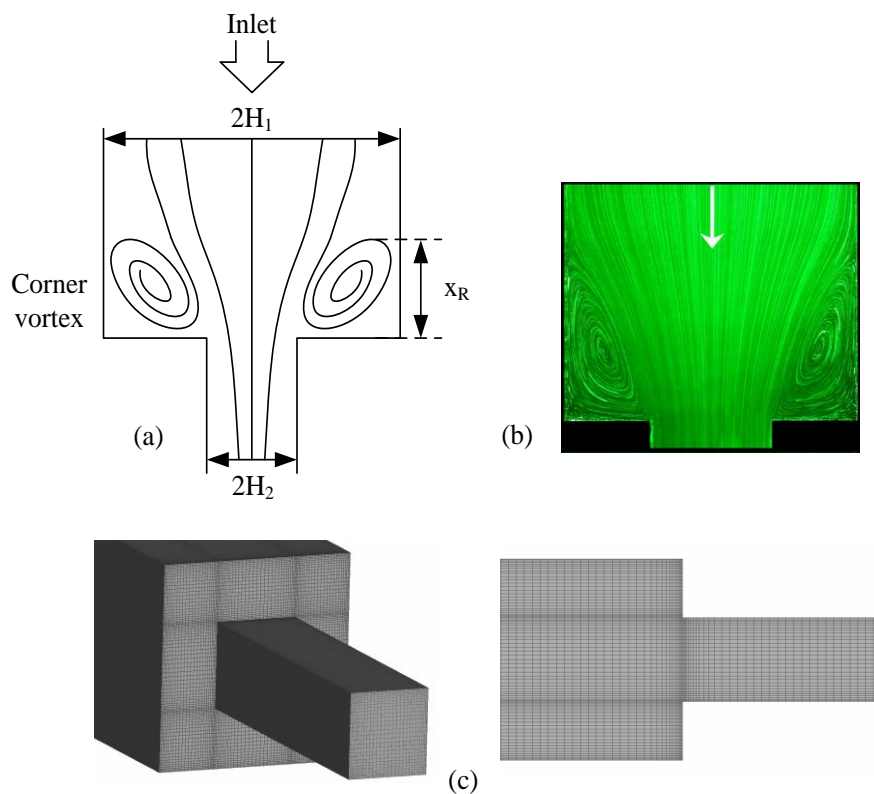


Figure 3-5. (a) Schematic representation of the flow in the contraction, (b) streak line photography images showing the corner vortices and the flow path and (c) the computational grid with near-wall refinement for the simulations

The viscoelastic fluid in this study is an aqueous solutions of polyacrylamide (PAA) which is composed of 40.0% wt% of glycerol, 59.9% wt% of water and PAA at weight concentration

of 600 ppm. The fluid properties are measured using a shear rheometer and the following parameters were used for the PTT model accordingly: solvent viscosity  $\mu_s = 0.03$  Pa.s, polymer viscosity  $\mu_p = 1.62$  Pa.s, polymer relaxation time  $\lambda = 32$  s and extensibility parameter  $\varepsilon = 0.06$  (Sousa et al., 2011).

A uniform velocity profile is imposed at the inlet, outflow boundary condition is set at the outlet and no-slip wall boundary conditions is used at the solid walls. A coupled pressure based solver is used in order to achieve a faster convergence rate. In the coupled solver algorithm, the pressure and momentum are solved simultaneously and the pressure corrector is used to update the velocities. The transient formulation is first order implicit and the time step is adaptive to keep the CFL number below 0.1. The momentum equations are solved using a second order gamma differencing (bounded central differencing) scheme and the constitutive equations are solved using a first order upwind scheme.

The size of the corner vortex measured in the experiment is reported in the non-dimensional form  $X_R/2H_1$  in Table 3-3 along with the simulation results. The results indicate that the PTT code can accurately predict the vortex enhancement by increasing the flow velocity.

#### CR 2.4

De	X <sub>R</sub> /2H <sub>1</sub> (experiment)	X <sub>R</sub> /2H <sub>1</sub> (CFD)
<b>1.07</b>	0.199	0.178
<b>9.63</b>	0.467	0.420
<b>77.3</b>	1.486	1.213

#### CR 4

De	X <sub>R</sub> /2H <sub>1</sub> (experiment)	X <sub>R</sub> /2H <sub>1</sub> (CFD)
<b>0.51</b>	0.205	0.183
<b>1.14</b>	0.245	0.244
<b>2.41</b>	0.312	0.310
<b>5.96</b>	0.485	0.442

*Table 3-3. Test case conditions and the non-dimensional vortex length values measured experimentally and numerically for contraction ratios 2.4 and 4. Deborah number is defined based on velocity and channel length inside the contraction  $De = \lambda U_2/H_2$ .*

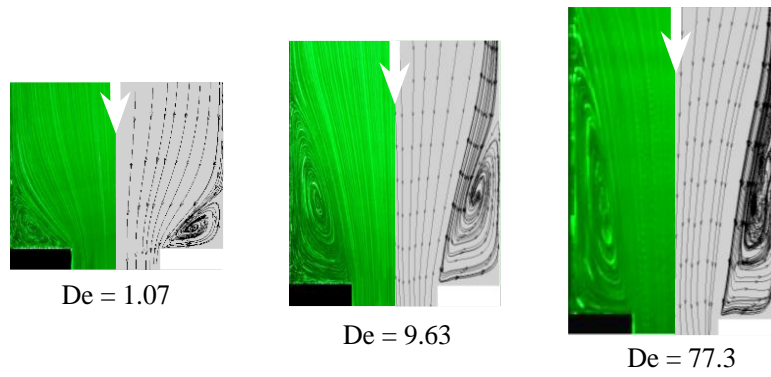


Figure 3-6. Comparison of flow streamline images from the experimental study (green) and the PTT model predictions (grey) for CR 2.4 at different  $De$

In Figure 3-6 the streamlines predicted by the CFD code are compared to the experimental images at different Deborah numbers. The images present the corner vortex in the centre plane of the contraction. It is evident in the simulation data, the size and shape of the corner vortices is in qualitative agreement with the experiments although, the code generally underpredicts the vortex length and this becomes evident more clearly at higher Deborah numbers. The CFD and experimental data are quantitatively compared in Figure 3-7, and the simulations can capture the trend in the vortex size. The vortex size matches closely with the experiments at lower Deborah numbers ( $De < 10$ ) but underestimates it at higher values. The overall discrepancy between the simulations and the experiment is  $\sim 9\%$  which is mainly at CR 2.4 ( $\sim 18\%$ ), while the CR 4 predictions match the experiments closely ( $\sim 5\%$  error). The high Deborah number results are expected to improve by using higher order schemes for the constitutive equations.

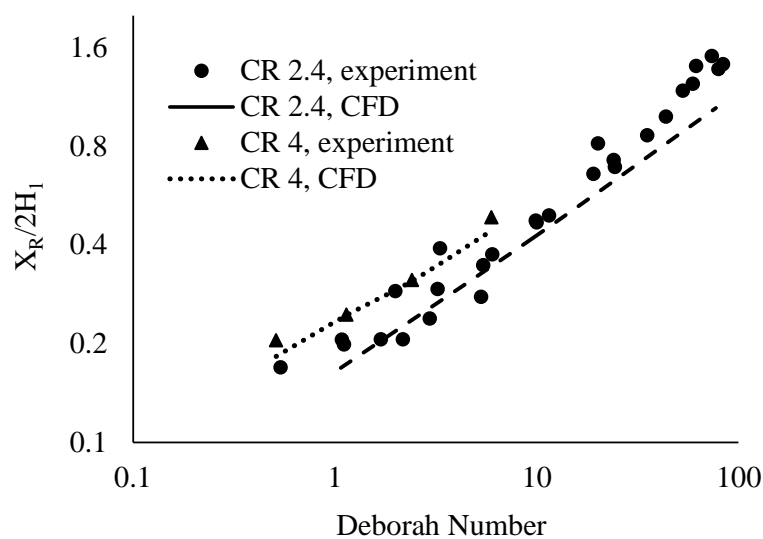


Figure 3-7. Dimensionless corner vortex length at different Deborah numbers for contraction ratios of 2.4 and 4, the results are measured in the centre plane of the contraction geometry

### **3.5. Test cases, boundary conditions and solution methods**

In the following sections, the test cases investigated in this study are presented along with the relevant boundary conditions and solution methods for each case. For the preliminary study, cavitation formation inside an axisymmetric nozzle is investigated to compare the results with vapour fraction distribution inside the nozzle measured with X-ray CT. Subsequently, a more recent study in an asymmetric nozzle is investigated and the modified RANS model are employed for improving the unsteady results. The comparison of vapour volume fraction predictions with the X-ray CT measurements in this case serves as a validation for the cavitation model. Due to the large domain of these nozzles, a full LES simulation would not be affordable, especially for further parametric studies and for the viscoelastic fluid model. Therefore, a step nozzle test case is selected for which laser doppler velocimetry data are available to validate the performance of various turbulence models. Finally, the effect of viscoelasticity on flow and cavitation is investigated in the step nozzle test case and in a realistic fuel injector nozzle.

#### **3.5.1. Axisymmetric nozzle**

In order to generate a quasi-steady and symmetric cavitation cloud, a single hole nozzle with a cylindrical constriction upstream the nozzle entrance has been designed as shown in Figure 3-8 (Bauer et al., 2012). The constriction forces the flow to enter the nozzle at a sharp angle, forming a cloud of cavity. In order to limit flow recirculation regions forming below the cylinder, the cylinder edges have a fillet radii that prevent sharp edges. The upstream inlet is sectioned into 3 identical tubes in 120° intervals.

The fluid is delivered into the test section by a pump in a closed loop hydraulic test rig and returns back to the storage tank, while several pressure transducers are employed to monitor the pressure in the test section. The vapour fraction measurements are carried out using a hospital CT scan device. The X-rays pass through the cavitation channel and the radiation received by the detector represents the line integral of the attenuation coefficient along its path. This information is then used to obtain the time-averaged vapour fraction in 6 planes along the channel (Bauer et al., 2012).

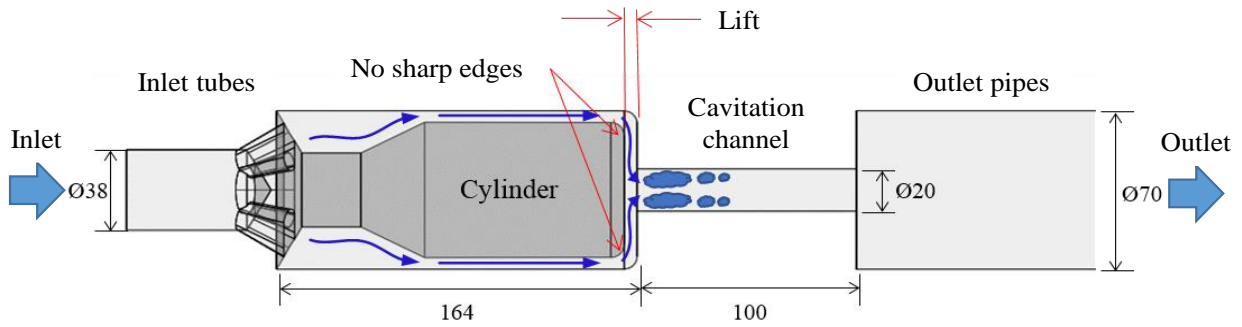


Figure 3-8. Schematic of the axisymmetric nozzle test section with the main dimensions (all in mm), the flow path is shown using blue arrows

For the computational domain, the inlet and outlet pipes are extended to achieve a developed inlet velocity profile and avoid the recirculation regions at the outlet boundary. The computational domain is presented in Figure 3-9 together with cut sections showing the interior fluid domain mesh. Apart from the  $120^\circ$  separated inlet geometry (Figure 3-9 (a) inset) which consists primarily of tetrahedral cells, the rest of the domain is mainly made of hexahedral elements with extra refinement near the walls. The near wall refinement inside the channel is set such that the dimensionless wall distance  $Y^+$  equals  $\sim 30$  and the size of the cells inside the channel is  $\sim 0.4$  mm.

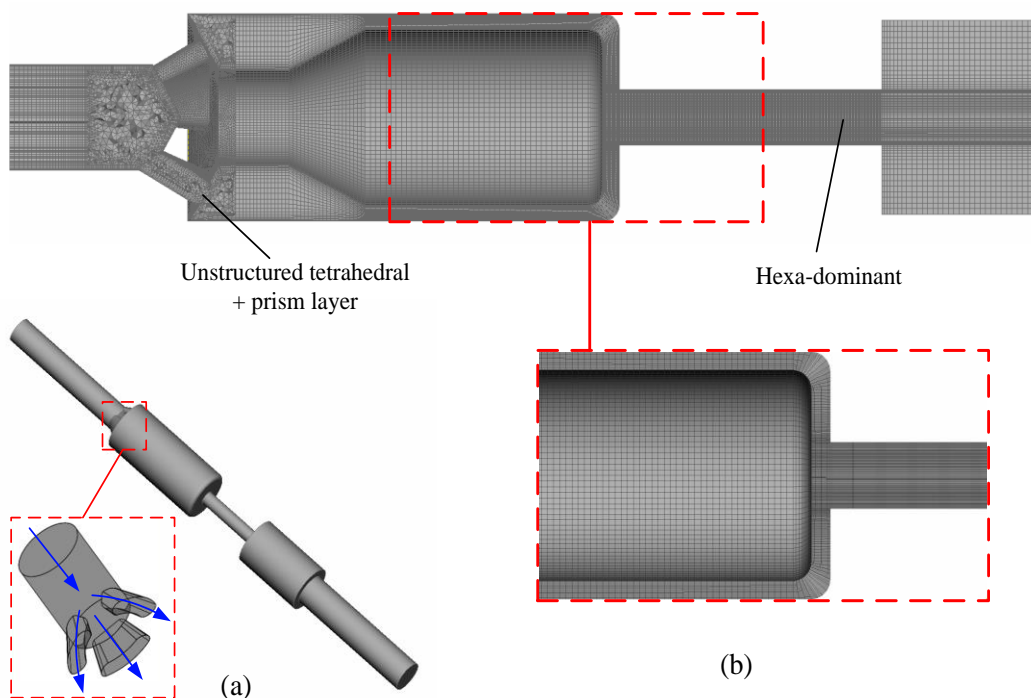


Figure 3-9. The computational domain and the grid used for the axisymmetric nozzle. (a) the geometry and flow path (blue arrows), the inlet tubes separated by  $120^\circ$  are demonstrated in the inset, (b) magnified image shows the grid cross-section in more detail

The lift height for the conditions of this study is fixed at 6mm (see Figure 3-8.) and water enters the nozzle at 3.1 lit/s. This information is used to fix the inlet velocity at 2.73 m/s and the outlet pressure was adjusted according to the experiment to match the flowrate ( $P_{\text{out}} = 105$  kPa). A no-slip wall boundary condition is used at the solid walls. The inlet pressure measured for this condition is 205 kPa, corresponding to cavitation number of  $CN = 0.95$  and the Reynolds number in the nozzle is  $Re \approx 44000$ . Both the  $k-\varepsilon$  RNG and the  $k-\omega$  SST models as well as their modifications, explained in section 3.2.1.4 of this chapter, are investigated. The turbulent intensity and turbulent viscosity ratio are set to 5% and 10 respectively at the inlet and outlet boundaries. The Schnerr-Sauer cavitation model is used to predict the cavitation volume fraction within the mixture multiphase framework.

A cavity cloud form inside the nozzle in this conditions, reaching to  $\sim 20$  mm downstream the entrance. In order to capture the unsteady nature of cavity growth and shedding, the simulations started with a time step of  $150 \mu\text{s}$  initially (corresponding to Courant–Friedrichs–Lewy (CFL) number of  $\sim 10$ ) until the flow develops and then reduced to  $15 \mu\text{s}$  ( $CFL \approx 1$ ) to avoid the dissipation of perturbations as far as possible. The  $k-\omega$  SST model which had a better performance in predicting the cavitation presence in incipient condition is used to further investigate a higher cavitation number condition  $CN = 1.5$  corresponding to  $Re \approx 54000$ .

The pressure and velocity coupling is done using the pressure implicit with splitting of operator (PISO) algorithm which is based on a predictor-corrector approach. Initially, the momentum equation is solved using a guessed pressure field. A pressure correction equation, which is derived from the momentum and continuity equations, is then used to correct the velocities (Issa, 1985). The momentum equations are solved using the gamma differencing scheme (Jasak, Weller, & Gosman, 1999). Turbulence model equations ( $k$  and  $\varepsilon$  or  $\omega$ ) are discretized using a second order upwind scheme and the volume fraction is discretized using the quadratic upstream interpolation for convective kinetics (QUICK) scheme to achieve an accurate representation of the high density ratio field. The transient formulation is second order backward implicit.

### 3.5.2. Asymmetric nozzle

A more realistic flow condition that replicates the asymmetric injector flow in a valve-covered orifice or mini-sac type orifice has been designed in a portable closed flow circuit, which can be used in open-type X-ray sources that are more commonly used for academic research



(Koukouvinis et al., 2017). A high pressure pump delivers the fuel to a single hole injector, that has an asymmetrical needle positioned upstream the nozzle entrance partially blocking the flow and forcing the fluid to enter the nozzle from one side. Moreover the nozzle hole is also positioned off-axis to promote further asymmetry and replicate the orifice hole location inside a fuel injector sac volume (see Figure 3-10).

The grid is presented in Figure 3-11 with magnified images showing the grid in the vicinity of the cavitation nozzle. In the region of flow blockage by the needle, tetrahedral elements are used due to the complex geometry in this region. Apart from the aforementioned section, the rest of the grid consists mainly of hexahedral cells and extra refinement is used near the solid walls. The grid spacing near the walls inside the nozzle is set to achieve a maximum  $Y^+$  value of  $\sim 30$  and the size of the cells in the core of the channel is  $\sim 50 \mu\text{m}$ .

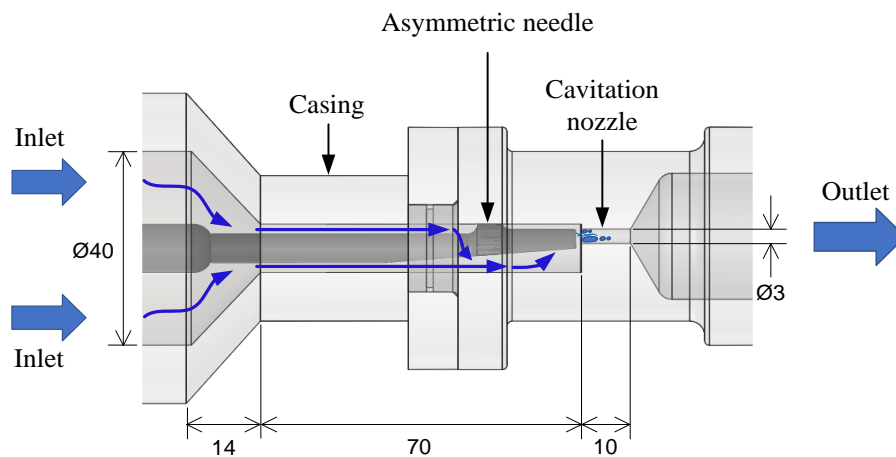


Figure 3-10. Schematic of the asymmetric nozzle geometry and the flow direction (blue arrows), the main dimensions of the nozzle are presented (in mm), for full details of the test section geometry see (Koukouvinis et al., 2017)

A section of the upstream inlet pipes is eliminated from the computational domain to reduce the computational resources requirements and precursor simulations are performed to specify the pressure drop in the eliminated sections. As a result, the pressure at the inlet and outlet boundaries is fixed at 5450 kPa and 1720 kPa respectively, corresponding to cavitation number of  $CN = 2.18$ . Diesel fuel is pumped into the test section at the flowrate of 0.46 lit/s, therefore the Reynolds number inside the cavitation channel is  $Re = 77000$ . The modified  $k-\omega$  SST model is used to model the flow turbulence and the turbulent intensity and turbulent viscosity ratio are set to 5% and 10 respectively at the inlet and outlet boundaries. The Schnerr-Sauer cavitation model is used to predict the cavitation volume fraction within the mixture framework.

The cavitation cloud in this test case covers more than 80% of the nozzle length and has a cyclic shedding behaviour. The characteristic Strouhal number for cloud cavities ( $St = Lf/U$ , where  $f$  is the cavity cloud shedding frequency, and  $L$  and  $U$  are the characteristic length scales and velocity scales inside the channel) is in the range of 0.2-0.4 (Callenaere et al., 2001), therefore the cloud shedding frequency is  $\sim 10$  kHz, while each cycle lasts for  $\sim 0.1$  milliseconds. The time step is set to  $1 \mu s$  corresponding to CFL number of  $\sim 4$  and time-averaged data is collected for 4 milliseconds to collect the statistics for  $\sim 40$  shedding cycles.

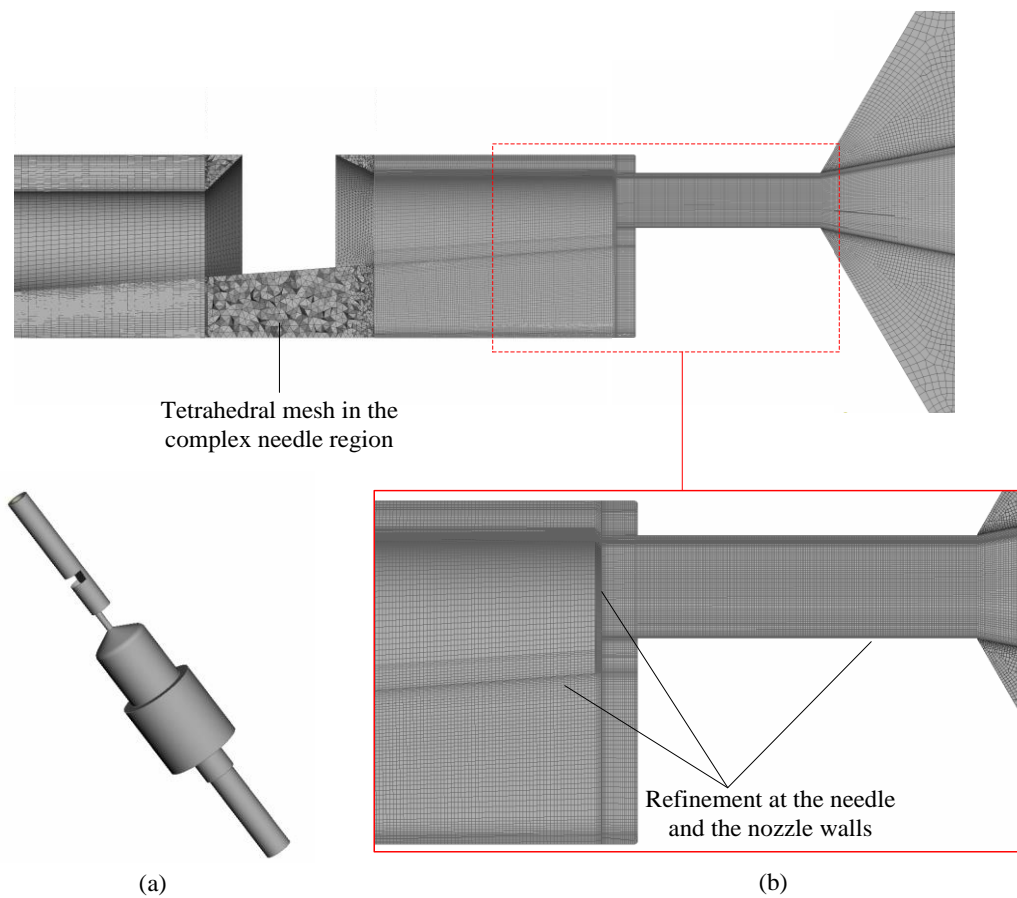


Figure 3-11. (a) The computational domain and the grid used for the asymmetric nozzle, (b) magnified image shows the grid cross-section in more details

The pressure and velocity coupling is done using the PISO algorithm. The momentum equations are solved using the gamma differencing scheme. Turbulence model equations ( $k$  and  $\omega$ ) are discretized using a second order upwind scheme and the volume fraction is discretized using the QUICK scheme to achieve an accurate representation of the high density ratio field. The transient formulation is second order backward implicit.

### 3.5.3. Step nozzle

A step nozzle test case is chosen in order to perform a comprehensive parametric study about the turbulence and cavitation models performance in predicting the in-nozzle flow. The geometry of the step nozzle is shown Figure 3-12 which is based on an experimental study (Sou, Biçer, & Tomiyama, 2014) designed to investigate cavitation in a rectangular injector. Cavitation development inside the nozzle from the incipient condition to fully developed condition is visualized using high speed imaging; moreover LDV measurements of streamwise velocity and RMS of turbulent velocity are provided for the incipient cavitation condition. The data are only available for water, and to the best of our knowledge no studies in the literature provide similar data for viscoelastic cavitating flows.

In the experiments, water flows through the nozzle with a flow rate of 48 ml/s, and the pressure difference across the nozzle is 1.38 bars, while the injected liquid is discharging into the atmospheric pressure. The cavitation number is  $CN = 1.38$  and the Reynolds number based on average liquid velocity in the nozzle is  $Re = 27700$ .

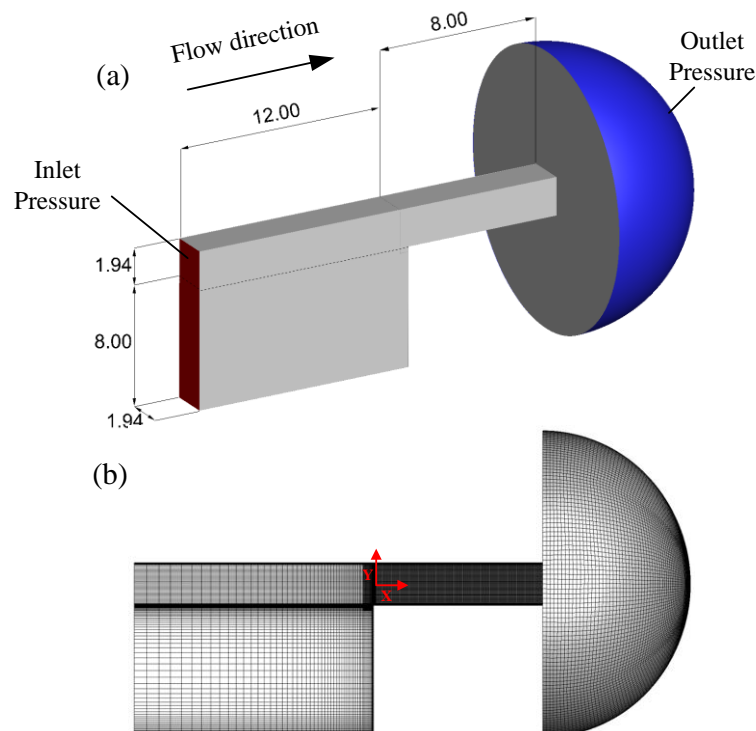


Figure 3-12. (a) Geometry of the step nozzle and the relevant dimensions in mm, inlet boundary (red color) and outlet boundary (blue color) surfaces are shown; all the other surfaces are no-slip walls (gray color). (b) Computational grid with additional refinement inside the nozzle

A hemispherical outlet geometry is added to the domain with 14mm diameter to allow a uniform assignment of the outlet pressure boundary condition away from the nozzle exit. The computational grid consists of unstructured hexahedral cells, and additional refinement is used inside the constriction to achieve the cell size below the Taylor length scale  $\lambda_g$  (approximated from the characteristic length scale  $L= 1.94\text{mm}$  and Reynolds number,  $\lambda_g = (10/\text{Re})^{0.5} L= 39 \mu\text{m}$ ). Estimation of Taylor microscale provides a guideline for grid resolution in practical LES studies (Addad, Gaitonde, Laurence, & Rolfo, 2008; Howard & Pourquie, 2002); by refining the mesh below this value the large scale turbulent eddies are captured as  $\lambda_g$  theoretically lies in the high wavenumber end of the inertial subrange. Taylor length scale characterizes the mean spatial extension of the velocity gradients (Lesieur, 2012; Lesieur, Métais, & Comte, 2005) and is always much smaller than the integral scale (but not the smallest scale) (Tennekes & Lumley, 1972). The cell size inside the nozzle is  $20 \mu\text{m}$  and it is refined to  $2.5 \mu\text{m}$  near the walls, corresponding to  $Y^+$  values of 0.2-1. The time step corresponding to a CFL number of 0.5 is set to  $1 \mu\text{s}$  in the Newtonian test case, and for the viscoelastic case the time step is reduced to  $0.5 \mu\text{s}$  for a CFL number of 0.25.

Temporal integration is performed using second order implicit backward discretization. Momentum equations are solved using the gamma differencing scheme, and viscoelastic stress terms are discretized with the first order upwind scheme. Moreover, an artificial diffusion term is added to the viscoelastic stress transport equations, such that the dimensionless artificial diffusivity ( $D=k/u_\tau H$ , where  $k$  is the constant artificial diffusivity,  $u_\tau$  is the friction velocity, and  $H$  is the nozzle width) is kept below 0.1, this was necessary in order to achieve a stable solution by smoothing the sharp gradients in the viscoelastic stress terms (Sureshkumar & Beris, 1995). The vapour volume fraction transport equation is discretized with the QUICK scheme and pressure and velocity are fields are linked using the PISO algorithm.

For the viscoelastic test case, the polymer viscosity is  $0.009 \text{ Pa}\cdot\text{s}$  and polymer relaxation time is  $0.04 \text{ s}$ . The polymer relaxation times chosen in this study are in the range measured for dilute viscoelastic solutions in low viscosity solvents (Giudice, Haward, & Shen, 2017). The molecular weight of the polymer used in the study is reported  $1.6 \text{ g/mol}$  for the polymer in the aqueous solution, and the concentration range corresponding to the chosen relaxation times is  $\sim 0.1 \text{ wt. \%}$ . The relaxation times are large compared to the flow time scales such as the turnover time of large and small eddies, so it is expected that they alter the flow topology. When polymer relaxation times are comparable to the flow time scales, the turbulent kinetic energy cascade

can be altered, resulting in turbulent drag reduction (C. Li et al., 2006; Valente, da Silva, & Pinho, 2016).

To characterize the polymer viscosity, the viscosity ratio is used ( $\beta = \mu_s/\mu_0$ , where  $\mu_s$  and  $\mu_p$  are the solvent and the polymer viscosities.  $\mu_0$  is the total viscosity  $\mu_p + \mu_s$ ). One of the main objectives of this study is to examine how viscoelasticity can affect the cavitation structures. For this purpose, preliminary tests were conducted on the effect of the polymer viscosity and clear changes were observed (instantaneous and time-averaged) in cavitation volume fraction when the viscosity of the polymer was large compared to the solvent viscosity. High polymer viscosity values (when  $\beta$  is as small as 0.2) can damp the turbulent shear stress and contribute to the reduction of the turbulent drag (Yu et al., 2004).

#### 3.5.4. **Injector nozzle**

A common rail injector geometry section as shown in Figure 3-13 is simulated which has a more complex flow and cavitation mechanism compared to the step nozzle. This is a real-size diesel fuel injector tip with five uniformly distributed holes, and the nozzle holes are slightly tapered with a  $k$  factor of 1.1. ( $k = (D_{in} - D_{out}) / 10$ , where  $D_{in}$  and  $D_{out}$  are the injector holes inlet and outlet diameters respectively). The nozzle has an inlet and exit diameter of 0.37 mm 0.359 mm respectively, and is 1.26 mm long. Nozzle hole tapering is linked to reduction of cloud cavitation but at the same time, formation of vortex or string cavities inside the nozzle. By using tapered holes instead of cylindrical holes, string cavitation which forms inside large scale vortices entering the nozzle from the sac volume can be intensified, while cloud cavitation is reduced (Gavaises et al., 2009). In this test case, the fuel flows through the needle passage before entering the sac volume where it recirculates while entering the nozzle. A cavitation cloud forms at the top corner of the nozzle entrance due to the sharp turn in the flow streamline. Moreover, a large vortex enters the nozzle from the sac volume, with string cavitation forming in the core of the vortex inside the nozzle. A recent fully compressible implicit LES of a 9-hole injector with needle motion (Felix Örley, Hickel, Schmidt, & Adams, 2017) shows that elongated vortical structures which enter the nozzle from the sac volume, and the overall flow features are present when compared to steady needle simulations at full lift.

The Reynolds number inside the nozzle and the sac volume reaches above 30000, indicating the highly turbulent flow conditions of the injector. Considering the mesh resolution and the small time step required for simulating this case, the computational cost of simulating the

complete 5-hole geometry for Newtonian and viscoelastic fluids is not affordable, so 1/5th of the injector geometry ( $72^\circ$ ) is simulated as shown in Figure 3-12 and periodic boundary conditions are employed on either side of the geometry.

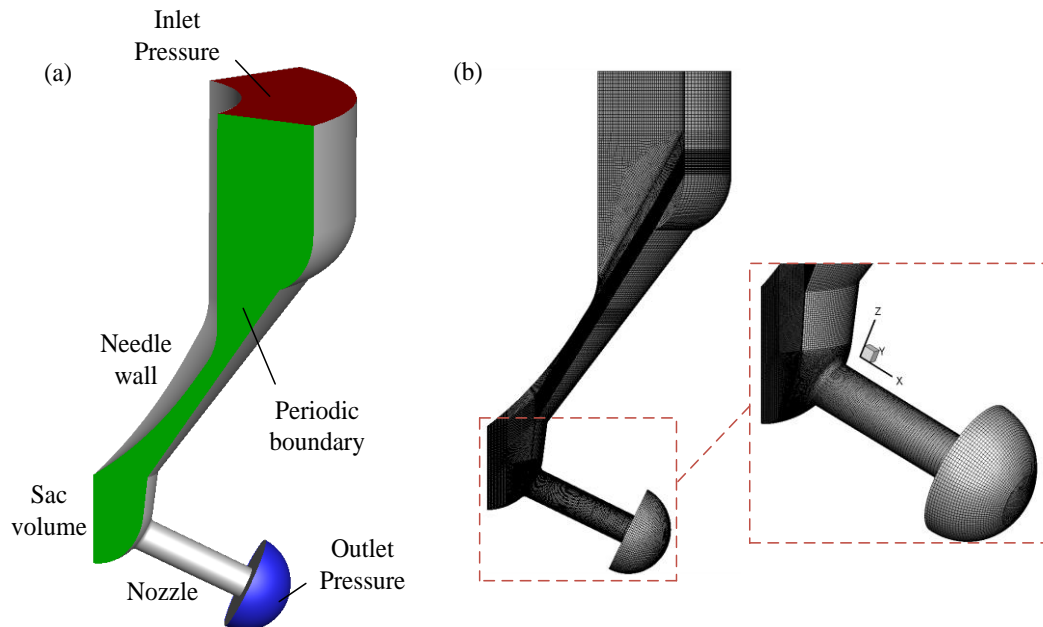


*Figure 3-13. (a) Simulation domain for the injector test case. The boundary conditions are indicated by coloured surfaces; inlet and outlet boundaries are coloured in red and blue, respectively, and the green surface shows the periodic boundary (another periodic boundary with the same cross section is located on the opposite side of the geometry); all the other surfaces are no-slip walls (grey colour), (b) The computational grid for the injector; the domain is partitioned using blocking and it is hex-dominant except from an unstructured tetrahedral section in the sac volume*

Inlet and outlet total pressures are fixed at 1800 bars and 50 bars respectively. Cavitation number for this condition is  $CN = 35.9$ , which is much higher than the step nozzle test case due to the higher pressure difference from the inlet to the outlet. In this condition, a fully developed cloud cavitation is located in the top surface of the nozzle, while the string cavity has a more intermittent appearance. For the viscoelastic test case, the polymer viscosity is 0.02 Pa.s and the polymer relaxation time is 0.008 s.

A hex-dominant block mesh is used for most parts of the geometry, except for a section in the sac volume upstream of the nozzle entrance, where unstructured tetrahedral mesh is used. The mesh resolution in the nozzle and the sac volume where cavitation develops is  $7.5 \mu\text{m}$  with additional refinement near the walls. With this resolution, large scale flow structures, unsteady cavitation dynamics, and vortex shedding can be captured. The time step for the Newtonian flow condition is 5 ns for a CFL number of  $\sim 0.4$ , and for the viscoelastic case it is reduced to 2 ns and a CFL number of  $\sim 0.15$ .

Temporal integration is performed using second order implicit backward discretization. Momentum equations are solved using the gamma differencing scheme, and viscoelastic stress terms are discretized with the first order upwind scheme. The artificial diffusivity terms is employed for the viscoelastic fluid simulations, in the same manner as the step nozzle case. The vapour volume fraction transport equation is discretized with the QUICK scheme. A coupled pressure based solver is used in order to achieve a faster convergence rate compared to the segregated solver.

A summary of the flow conditions for each tested geometry is provided in Table 3-1:

<b>Axisymmetric Nozzle</b>		<b>Step Nozzle</b>	
Inlet pressure (CN 0.95)	205 kPa	Inlet pressure	238.2 kPa
Outlet pressure (CN 0.95)	105 kPa	Outlet pressure	101.3 kPa
Inlet pressure (CN 1.5)	270 kPa		
Outlet pressure (CN 1.5)	105 kPa		
<b>Asymmetric Nozzle</b>		<b>Injector Nozzle</b>	
Inlet pressure	5450 kPa	Inlet pressure	182385 kPa
Outlet pressure	1720 kPa	Outlet pressure	5066.2 kPa

*Table 3-4. Static pressure values used at the inlet and outlet boundaries for the simulations*

## **4. Turbulence and Cavitation Models for Cavitation Simulation**

---

In this chapter, capabilities of different turbulence and cavitation modelling approaches are investigated in modelling nozzle cavitation. In order to validate the cavitation models, two test cases for which X-ray measurements of in-nozzle vapour fraction is available are investigated. Following, a step nozzle case with LDV measurements of in-nozzle velocity and RMS of velocity is chosen for a more exhaustive investigation of the turbulence models.

### **4.1. Preliminary studies: Cavitation modelling validation**

The aim of this preliminary study is to present a numerical framework for simulating nozzle cavitation while comparing the vapour volume fraction values predicted by the CFD models with the X-ray CT measurement in the experiments. One of the earliest experiments that provided quantitative measurements of cavitation void fraction was presented by Bauer et al. (Bauer et al., 2012) which is referred to in this chapter as the axisymmetric nozzle. More recently, the study conducted by the cavitation research group at City, University of London (Koukouvinis et al., 2017; Mitroglou et al., 2016) provides a full 3D X-ray measurements of void fraction in an asymmetric nozzle and it is presented as an additional validation test case for the numerical results in section 4.1.2.



### 4.1.1. Axisymmetric nozzle

In this section, the flow in a axisymmetric nozzle according to an X-ray CT experiment (Bauer et al., 2012) is investigated. Water is injected into the atmospheric pressure with an injection pressure of  $\sim 2$  bar, while passing through a 20 mm diameter and 100 mm long nozzle. A cavitation cloud forms at the constriction inlet as shown in Figure 4-1 (a). As the injection pressure is increased to  $\sim 2.7$  bar, a fully developed cavitation regime grows inside the nozzle, see Figure 4-1 (b). The cavitation structures evolve into a film-like cavitation regime (or sheet cavitation), with a vapour film covering the periphery of the nozzle that breaks-up into a highly transient bubbly mixture dominating the nozzle outlet region before fully collapsing.

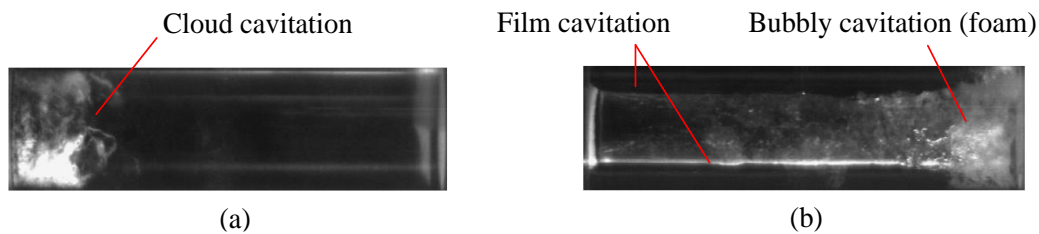


Figure 4-1. Photography image of the cavitation cloud forming inside the nozzle for (a) incipient cavitation regime  $CN = 0.95$  and (b) developed cavitation regime  $CN = 1.5$  (Bauer et al., 2012)

Both the  $k-\epsilon$  RNG and the  $k-\omega$  SST models are tested and the vapour volume fraction transport equation is modelled according to the Schnerr and Sauer formulation. The aforementioned turbulence models have shown a superior performance compared to standard RANS models especially in flows with recirculation regions and strong streamlines curvatures.

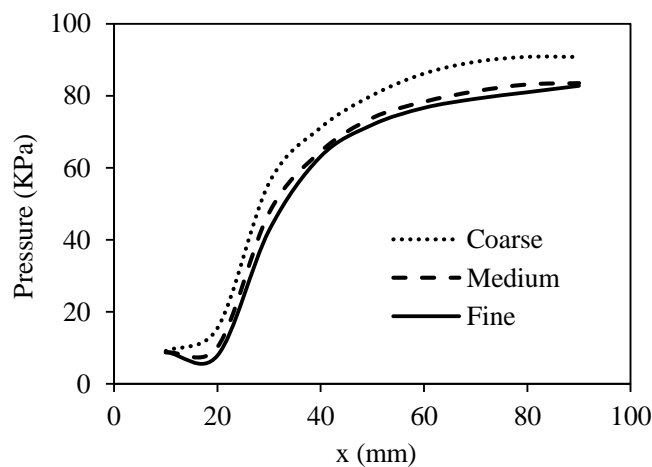


Figure 4-2. Effect of successive grid refinement on pressure distribution inside the cavitating nozzle, the area-averaged pressure values are calculated in several slices along the nozzle

A grid dependency study is initially conducted by refining the cell size inside the nozzle from  $\sim 0.5$  mm to  $\sim 0.3$  mm and the minimum  $Y^+$  value due to near-wall refinement is reduced from  $\sim 40$  to  $\sim 30$ , while the cell count is increased from 3 million cells (coarse) to 11 million cells (fine). The effect of successive grid refinements on pressure distribution inside the nozzle is displayed in Figure 4-2. It is evident that as the grid is refined beyond the medium refinement, the effect on in-nozzle pressure variations is insignificant (less than  $\sim 5\%$  overall), therefore the medium grid with 0.4 mm cell size inside the nozzle,  $Y^+$  values  $\sim 30$  and 5 million cell count is used for the rest of this study.

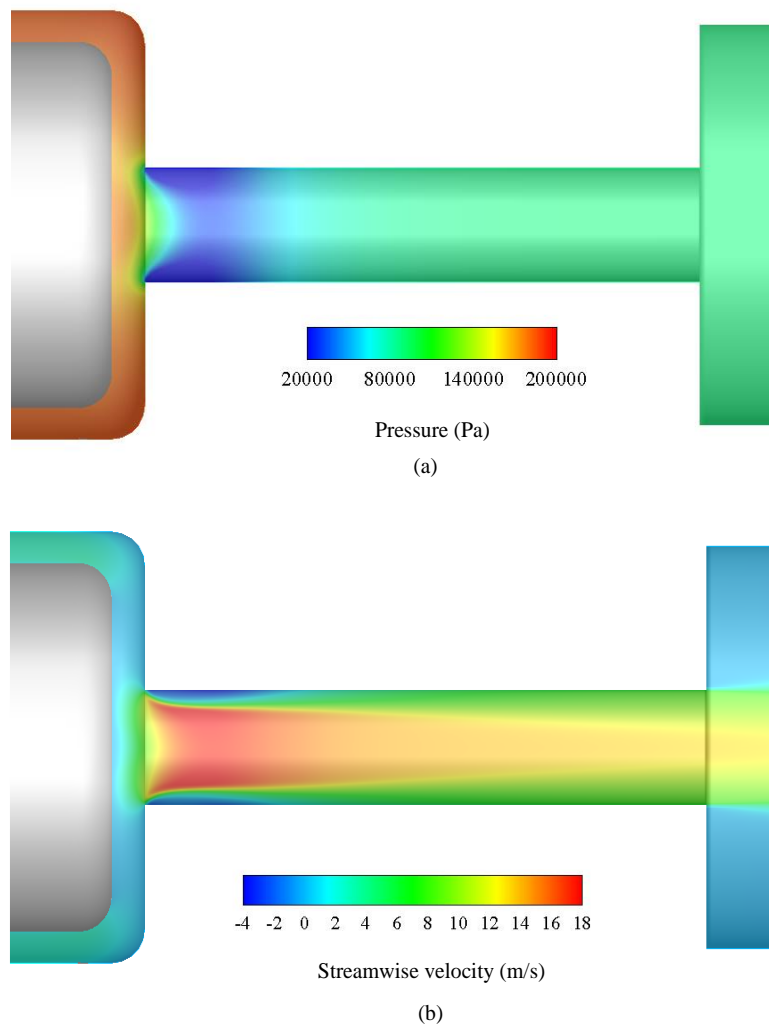


Figure 4-3. (a) Pressure (a) and streamwise velocity distribution inside the nozzle predicted by the  $k-\epsilon$  RNG model

The pressure distribution predicted by the  $k-\epsilon$  RNG model for the  $CN = 0.95$  case is presented in Figure 4-3 (a). The sharp pressure drop at the nozzle entrance coincides with the cavitation cloud region, however the minimum pressure inside the nozzle is  $\sim 5800$  Pa, which is larger than the vapour pressure, and therefore, cavitation inception is not predicted by this model. In

low cavitation number condition, inception occurs in the core of small eddies forming in the shear layer between the high velocity core and the low velocity recirculating flow (see Figure 4-3.(b)). However, the  $k-\varepsilon$  models are known for over-predicting the turbulent viscosity at stagnation points, resulting in fast decay of swirling motions.

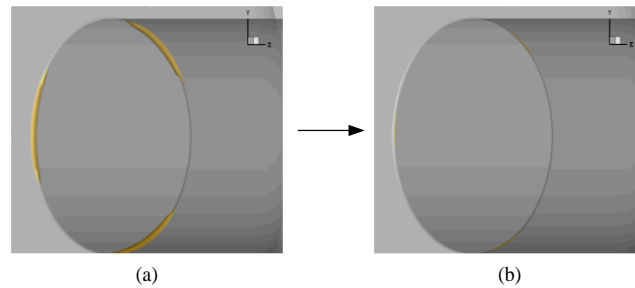


Figure 4-4. Iso-surface of 70% vapour volume fraction artificially introduced at the nozzle inlet (a), cavitation vapours diminish after  $\sim 1$  ms (b) (results predicted by the  $k-\varepsilon$  RNG model)

Cavitation inception is necessary in order to apply the turbulent viscosity modification, since the function  $f(\rho)$  is calculated based on the vapour volume fraction  $\alpha$ . Therefore, a small amount of vapour is artificially introduced at the nozzle inlet to trigger the cavitation model and the turbulence model modification (see Figure 4-4). However, the vapour structures diminish after a few time steps ( $\sim 1$  ms) as the flow unsteadiness at the nozzle inlet is damped.

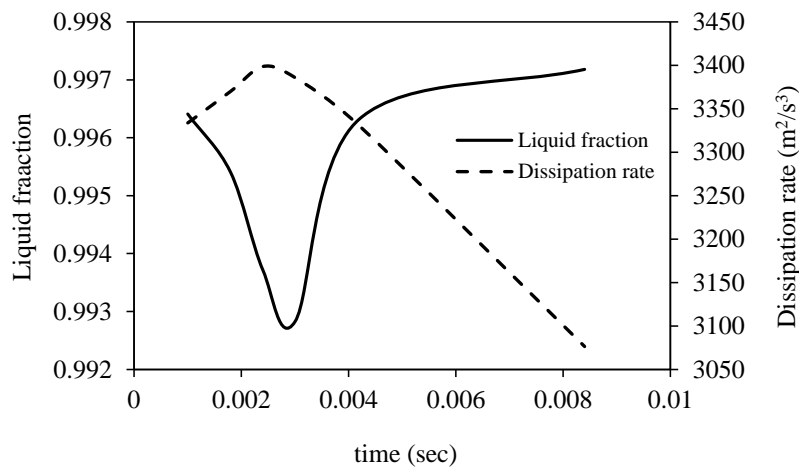
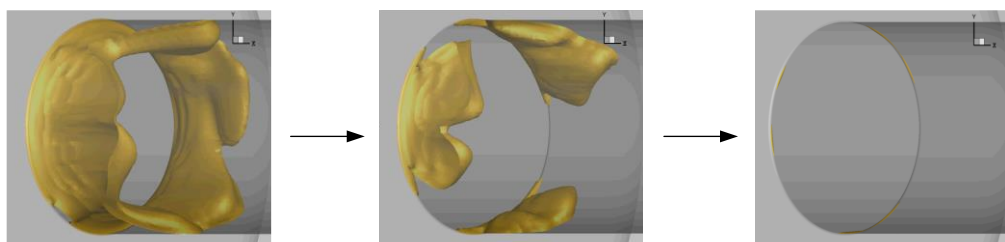


Figure 4-5. Time variations of the liquid fraction (solid line) and the turbulence kinetic energy dissipation rate (dashed line) at the nozzle entrance

In Figure 4-5 the temporal changes in the liquid fraction and the turbulence kinetic energy dissipation rate ( $\varepsilon$ ) are plotted to present the relation between the two variables. The area-averaged values are calculated in a plane located at the nozzle entrance. It is evident that as the liquid fraction is reduced (cavitation develops), the dissipation rate peaks, and it later decays

as the vapour fraction is reduced. The transport equation for the dissipation rate can be a source of inaccuracy in RANS models (Gatski, Hussaini, & Lumley, 1996). When the dissipation rate is underestimated, the TKE values become unphysically large, resulting in suppression of small-scale perturbation and instead prediction of non-cavitating large scale eddies.

The  $k-\omega$  SST model is able to predict the inception of cavitation and the length of the cavitation cloud is initially in agreement with the experimental images (see Figure 4-6). However, while the cavitation vapours last longer than the  $k-\varepsilon$  RNG model predictions ( $\sim 10$  ms), eventually the cavity decays as the simulation progresses and the minimum pressure reaches above the vapour pressure. As mentioned earlier, prediction of the highly unsteady cavity cloud forming in incipient cavitation conditions and the periodic shedding behaviour of the cloud requires capturing the shear layer instabilities. Although the  $k-\omega$  SST model is capable of predicting the cavitation inception, other factors such as accurate prediction of temporal variations of turbulent viscosity and the turbulence anisotropy are essential for predicting the vapour transport, but RANS simulations have a limited capability in resolving such effects as they are highly diffusive. In fact, this shortcoming of RANS models in predicting incipient cavitation has been previously reported even for the more specialized  $\overline{v^2} - f$  RANS model which takes into account the near-wall turbulence anisotropy effects and the velocity fluctuations caused by non-local pressure strain effects (Edelbauer et al., 2014). Moreover, prediction of shear layer microvortices in incipient cavitation requires using scale-resolving simulations to capture the instantaneous pressure drops in the vortex cores, which are not present in the averaged flowfield predicted by RANS approach (Koukouvinis, Naseri, et al., 2016).



*Figure 4-6. Iso-surfaces of 70% vapour volume fraction at the nozzle inlet, cavitation vapours diminish after  $\sim 10$  ms (results predicted by the  $k-\omega$  SST model)*

The next test case investigated in this nozzle is the fully developed cavitation condition. For this case, the  $k-\omega$  SST model is used as it proved to have a superior performance in predicting the cavitation inception. The liquid fraction iso-surfaces inside the nozzle are compared to the

image of in-nozzle cavitation in Figure 4-7. As explained earlier, when the pressure difference between the upstream and downstream of the nozzle is increased, a film cavitation stage develops where a layer of vapour (film) forms between the liquid flow in the core of the nozzle and the nozzle wall. At this point, the pressure at the nozzle walls in the film cavitation region matches the water vapour pressure and as the film disintegrates further downstream into a bubbly cloud due to the collapse of the vapours, the pressure recovers to higher values at the nozzle exit (Bauer et al., 2012). The physical characteristics of the bubbly cloud is similar to the cloud cavity in incipient cavitation stage with small-scale microvortices and distinct bubbles at the nozzle exit.

The pressure field in the film region closely matches the water vapour pressure and is more stable than the cloud; therefore, cavitation can be accurately predicted by the RANS approach in this region. However, downstream in the bubbly cavitation region, an unsteady turbulent pressure field governs the cavity shedding, the velocity fluctuations and the flow mixing region, hence the RANS predictions fail to represent such effects accurately and scale resolving simulations are required to capture the effect of small scales.

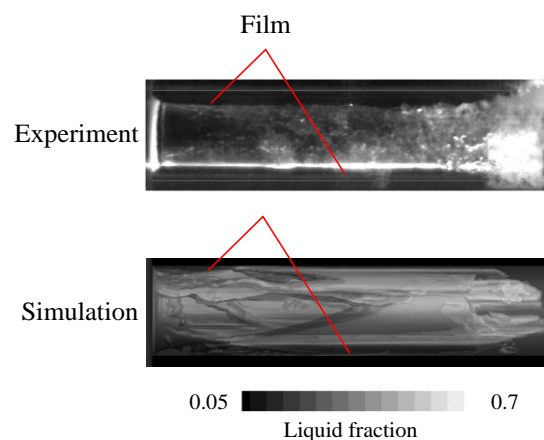


*Figure 4-7. Comparison of cavitation distribution inside the nozzle as shown by the experimental image and iso-surfaces of liquid fraction predicted by CFD for the  $CN = 1.5$  condition. In the simulation results, five translucent iso-surfaces show regions of 5%, 30%, 50%, 70% and 90% liquid fraction*

The liquid fraction distribution in 6 cross sectional planes along the nozzle is presented in Figure 4-8. Cavitation starts to form and cover the nozzle walls in an annular shape, while pure liquid passes in the core of the nozzle in locations (a) and (b). As it was shown in the previous chapter, the inlet pipe delivering the water to the nozzle is separated into three sections separated by  $120^\circ$ . Therefore, the intensity of the cavitation vapours is enhanced in  $120^\circ$  intervals, which is mainly visible in locations (b)-(d). Formation of the annular shaped film cavitation and the

120° separated vapour structures is captured in the simulations. However, it is evident that as the film switches to the bubbly cloud regime, the simulations fail to predict the cavitation presence accurately; the flow exiting the nozzle is a rather homogenous mixture of ~50% liquid/vapour whereas in the simulations the cavitation vapours fully collapse before reaching the nozzle exit. The values of the liquid fraction predicted by the CFD are compared to the experiment in Figure 4-9.

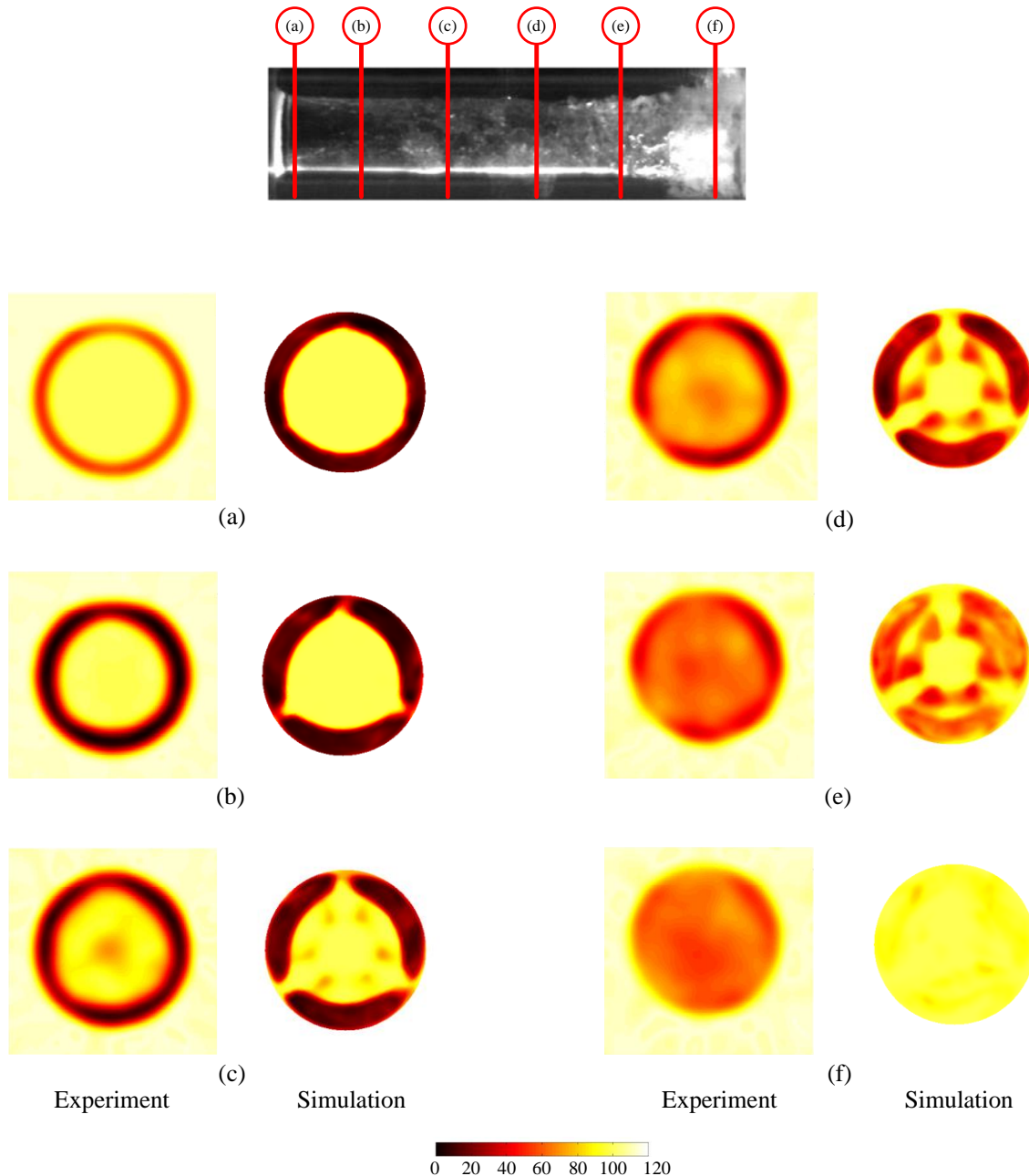


Figure 4-8. Cross sectional liquid fraction measurement locations along the nozzle are indicated at (a) 4.25 mm, (b) 19.25 mm, (c) 40.25 mm, (d) 59.75 mm, (e) 80.75 mm and (f) 94.25 mm downstream the nozzle entrance, the experimental and numerical values for the liquid fraction are compared side by side. Liquid fraction values higher than 100 represent the solid walls made of Perspex (all values are time-averaged)

The pressure inside the channel is measured experimentally using six pressure tapping along the nozzle and in Figure 4-9 (a) these values are compared to the CFD predictions of pressure at the vicinity of the nozzle wall. The first five points ( $x < 60$  mm) correspond to the regions covered with the film cavitation vapours, therefore the pressure in these locations is close to the water vapour pressure. The last point falls inside the bubbly mixture at the nozzle outlet and so the pressure in this region is between 1 bar and the water vapour pressure ( $\sim 0.5$  bar). The CFD predictions are largely in agreement with the experimental measurements and can accurately capture the pressure distribution along the nozzle with  $\sim 15\%$  relative error.

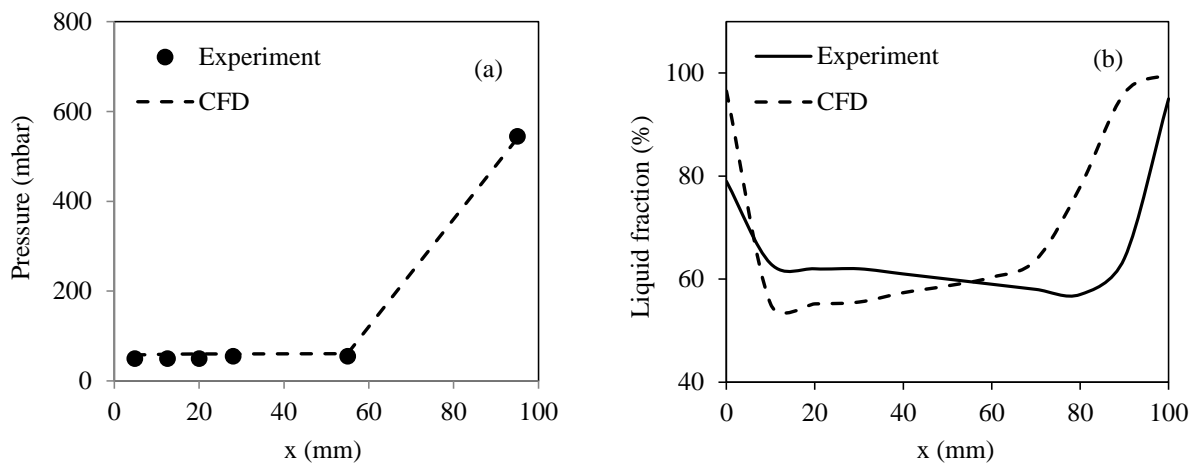
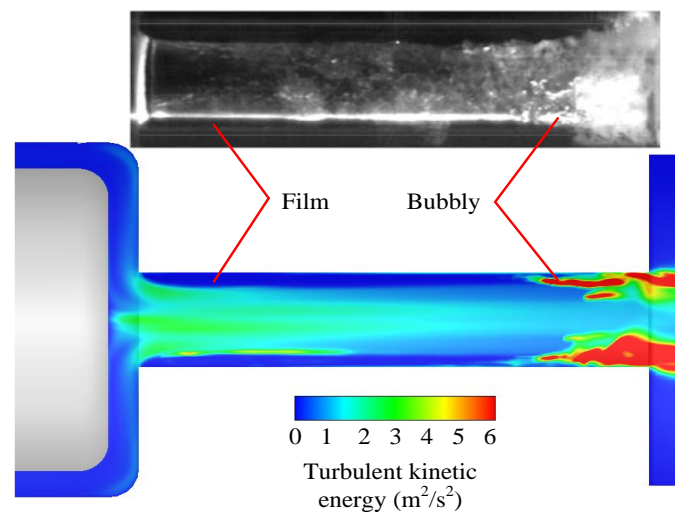


Figure 4-9. (a) Pressure tapping measurements (experiment) and CFD predictions of pressure along the cavitating nozzle length, (b) spatially averaged liquid fraction measured using the X-ray CT and the corresponding predictions by CFD simulations

In Figure 4-9 (b), the spatially averaged values of the liquid fraction measured by the X-ray experiments is compared to CFD predictions calculated in several planes along the nozzle. In the first half of the nozzle where mainly the film cavitation appears ( $x < 50$  mm), the liquid fraction is slightly under-predicted, still the CFD predictions are within  $\pm 10\%$  of the experimental measurements. However, in the region of  $x > 50$  mm where the film breaks down, RANS fails to predict the formation of the bubbly cloud and therefore the liquid fraction is over-predicted by  $\sim 20\%$ .

The results presented in this section show the situational performance of RANS models in predicting the vapour formation depending on the cavitation regime. In regions of film cavitation, the flow is more stable with smaller velocity fluctuations compared to the bubbly cloud region as demonstrated by the turbulent kinetic energy contour in Figure 4-10. Therefore,

modelling the film cavitation formation caused by the abrupt pressure drop in the flow recirculation regions in the periphery of the nozzle is less sensitive to the choice of the turbulence model. However, the vapour film breaks down into a bubbly cloud by the re-entrant jet motion in a periodic manner. Modelling the formation and interaction of the bubbles in regions with cloud-like cavitation requires capturing the instantaneous velocity fluctuations, but the RANS models only provide the average representation of the flow and fail to calculate the small scales involved in the dynamics of these highly transient cavitation clouds. Moreover, in the bubbly flow region, the physics of liquid/vapour interface cannot be fully described by a mixture multiphase model and therefore interface capturing or tracking methods are required accurately define the flow dynamics in these conditions. However, capturing the sharp interface requires a level of grid refinement that would hugely increase the cell count and consequently the computational costs, making the simulation unaffordable with the current resources.



*Figure 4-10. Distribution of TKE inside the nozzle and the experiment image of the cavitating flow*

Finally, it is worth mentioning that there is an ambiguity with the boundary condition values provided by the experimental study used in this section, as the reported pressure values fall inside flow recirculation regions where pressure tapping can give inaccurate readings. This additional factor increases the discrepancy between the experimental and the numerical results. Therefore in the following section, simulation results in an asymmetric nozzle are presented for which the experimental conditions are more clearly defined through close communication with the authors of the study.



### 4.1.2. Asymmetric nozzle

The nozzle configuration and experimental setup used in this study was designed to resemble the flow in a valve-covered orifice diesel injector. An asymmetric needle positioned off-axis the nozzle, blocks the fuel (diesel) from one side and forces the majority of the flow to enter the nozzle from the other side of the nozzle entrance. The resulting cavitation pattern is a large cloud of vapour confined to the side of the nozzle where the main flow enters the hole. The cavitation cloud periodically grows and sheds while smaller scale cavitating vortices detach from the cloud.

For the simulations, the  $k-\omega$  SST turbulence model and the Schnerr and Sauer cavitation model are used similar to the previous section. The shadowgraphy image of the cavitation cloud inside the nozzle is compared to the iso-surfaces of liquid fraction (ranging from 10% to 90%) in Figure 4-11. The experimental and numerical results are in qualitative agreement and the length and extent of cavitation predicted by the simulation matches with the shadowgraphy image.

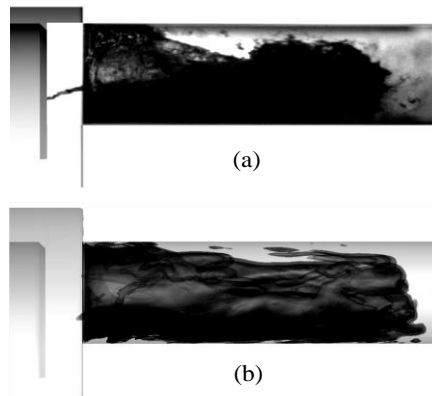


Figure 4-11. (a) Shadowgraphy image of the cavitation cloud (Koukouvinis et al., 2017) and (b) translucent iso-surfaces of liquid fraction ranging from 10% to 90%.

The time-averaged contours of the liquid fraction in the nozzle are presented in four slices at 1mm, 4mm, 6mm and 8mm downstream of the nozzle entrance in Figure 4-12. A cavitation ring (film) forms at 1mm location as the fluid enters the nozzle. The ring covers the nozzle periphery as shown in both the experimental and the numerical data and it is thicker in the lower side of the plane where the majority of the flow enters the nozzle. Further downstream (4 mm and 6 mm), the ring breaks down and forms a large cloud of vapour covering mainly one side of the nozzle, allowing the pure liquid phase to pass above the cloud (as also seen in Figure 4-11). Finally, the liquid fraction increases as the vapours reach to the vicinity of the nozzle exit at 8mm and the cavitation cloud starts to collapse.

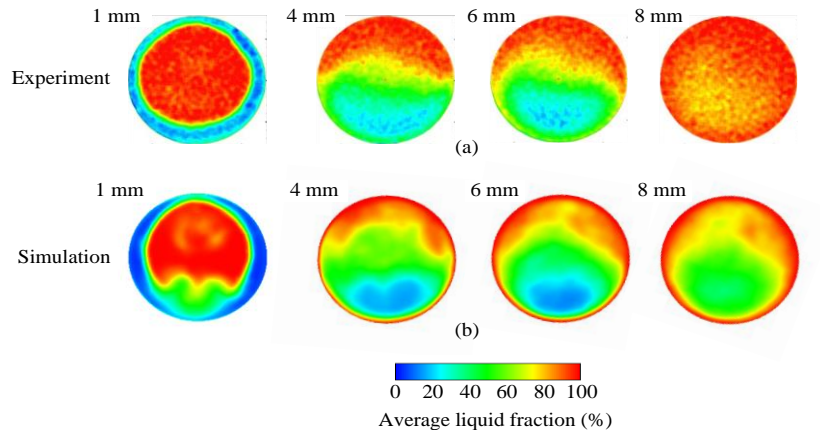


Figure 4-12. Time-averaged contours of liquid fraction in four slices along the nozzle (a) as measured by the X-ray CT experiment and (b) as predicted by RANS simulation

The area-weighted average value of liquid fraction is calculated in several planes along the nozzle length and compared to experimental values in Figure 4-13. The experimental data carry  $\pm 4\%$  of measurement error which is indicated with the error bars in the graph. Up to  $\sim 4\text{mm}$  into the nozzle length, the CFD predictions of the liquid fraction are within  $\pm 10\%$  of the experimental measurements. Further downstream, the CFD results predict a higher cavitation presence compared to the experiment and therefore the liquid fraction is underestimated by up to  $\sim 25\%$  at the 7mm location. Overall, the simulations can predict the liquid fraction inside the nozzle with  $\sim 12\%$  relative error. In the second half of the nozzle (after 5 mm nozzle length), small-scale cavitating vortices and bubbles start detaching from the vapour cloud due to the cavitation shedding process that leads to collapse of the cloud. The prediction of this cascading cavitation regime depends on capturing the formation of the re-entrant jet motion and micro-vortex cavities detaching from the cloud.

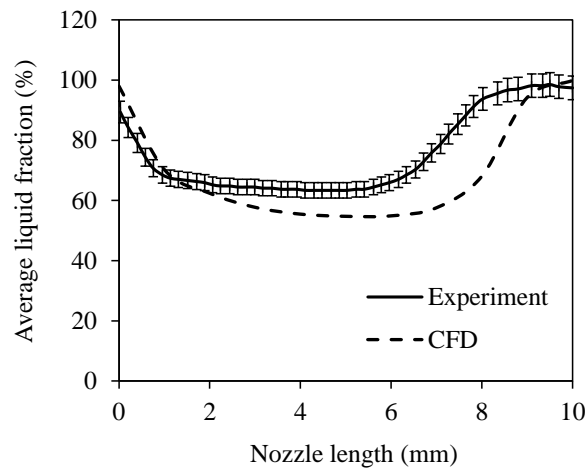


Figure 4-13. Average liquid fraction values in the nozzle, the experimental X-ray measurements are compared to the numerical predictions and the values are calculated in several slices along the nozzle

In Figure 4-14 the transient dynamics of the cavity cloud is presented using shadowgraphy images and it is compared to iso-surfaces of vapour fraction predicted by RANS simulations in the range of 10% to 90% (0.1 to 0.9). The regions indicated with green and red circles display the most stochastic behaviour and are the main source of discrepancy between the experimental and the numerical results.

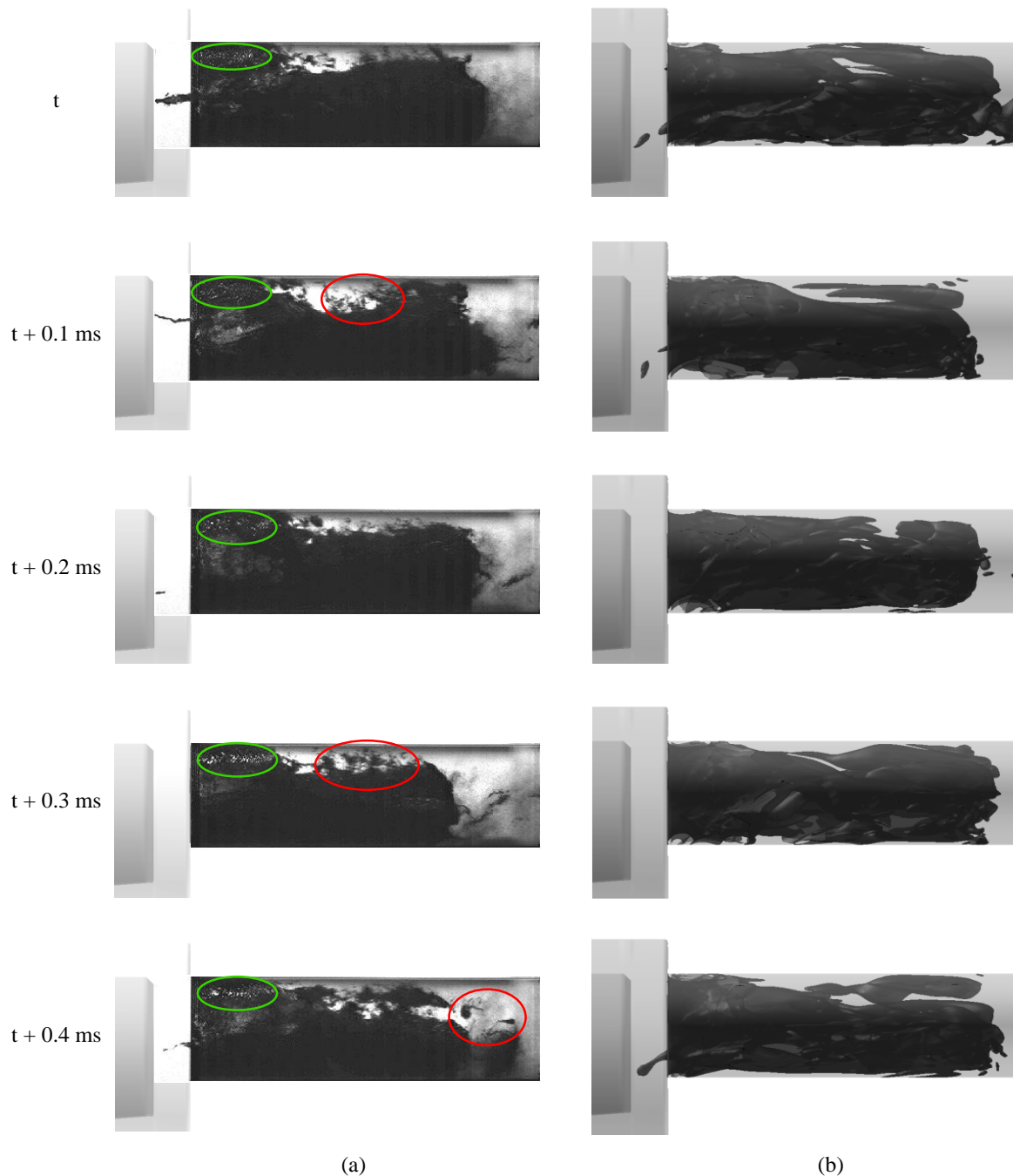
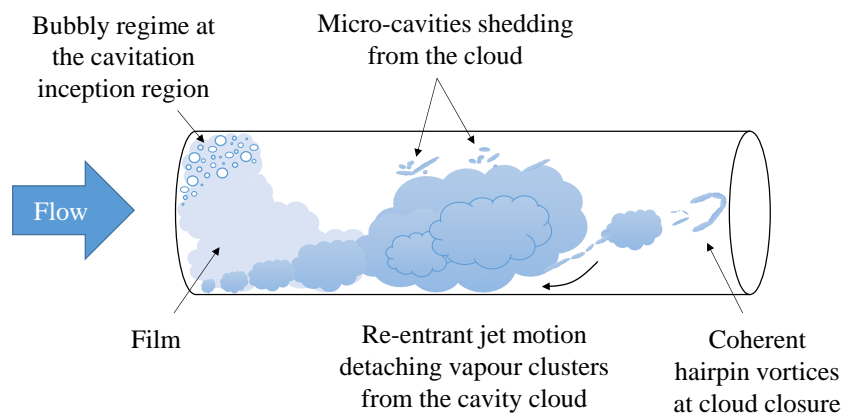


Figure 4-14. (a) Shadowgraphy images of the cavity cloud (b) and iso-surfaces of vapour fraction from the simulations, iso-surface values ranging from 10%-90% at 0.1 ms intervals, green circles in the shadowgraphy images indicate the bubbly cloud regions at the nozzle inlet with a foamy appearance and red circles show the small-scale vortices shedding from the cloud

The green circles in the vicinity of the nozzle entrance indicate the bubbly cavitation regime which is also observed in the preliminary study in section 4.1.1. As cavitation starts to form at the entrance of the nozzle, a porous liquid (bubbly) region appears, occupying this area with an intense liquid/vapour interface (see also Figure 4-15). As mentioned in the previous section, the physics of multiphase flows with a high population of distinct bubbles is most accurately described by scale resolving simulations in conjunction with interface capturing/tracking methods rather than the mixture methodology. Therefore, the RANS simulations presented here slightly under-predict the extent of vapour in the bubbly regions. On the other hand, the film region at the nozzle entrance (~0 mm to ~3 mm) and the attached part of the cavity cloud covering ~ 75% of the nozzle resemble the shadowgraphy images. Moreover, the intermittent behaviour of a string cavitation forming below the needle upstream the nozzle entrance is also captured in the simulations.



*Figure 4-15. Schematic demonstrating the unsteady cavitation cloud structures inside the nozzle (blue colour), the bubbly cloud at the entrance and the small-scale micro-cavities are the major source of discrepancy between the experiments and the CFD results*

The red circles in Figure 4-14 (a) indicate the small scale vaporous vortices detaching and shedding from the cavitation cloud. The periodic shedding of the cavity cloud is attributed to a secondary flow motion, i.e. the re-entrant jet, which impinges on the cloud above the boundary layer at the cavity closure, while detaching smaller vapour clouds from the bulk of the cavity (see also Figure 4-15). This process leads to development of further small-scale flow instabilities and micro-cavities in the vicinity of the cloud. Moreover, after the onset of cloud shedding and separation of vapour clusters, hairpin vortices emerge from the coherent turbulent structures at the cloud closure (Mitroglou, Stamboliyski, Karathanassis, Nikas, & Gavaises, 2017). Furthermore, collapse of the cavitation vapours increases the vorticity near the nozzle

outlet, which further promotes flow instability and mixing. Dynamics of the micro-cavities shedding from the cloud and the small-scale coherent structures in the vicinity of the cloud is highly stochastic and RANS simulations are unable to predict these structures. Therefore, the cloud shedding process cannot be fully calculated and the length of the cloud is overpredicted as seen in Figure 4-14.

## 4.2. Turbulence modelling

The aim of this study is to examine the influence of various turbulence models, including some common RANS models e.g.  $k-\epsilon$ ,  $k-\omega$ , RSM, as well as their modifications that have been proposed for the compensation of mixture compressibility effects, namely the Reboud *et al.* correction (Reboud et al., 1998). The application is on a square throttle with a sudden constriction which has been examined in the past (Sou et al., 2014), this configuration bears resemblance to the constrictions inside injector passages. Cavitation effects have been modelled using a mixture multiphase model, and phase change is governed by the Schnerr and Sauer and Zwart-Gerber-Belamri models. In addition, the homogenous equilibrium model described in the methodology chapter is also examined.

Water is discharged into a rectangular step nozzle with 48 ml/s flow rate and the outlet is subjected to atmospheric pressure. At these conditions a recirculation region forms downstream of the sharp step constriction and cavitation develops at the shear layer between the recirculation zone and the formed jet. The dimensions of the constriction are 1.94x1.94x8 mm (WxHxL). In the simulations the outlet is not placed directly at the end of the throttle, but rather further downstream in order to minimise its interference to the flow pattern developing in the throttle. The average velocity through the nozzle ( $v$ ) is 12.8 m/s and the Reynolds number is  $Re = 27700$ ; the cavitation number in the experimental study is calculated from the following relation, this is an alternative definition for cavitation number where  $CN = 1/\sigma$ :

$$\sigma = \frac{P_{amb} - P_v}{\frac{1}{2}\rho v^2} = 1.2 \quad \text{Equation 4.1}$$

where  $P_{amb}$  is the ambient pressure. In order to specify the grid and time step requirements for the LES simulations, Kolmogorov time and length scales and Taylor length scale are calculated (Pope, 2000):

$$\text{Kolmogorov length scale } \eta = \left(\frac{\nu^3}{\varepsilon}\right)^{1/4} = 0.98 \mu\text{m} \quad \text{Equation 4.2}$$

$$\text{Kolmogorov time scale } \tau_\eta = \left(\frac{\nu}{\varepsilon}\right)^{1/2} = 0.96 \mu\text{s} \quad \text{Equation 4.3}$$

$$\text{Taylor length scale } \lambda_g = \sqrt{10} Re^{-0.5} L = 39 \mu\text{m} \quad \text{Equation 4.4}$$

where  $\nu$  is the kinematic viscosity,  $\varepsilon$  is the turbulent dissipation rate estimated from  $U^3/L$ , and  $U$  and  $L$  are the characteristic velocity and length scales respectively. The computational mesh employed in all cases is block-structured. Mesh refinement with inflation layers, is employed in critical areas, such as in the vicinity of the walls. Furthermore, telescopic refinement is employed inside the throttle and the throttle edge. The average mesh resolution for the grid dependence study for RANS simulations is 90  $\mu\text{m}$ , 75  $\mu\text{m}$  and 50  $\mu\text{m}$ , corresponding to 1M, 2.4M and 6.8M cells. The temporal resolution for the unsteady RANS is 1  $\mu\text{s}$ .

Estimation of Taylor microscale provides a guideline for grid resolution in practical LES studies (Addad et al., 2008; Howard & Pourquie, 2002); by refining the mesh below this value the large scale turbulent eddies are captured as  $\lambda_g$  theoretically lies in the high wavenumber end of the inertial subrange. Taylor length scale characterizes the mean spatial extension of the velocity gradients (Lesieur, 2012; Lesieur et al., 2005) and is always much smaller than the integral scale (but not the smallest scale) (Tennekes & Lumley, 1972). The cell size inside the nozzle is 20  $\mu\text{m}$  and it is refined to 2.5  $\mu\text{m}$  near the walls, corresponding to  $Y^+$  values of 0.2-1. Given that an average velocity of  $\sim 12.8$  m/s occurs inside the throttle, a relevant time scale is 2  $\mu\text{s}$ . The time step size chosen is 1  $\mu\text{s}$ , which corresponds to a CFL number of 0.5, enough to properly describe the time scales of fluid motion.

In all cases, the interest is on the average velocity distribution and RMS of velocity fluctuations in locations for which experimental measurements exist. i.e. at 1.5 mm, 3 mm and 6 mm downstream of the nozzle entrance. It should be noted that since experimental data have been collected on the cross-sectional plane using laser doppler velocimetry, this limits the information of the average velocity and RMS velocity fluctuations only to the x and z velocity components.

Initially a grid dependency test is conducted for RANS simulations. The flowrate, measured experimentally to be 48 ml/s, is used as inlet boundary condition and the pressure at the inlet was measured as the convergence criterion for the grid study and boundary condition for the rest of the simulations.

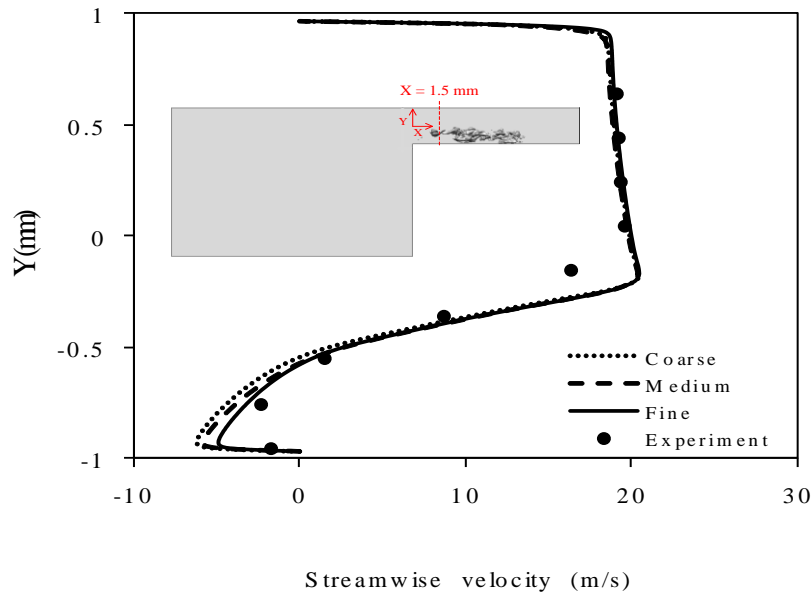


Figure 4-16. Effect of grid refinement on streamwise velocity profile predictions at  $X = 1.5$  mm downstream the nozzle entrance (nozzle geometry and measurement location is shown in the inset)

The velocity profile (time-averaged) downstream the nozzle entrance is presented in Figure 4-16 at the location  $X = 1.5$  mm as indicated in the inset. It is worth mentioning that the LDV measurements provided by the experimental study are unable to account for those instances where cavitation vapours are present in the laser path. Therefore, there the CFD results mainly deviate from the experimental data in the region of  $-0.97 \text{ mm} < Y < 0 \text{ mm}$  where cavitation appears. The results indicate that changes in the velocity profile with successive grid refinements are negligible (less than  $\sim 3\%$  change in the velocity profile) compared to the additional computational cost.

Grid	Cells	Max $Y^+$	Min $Y^+$	Total Pressure at inlet [Pa]
<b>Coarse</b>	1M	55	1	237260
<b>Medium</b>	2.3M	45	0.5	238270
<b>Fine</b>	6.8M	37	0.2	238220

Table 4-1. Grid parameters and their effect on inlet pressure convergence

The grid with the medium refinement can capture the velocity profile with ~1% relative error in the single-phase region ( $Y > 0$  mm) so it is used for the remaining RANS simulations. The calculated total pressure at inlet is affected less than 0.5%, giving confidence to use it as a boundary condition for the rest of the simulations.

The next step is to examine the effect of RANS models. The investigated models are, Realizable  $k$ - $\epsilon$ , SST  $k$ - $\omega$  and Reynolds Stress Model. These simulations and the grid dependency tests are examined in steady state conditions. The Reboud *et al.* correction (Reboud et al., 1998) for both Realizable  $k$ - $\epsilon$  and SST  $k$ - $\omega$  models was used to improve the RANS model predictions in the two-phase region. These corrections are only relevant in the cavity shedding process, hence they must be used in transient simulations. Finally, the WALE LES model is used to study the Schnerr-Sauer, Zwart-Gerber-Belamri, the modified Zwart-Gerber-Belamri model and the HEM cavitation model.

#### 4.2.1. RANS Simulations

In this section, performance of the RANS models in predicting the velocity distribution inside the nozzle, the level of turbulence and formation and shedding of cavitation is assessed. Figure 4-17 shows the velocity and RMS of velocity fluctuations values compared to the experimental data for the standard RANS models. All RANS models give an adequate prediction of the velocity distribution at locations  $X = 1.5$  mm and  $X = 3$  mm, while the 2-equation models are rather more accurate than the RSM model. At  $X = 6$  mm there is a more pronounced discrepancy mainly at the region of the flow recirculation and reattachment, at  $-0.97$  mm  $< Y < -0.5$  mm. This is mainly due to the high experimental uncertainty associated with the LDV measurements in the two-phase flow region.

Considering the RMS of turbulent fluctuations, the RSM model behaves better at locations  $X = 1.5$  mm and 3mm, predicting a narrower zone of high turbulent flow, around  $Y = -0.5$  mm, in accordance to the experiments. The results indicate that, the 2-equation models predict a thicker zone of high turbulence, from  $\sim Y = -0.97$  mm to  $-0.2$  mm. However, all the examined models fail to accurately predict the turbulent fluctuations at  $X = 6$ mm and in the whole flow in  $0$  mm  $< Y < 0.97$  mm. The under-prediction of velocity fluctuations is related to the fact that none of the models are capable of predicting the cavitation formation. The two-way interaction between flow turbulence and cavitation and generation of vorticity due to collapse of cavitation bubbles enhance the velocity fluctuations, but RANS simulations fail to predict such effects.



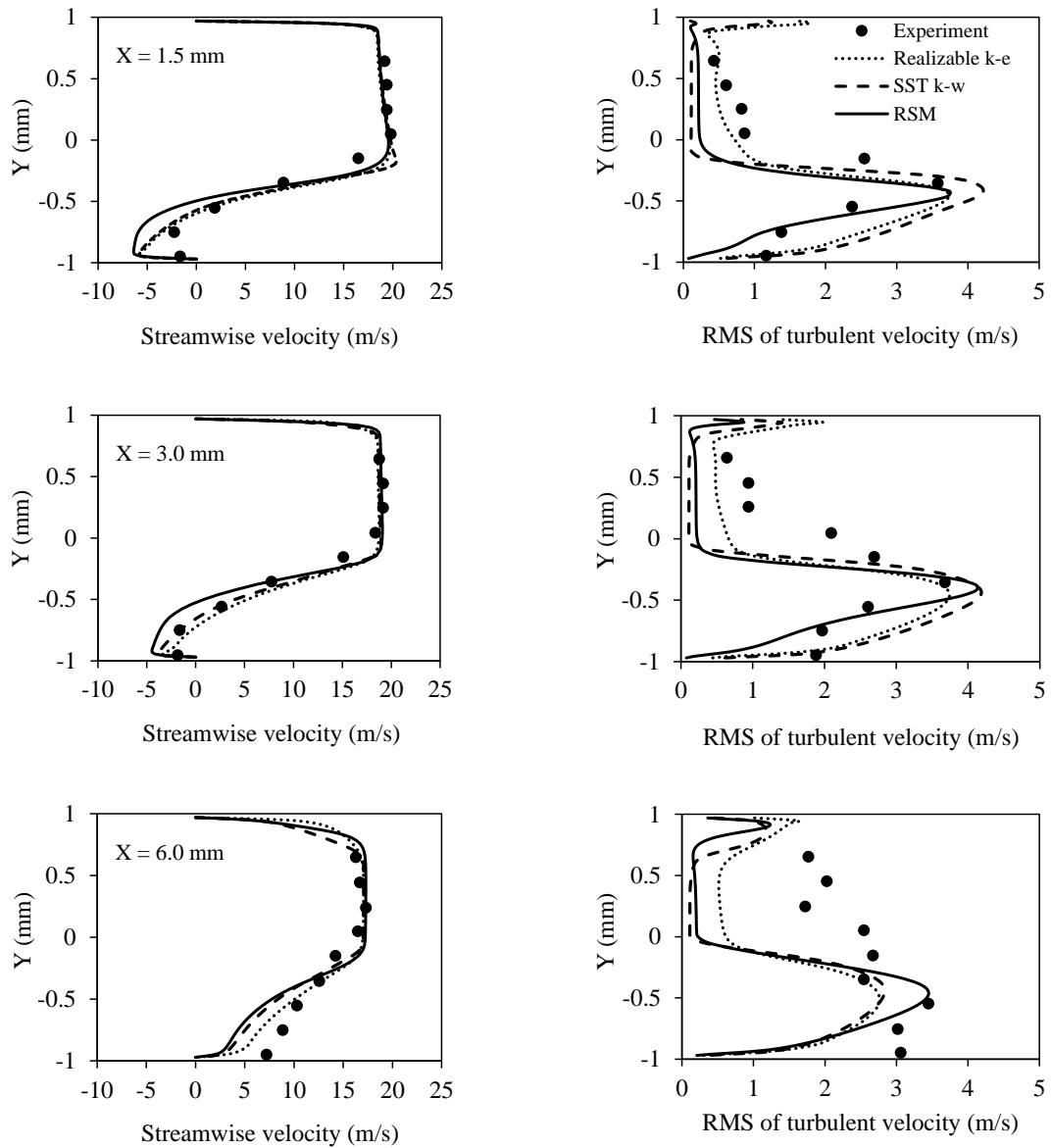


Figure 4-17. Streamwise velocity and RMS of turbulent velocity at three locations downstream the nozzle inlet, experimental data are compared to the standard RANS models

A very important observation, and a key conclusion of the present study, is that the steady state RANS models examined so far, fail to predict the onset of cavitation. To be more precise, the minimum pressure in the whole computational domain predicted by each one of the models, as described so far, is:

- Realizable k- $\epsilon$ : 12970 Pa
- k- $\omega$  SST: 10590 Pa
- RSM: 13770 Pa

It becomes clear that these minimum pressures are almost 5-6 times the saturation pressure of water, so cavitation is not predicted; in fact even applying corrections that increases the cavitation threshold pressure due to the influence of turbulence fluctuations (see e.g. ((Singhal et al., 2002)) still fail to produce cavitation. Assuming a cavitation threshold of the form:

$$p_v = p_{sat} + \frac{1}{2}(0.39\rho k) \quad \text{Equation 4.5}$$

where  $p_{sat}$  is the saturation pressure,  $k$  the local turbulent kinetic energy and  $\rho$  the liquid density, the maximum threshold pressure for cavitation formation throughout the whole computational domain is:

- Realizable k- $\epsilon$ : 6515Pa
- k- $\omega$  SST: 7128Pa
- RSM: 8047Pa

which is still significantly lower, almost half, of the minimum liquid pressure that has been predicted in the computational domain by each model.

#### 4.2.2. Modifications of RANS models

Further examination of this case with unsteady RANS models is conducted to investigate if transient simulations can capture the cavitation phenomenon. Additionally, since it is known from the experiment that cavitation shedding occurs due to the shear instabilities at the border of the recirculation zone, it was chosen to resort to the RANS modifications described in the methodology section, which are known to be able to predict such effects (Reboud et al., 1998).

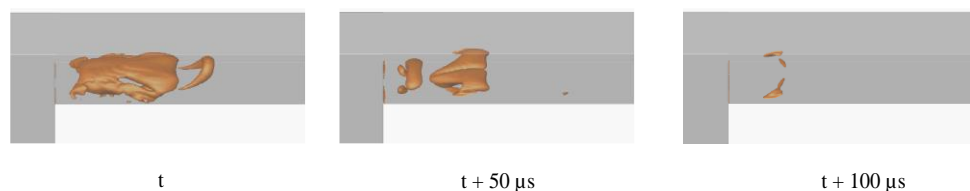


*Figure 4-18. Iso-surface of 50% vapour volume fraction predicted by the modified k- $\omega$  SST model, the cavitation vapours completely shed after a few cycles at  $\sim 100 \mu s$  and the eventually only the liquid phase remains*

The vapour pressure is reduced so that both of the modified models (k- $\omega$  SST and k- $\epsilon$  RNG) predict the inception of cavitation in the shear layer; this is required in order to apply the eddy

viscosity modifications (see Figure 4-18). Initially, the cavitation cloud dynamics is correctly predicted as the vapour grows, sheds and regrows in a cyclic manner. However, after each shedding cycle, the length of the cavity shrinks until finally, the cloud completely disappears and the simulations reach a steady single phase (liquid only) solution. The same behaviour is observed for both  $k-\omega$  and  $k-\epsilon$  models, this shows that even though flow unsteadiness has initially been introduced, but still the unsteady RANS simulations fail to accurately predict the cavitation dynamics.

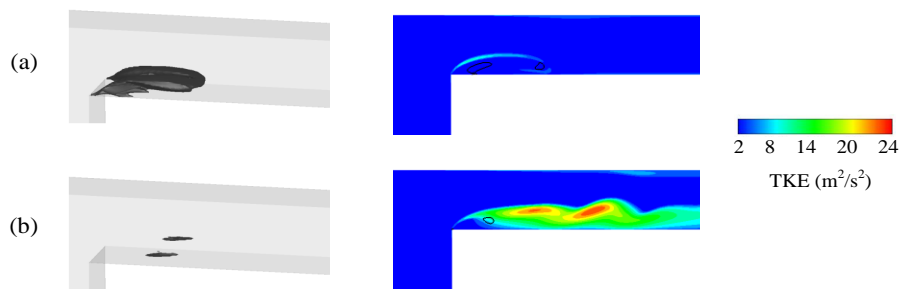


Figure 4-19. Iso-surface of 50% vapour volume fraction (left) and contours of TKE in the nozzle midplane (right) as predicted by the modified  $k-\omega$  SST model, results presented at the beginning of the simulation (a) and after  $\sim 200 \mu\text{s}$  (b), black lines show regions below vapour pressure

The modified RANS models are intended to improve the performance of standard RANS models by reducing the turbulent viscosity in cavitation regions. Indeed, at the beginning of the simulations as the cavitation vapours start to form, the turbulence kinetic energy (TKE) is mainly confined to the shear layer region as shown in Figure 4-19 (a). However, as the cavitation shedding cycle starts, the TKE starts building up inside the nozzle (see Figure 4-19 (b)) resulting in over-prediction of turbulent viscosity and therefore damping of the small scales. The reason for the TKE build-up is that the turbulence dissipation process relies on capturing the microvortices and small eddies which are often omitted due to the averaging operation in RANS models.

As shown in Figure 4-20, comparison between the modified URANS models and experimental data shows a better agreement than the steady state RANS cases. Most notably in the region of flow recirculation at  $-0.97 \text{ mm} < Y < -0.5 \text{ mm}$ , at locations of  $X = 1.5 \text{ mm}$  and  $3 \text{ mm}$ , the negative velocities are not over-estimated as in the standard RANS results, therefore, the velocity profile after the flow reattachment at  $X = 6 \text{ mm}$  closely matches the experimental results. However, as the cavitation dynamics is not calculated accurately, both of the tested models under-predict the values of the RMS of turbulent velocity.

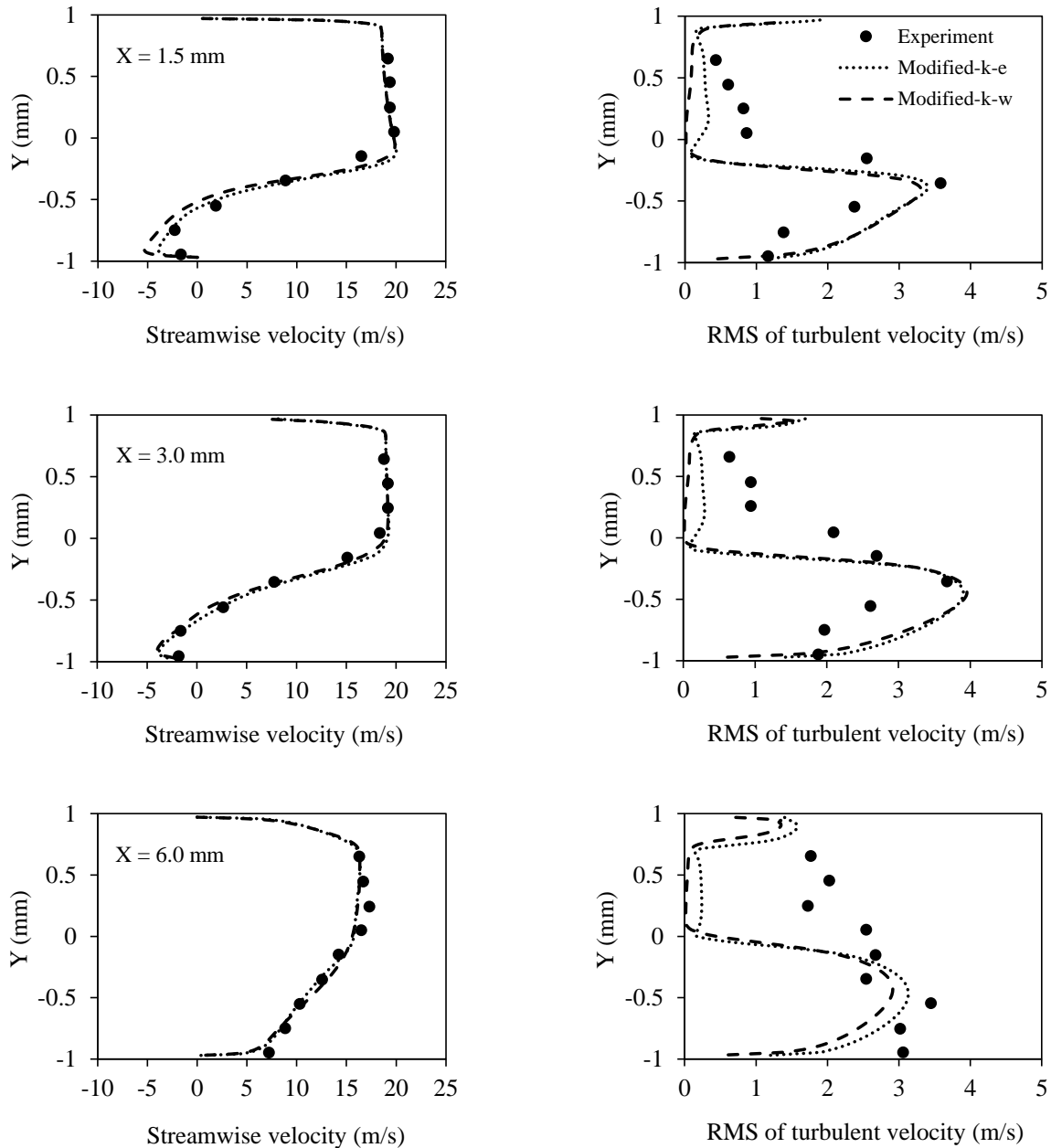


Figure 4-20. Streamwise velocity and RMS of turbulent velocity at three locations downstream the nozzle inlet, Experimental data are compared the modified RANS models

### 4.2.3. LES Simulations

The next step is to investigate whether cavitation can be predicted using the WALE LES model. It is expected that by using the LES formulation, the simulations would predict the instantaneous pressure fluctuations in the core of shear layer vortices that lead to cavitation inception and shedding. All the cavitation models presented in the methodology section, i.e. the barotropic model and the Scherr-Sauer and Zwart-Gerber-Belamri model are tested in this

section. Increasing the mass transfer rate of any of the two-phase models pushes the cavitation process towards thermodynamic equilibrium, therefore, a modified version of the ZGB model is also tested by increasing the condensation and evaporation coefficients to values of the order of  $10^6 \text{ m}^{-1}$ . In principal, the mass transfer rate coefficients should tend toward infinity to represent an instantaneous process (equilibrium), however, higher mass transfer rates cause numerical instabilities in the solution.

Comparing the simulation and the experimental data in Figure 4-21, it is evident that LES model succeeds in predicting the velocity distribution accurately at all locations and provides a close estimate of the turbulent fluctuations both in the recirculation zone and the jet formed at the core of the nozzle. Moreover, vapour formation is predicted with all cavitation models, predicting a very similar velocity profile, showing that the velocity distribution is rather weakly related to cavitation presence; this is explained by the low cavitation intensity in the examined configuration. The predictions of the RMS of turbulent velocity is remarkably improved compared to the RANS simulations. Particularly in the upper half of the nozzle ( $0 \text{ mm} < Y < 0.97 \text{ mm}$ ) where the RANS results severely under-predict the turbulence level, the LES model succeeds in predicting a more realistic distribution of RMS along the nozzle section.

Considering the minimum pressures that develop inside the whole computational domain:

- The modified ZGB model: instantaneous minimum  $\sim -3000\text{Pa}$  and minimum average  $\sim 7200\text{Pa}$ .
- The barotropic model: instantaneous minimum  $\sim 500\text{Pa}$  and minimum average  $\sim 9800\text{Pa}$ .
- The standard ZGB model: instantaneous minimum  $\sim -12000\text{Pa}$  and minimum average  $\sim 7800\text{Pa}$ .
- The standard SS model: instantaneous minimum  $\sim -20000\text{Pa}$  and minimum average  $\sim 8600\text{Pa}$ .

The barotropic model is the only cavitation model that predicts a positive minimum pressure, due to the homogenous equilibrium assumption; in fact, a negative pressure in the barotropic model does not have any meaning, since it corresponds to negative density and unphysical speed of sound.

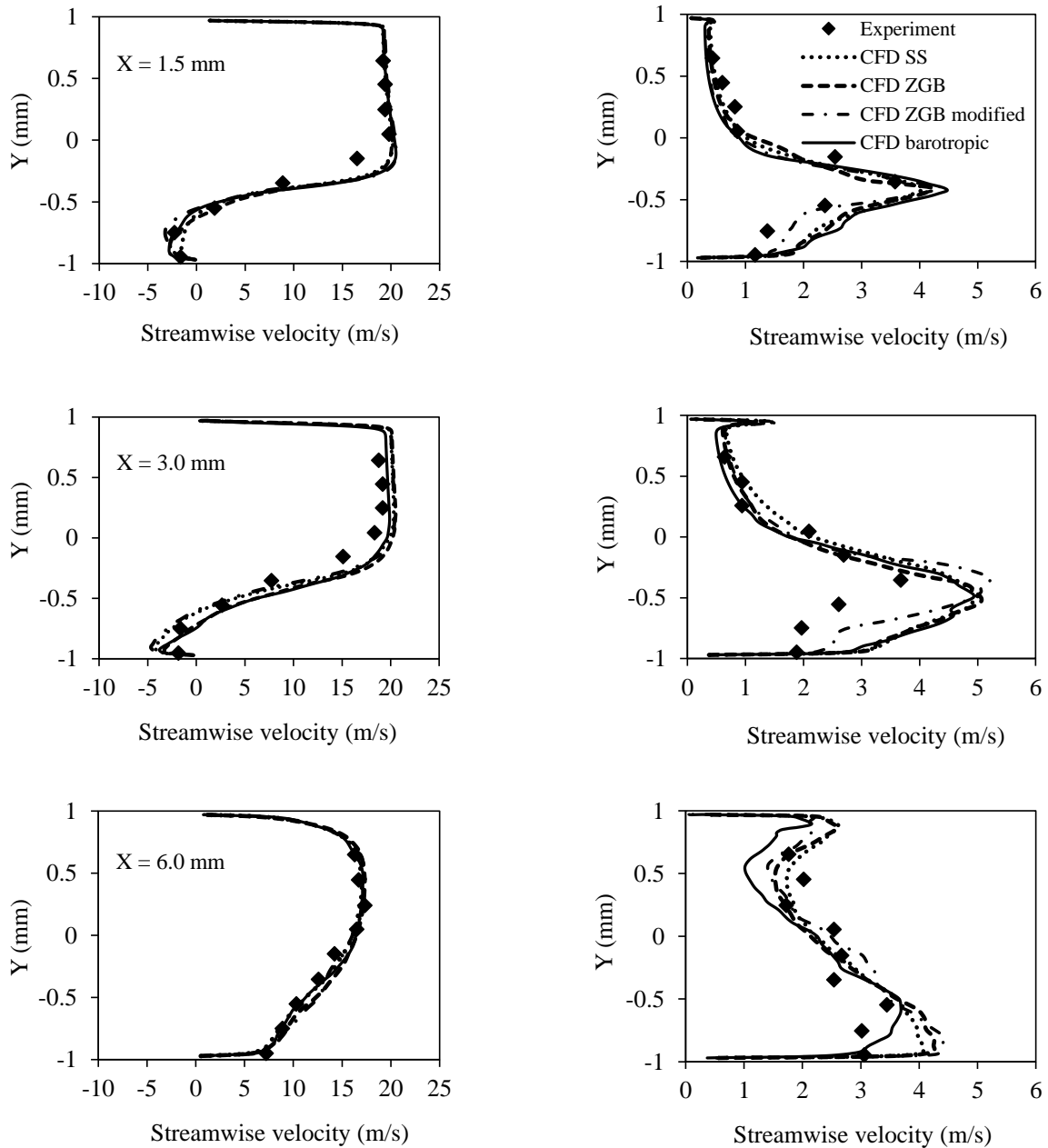


Figure 4-21. Streamwise velocity and RMS of turbulent velocity at three locations downstream the nozzle inlet, results presented for LES simulations with different cavitation models

Indicative flow instances are presented in Figure 4-22, showing the shedding of cavitation structures and the transient pressure distributions predicted by the SS cavitation model along with the shadowgraphy images from the experimental study. It is evident that the cavitation vapours start to appear in the core of small-scale eddies in the shear layer. The cavitating microvortices appearing in the shear layer can be as small as 100  $\mu\text{m}$  and further downstream, they merge to form larger cloud structures in the order of 0.5 mm. The regions of cavitation inception where the pressure locally drops below the vapour pressure are indicated using black

iso-lines in the pressure contours. It becomes clear from the time-averaged pressure data that the minimum average pressure in the whole domain is above the saturation pressure. This indicates that instantaneous minimum pressure data are required in order to capture the cavitation inception regions, therefore the results predicted by RANS models fail to accurately predict cavitation while the LES simulations can predict the pressure field fluctuations and the subsequent unsteady dynamics of the cavitation cloud.

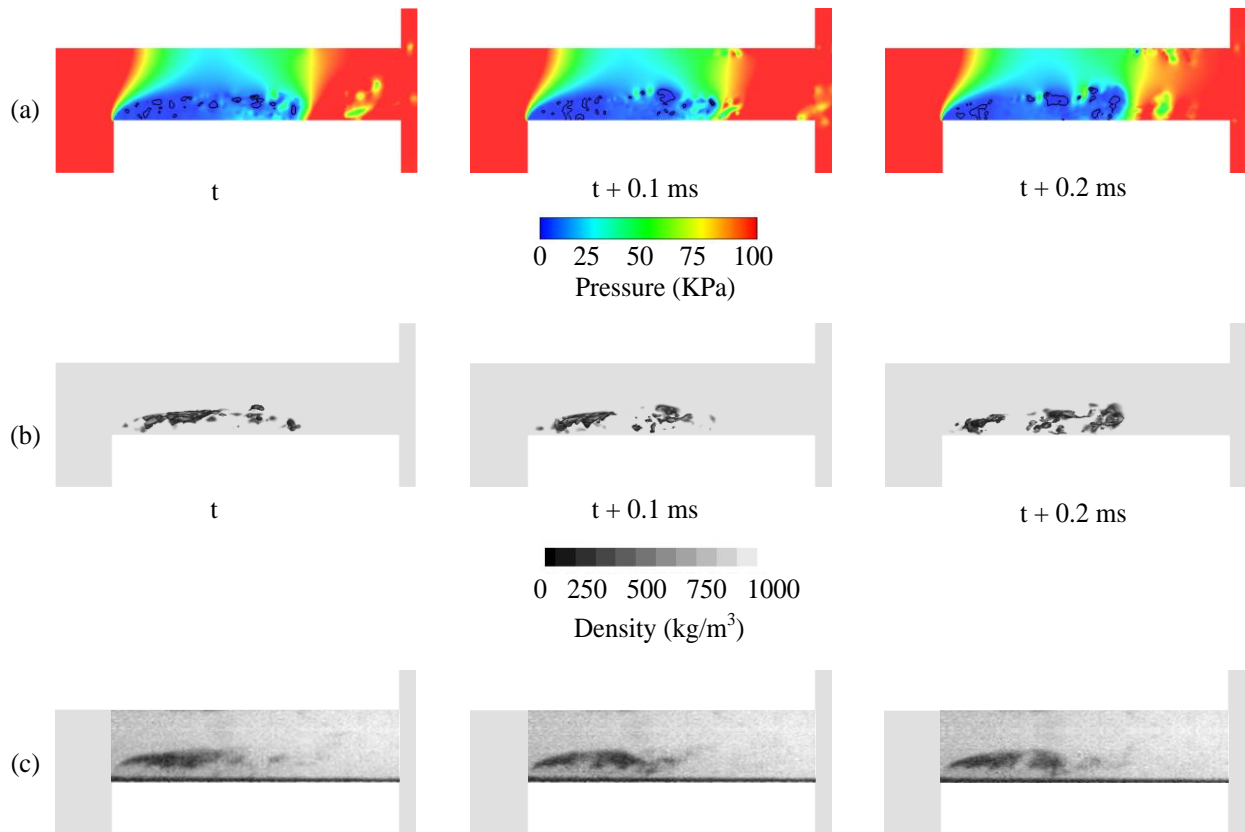


Figure 4-22. Indicative (a) pressure and (b) density contours in the nozzle midplane, (c) three instances of shadowgraphy images showing the in-nozzle vapour distribution in the experimental study (Sou et al., 2014). Black iso-lines in the pressure contour (a) indicate regions where the pressure drops below the saturation pressure and iso-surfaces of 75% liquid fraction are added to the density contours in (b)

### 4.3. Cavitation Models

The effect of cavitation model on the quantity of cavitation is assessed by comparing the time-averaged cavitation volume fraction data predicted by the two-phase models and the barotropic model. In Figure 4-23 the liquid fraction contours in the midplane of the nozzle is plotted as calculated by the SS model, the ZGB model, the modified ZGB model and the barotropic model. The overall dimensions of the cavitation cloud is similar for all the two-phase models

(~ 1 mm thickness and ~5 mm length) while the cloud predicted by the barotropic model is slightly shorter (~ 4 mm). However, all the models show that the cavitation inception (the region with the lowest liquid fraction/highest vapour fraction) starts at ~ 3 mm above the lower wall of the nozzle ( $Y \sim -0.7$  mm) which corresponds to the position of the shear layer. Furthermore, the ZGB model predicts the highest quantity of vapour developed in the core of the cloud (average liquid fraction inside the nozzle  $(1-\bar{\alpha})_{\text{Nozzle}} = 94.36\%$ ), while the SS and the modified ZGB models predict a similar cloud pattern ( $(1-\bar{\alpha})_{\text{Nozzle}} = 95.75\%$  and  $95.05\%$  respectively) and the barotropic model predicts the least amount of cavitation produced compared to all the two-phase models ( $(1-\bar{\alpha})_{\text{Nozzle}} = 97.36\%$ ). This is due to the thermodynamic equilibrium and the instantaneous mass transfer rate assumptions used in the barotropic model. Thermodynamic equilibrium implies that the rate of phase change theoretically approaches to infinity, therefore the cloud formation and collapse happen at a faster rate compared to the two-phase models that are based on a prescribed mass transfer rate. Moreover, the barotropic model is fully compressible because it is based on equation of state for all the phases, whereas the two-phase models are only compressible in the mixture region (Franc & Michel, 2005).

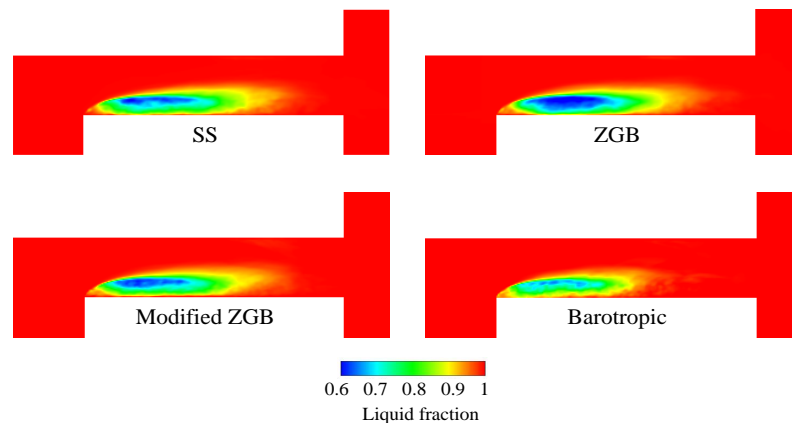


Figure 4-23. Contours of liquid fraction in the midplane of the nozzle predicted by the two-phase models (SS, ZGB and the modified ZGB) and the barotropic model

Nevertheless, it is not possible to identify which of the cavitation models more accurately predicts the vapour fraction because the experimental study only provides qualitative shadowgraphy images of the in-nozzle cavitation. However, the barotropic model is expected to have a more robust physical formulation compared to the two-phase models, because it is based on the equation of state of the phases rather than the rate of mass transfer rate between the phases, which in general is unknown.



By increasing the mass transfer rate in the modified ZGB model, the results move closer to the thermodynamic equilibrium (Koukouvinis, Naseri, et al., 2016), therefore the magnitude of the negative pressure as predicted by the default ZGB model is reduced at higher mass transfer rates. It is worth mentioning that for water there is some evidence that cavitation behaves as a thermodynamic equilibrium process and pressure at the cavitation region matches closely the saturation pressure at the given temperature (Washio, 2014). Moreover, quantitative comparison of the cavity shapes predicted by the standard ZGB model and the ZGB model with higher mass transfer rate shows that the interface of the modified model is less diffusive (see Figure 4-24). This is because as the mass transfer rate is increased, the mixture speed of sound is reduced ( $\dot{m}$  and  $c$  are inversely proportional) (Franc & Michel, 2005). Therefore, at high mass transfer rates, the flow in the liquid/vapour mixture region becomes locally supersonic and hence the field variables separation is faster, resulting in a sharper interface

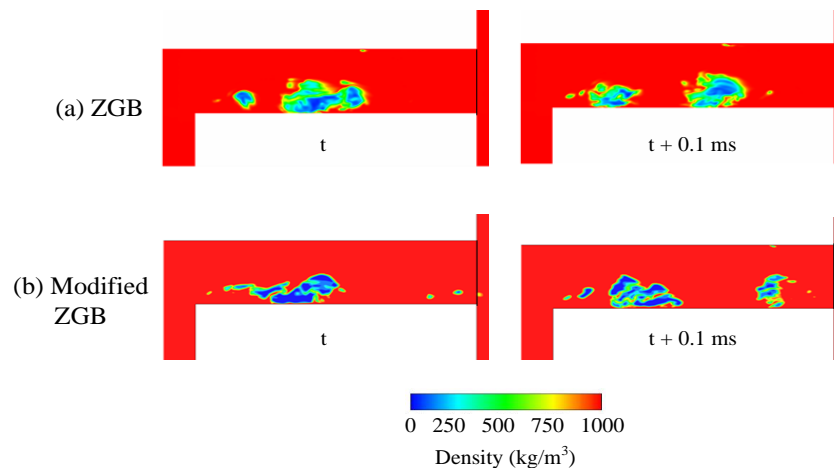


Figure 4-24. Instantaneous density contours for (a) standard ZGB model and (b) modified ZGB model at 0.1 ms intervals

Although by increasing the mass transfer rate for the two-phase models, the cavitation prediction can be improved as the results tend towards the barotropic equation of state, it comes at the cost of numerical stability because the solver cannot handle infinite or extremely large values of mass transfer rate. The SS model predictions of the liquid fraction (Figure 4-23) and the average liquid fraction in the nozzle ( $(1-\bar{\alpha})_{\text{Nozzle}}$ ) match the barotropic model predictions more closely compared to the other tested models. Therefore, the SS model is used for the viscoelastic fluid simulations in the next chapter, as there are no information available regarding the equation of state for additised fluids.

## 4.4. Chapter summary

The aim of the studies performed in this chapter is to identify an accurate framework for modelling nozzle cavitation and investigate the performance of turbulence and cavitation models in various cavitation regimes.

Initially, an axisymmetric nozzle with cloud and film cavitation regimes forming inside the nozzle is investigated. The RANS simulations are unable to predict the bubbly cloud forming in low cavitation number ( $CN = 0.95$ ) but have a better performance in higher cavitation number ( $CN = 1.5$ ) where both cloud and film cavitation regimes are present. The results indicate that while the film-like cavitation can be predicted by RANS, the highly unstable cloud cavity and the bubbly region with a high population of distinct bubbles is under-predicted. Nevertheless, the CFD predictions of the vapour volume fraction at high  $CN$  are largely in agreement with the X-ray CT measurements with overall  $\sim 15\%$  relative error.

The second test case is an asymmetric nozzle with flow conditions and cavitation patterns similar to those realised in fuel injectors; a cavity cloud occupies a large portion of the nozzle internal volume with a cyclic shedding behaviour, while bubbly and film cavitation regimes are also present at the nozzle entrance. The RANS simulations predict the formation of the film-like region at the entrance as well as the attached part of the cloud inside the nozzle. However, in the bubbly region, the micro cavities shedding from the cloud and the coherent vortices at the cloud closure are not captured. Therefore, the cloud shedding process is not fully predicted and the length of the cloud is overestimated. Still, the results are in a good agreement with the experimental data in terms of cavitation structures and vapour volume fraction values with less than  $\sim 12\%$  relative error.

The last test case is a more comprehensive parametric study conducted on a step nozzle with several RANS models, WALE LES model and two-phase and barotropic cavitation models. In this test case, cavitation inception occurs in the core of microvortices in the shear layer, forming a cloud above the flow recirculation region. It is noted that various RANS models in their default form (Realizable  $k-\epsilon$ , SST  $k-\omega$  and RSM) are unable to predict the inception of cavitation, although the time-averaged velocity profiles is in a good agreement with LDV experimental measurements. This is because the minimum pressure predicted by these models is always above the vapour pressure in the entire fluid domain.

Subsequently, a two-phase mixture correction is applied to the eddy viscosity formulation for Realizable  $k$ - $\epsilon$  and SST  $k$ - $\omega$  models (Reboud *et al.* correction (Reboud et al., 1998)) in order to reduce the turbulent viscosity in cavitation regions. At the start of the simulations, cavitation inception is artificially introduced by reducing the vapour pressure in order to apply the modifications, which are only relevant in two-phase flows. The modified RANS models can initially predict the shape, length and shedding of the cloud. However, after a few shedding cycles, the turbulent viscosity starts to build-up inside the nozzle and stabilize the transient shedding and regrowth of the cavity cloud, until eventually the simulations reach a single phase condition as all the cavitation vapours collapse.

The WALE LES model is capable of predicting the transient microvortices forming in the shear layer and the inception, growth and cyclic shedding of the cavitation cloud is correctly predicted. Moreover, predictions of the average velocity and the RMS of turbulent velocity are also improved as the interaction between the flow turbulence and cavitation and turbulence generation due to the cloud collapse is captured.

Finally, the predictions of the ZGB and the SS cavitation models (two-phase models) is compared to the barotropic model, and the ZGB model is modified by increasing the mass transfer rate to push the model towards thermodynamic equilibrium. All the models predict a similar cavitation pattern and length, while the barotropic model predicts slightly smaller amount of vapour, which is attributed to the full compressibility of the phases and the higher mass transfer rate in the barotropic model. Moreover, it is observed that the by increasing the mass transfer rate, the two-phase model results approach to the barotropic model predictions and the liquid/vapour interface becomes less diffusive due faster separation of the variables in the mixture region. However, increasing the mass transfer rate of two-phase models comes at the cost of solver stability and it can cause numerical issues for test cases with complex flows.

In conclusion, the situational applicability of the RANS models in predicting cavitation is demonstrated; while they are able to predict the more stable cavitation regions (film cavity or attached cloud), they fail at predicting the highly transient regions (bubbly clouds, microcavities and the shedding process). Furthermore, it is demonstrated that by increasing the mass transfer rate in the two-phase models, the results can be improved by approaching the thermodynamic equilibrium (barotropic model). LES simulations are capable of capturing the transient inception and shedding of the cavity cloud.

## 5.Cavitation in Viscoelastic Fluids

---

In the previous chapter, the accurate numerical framework for modelling cavitating nozzle flows is presented and various turbulence and cavitation models are tested while their performance is validated against experimental data. As mentioned in the introduction, the main purpose of this study is to examine the effect of viscoelasticity on flow and cavitation, in an attempt to explain the flow enhancement mechanism in additised fuels. In this chapter, initially the step nozzle test case is examined to understand the interaction between cavitation and viscoelasticity. In the step nozzle conditions, only cloud cavitation is forming, however in fuel injectors both cloud and string type cavitation vapours can appear. Therefore, in the final section of this study, the effect of viscoelastic additives on the flow inside a real size diesel injector operating at realistic pressure conditions is investigated.

### 5.1. Step Nozzle

As discussed earlier, certain fuel additives are capable of enhancing the flowrate through injectors while suppressing the amount of cavitation vapour forming inside the injector nozzles. However, the experimental evidence only show the effect of these additives on the flow and lack providing an explanation for the flow enhancement and cavitation suppression mechanism, especially since the bulk fuel properties remain unchanged in the base fuel and additised fuels. Initially it was postulated that additives act by changing the fuel viscosity, hence a pilot study is performed to understand the effect of fluid viscosity on the cavitating

nozzle flow. Taking into consideration further evidence regarding the viscoelastic properties of the additised fuels, the main focus of this section is later on demonstrating the interaction between viscoelasticity, turbulence and cavitation.

### 5.1.1. Effect of fluid viscosity

In this preliminary study, the effect of fluid viscosity on the flowfield and cavitation is investigated to determine whether flow enhancement and cavitation suppression can be achieved by additives that only modify the fluid viscosity. In four separate test cases, the viscosity of the base fluid is reduced by a factor of 0.5 and 0.25 and increased by a factor of 2 and 4. Increasing the fluid viscosity is expected to increase the viscous drag but also it can reduce secondary flows, therefore, it is expected to result in a smaller flow-recirculation and less cavitation. The aim is to verify if suppression of the secondary flows and cavitation can overcome the increased viscous drag and result in overall flow enhancement using LES simulations and the Schnerr-Sauer cavitation model.

The time-averaged data for the streamwise velocity and the liquid volume fraction are presented in Figure 5-1, the region inside the black iso-line shows the areas with velocities exceeding 18 m/s. It is evident that as the viscosity of the fluid is increased, the area of high velocity jet is reduced and the negative velocity region (blue colour), becomes shorter. As mentioned earlier in chapter 4, the cavitating microvortices form in the shear layer between the high velocity jet and the low velocity flow in the flow-recirculation region. Therefore, as the velocity and the size of the jet and the recirculating flow are reduced in the high viscosity fluids, the size of the cavitation cloud is also reduced as shown in the liquid volume fraction contours in Figure 5-1.

The mass flowrate through the nozzle is affected by both the cavitation and the viscous drag; while fluids with lower viscosity experience less viscous drag, at the same time they form a larger vapour cloud, which blocks the main flow passing through the nozzle. The mass flowrate of the standard viscosity fluid and the x0.5 viscosity fluid are the same, whereas the mass flowrate of the x0.25 viscosity test case is increased by ~1%. Furthermore, the x2 viscosity and x4 viscosity test cases have ~1% and ~3.5% smaller mass flowrates than the standard test case respectively. The results presented here, indicate that although by increasing the fluid viscosity it is possible to partially suppress the cavitation, the higher viscous drag force outweighs the cavitation suppression effect and overall, the mass flowrate is reduced.

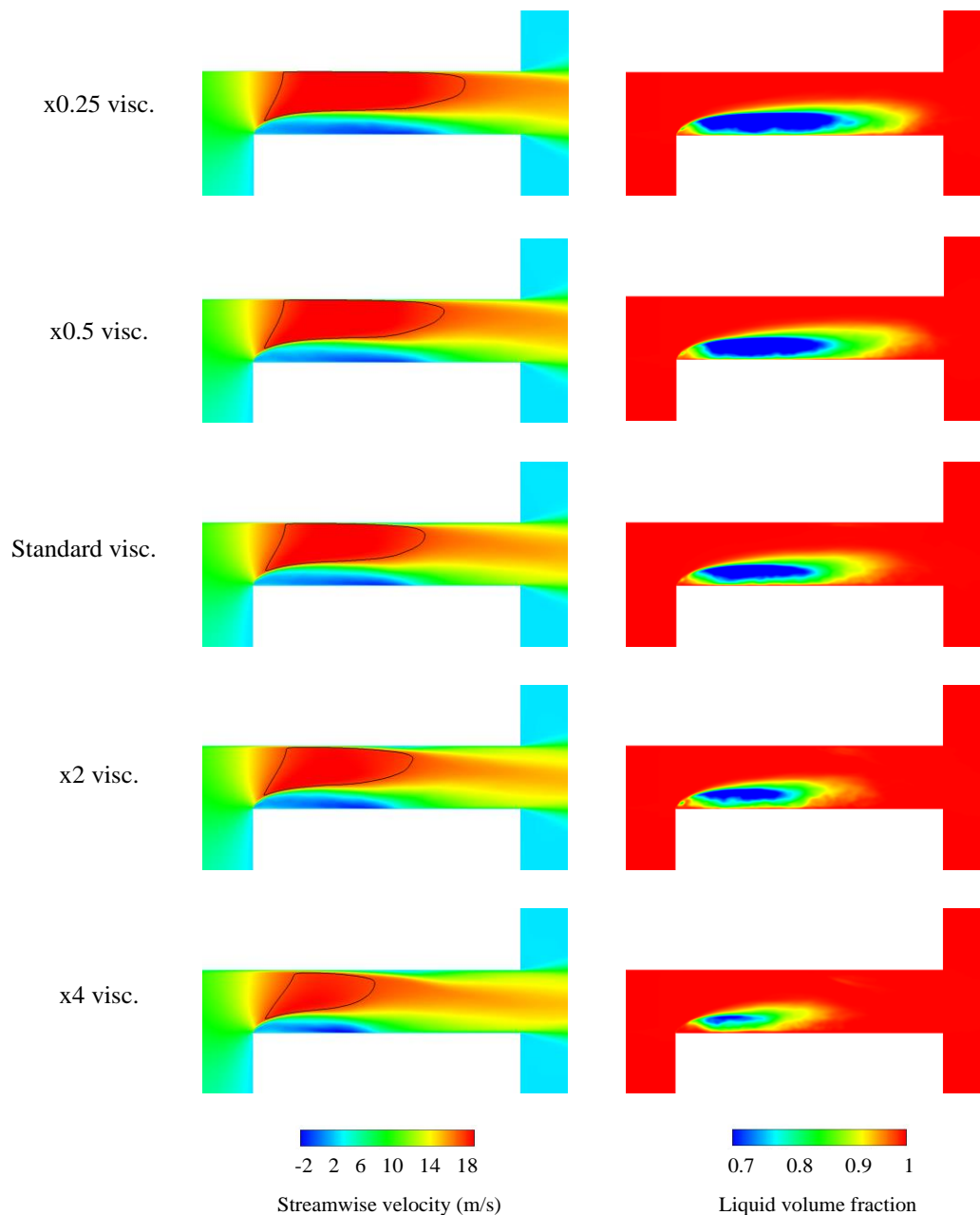


Figure 5-1. Contours of time-averaged velocity (left) and liquid volume fraction (right) in the midplane, data presented for the standard viscosity fluid, reduced viscosity fluids (by factors of  $x0.25$  and  $x0.5$ ) and increased viscosity fluids (by factors  $x2$  and  $x4$ ), the black iso-lines indicate regions with velocities higher than 18 m/s

### 5.1.2. Effect of viscoelasticity on flow and cavitation

In this section, the effect of viscoelasticity on flow, turbulence, cavitation and time-averaged flow statistics in the step nozzle is reported.. Contours of velocity magnitude in the mid-plane of the nozzle for the Newtonian fluid and the viscoelastic fluid are presented in Figure 5-2. It is evident that the flowfield in the viscoelastic fluid appears to have a more homogenous gradient. The black iso-lines show the areas where pressure drops below the vapour pressure, i.e. the regions of cavitation inception. The cavitation inception regions appear more frequently

in the Newtonian fluid, indicating that more vapour is being produced in this fluid. It is reported in the literature that the minimum pressure at a cavitation inception point (the core of a vortex developing in the wake of a cylinder) increases as vorticity is reduced due to viscoelasticity (Richter, Iaccarino, & Shaqfeh, 2012).

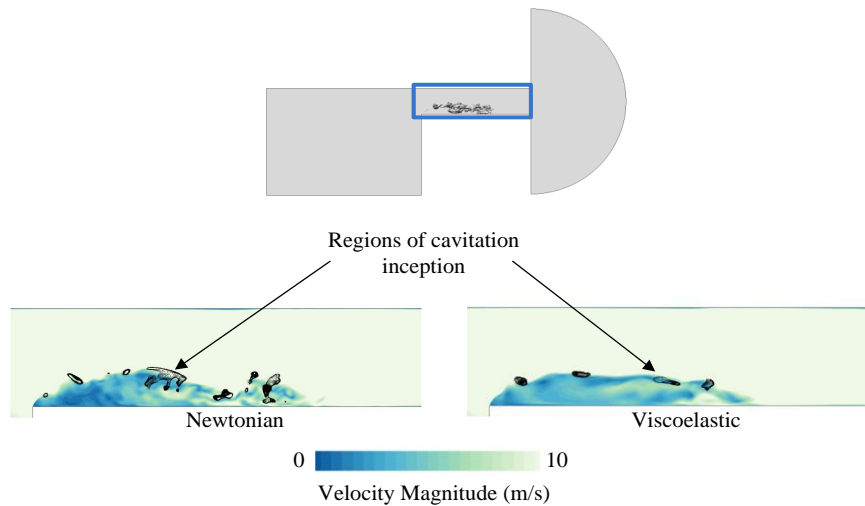


Figure 5-2. Nozzle geometry and cavitation in the shear layer (top), contours of the velocity magnitude for the Newtonian and the viscoelastic fluid in the mid-plane of the nozzle, the black iso-lines show regions with pressures below the vapour pressure (bottom)

The structure of the vortical features in the flow is shown in Figure 5-3 by means of the second invariant of the velocity gradient tensor (Haller, 2005) calculated from  $II_a = -\frac{1}{2} \frac{\partial U_i}{x_j} \frac{\partial U_j}{x_i}$ . Spanwise Kelvin-Helmholtz-like vortices form downstream the nozzle inlet as shown in Figure 5-3 (a), it can be clearly seen that significantly fewer vortices appear in the viscoelastic fluid. Inhibition of shear instability by polymer injection has previously been reported in the literature (Cadot & Lebey, 1999). The ‘polymer torque’, which is the contribution of the viscoelastic stress to vorticity evolution, increases the flow resistance to rotational motion and can inhibit the vortex sheet roll-up (Richter et al., 2012).

Further downstream, the vortex sheet breaks down, developing a range of small-scale and large-scale structures. It is evident that in the viscoelastic fluid, spanwise vortices are inhibited while longitudinal vortices become more dominant. Enhancement of large scale coherent structures in the mixing layer is due to hindering of development of perturbations and a stronger vorticity diffusion in viscoelastic fluids (Lin, Yu, & Shao, 2004). This results in slower rotational motion of the neighboring vortices and delay of vortex pairing and merging, therefore the lifetime and the scale of the coherent structures is increased.

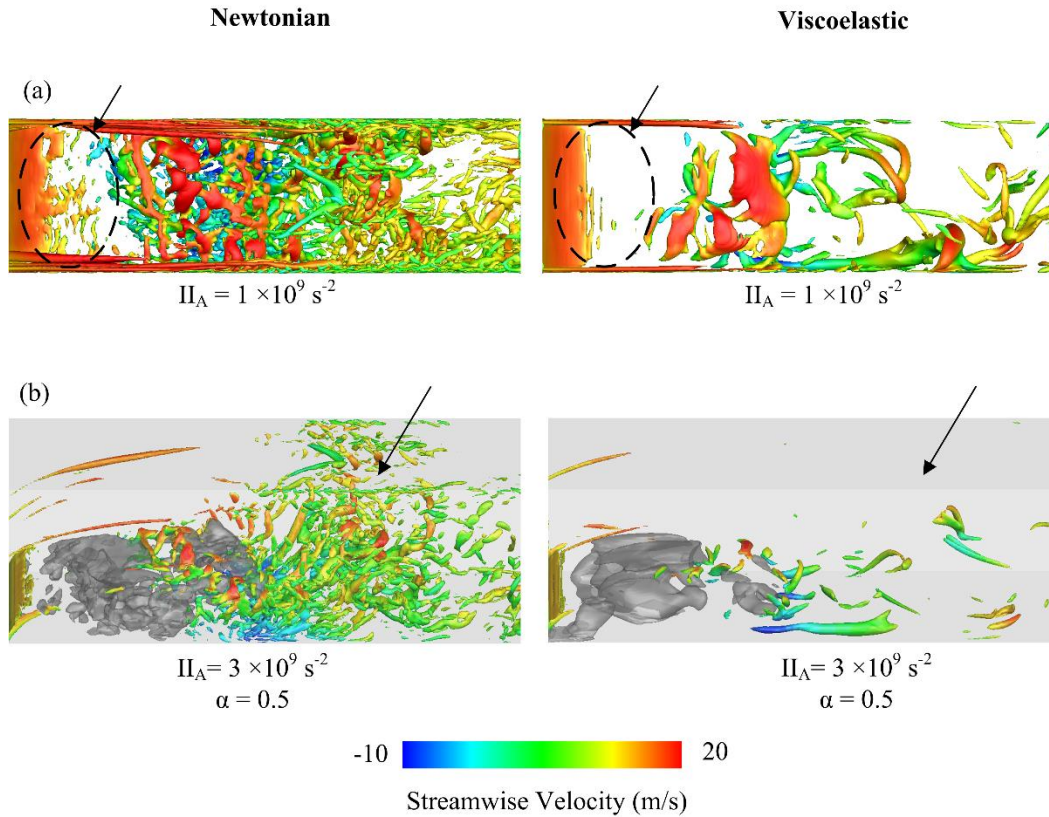


Figure 5-3. (a) Iso-surface of the second invariant of the velocity gradient with the value  $1 \times 10^9 \text{ s}^{-2}$  coloured with the streamwise velocity, (b) 3D view of the iso-surface of the second invariant of the velocity gradient at  $3 \times 10^9 \text{ s}^{-2}$  coloured with the streamwise velocity along with iso-surface of 50% vapour volume fraction (grey colour)

In Figure 5-3 (b) the iso-surface of 50% vapour volume fraction is presented along with the  $\Pi_A$  iso-surface. After the collapse of the cavity cloud in the Newtonian fluid, a strong mixing region forms inside the nozzle. In the viscoelastic fluid however, the mixing is weaker and mainly vortices with larger diameters are forming as local instabilities are suppressed and vortical sub-structures are damped. Likewise, enlargement of streamwise vortical structures and their elongation in the streamwise direction is reported in turbulent channel flows (Pereira et al., 2017). This is due to tendency of polymers to strongly align in the streamwise direction, partially suppressing wall-normal and spanwise velocity fluctuations (Pereira et al., 2017). Moreover, the polymer viscosity resists the extensional deformation imposed by the motion of turbulent eddies (Housiadas & Beris, 2005; Seyer & Metzner, 1969).

The time variation of the fluid density inside the nozzle is plotted in Figure 5-4 (a) presenting three cycles of cavitation formation and shedding. The fluid density in the Newtonian case is constantly below the viscoelastic fluid density, indicating a higher liquid fraction and hence cavitation suppression in the viscoelastic fluid. In Figure 5-3 it is demonstrated that the turbulent eddies observed in the Newtonian fluid are partly suppressed in the viscoelastic fluid,



therefore it is expected that vorticity levels would also be lower in the viscoelastic fluid. This data is presented in Figure 5-4 (b) which shows the magnitude of the streamwise vorticity inside the nozzle for the two fluids. Vorticity magnitude in the Newtonian fluid is higher in all locations inside the nozzle, which can also be seen in the contour plots (Figure 5-4 (c)), in fact streamwise vorticity magnitude is reduced by ~88% inside the whole nozzle for the viscoelastic fluid. Moreover, regions of peak vorticity corresponding to the vortex cores in Figure 5-4 (c), are in agreement with observations of Figure 5-3, showing that smaller eddies are suppressed by viscoelasticity and large scale vortices become more dominant. It is also noted that vorticity generation downstream of the recirculation region ( $x > 4$  mm) is strongly suppressed in the viscoelastic fluid.

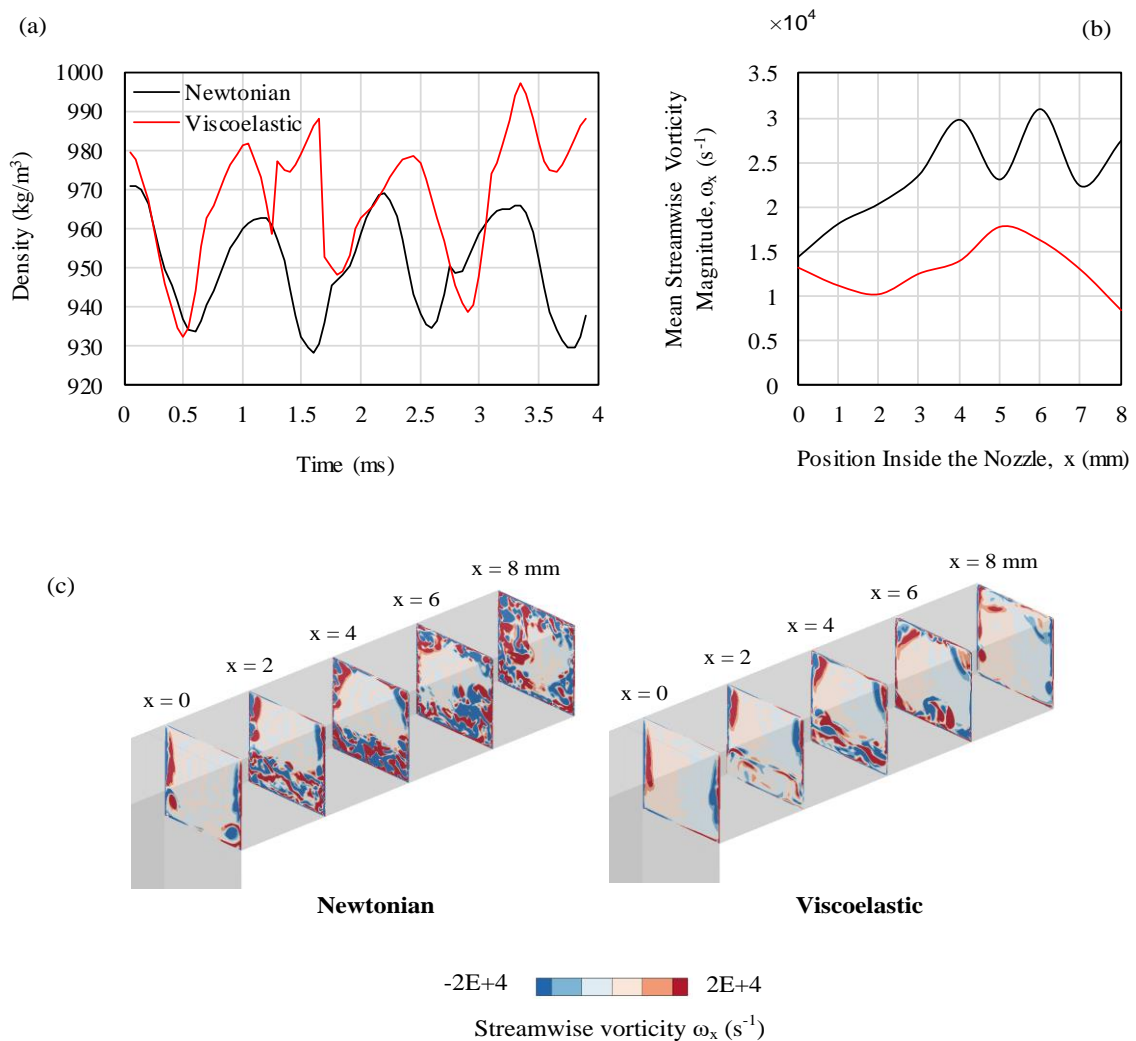
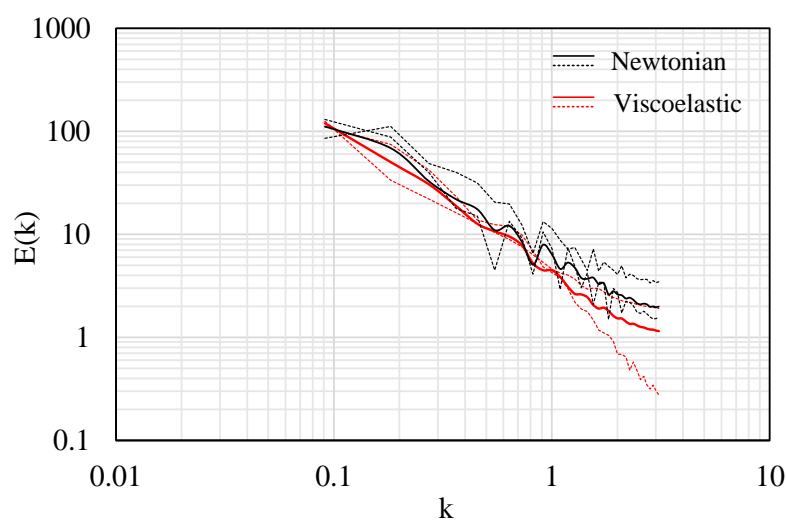


Figure 5-4. (a) Density variations inside the nozzle during three cavitation cycles, (b) magnitude of the streamwise vorticity, mean values are calculated in several planes along the nozzle length, (c) contour plots of streamwise vorticity inside the nozzle

The turbulence kinetic energy spectrum for the Newtonian and the viscoelastic fluid is shown in *Figure 5-5*, where  $k$  is the wave number and  $E(k)$  is the amplitude of the kinetic energy FFT calculated inside the nozzle. The graph represents the spatial spectrum of the turbulence kinetic energy, where  $k = 2\pi n/L$  and  $n$  and  $L$  are the incremental spatial frequency number and the wavelength respectively.

Energy content of the low wavenumber scales is higher by ~15% in the Newtonian fluid, however the decay slope is also slightly faster ( $-5/3$  in the Newtonian fluid in competition with  $\sim -4/3$  in the viscoelastic fluid) so the flow energy mainly contained within the inertial subrange eddies is similar in both cases.

At higher wavenumbers, the difference becomes more evident as the Newtonian fluid has ~38% higher turbulence kinetic energy content, indicating that the small-scales in this fluid are more pronounced. This observation is expected as the small-scales are suppressed in the viscoelastic fluid as seen in *Figure 5-3*. This is consistent with experimental measurements of power spectra in wall-bounded polymeric flows which show that viscoelasticity can suppress turbulence kinetic energy at small-scales while having a negligible effect on large scales (Xie et al., 2015). Moreover, in viscoelastic fluids, the kinetic energy removed from the large scales is partially dissipated by small-scales and partially converted into elastic energy, which is then transferred back into the large scales. This will alter the nature of energy cascade usually seen in Newtonian fluids and reduce the energy content at the small-scales (Valente et al., 2016).



*Figure 5-5. Energy spectra inside the step nozzle for the Newtonian and the viscoelastic fluid, dashed lines (..... and ..... ) show indicative examples of the spectra and continuous lines (— and —) show the mean value of the spectra for the Newtonian and viscoelastic fluid*

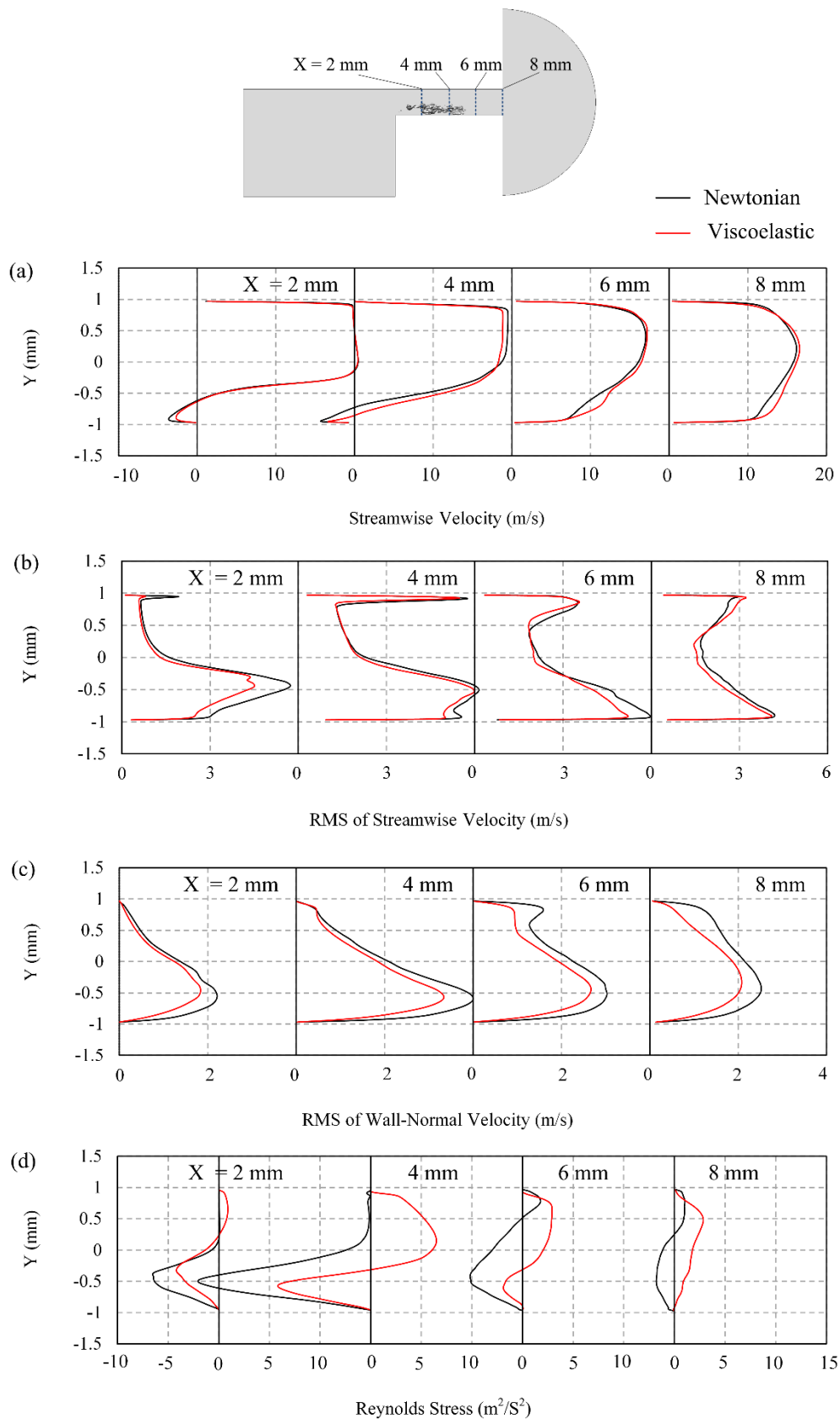


Figure 5-6. Comparison of time-averaged values of the streamwise velocity, RMS of streamwise velocity, RMS of wall-normal velocity and Reynolds stress ( $-\overline{u'v'}$ ) in the Newtonian and the viscoelastic fluid, data are presented in the mid-plane of the step nozzle at four different X locations along the nozzle

In *Figure 5-6 (a)*, development of the streamwise velocity component in the mid-plane of the nozzle presented. Magnitude of the negative velocity in the recirculation region ( $-0.94 \leq Y \leq -0.4$ ) is larger in the Newtonian fluid on average by  $\sim 28\%$  at  $X = 2\text{mm}$  and  $\sim 41\%$  at  $X = 4\text{mm}$ . The re-entrant jet velocity is responsible for detachment and shedding of the cavity cloud (Callenaere et al., 2001), therefore larger velocities in the recirculation region of the Newtonian fluid are indicative of a faster shedding process in this flow.

In *Figure 5-6 (b)*, the RMS of streamwise velocity which indicates the turbulent velocity, is plotted along the nozzle. Overall, RMS of streamwise velocity inside the nozzle ( $0\text{ mm} < X < 8\text{ mm}$ ) is reduced by 11% in the viscoelastic fluid. In *Figure 5-6 (b)*, this effect is mainly visible in the lower half of the nozzle ( $-0.94\text{ mm} \leq Y \leq 0\text{ mm}$ ), corresponding to the shear layer and flow-recirculation regions. The effect of viscoelasticity on velocity fluctuations is more evident in *Figure 5-6 (c)* which shows the RMS of wall-normal velocity along the nozzle. Suppression of velocity fluctuations is stronger in the wall-normal direction compared to the streamwise direction and overall the RMS of wall-normal velocity is reduced by 27.5% inside the nozzle for the viscoelastic fluid.

In *Figure 5-6 (d)*, Reynolds stress in the XY plane ( $-\overline{u'v'}$ ) is plotted along the nozzle, positive and negative values of the Reynolds stress correspond to turbulence suppression and production respectively (Soldati & Banerjee, 1998). Negative values of Reynolds stress are produced by ejection and sweep motions which contribute to positive turbulence production and in general increase drag. Positive Reynolds stress values correspond to turbulence suppression and their increase generally results in drag reduction (Soldati & Banerjee, 1998). It is evident that in the recirculation region ( $-0.94\text{ mm} \leq Y \leq 0\text{ mm}$ ) the Newtonian fluid has about twice the amount of Reynolds stress generated in the viscoelastic fluid, resulting in a higher level of turbulence produced in this region. In the bulk of the flow outside the recirculation zone, Reynold stresses have a positive value with a higher magnitude in the viscoelastic fluid indicating a stronger turbulence damping. Overall, stronger turbulence damping and lower turbulence levels generated in the viscoelastic fluid as seen in *Figure 5-6 (b)-(d)*, can contribute to turbulence drag reduction and the mass flowrate is increased by  $\sim 2\%$ .

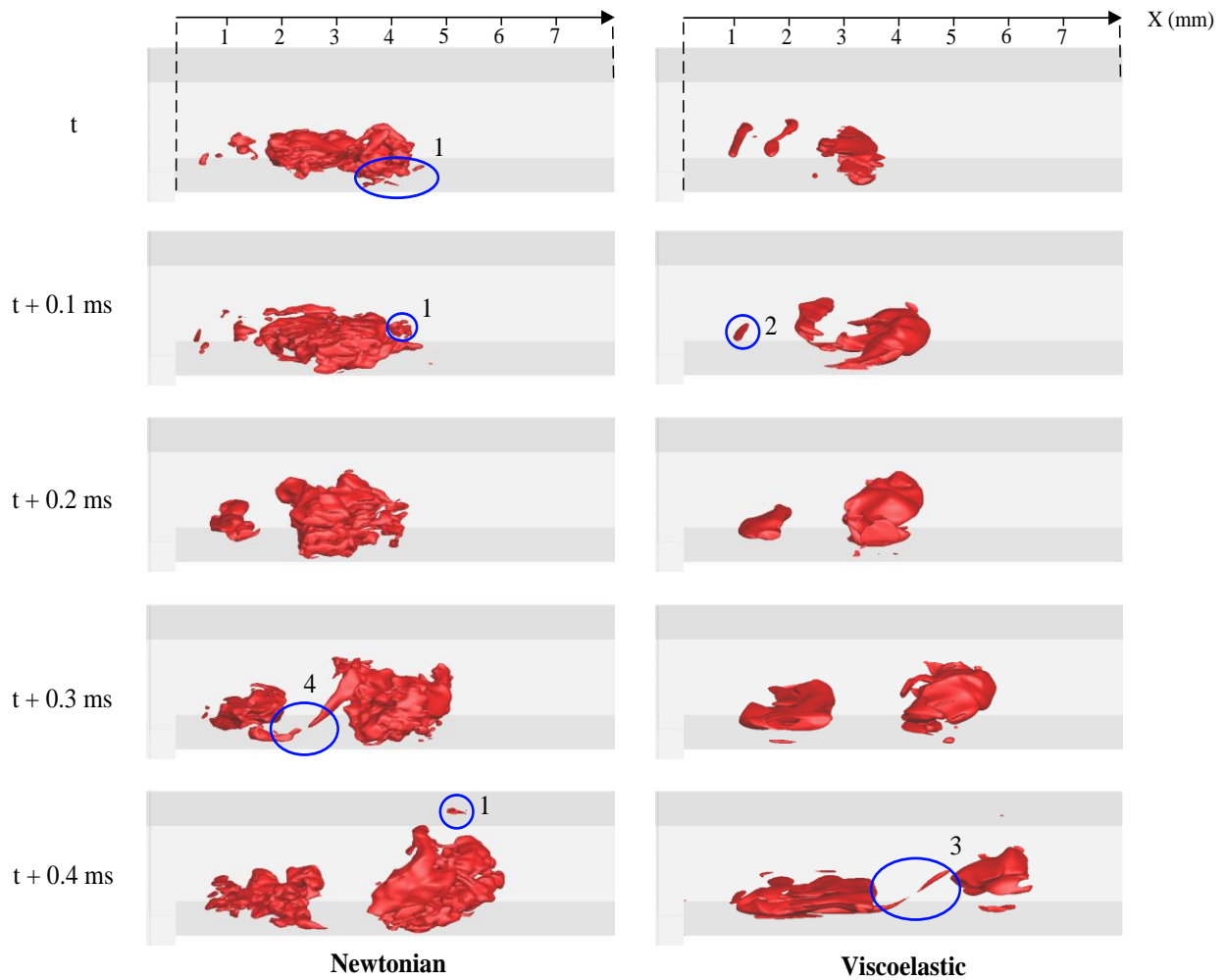


Figure 5-7. Cavitation development inside the step nozzle presented by means of iso-surfaces of 50 % vapour volume fraction, data are presented every 0.1 ms. Small microcavities shedding from the cloud (blue circle 1) are not present in the viscoelastic fluid, cavitation vapours can initially shrink before growing (red circle 2) and elongated streamwise vortices appear between the detached cloud and the cavitation cloud (red circle 3 and 4)

In Figure 5-7, development of cavitation inside the nozzle for the Newtonian and the viscoelastic fluid is compared in terms of 50% vapour volume fraction iso-surfaces. Cavitation is initiated in the core of microvortices forming in the shear layer and it grows as larger eddies form after the vortex sheet breakdown. Following, they form a cavity cloud that detaches due to the re-entrant jet motion and is convected toward the nozzle exit.

In the Newtonian fluid, small cavitation structures can be observed (blue circle 1) with microcavities of various sizes (approximate diameter range of 30  $\mu\text{m}$ -200  $\mu\text{m}$ ) shedding from the cloud, however such structures are not present in the viscoelastic fluid.

The growth of the shear layer cavitating microvortices is rather faster in the Newtonian fluid; in the viscoelastic fluid it appears that the cavity initially shrinks (blue circle 2) before growing. This can be due to the action of viscoelastic force resisting the fast deformation by liquid

evaporation. Furthermore, cavitation structures in the viscoelastic fluid become stretched and elongated streamwise cavitating vortices appear between the shear layer cavities and the detached cloud compared to the Newtonian fluid (see blue circles 3 and 4).

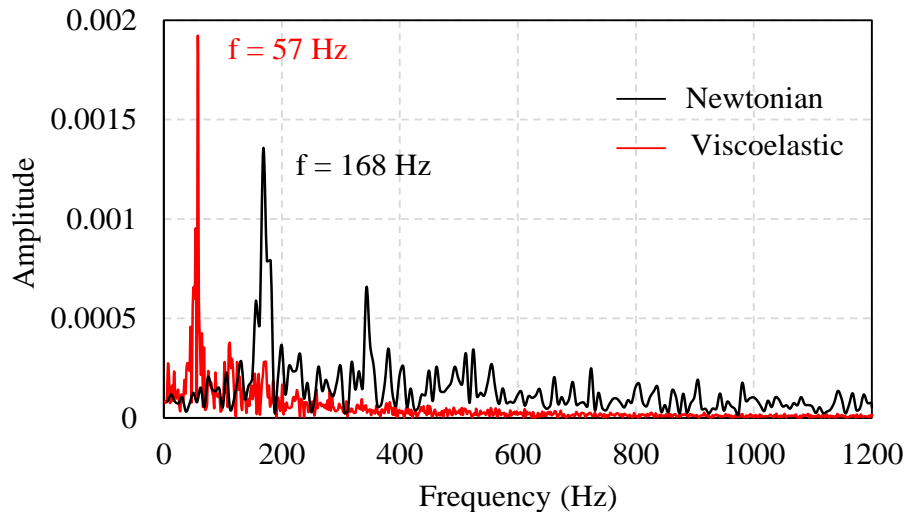


Figure 5-8. FFT of mass flowrate fluctuations at the outlet of the step nozzle for the Newtonian and the viscoelastic fluid, the dominant frequency corresponds to frequency of mass flowrate fluctuations induced by cyclic growth and shedding of large cavity clouds

Due to the cyclic enlargement and shrinkage of the flow recirculation zone and the subsequent detachment and shedding of the cavitation vapours, the mass flowrate in the nozzle also fluctuates in a cyclic manner. The FFT of mass flow rate time-evolution at nozzle outlet is presented in Figure 5-8 to indicate the dominant frequencies of the mass flowrate fluctuations. The dominant frequency in the Newtonian fluid is  $f = 168$  Hz whereas in the viscoelastic fluid this value is reduced to  $f = 57$  Hz, while the peak amplitude is increased by 42%. First and second harmonics of the dominant frequency can also be identified for both fluids at  $\sim 2f$  (343 Hz for the Newtonian fluid and 110 Hz for the viscoelastic fluid) and  $\sim 3f$  (524 Hz for the Newtonian fluid and 169 Hz for the viscoelastic fluid). Second harmonics with about double the dominant frequency are reported in pressure signals past a cavitating converging-diverging nozzle (Pelz et al., 2014) and in the wake of a rectangular cavitating obstacle (Hegedús, Hós, Pandula, & Kullmann, 2010).

The reduction of the cavity shedding frequency can be due to the resistance of the viscoelastic fluid to development of vortical structures and therefore suppression of cavity growth in the core of vortices. Moreover, development of the cavitation cloud can be delayed as the cavity volume can shrink before growing in the viscoelastic fluid due to memory effects produced by fluid elasticity. In fact, it is observed that some of the shedding events are completely

suppressed while vapour builds-up in the cloud region. Therefore, the subsequent shedding event is more violent in the viscoelastic fluid, so while the dominant frequency is reduced its peak amplitude is higher.

Unlike the Newtonian fluid, at frequencies above ~400Hz there are effectively no fluctuations in the viscoelastic fluid, indicating that the viscoelastic fluid damps out the high frequency fluctuations. As the small-scale microcavities shedding from the cavitation cloud are suppressed (Figure 5-7), the subsequent velocity fluctuations due to growth, collapse and oscillations of these cavities can also be inhibited, resulting in damping of high frequency fluctuations.

The Strouhal number for vapour cloud shedding ( $St_v$ ) based on the mass flowrate fluctuation frequency ( $f$ ), the cavity length ( $L_v$ ) and the average streamwise velocity in the cavity region ( $U_v$ ) is defined as:

$$St_v = \frac{fL_v}{U_v} \quad \text{Equation 5-1}$$

For the Newtonian case, the Strouhal number based on the dominant frequency is 0.22 and in the viscoelastic fluid, the Strouhal number is reduced to 0.08. For Newtonian fluids, a characteristic Strouhal number of 0.2 has been identified for cavitation cloud shedding in a diverging step (Callenaere et al., 2001). The detachment and shedding of the cavitation cloud is partially driven by the re-entrant jet mechanism and the Strouhal number is proportional to the re-entrant jet velocity (Callenaere et al., 2001), hence longer shedding periods can be due to reduction of the re-entrant jet velocity. Observations regarding the reduction of Strouhal number by viscoelasticity due to prolonged oscillation times has been reported for vortex shedding past an obstacle (B. K. Kim & Telionis, 1989; Norouzi, Varedi, & Zamani, 2016; Oliveira, 2001).

Shedding of cavitation clouds is closely related to the amount of erosion damage on solid surfaces. Cavitation erosion occurs due to the high local pressures building up during the collapse of bubble clusters; the severity of the erosion damage can vary depending on the frequency and size of the bubble clouds and the pressure peaks in a fuel injector nozzle can reach above 4000 bar (Koukouvinis, Gavaises, Li, & Wang, 2016). In order to compare the extent of predicted damage in the Newtonian fluid and the viscoelastic fluids, the highest

pressure in the flow domain in each cell is recorded and this value is updated every time step to obtain the maximum pressure during the simulation time. The regions of maximum pressure coincide with the cavitation erosion locations inside the nozzle (Koukouvinis, Gavaises, et al., 2016) and the relevant data for the Newtonian and the viscoelastic fluid are presented in Figure 5-9.

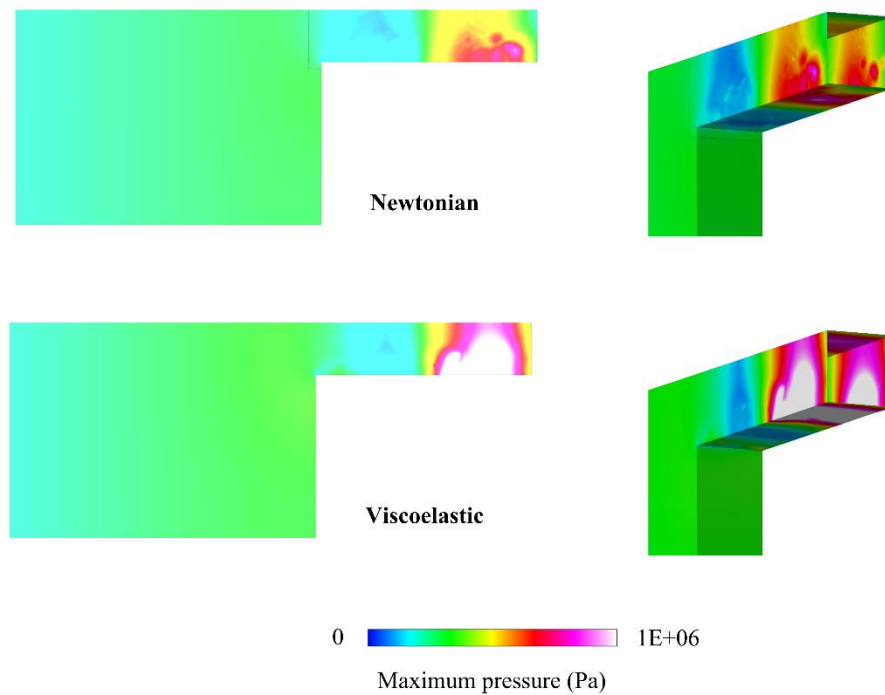


Figure 5-9. Maximum pressures recorded for the Newtonian (top row) and the viscoelastic fluid (bottom row), images show from the side view (left) and in a 3D view (right)

The result indicate that despite the fact that cavitation is reduced in the viscoelastic fluid, the collapse events have a higher impact compared to the maximum pressures recorded in the Newtonian fluid. This is because, as seen in Figure 5-8, although the shedding events in the viscoelastic fluid occur less frequently in the viscoelastic fluid, these events have a much higher amplitude compared to the Newtonian fluid. Therefore the cloud shedding is less frequent, but a larger bubble cloud detaches and collapses at each event, eventually resulting in a higher pressure accumulation. However, it must be noted that in real injector flows, the cloud shedding process is altered by the interaction between the cloud and string cavity, therefore the conclusion on higher erosion impact is only applicable to cloud cavitation regimes.

The time averaged pressure and vapour volume fraction data inside the nozzle are presented in Figure 5-10. Pressure in the cavitation cloud region ( $\sim 1 \text{ mm} < x < \sim 5 \text{ mm}$ ) is increased in the



viscoelastic fluid on average by  $\sim 3.5$  KPa. Moreover, the pressure drop across the nozzle is reduced in the viscoelastic fluid, which can be because of the reduction of form drag due to smaller size of the cavitation and recirculation region and reduction of the turbulent drag. The reduction of vapour volume fraction in the viscoelastic fluid is more pronounced, where the cavitation volume fraction inside the nozzle is decreased by  $\sim 50\%$ , indicating that more liquid is being delivered in the viscoelastic flow. Suppression of cavitation and reduction of turbulence level in the nozzle result in flow enhancement and so the mass flow rate is increased through the nozzle in the viscoelastic fluid.

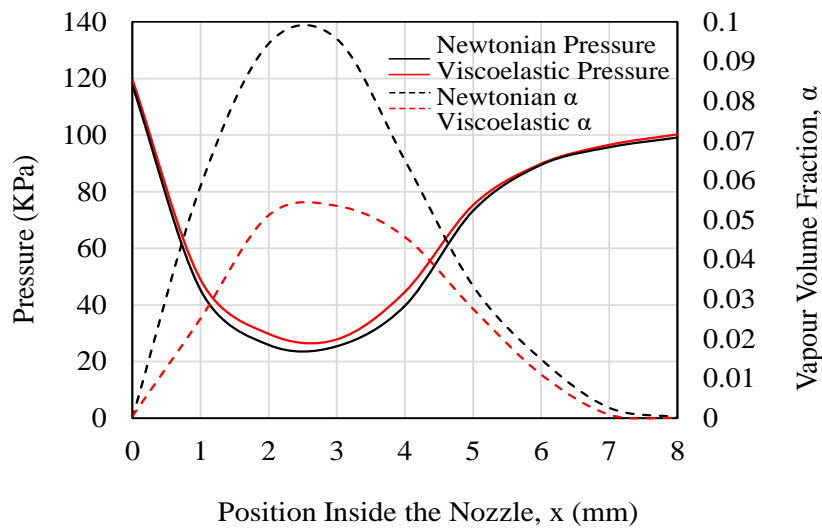


Figure 5-10. Time-averaged data for pressure and vapour volume fraction inside the nozzles

Finally, the time-averaged effect of viscoelasticity on the cavitation field is presented in Figure 5-11 by comparing the average liquid volume fraction inside the nozzle. It can be seen from Figure 5-11 (a) that the cavitation inception point is shifted further downstream the nozzle entrance; so vapour mainly starts to form at  $X \approx 0.3$  mm in the Newtonian fluid and at  $X \approx 0.8$  mm in the viscoelastic fluid. Moreover, the thickness of the cavity cloud in this region is reduced from  $\sim 0.69$  mm in the Newtonian fluid to  $\sim 0.58$  mm in the viscoelastic fluid ( $\sim 16\%$  reduction).

In Figure 5-11 (b) values of the liquid volume fraction in four locations inside the cavitation cloud are compared. In all these locations the liquid volume fraction in the viscoelastic fluid is constantly higher. The average vapour volume fraction in the viscoelastic fluid integrated over the volume of the nozzle ( $0 \text{ mm} < X < 8 \text{ mm}$ ) is reduced by 51%. Moreover it is evident that the cavitation suppression effect is stronger at the lower half of the cavity cloud  $-0.94 \text{ mm} \leq Y$

$\leq -0.5$  mm (closer to the nozzle wall). Reduction of near wall vorticity fluctuations inhibits the near-wall eddies in viscoelastic fluids (Sureskumar, Beris, & Handler, 1997) which can be responsible for production and transport of cavitation vapours in this region.

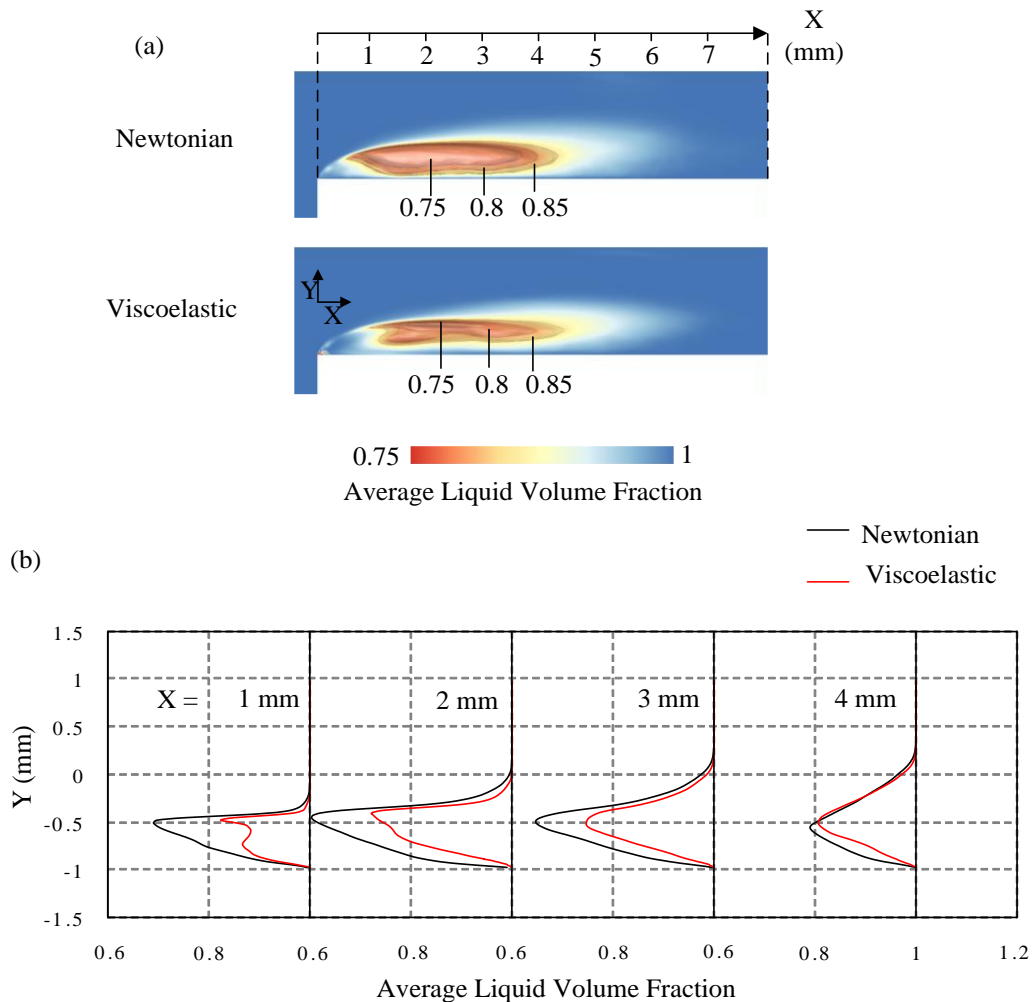


Figure 5-11. (a) Average liquid volume fraction ( $1-\alpha$ ) in the step nozzle mid-plane along with iso-surfaces of 75%, 80% and 85% average liquid volume fraction in the Newtonian and the viscoelastic fluid, (b) Average liquid volume fraction ( $1-\alpha$ ) inside the cavitation cloud for the Newtonian and the viscoelastic fluid, values taken along 4 lines passing through the cavitation cloud in the nozzle mid-plane

In Figure 5-12 the pressure spectrum inside the nozzle is compared for the Newtonian and the viscoelastic fluid. The graph represents the spatial spectrum of pressure and  $k$  is the wavenumber, where  $k = 2\pi n/L$  and  $n$  and  $L$  are the incremental spatial frequency number and the wavelength respectively. The low wavenumber region in the spectrum, corresponding to the large energy-containing eddies, has a higher pressure in the viscoelastic fluid. The vortices in this range are mainly located in the shear layer i.e. the cavitation inception region, and their higher pressure content results in less vapour formation in the viscoelastic fluid. However, the pressure levels for the high wavenumber range of the spectrum corresponding to the small scale

eddies, is reduced in the viscoelastic fluid as the small-scale flow structures are suppressed. After the breakdown of the vortex sheet, smaller eddies transfer the cavitation vapours towards the nozzle exit or back into the recirculation region. Hence, their suppression in the viscoelastic fluid may also result in less vapour being convected back into the recirculation region.

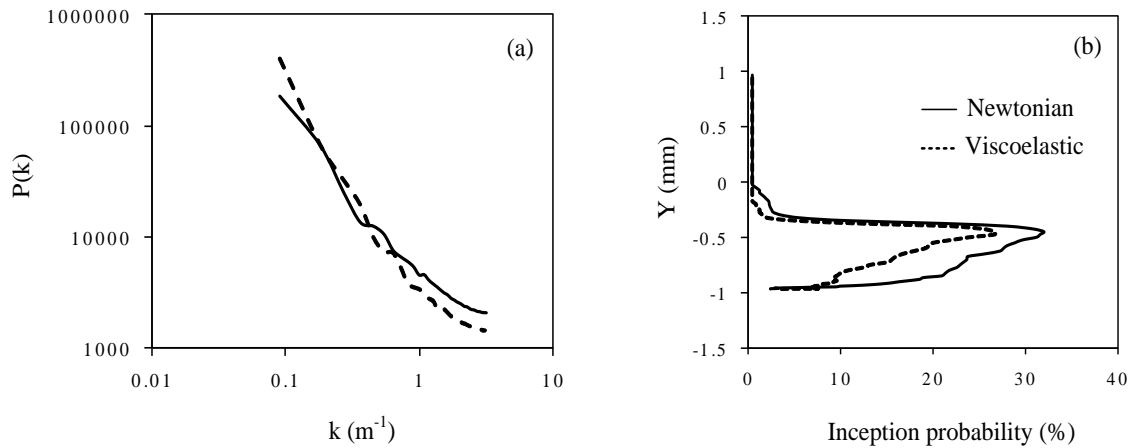


Figure 5-12. Pressure spectrum inside the nozzle for the Newtonian and the viscoelastic fluid showing the additive can either increase or decrease the local pressure, depending on the flow scale (a) Probability of cavitation inception at  $X = 2$  mm for the Newtonian and the viscoelastic fluid (b)

The probability of cavitation inception is approximately estimated from the spatial distribution of pressure and the vapour volume fraction (Ran & Katz, 1994):

$$\varphi_{inception} = \varphi(P < P_v)\varphi(\alpha > 0) \quad \text{Equation 5-2}$$

Figure 5-12(b) shows the probability of cavitation inception in the shear layer in  $X = 2$  mm, this figure indicates that viscoelasticity can inhibit cavitation formation across the a range of flow scales in the recirculation region. It shows that cavitation inception is more likely to happen at the location  $Y \approx -0.5$  mm i.e. in the core of the shear layer where mainly larger vortices appear while the probably of cavitation inception in smaller scale vortices ( $Y < -0.5$ ) is reduced.

## 5.2. Injector Nozzle

In this section, the effect of viscoelasticity on cavitation inside a realistic diesel injector geometry is investigated. In the injector nozzle, two distinct regions for cloud cavitation and string cavitation can be identified. The experimental studies presented in the introduction section, indicated that the effect of viscoelasticity on different cavitation regimes may not be consistent. This study aims to investigate the effect of viscoelastic additive on string cavitation and cloud cavitation in realistic injector conditions.

### 5.2.1. Cloud cavitation and string cavitation

Characteristics of different cavitation mechanisms in injector nozzles is described in the literature (Afzal, Arcoumanis, Gavaises, & Kampanis, 1999; Duke et al., 2014; Gavaises et al., 2009). The cloud cavitation forms in a similar manner to the cavitation in the step nozzle; as the fluid enters the nozzle it takes a sharp turn at the entrance forming a fully developed vapour cloud which is mainly attached to the top surface of the nozzle and can have a cyclic shedding. The string cavitation forms in the high vorticity core of a large vortex entering the nozzle from the sac volume and it is located in the vicinity of the nozzle centre (the streamlines and vectors forming the string cavitation are presented in Figure 5-13 (a)).

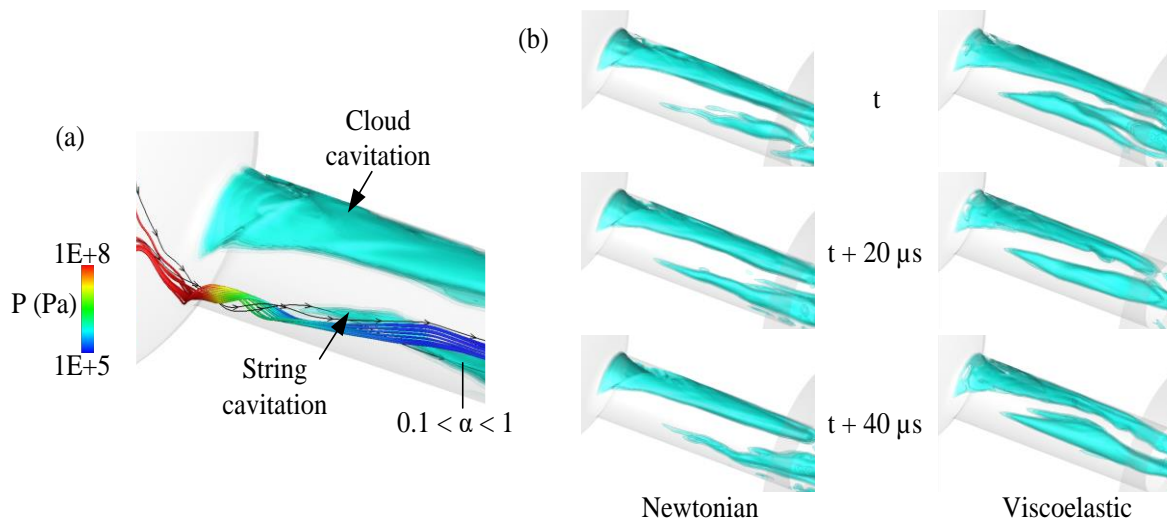


Figure 5-13. (a) Two distinct cavitation regions forming inside the injector nozzle, cavitation vapours are presented using 5 translucent vapour volume fraction iso-surfaces ranging from 0.1 to 1, cavitating vortex is presented by streamlines coloured with pressure, (b) Indicative cavitation structures inside the nozzle at 20  $\mu\text{s}$  intervals ( $0.1 < \alpha < 1$ ) showing a larger string cavity in the viscoelastic fluid.

Locally the pressure drops from 100 MPa in the sac volume to 0.1 MPa (below the saturation pressure) inside the nozzle as the string cavity starts to form. The string cavity has an intermittent appearance as it can distort, break-up and elongate inside the nozzle, however in the viscoelastic fluid a larger and more stable vaporous core appears and time averaged values of vapour volume fraction will be used to further investigate this matter.

Since the cloud cavitation and the string cavitation occur at different locations inside the nozzle, it is possible to examine the effect of viscoelasticity on each cavitation mechanism by geometrically separating the cavitation vapour regions as seen in Figure 5-14 (a), which shows the separated cloud and string cavitation structures in the same time step. The time-averaged vapour volume fraction data are separated into a cloud region and a string region by splitting

the cross section of the nozzle into a top section (cloud,  $Y > 35 \mu\text{m}$ ) and a bottom section (string,  $Y < 35 \mu\text{m}$ ) using a plane along the nozzle axis. The vapour volume fraction in the string and the cloud region is calculated in slices along the nozzle and the area weighted average value is used to get the total vapour volume fraction. Vapour structures in the cloud and the string region marginally intersect inside the nozzle, however near the nozzle exit, this overlap can contribute to up to  $\sim 20\%$  variations in the average vapour volume fraction in each region. The overlapping regions are identified to be located in the area approximately  $\pm 40 \mu\text{m}$  from the nozzle axis and are displayed in the graph as error bars.

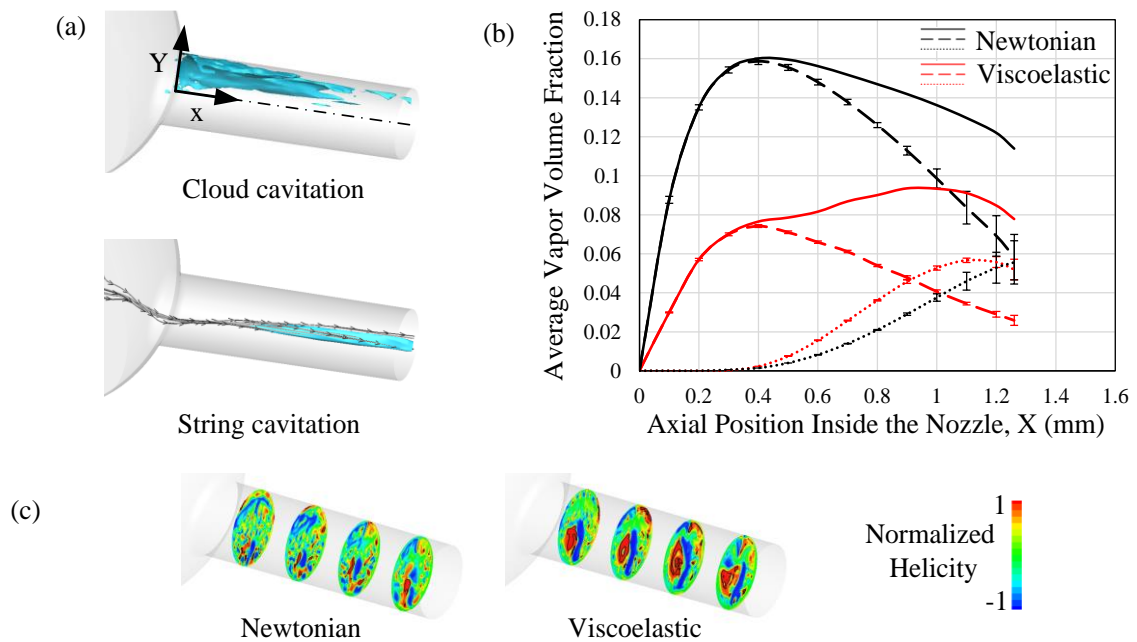


Figure 5-14. (a) Separated vapour volume fraction regions inside the injector nozzle showing the cloud cavitation and the string cavitation in term of iso-surfaces of 80% vapour volume fraction, (b) Development of the string cavitation (dotted lines ..... and .....), the cloud cavitation (dashed lines — — and — —) and the total vapour volume fraction (continuous lines — and —) inside the injector nozzle for the Newtonian and the viscoelastic fluid calculated in several slices along the nozzle axis using area weighted averages, error bars indicate the overlap of the vapour volume fraction in the string and cloud region in  $\pm 40 \mu\text{m}$  in the vicinity of the nozzle axis, (c) Normalized helicity ( $H_n$ ) contours in four slices inside the injector nozzle (at  $X = 0.2 \text{ mm}$ ,  $0.5 \text{ mm}$ ,  $0.8 \text{ mm}$  and  $1.1 \text{ mm}$ ), the black iso-lines show the regions of  $H_n = 0.95$  and  $H_n \rightarrow 1$  in vortex cores

The time-averaged value of the total vapour volume fraction inside the nozzle is plotted for the Newtonian and the viscoelastic fluid in Figure 5-14 (b). It is evident that the in-nozzle cavitation mechanism is mainly due to cloud cavitation in the Newtonian fluid and overall the vapour volume fraction in the Newtonian fluid is higher by 44%. Initially, cavitation develops at the nozzle entrance due to the cloud cavitation mechanism, increasing the vapour volume fraction in the nozzle up to  $\sim 0.16$  in the Newtonian fluid and up to  $\sim 0.08$  in the viscoelastic fluid until  $X \approx 0.4 \text{ mm}$ . After this point cloud cavitation declines and string cavitation starts to

develop while reaching the nozzle exit. In the viscoelastic fluid the vapour volume fraction of the cloud cavitation is higher than string cavitation up to  $X \approx 0.9$  mm (70% into the nozzle length), and after this location the string cavitation becomes more dominant. In the Newtonian fluid the rate of reduction of the cloud cavity is  $\sim 17\%$  faster than the rate of formation of string cavity, hence the total vapour volume fraction is reduced after  $X \approx 0.4$  mm. Whereas in the viscoelastic fluid, the string cavitation forms more abruptly at a rate  $\sim 46\%$  faster than the decline of the cloud cavity, hence the total vapour volume fraction increases steadily up to  $X \approx 1$  mm, after this point vapour volume fraction is reduced as the string cavitation growth declines.

The main observation from comparing the changes in the vapour volume fraction in different mechanisms is that, viscoelasticity reduces cavitation formation in the cloud cavitation region while increasing the string cavitation. This indicates that the strength of the cavitating vortex in the nozzle core is increased in the viscoelastic fluid, which can be related to the alignment of the cavitating vortex with respect to the main flow direction. The string cavitation is forming in the core of the quasi-streamwise vortex in the centre of the nozzle, whereas the cloud cavitation vortices can have large radial velocity components, which are expected to be inhibited by viscoelasticity.

In the core of vortices the angle between the velocity vector ( $U$ ) and the vorticity vector ( $\omega$ ) tends to zero as the vectors become aligned, hence the normalized helicity ( $H_n$ ), which is effectively the cosine of this angle, tends towards unity (Degani, Seginer, & Lecy, 1990):

$$H_n = \frac{U \cdot \omega}{|U||\omega|} \quad \text{Equation 5-3}$$

The normalized helicity contours are plotted in Figure 5-14(c) in several locations inside the nozzle along with black iso-lines of  $H_n = 0.95$ . It is evident that in the viscoelastic fluid, the string cavitation core covers a larger area, whereas in the Newtonian fluid a smaller vortex core can be identified. Likewise, in the step nozzle test case presented in the previous section, it is reported that the streamwise vortices become more dominant by viscoelasticity as the smaller scale vortices are damped. In wall-bounded viscoelastic flows (K. Kim, Adrian, Balachandar, & Sureshkumar, 2008; Tsukahara, Motozawa, Tsurumi, & Kawaguchi, 2013) it is reported that streamwise vortices can become elongated and larger as wall-normal fluctuations are damped. It is argued that suppression of cross-stream fluctuations can further inhibit their auto-

generation and therefore increase the lifetime and strength of the longitudinal vortices. Likewise in this case, suppression of small-scale eddies inside the injector nozzle can be responsible for stabilizing the local turbulence in the vicinity of the string cavity, allowing the development of a larger streamwise vortex and delaying the vortex breakdown, which in turn can result in higher amounts of vapour being produced in the vortex core.

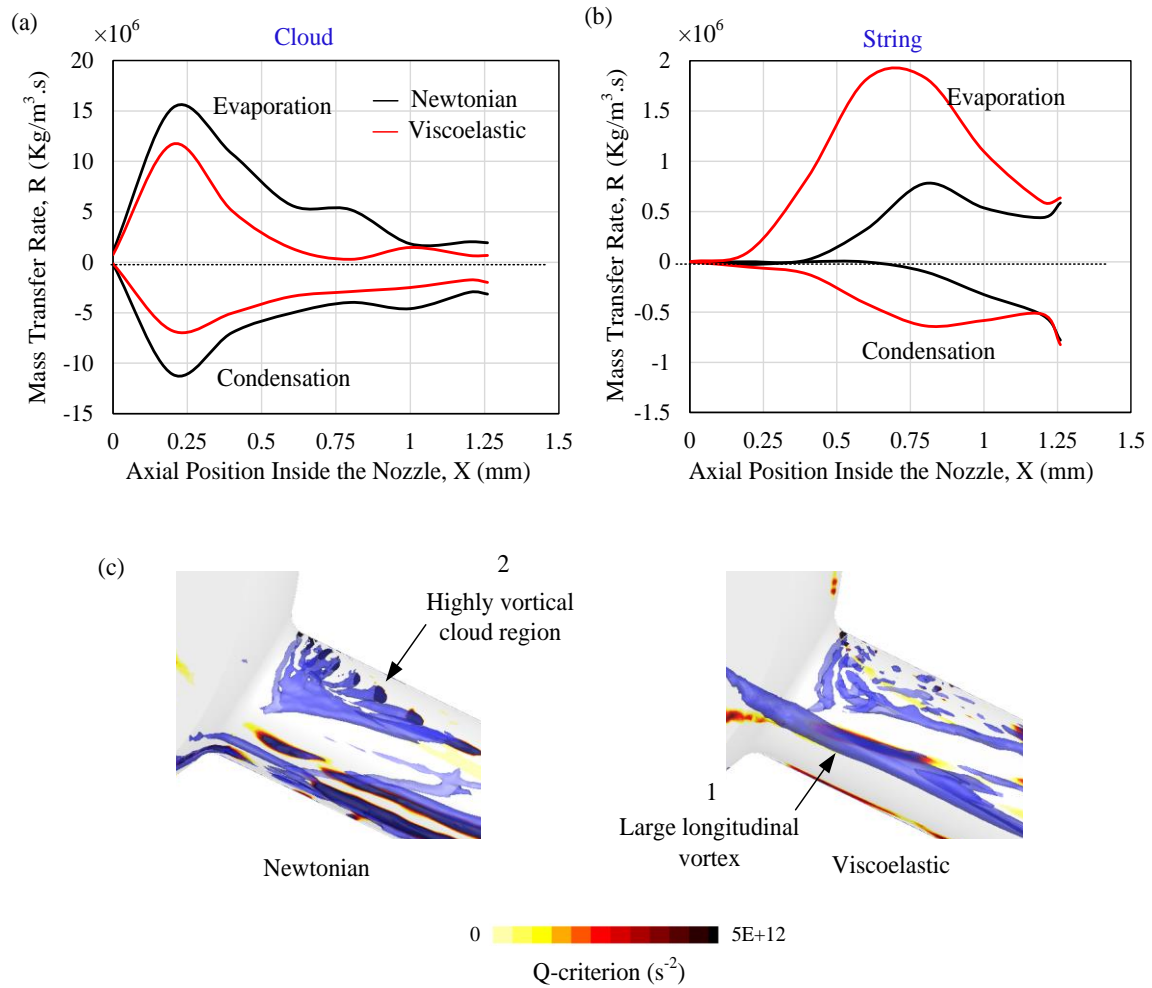


Figure 5-15. (a) and (b) evaporation and condensations rates computed by the mass transfer rate cavitation model in the cloud and the string cavitation region of the Newtonian and the viscoelastic fluid, (c) vortical flow structures in the vicinity of the injector nozzle entrance plotted using the contours of second invariant of the velocity gradient ( $Q$ -criterion) in the nozzle mid-plane and translucent iso-surfaces of  $Q$ -criterion at  $5E+12 \text{ s}^{-2}$

In the cavitation model of Schnerr and Sauer (Schnerr & Sauer, 2001), the vapour volume fraction equation source term describes the mass transfer rate ( $R$ ) between the two phases, so the positive values of  $R$  represent the evaporation rate and the negative values are the condensation rate:

$$R = \frac{\rho_v \rho_l}{\rho} \alpha (1 - \alpha) \frac{3}{\Re_B} \sqrt{\frac{2 |P - P_v|}{3 \rho_l}} \text{sign}(P - P_v) \quad \text{Equation 5-4}$$

In Figure 5-15 (a) and (b) the phase change rates in the cloud cavitation and the string cavitation region at an instance are compared. The mass transfer rates are higher in the cloud cavitation region, reaching  $15 \times 10^6 \text{ Kg/m}^3 \cdot \text{s}$  as opposed to  $0.5 \times 10^6 \text{ Kg/m}^3 \cdot \text{s}$  in the string region of the Newtonian fluid, subsequently cloud cavitation is the main mechanism of vapour production as seen in Figure 5-14 (b). In the cloud cavitation graph, mass transfer starts at the  $X = 0 \text{ mm}$  as the fluid enters the nozzle and peaks at  $X \approx 0.25 \text{ mm}$ , however the string cavitation starts effectively at  $X > 0.2 \text{ mm}$  in the viscoelastic fluid and  $X > 0.4 \text{ mm}$  in the Newtonian fluid. The evaporation and condensation rates in the cloud region are reduced in the viscoelastic fluid by about a half, resulting in reduction of the vapour volume fraction in this region. However, in the string cavitation region this trend is reversed, i.e. evaporation rate is  $\sim 9$  times higher and condensation rate is  $\sim 2.5$  times higher in the viscoelastic fluid.

The difference in the effect of viscoelasticity on cloud and string cavitation regimes can be linked to the alignment of the vortical structures in each region with respect to the direction of the main flow. The vortex cores identified in terms of the second invariant of the velocity gradient are presented in Figure 5-15 (c). It is evident that viscoelasticity does not affect the cloud and string vortical structures in the same manner. The vortex which forms the string cavitation in the vicinity of the nozzle centre (see arrow 1), is enlarged by viscoelasticity while the vortical structures formed at the nozzle entrance in the cloud region (see arrow 2) are strongly suppressed and only remnants of the vortices are visible in the viscoelastic fluid. In the cloud cavitation region, vortices form in the shear layer between the recirculating flow and the main flow, therefore they can have large radial velocity components as the vorticity vector is likely to be located in the cross-sectional plane of the nozzle (i.e. vortices rotating out of the cross sectional plane). However, in the string region the cavitating vortex is positioned in the streamwise direction (vorticity vector in the axial direction). Therefore, as the polymers tend to align with the main flow direction (Pereira et al., 2017) and suppress the cross flow fluctuations (Yu et al., 2004), viscoelasticity tends to damp the vortices in the cloud region while stimulating the string cavity vortex.

As mentioned earlier, the vortex forming the string cavitation enters the nozzle from the sac volume and is formed by the swirling flow inside the sac volume (Gavaises et al., 2009). Hence



the level of turbulence upstream the nozzle entrance, can have a significant effect on the strength of the cavitating vortex. In Figure 5-16 (a) the flow structures in the sac volume in terms of the second invariant of the velocity gradient are displayed. Circumferential perturbations on the interface of a cavitating vortex can cause strong radial oscillations which result in splitting and collapse of the cavity core (Choi, Hsaio, Chahine, & Ceccio, 2009). Moreover, flow instabilities upstream the vortex can cause the divergence of the stream tubes forming the vortex core, eventually breaking down the vortex (Hall, 1972). The turbulent eddies in the sac volume in the Newtonian fluid (Figure 5-16 (a)) appear to breakdown the coherence of the vortex entering the nozzle. Furthermore, fluid elasticity can suppress or delay the vortex breakdown as it prevents sharp velocity variations along the vortex centreline, which initiate the breakdown process (Stokes, W Graham, Lawson, & Boger, 2001).

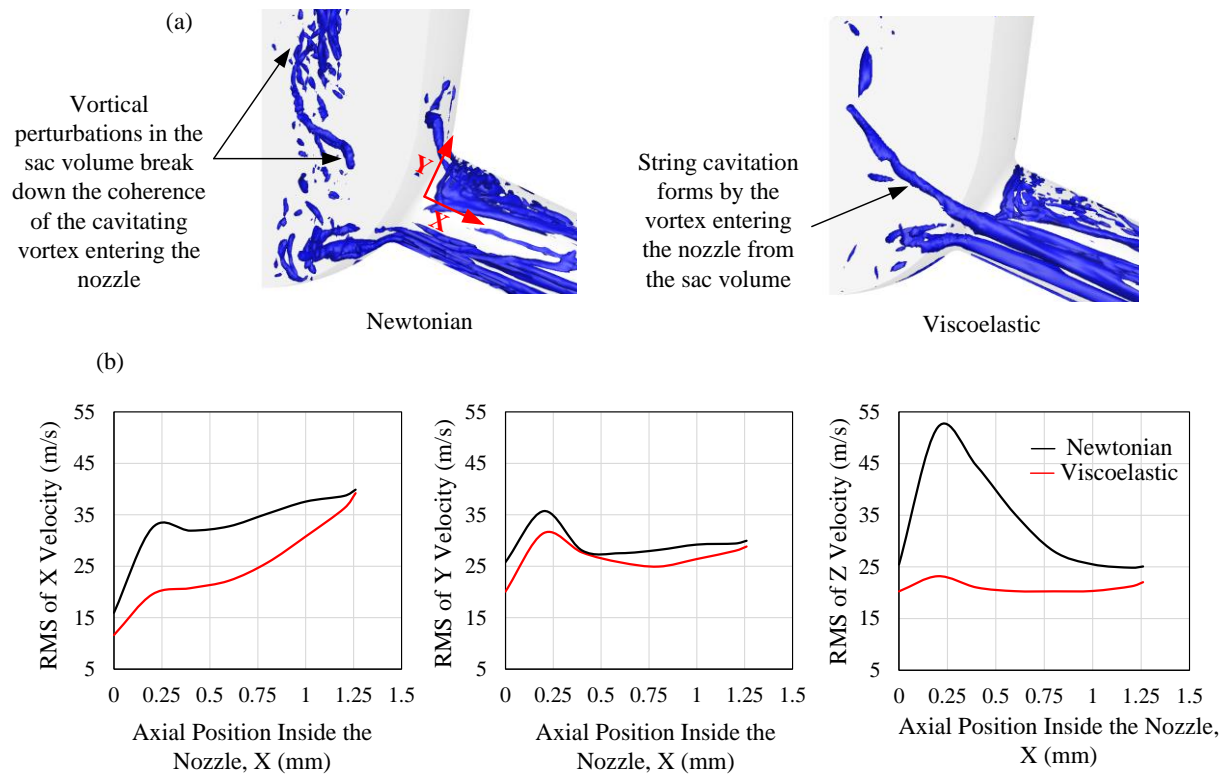


Figure 5-16. (a) Vortex structures inside the sac volume visualized using the iso-surface of second invariant of the velocity gradient at  $4E+12 \text{ s}^{-2}$ , (b) velocity fluctuations inside the nozzle plotted in terms of RMS of X, Y and Z velocities, values obtained from surface-averaged data calculated in slices along the nozzle

The vortex disturbance inside the sac volume is significantly lower in the viscoelastic fluid compared to the Newtonian fluid in Figure 5-16 (a) and the large vortex entering the nozzle can be clearly identified. Reduction of vortex interactions in the sac volume contributes to

stabilization of the cavitating vortex upstream of the nozzle entrance, which in turn allows a stronger string cavity to develop inside the nozzle. The fluctuations inside the nozzle in terms of RMS of the velocity components are plotted in Figure 5-16 (b). It is evident that due to the stabilizing effect of viscoelasticity on flow turbulence, all three components of velocity fluctuations are reduced in the viscoelastic fluid (by 23%, 9% and 31% in X, Y and Z directions respectively). This will therefore reduce the perturbations that destabilize the string cavity coherence inside the nozzle, allowing the cavitation structures to last longer.

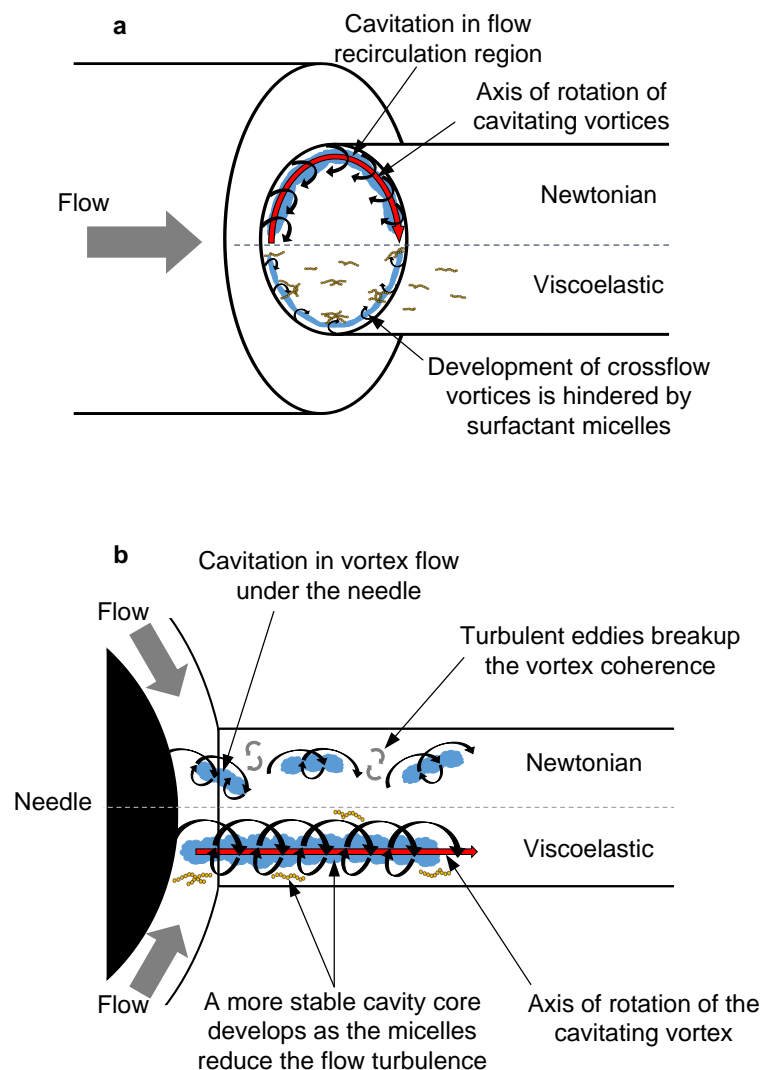


Figure 5-17. Schematic representation of the additive effect on the cavitating vortices, black arrows indicate the cavitating vortices and the red arrow shows the axis of rotation of the vortices, cavitation is presented by the blue clouds and the micelles are presented by yellow worms. (a) Cavitating vortices in the recirculation region in the Newtonian fluid (top) and the viscoelastic fluid (bottom), micelles align with the flow and suppress vortices rotating out of the nozzle cross sectional plane, (b) Vortex (string) cavitation under the needle in the Newtonian fluid (top) and the viscoelastic fluid (bottom), perturbations by the turbulent eddies can decay the string coherence and breakup the cavitating vortex, micelles can reduce the flow turbulence and contribute to development of a more stable longitudinal vortex and cavity core.

The effect of additive on the nozzle flow is discussed here using the schematic in *Figure 5-17*. Cavitation formation in the flow recirculation regions (such as cloud cavitation and the the X-ray micro-CT study), is inhibited by the additive as the micellar structures tend to align in the main flow direction and suppress the secondary flow. In the vortex cavitation region (such as injector flow and X-ray phase contrast imaging study), turbulent perturbations can breakdown the coherence of the streamwise vortex that forms under the needle, therefore reducing the lifetime of the cavity. As the vorticity vector in the cavitating vortex is positioned in the streamwise direction, turbulence suppression by the micelles can promote the formation of a more stable cavity core as indicated by XPCI results. However, in injector flow conditions, cloud cavitation is the main mode of vapour formation and hence the cavitation suppression effect becomes the dominant part of the interaction of the viscoelastic additive and cavitation. The combined effect of turbulence and cavitation suppression by the viscoelastic fuel composition in the injector can reduce the overall flow resistance and enhance the flowrate in the fuel injection system.

### **5.3. Chapter summary**

In this chapter, the effect of fluid viscosity and viscoelasticity on the flow and cavitation is investigated. The viscosity study aims to provide a proof of the concept that although cavitation can be suppressed by increasing a fluid's viscosity, high viscosity fluids cannot provide the flow rate enhancement effect observed in the additised fuels.

The effect of viscoelasticity on formation and development of cavitation inside a step nozzle and an injector nozzle is studied in PTT fluids using the Schnerr-Sauer cavitation model and the WALE turbulence model. In the step nozzle, incipient cloud cavitation is forming whereas in the injector the cavitation cloud is fully developed, while a string cavitation is forming in the core of the vortex originating from the sac volume.

In the step nozzle case, larger coherent structures become more dominant in the flow as the smaller eddies are suppressed due to flow resistance to rotational motion in the viscoelastic fluid. The dominant frequency of mass flowrate fluctuations is significantly reduced from 168 Hz in the Newtonian fluid to 57 Hz in the viscoelastic fluid and higher frequency (smaller amplitude) fluctuations are damped. However, the amplitude of the dominant fluctuations is increased by more than 40%. Reduction of the mass flowrate fluctuation frequency in the viscoelastic fluid, results in larger clouds forming in each cycle. Therefore, while the cloud

shedding is less frequent in the viscoelastic fluid, it has a higher impact in each cycle. Consequently, the cavitation erosion risk, indicated by pressure peak locations on the nozzle walls, is higher in the viscoelastic fluid.

Moreover, fewer cavitating microvortices appear in the viscoelastic fluid and the cavitation cloud structures are altered by viscoelasticity as large-scale cavitating vortices appear stretched and enlarged compared to the Newtonian fluid. Time-averaged statistics show that the vapour volume fraction is reduced by more than 50% in the viscoelastic fluid and the cavitation cloud is pushed away from the nozzle wall, while the cloud thickness is reduced by more than 15%.

In the injector test case, the total vapour volume fraction is reduced in the viscoelastic fluid by more than 40%, however there are significant differences in the effect of viscoelasticity on the cloud cavitation and the string cavitation mechanisms. In the cloud cavitation region, viscoelasticity reduces the vapour volume fraction, whereas in the string cavitation region, vapour volume fraction is enhanced. String cavitation forms in the core of the quasi-streamwise vortex inside the nozzle and it is prone to breakdown by velocity fluctuations upstream of the nozzle and inside the nozzle. The cavitating vortex becomes more stable as viscoelasticity stimulates the longitudinal vortices while suppressing the cross-stream fluctuations inside the nozzle and reducing the vortical perturbations in the sac volume. However as vortices in the cloud region rotate out of the cross-sectional plane (vorticity vector positioned in the cross-flow direction), they are damped by viscoelasticity, resulting in cavitation suppression. In injector flow, the main mechanism of vapour production is the cloud cavitation, therefore overall, addition of the viscoelastic additive to the injector results in cavitation suppression.

## 6. Conclusions and Future Work

---

This study presents for the first time numerical simulations to examine the effect of viscoelasticity on turbulent cavitating flows. The interaction between deposit control additives containing quaternary ammonium salts with in-nozzle cavitation is investigated in order to explain the flow enhancement and cavitation suppression effects in additised fuels.

A numerical framework is developed to model the dynamic network of surfactant microstructures based on the Phan-Thien-Tanner viscoelastic model. The validity of the model is tested against the analytical solution for channel flow and experimental data for corner vortex development in a contraction flow. Cavitation in viscoelastic fluids is investigated in a step nozzle in incipient cavitation condition and a fuel injector with string and cloud cavity structures, using WALE LES turbulence model and Schnerr-Sauer cavitation model.

The flow physics in Newtonian and viscoelastic fluids is analysed using instantaneous and statistical data to provide new insight about cavitation inception and development, cavitation vapour structures and cavitation cloud shedding dynamics. Viscoelasticity has a suppressive effect on cloud cavitation, while it can improve the string cavitation development; a finding that has also been observed in X-ray micro-CT and XPCI studies. Microcavities shedding from the cavitation cloud are suppressed, while larger streamwise vapours become more dominant. FFT analysis of temporal evolution of mass flowrate shows that the frequency of the cloud shedding is reduced in the viscoelastic fluid, while larger vapour clouds collapse in each cycle.

The collapse impact and erosion risk is increased in incipient cavitation condition when the cloud collapses inside the nozzle. Overall, the results show that viscoelastic additives reduce the flow resistance due to intense mixing, flow turbulence and cavitation.

The findings of the numerical study are in line with the experimental measurements of the additive effect on fuel injection systems. The simulations show that viscoelasticity can suppress the pressure losses across the injection nozzle and enhance the mass flowrate. Lubrizol uses the conclusions regarding the rheology effects on flow dynamics for development of new deposit control additives to enhance the engine power and the volumetric efficiency of the fuel injection system. Follow-up experiments and simulations are being carried out in the author's research group to quantify the link between the additive and cavitation erosion.

The numerical framework for cavitation modelling is assessed by comparing the performance of different turbulence and cavitation models in modelling the in-nozzle flow in a wide range of test cases and cavitation regimes. More-specifically,  $k-\epsilon$  RNG, realizable  $k-\epsilon$ ,  $k-\omega$  SST, RSM RANS models and WALE LES model in combination with mass transfer rate and the homogeneous equilibrium cavitation models is examined. The Reboud *et al.* eddy viscosity correction is utilized to compensate the effect of mixture compressibility to develop stronger shear flow in the two-phase region. Performance of the  $k-\omega$  SST model with the Reboud *et al.* modification is validated against X-ray CT measurements of liquid fraction in film cavitation regime. The LES model can predict the cavitation cloud inception and shedding, where the RANS models fail, and the turbulent flow field is validated against the LDV measurements for in-nozzle flow. The ZGB and SS mass transfer rate models, which are based on the Rayleigh–Plesset equation for bubble dynamics, are compared to the HEM model. The barotropic model uses the Wallis speed of sound formula, the isentropic gas EoS for the vapour phase and the Tait EoS for the liquid phase. The barotropic model and two-phase models with higher mass transfer rates predict a faster separation of flow variables and therefore, a sharper interface.

## 6.1. Future work

This study shows that viscoelasticity can reduce the vapour volume fraction in cavitating flows and suppress the near-wall cavitation. It is possible to make use of this property of viscoelastic fluids to design additives for various applications. For example, bubbles can appear in lubricating oils used in confined gaps of rotating machinery such as bearings and gear pumps. Cavitation can have a negative impact on the performance of rotating machinery by reducing

the lubricant oil thickness and disrupting the fluid flow. Viscoelastic additives can be used in these oils to delay the onset of cavitation inception, which in turn can enhance their performance and may protect the equipment from erosion damage.

A related application for viscoelastic additives in two-phase flows can be suggested in mixing tanks and fermentation tanks. The turbulent drag reduction property of the additive can reduce the stirring power requirements and cavitation suppression can offer protection for the impellers while allowing a higher rate of gas release.

Cavitation in aviation fuel pumps and fuel injection systems can have a detrimental effect on their performance and the cavitation suppressing property of viscoelastic additives can be advantageous in this application. Moreover, mist formation in fuel storage tanks poses a fire safety hazard and in fact, a body of literature exists that propose the usage of viscoelastic additives as anti-misting agents.

While viscoelasticity can suppress cavitation formation, it is shown that when the bubble cloud collapses inside the nozzle, it can have a higher impact and increase the material loss. This property can be beneficial in devices that employ cavitation for cleaning or cutting of surfaces. Therefore, an area for further research is to investigate the effectiveness of viscoelastic additives to increase the erosion in liquid jets and cutting tools for applications such as cleaning of biofouling for ships and underwater heat exchangers.

Moreover, cavitation reactors employ the bubble collapse energy to enhance the rate of physical and chemical processes, for example for preparation of emulsions and in industrial food processors. Viscoelastic additives can be useful in these applications as the higher cavitation collapse impacts can improve the process rates.

Finally, the focus of this thesis is on the effect of viscoelastic additives on fuel injection systems. Indeed, this is a novel research direction for development of new additive chemistries. By using the combination of CFD and rheology, smart surfactant additives can be developed for fuels and alternative fuels, which can lead to more efficient fuel delivery and consumption.





# Appendix A

---

## Implementation of Phan-Thien-Tanner Viscoelastic Model in FLUENT Through User Defined Functions

The implementation of  $\tau_{v11}$  is describe here as the procedure is similar for the other 5 scalars.

Note that in FLUENT the general form of the scalar transport equations is:

$$\frac{\partial \rho \phi_k}{\partial t} + \frac{\partial}{\partial x_i} \left( \rho u_i \phi_k - k \frac{\partial \phi_k}{\partial x_i} \right) = S_\phi \quad \text{Equation 0-1}$$

where  $\phi_k$  is the scalar,  $k$  is the diffusion coefficient and  $S_\phi$  is the scalar source term. As the fluid density is included in this transport equation, all the viscoelastic stress source term components in Equation 3-51 should also be multiplied by the fluid density. Therefore, the source term for first scalar  $\tau_{v11}$  is defined as (see Equation 3-51):

*source term for  $\tau_{v11}$*

$$\begin{aligned} &= \rho \left[ \left( \frac{2\mu_p}{\lambda} \frac{\partial u}{\partial x} \right) + \left( 2\tau_{v11} \frac{\partial u}{\partial x} \right) + \left( 2\tau_{v12} \frac{\partial u}{\partial y} \right) \right. \\ &\quad \left. + \left( 2\tau_{v13} \frac{\partial u}{\partial z} \right) - \left( f(\text{tr}(\tau_v)) \frac{\tau_{v11}}{\lambda} \right) \right] \end{aligned} \quad \text{Equation 0-2}$$

The implementation is demonstrated using the DEFINE\_SOURCE(t11\_source, c, t, dS, eqn)code below for defining the first scalar source term. The number of required UDSs is specified after declaring the headers and constants (6 for 3D simulations and 3 for 2D):

```
/******stress tensor components******/
```

```
enum
```

```
{
```

```

uds_t11,

uds_t12,

uds_t13,

uds_t22,

uds_t23,

uds_t33,

N_REQUIRED_UDS

};

```

```

/*****/

```

\*note that the stress components are termed  $t_{ij}$  in the code rather than  $tv_{ij}$  as in equations

In order to define the scalar source terms in the DEFINE\_SOURCE macro, the following cell macros are used to access the fluid properties (density and viscosity), viscoelastic stress tensor components and the velocity gradient tensor components. The general form of these macros are given below, the remaining tensor components can be accessed using the proper macro index:

```

/*****fluid property macros*****/

```

```

rho = C_R(c,t);

```

```

mu_s = C_MU_L(c,t);

```

```

/*****macro for the first component of the viscoelastic stress tensor*****/

```

```
t11 = C_UDSI(c,t,uds_t11);
```

```
/******macro for the first component of the velocity gradient stress tensor******/
```

```
du_dx = C_U_G(c,t)[0];
```

```
/******
```

The  $\tau_{v_{11}}$  scalar transport source term can now be defined using the DEFINE\_SOURCE macro:

```
/******source term for the first component of the viscoelastic stress tensor t11******/
```

```
DEFINE_SOURCE(t11_source, c, t, dS, eqn)
```

```
{
```

```
    real source, mu_s, rho;
```

```
    real t11, t12, t22, t13, t33, f;
```

```
    real du_dx, du_dy, du_dz;
```

```
    rho = C_R(c,t);
```

```
    mu_s = C_MU_L(c,t);
```

```
    t11 = C_UDSI(c,t,uds_t11);
```

```
    t12 = C_UDSI(c,t,uds_t12);
```

```
    t22 = C_UDSI(c,t,uds_t22);
```

```
    t13 = C_UDSI(c,t,uds_t13);
```

```
    t33 = C_UDSI(c,t,uds_t33);
```

```
    du_dx = C_U_G(c,t)[0];
```

```

du_dy = C_U_G(c,t)[1];

du_dz = C_U_G(c,t)[2];

f = 1. + (eps * lambda * (t11 + t22 + t33)/mu_p);

dS[eqn] = rho * (-f / lambda + 2 * du_dx);

source = rho * ((2. * mu_p / lambda) * du_dx);

source += rho * (2. * t11 * du_dx);

source += rho * (2. * t12 * du_dy);

source += rho * (2. * t13 * du_dz);

source -= rho * f * t11 / lambda;

return source;

}

/*****/

```

The X momentum source term can be written as:

$$x \text{ momentum source} = \frac{\partial \tau_{v11}}{\partial x} + \frac{\partial \tau_{v21}}{\partial y} + \frac{\partial \tau_{v31}}{\partial z} \quad \text{Equation 0-3}$$

FLUENT stores the gradients of the user defined scalars using the cell macro C\_UDSI\_G, for instance, the gradient of the viscoelastic stress component  $\tau_{v11}$  with respect to x is  $(\frac{\partial \tau_{v11}}{\partial x})$ :

```

/**macro for the gradient of the viscoelastic stress component
t11**/

```

```

dt11_dx = C_UDSI_G(c,t,uds_t11)[0];

```

```

/*****

```

The remaining tensor components can be accessed using the proper C\_UDSI\_G macro index and the momentum source term in the X direction is defined as:

```

/*****define momentum source term in x direction*****/

```

```

DEFINE_SOURCE(xmom_source, c, t, dS, eqn)

```

```

{

```

```

    real source;

```

```

    dS[eqn] = 0.;

```

```

    source = C_UDSI_G(c,t,uds_t11)[0] + C_UDSI_G(c,t,uds_t12)[1] +
C_UDSI_G(c,t,uds_t13)[2];

```

```

    return source;

```

```

}

```

```

/*****

```

# Appendix B

## Summary table of test cases

The test cases performed for the purpose of this thesis are summarized in the table below along with details regarding the flow conditions and the models used in each case.

Test case	Details
2D channel flow	<ul style="list-style-type: none"> <li>- Verification for the PTT viscoelastic model implementation.</li> <li>- Tests performed at viscosity ratios: <math>\beta = 0.1, 0.5</math> and <math>0.8</math></li> </ul>
3D contraction flow	<ul style="list-style-type: none"> <li>- Validation of corner vortex prediction by the PTT viscoelastic model.</li> <li>- Deborah numbers for cases with contraction ratio of 2.4: <math>De = 1.07, 9.63</math> and <math>77.3</math></li> <li>- Deborah numbers for cases with contraction ratio of 4: <math>De = 0.51, 1.14, 2.41</math> and <math>5.96</math></li> </ul>
Axisymmetric nozzle	<ul style="list-style-type: none"> <li>- RANS simulations with Schnerr-Sauer cavitation model</li> <li>- Cavitation number <math>CN = 0.95</math> and <math>1.5</math></li> <li>- RANS models: <math>k-\varepsilon</math> RNG and <math>k-\omega</math> SST</li> <li>- <math>k-\varepsilon</math> RNG with Reboud <i>et al.</i> correction</li> <li>- <math>k-\omega</math> SST with Reboud <i>et al.</i> correction</li> </ul>
Asymmetric nozzle	<ul style="list-style-type: none"> <li>- RANS simulations with Schnerr-Sauer cavitation model</li> <li>- Cavitation number <math>CN = 2.18</math></li> <li>- RANS model: <math>k-\omega</math> SST with Reboud <i>et al.</i> correction</li> </ul>
Step nozzle (1)	<ul style="list-style-type: none"> <li>- RANS simulations</li> <li>- Cavitation number <math>CN = 1.38</math></li> <li>- RANS models: <math>k-\varepsilon</math> RNG, <math>k-\omega</math> SST, realizable <math>k-\varepsilon</math>, RSM</li> <li>- <math>k-\varepsilon</math> RNG with Reboud <i>et al.</i> correction</li> <li>- <math>k-\omega</math> SST with Reboud <i>et al.</i> correction</li> <li>- WALE LES simulations with Schnerr-Sauer, Zwart-Gerber-Belamri and barotropic cavitation models</li> </ul>
Step nozzle (2)	<ul style="list-style-type: none"> <li>- WALE LES simulations of Newtonian and PTT viscoelastic fluids</li> <li>- Cavitation number <math>CN = 1.38</math></li> <li>- Cavitation model: Schnerr-Sauer</li> </ul>
Injector nozzle	<ul style="list-style-type: none"> <li>- WALE LES simulations of Newtonian and PTT viscoelastic fluids</li> <li>- Cavitation number <math>CN = 35.9</math></li> <li>- Cavitation model: Schnerr-Sauer</li> </ul>



# Bibliography

- Addad, Y., Gaitonde, U., Laurence, D., & Rolfo, S. (2008). Optimal Unstructured Meshing for Large Eddy Simulations. In *In: J. Meyers, B.J. Geurts, P. Sagaut (eds) Quality and Reliability of Large-Eddy Simulations. Ercoftac Series* (Vol. 12, pp. 93–103). Springer, Dordrecht.
- Aeschlimann, V., Barre, S., & Djeridi, H. (2011). Velocity field analysis in an experimental cavitating mixing layer. *Physics of Fluids*, 23(5), 055105.
- Afzal, H., Arcoumanis, C., Gavaises, M., & Kampanis, N. (1999). Internal flow in diesel injector nozzles: modelling and experiments. *IMEchE Paper S*, (492), 25–44.
- Ahuja, V., Hosangadi, A., & Arunajatesan, S. (2001). Simulations of Cavitating Flows Using Hybrid Unstructured Meshes. *Journal of Fluids Engineering*, 123(2), 331–340.  
<https://doi.org/10.1115/1.1362671>
- Altimira, M., & Fuchs, L. (2015). Numerical investigation of throttle flow under cavitating conditions. *International Journal of Multiphase Flow*, 75, 124–136.  
<https://doi.org/10.1016/J.IJMULTIPHASEFLOW.2015.05.006>
- Andriotis, A., Gavaises, M., & Arcoumanis, C. (2008). Vortex flow and cavitation in diesel injector nozzles. *Journal of Fluid Mechanics*, 610, 195–215.  
<https://doi.org/10.1017/S0022112008002668>
- Arcoumanis, C., Gavaises, M., Flora, H., & Roth, H. (2001). Visualisation of cavitation in diesel engine injectors. *Mécanique & Industries*, 2(5), 375–381.
- Arndt, R. E. (1981). Cavitation in fluid machinery and hydraulic structures. *Annual Review of Fluid Mechanics*, 13(1), 273–326.
- Ausoni, P., Farhat, M., Escaler, X., Egusquiza, E., & Avellan, F. (2007). Cavitation Influence on von Kármán Vortex Shedding and Induced Hydrofoil Vibrations. *Journal of Fluids Engineering*, 129(8), 966–973. <https://doi.org/10.1115/1.2746907>
- Barbour, R. (2011). Method to provide power gain in an engine. *US Patent Number US9239000*.
- Barbour, Robert, Quigley, R., & Panesar, A. (2014). Investigations into fuel additive induced power gain in the CEC F-98-08 DW10B injector fouling engine test. *SAE*, 2014-01–2721.  
<https://doi.org/10.4271/2014-01-2721>
- Barker, J., Richards, P., Snape, C., & Meredith, W. (2011). Diesel injector deposits – an issue that has evolved with engine technology. *SAE*, 2011-01–1923. <https://doi.org/10.4271/2011-01-1923>
- Bauer, D., Chaves, H., & Arcoumanis, C. (2012). Measurements of void fraction distribution in cavitating pipe flow using x-ray CT. *Measurement Science and Technology*, 23(5), 055302.  
<https://doi.org/10.1088/0957-0233/23/5/055302>
- Bergwerk, W. (1959). Flow pattern in diesel nozzle spray holes. *Proceedings of the Institution of Mechanical Engineers*, 173(25), 655–660.  
[https://doi.org/10.1243/PIME\\_PROC\\_1959\\_173\\_054\\_02](https://doi.org/10.1243/PIME_PROC_1959_173_054_02)
- Berman, N. S. (1977). Flow time scales and drag reduction. *Citation: Physics of Fluids*, 20(10), S168–S174. <https://doi.org/10.1063/1.861726>
- Berret, J.-F., Gamez-Corrales, R., Séréro, Y., Molino, F., & Lindner, P. (2001). Shear-induced micellar growth in dilute surfactant solutions. *Europhysics Letters (EPL)*, 54(5), 605–611.  
<https://doi.org/10.1209/epl/i2001-00335-x>
- Bewersdorff, H.-W., & Ohlendon, D. (1988). The behaviour of drag-reducing cationic surfactant solutions. *Colloid & Polymer Science*, 266(10), 941–953. <https://doi.org/10.1007/BF01410851>
- Bin, J., Lou, X., Peng, X., & Wu, Y. (2013). Three-dimensional large eddy simulation and vorticity analysis of unsteady cavitating flow around a twisted hydrofoil. *Journal of Hydrodynamics, Ser.*



- B*, 25(4), 510–519.
- Bird, R. B., Armstrong, R. C., Hassager, O., & Curtiss, C. F. (1977). *Dynamics of polymeric liquids*. New York: Wiley.
- Brennen, C. E. (2013). *Cavitation and Bubble Dynamics*. Cambridge University Press.
- Brujan, E. A., Ohl, C. D., Lauterborn, W., & Philipp, A. (1996a). Dynamics of laser-induced cavitation bubbles in polymer solutions. *Acta Acustica United with Acustica*, 82(3), 423–430.
- Brujan, E. A., Ohl, C. D., Lauterborn, W., & Philipp, A. (1996b). Dynamics of laser-induced cavitation bubbles in polymer solutions. *Acta Acustica United with Acustica*, 82(3), 423–430.
- Brujan, E. A. (1999). A first-order model for bubble dynamics in a compressible viscoelastic liquid. *Journal of Non-Newtonian Fluid Mechanics*, 84(1), 83–103. [https://doi.org/10.1016/S0377-0257\(98\)00144-X](https://doi.org/10.1016/S0377-0257(98)00144-X)
- Brujan, E. A., Ikeda, T., & Matsumoto, Y. (2004). Dynamics of ultrasound - induced cavitation bubbles in non - Newtonian liquids and near a rigid boundary. *Physics of Fluids*, 16(7), 2402–2410. <https://doi.org/10.1063/1.1739405>
- Brujan, Emil Alexandru. (2008). Shock wave emission from laser-induced cavitation bubbles in polymer solutions. *Ultrasonics*, 48, 423–426. <https://doi.org/10.1016/j.ultras.2008.02.001>
- Budich, B., Schmidt, S. J., & Adams, N. A. (2018). Numerical simulation and analysis of condensation shocks in cavitating flow. *Journal of Fluid Mechanics*, 838, 759–813. <https://doi.org/10.1017/jfm.2017.882>
- Burshtein, N., Zografos, K., Shen, A. Q., Poole, R. J., & Haward, S. J. (2017). Inertioelastic Flow Instability at a Stagnation Point. *PHYSICAL REVIEW X*, 7(4). <https://doi.org/10.1103/PhysRevX.7.041039>
- Cadot, O., & Lebey, M. (1999). Shear instability inhibition in a cylinder wake by local injection of a viscoelastic fluid. *Physics of Fluids*, 11(2), 494–496.
- Callenaere, M., Franc, J., Michel, J., & Riondet, M. (2001). The cavitation instability induced by the development of a re-entrant jet. *J. Fluid Mech*, 444, 223–256. <https://doi.org/10.1017/S0022112001005420>
- Campo-Deaño, L., & Galindo-Rosales, F. (2011). Flow of low viscosity Boger fluids through a microfluidic hyperbolic contraction. *Journal of Non-Newtonian Fluids*, 166(21), 1286–1296.
- Cates, M., & Candau, S. (1990). Statics and dynamics of worm-like surfactant micelles. *Journal of Physics: Condensed Matter*.
- Caupin, F., & Stroock, A. D. (2013). The Stability Limit and other Open Questions on Water at Negative Pressure. *Liquid Polymorphism: Advances in Chemical Physics*, (51–80), 152.
- Chahine, G. L., Frederick, G. F., & Bateman, R. D. (1993). Propeller tip vortex cavitation suppression using selective polymer injection. *Journal of Fluids Engineering*, 115(3), 497–503. <https://doi.org/10.1115/1.2910166>
- Chahine, G. L., & Fruman, D. H. (1979). Dilute polymer solution effects on bubble growth and collapse. *The Physics of Fluids*, 22, 1406. <https://doi.org/10.1063/1.862754>
- Chahine, G. L., & Genoux, P. F. (1983). Collapse of a cavitating vortex ring. *Journal of Fluids Engineering*, 105(4), 400–405.
- Chang, N., Ganesh, H., Yakushiji, R., & Ceccio, S. L. (2011). Tip Vortex Cavitation Suppression by Active Mass Injection. *Journal of Fluids Engineering*, 133(11), 111301. <https://doi.org/10.1115/1.4005138>
- Chen, Y., & Heister, S. D. (1995). TWO-PHASE MODELING OF CAVITATED FLOWS. *Computers & Fluids*, 24(7), 799–809.
- Choi, J., Hsaio, C., Chahine, G., & Ceccio, S. (2009). Growth, oscillation and collapse of vortex cavitation bubbles. *Journal of Fluid Mechanics*, 624, 255–279.

<https://doi.org/10.1017/S0022112008005430>

- Coutier-Delgossa, O., Fortes-Patella, R., & Reboud, J. L. (2002). Simulation of unsteady cavitation with a two-equation turbulence model including compressibility effects. *Journal of Turbulence*, 3(1), 58–65.
- Coutier-Delgossa, O., Fortes-Patella, R., & Reboud, J. L. (2003). Evaluation of the turbulence model influence on the numerical simulations of unsteady cavitation. *Journal of Fluids Engineering*, 125(1), 38–45.
- Coutier-Delgossa, O., Reboud, J. L., & Dellanoy, Y. (2003). Numerical simulation of the unsteady behaviour of cavitating flows. *International Journal for Numerical Methods for Fluids*, 42(5), 527–548.
- Cruz, D. O. A. O. A., Pinho, F. T. T., & Oliveira, P. J. J. (2005). Analytical solutions for fully developed laminar flow of some viscoelastic liquids with a Newtonian solvent contribution. *Journal of Non-Newtonian Fluid Mechanics*, 132(1–3), 28–35.  
<https://doi.org/10.1016/j.jnnfm.2005.08.013>
- Degani, D., Seginer, A., & Lecy, Y. (1990). Graphical visualization of vortical flows by means of helicity. *AIAA Journal*, 28(8), 1347–1352. <https://doi.org/10.2514/3.25224>
- Dellanoy, Y., & Kueny, J. L. (1990). Two Phase Flow Approach in Unsteady Cavitation Modeling. *Cavitation and Multiphase Flow Forum, ASME FED*, 153–158.
- Den Toonder, J. M. J. ., Hulsen, M. A., Kuiken, G., & Nieuwstadt, F. (1997). Drag reduction by polymer additives in a turbulent pipe flow: numerical and laboratory experiments. *Journal of Fluid Mechanics*, 337, 193–231.
- Dimitropoulos, C. D., Sureshkumar, R., & Beris, A. N. (1998). Direct numerical simulation of viscoelastic turbulent channel flow exhibiting drag reduction: effect of the variation of rheological parameters. *Journal of Non-Newtonian Fluid Mechanics*, 79(2), 433–468.
- Dimitropoulos, C., Dubief, Y., Shaqfeh, E., Moin, P., & Lele, S. (2005). Direct numerical simulation of polymer-induced drag reduction in turbulent boundary layer flow. *Physics of Fluids*, 17(1), 011705. <https://doi.org/10.1063/1.1829751>
- Dittakavi, N., Chunekar, A., & Frankel, S. (2010). Large Eddy Simulation of Turbulent-Cavitation Interactions in a Venturi Nozzle. *Journal of Fluids Engineering*, 132(12), 121301.  
<https://doi.org/10.1115/1.4001971>
- Dollet, B., Marmottant, P., & Garbin, V. (2018). Bubble Dynamics in Soft and Biological Matter. *Annual Review of Fluid Mechanics*, 51, 331–355. <https://doi.org/10.1146/annurev-fluid-010518>
- Dubief, Y., White, C. M., Terrapon, V. E., Shaqfeh, E. S., Moin, P., & Lele, S. K. (2004). On the coherent drag-reducing and turbulence-enhancing behaviour of polymers in wall flows. *Journal of Fluid Mechanics*, 514, 271–280.
- Duke, D., Swantek, A., Tilocco, Z., Kastengren, A., Fezzaa, K., Neroorkar, K., ... Schmidt, D. (2014). X-ray imaging of cavitation in Diesel injectors. *SAE International Journal of Engines*, 7(2), 1003–1016. <https://doi.org/10.4271/2014-01-1404>
- Dular, M., & Coutier-Delgossa, O. (2008). Numerical modelling of cavitation erosion. *International Journal for Numerical Methods in Fluids*, 61, 1388–1410.
- Edelbauer, W., Strucl, J., & Morozov, A. (2014). large eddy simulation of cavitating throttle flow. *SimHydro Int. Conf. Modelling of Rapid Transitory Flows*. Sophia Antipolis, France, 11-13 June.
- Feng, Y., Chu, Z., & Dreiss, C. A. (2015). *Smart Wormlike Micelles*. Berlin, Heidelberg: Springer Berlin Heidelberg. <https://doi.org/10.1007/978-3-662-45950-8>
- Fischer, P., & Rehage, H. (1997). Non-linear flow properties of viscoelastic surfactant solutions. *Rheologica Acta*, 36(1), 13–27.
- FLUENT. (2017). ANSYS FLUENT Theory and User’s Guide. ANSYS Corporation.

- Fogler, H., & Goddard, J. (1970). Collapse of Spherical Cavities in Viscoelastic Fluids. *Physics of Fluids*, 13(5), 1135–1141.
- Franc, J.-P., & Michel, J.-M. (2005). *Fundamentals of Cavitation*. Springer Netherlands. <https://doi.org/10.1007/1-4020-2233-6>
- Ganesh, H., Makiharju, S., & Ceccio, S. (2016). Bubbly shock propagation as a mechanism for sheet-to-cloud transition of partial cavities. *J. Fluid Mech*, 802, 37–78. <https://doi.org/10.1017/jfm.2016.425>
- Ganippa, L. C., Bark, G., Andersson, S., & Chomiak, J. (2001). The Structure of Cavitation and its Effect on the Spray Pattern in a Single-Hole Diesel Nozzle. *SAE Technical Paper*, 2001-01–20. <https://doi.org/10.4271/2001-01-2008>
- Gatski, T. B., Hussaini, M. Y., & Lumley, J. L. (1996). *Simulation and Modeling of Turbulent Flows*. Oxford University Press.
- Gavaises, M. (2008). Flow in valve covered orifice nozzles with cylindrical and tapered holes and link to cavitation erosion and engine exhaust emissions. *International Journal of Engine Research*, 9(6), 435–447. <https://doi.org/10.1243/14680874JER01708>
- Gavaises, M., Andriotis, A., Papoulias, D., Mitroglou, N., & Theodorakakos, A. (2009). Characterization of string cavitation in large-scale Diesel nozzles with tapered holes. *Physics of Fluids*, 21(215), 52107–52107. <https://doi.org/10.1063/1.3140940>
- Giannadakis, E. (2005). *Modelling of Cavitation in Automotive Fuel Injector Nozzles*. University of London.
- Giannadakis, E., Gavaises, M., & Arcoumanis, C. (2008). Modelling of cavitation in diesel injector nozzles. *Journal of Fluid Mechanics*, 616, 153–193. <https://doi.org/10.1017/S0022112008003777>
- Giannadakis, E., Gavaises, M., & Roth, H. (2004). Cavitation Modelling in Single-Hole Diesel Injector Based on Eulerian-Lagrangian Approach. In *ThIESEL International Conference on Thermo-and Fluid Dynamic Processes in Diesel Engines*. (pp. 1–13).
- Giesekus, H. (1982). A simple constitutive equation for polymer fluids based on the concept of deformation-dependent tensorial mobility. *Journal of Non-Newtonian Fluid Mechanics*.
- Giudice, F. Del, Haward, S. J., & Shen, A. Q. (2017). Relaxation time of dilute polymer solutions: A microfluidic approach. *Journal of Rheology*, 61, 327–337. <https://doi.org/10.1122/1.4975933>
- Goldberg, B. B., Liu, J.-B., & Forsberg, F. (1994). ULTRASOUND CONTRAST AGENTS: A REVIEW. *Ultrasound in Med. & Biol*, 20(4), 319–333.
- Goncalves, E., & Patella, R. (2009). Numerical Simulation of Cavitating Flows with Homogeneous Models. *Computers & Fluids*, 38(9), 1682–1696.
- Gopalan, S., & Katz, J. (2000). Flow structure and modeling issues in the closure region of attached cavitation. *Physics of Fluids*, 12(4), 895–911.
- Graham, M. D. (2014). Drag reduction and the dynamics of turbulence in simple and complex fluids. *Physics of Fluids*, 26(10), 101301–101324. <https://doi.org/10.1063/1.2964639>
- Gyr, A., & Bewersdorff, H. W. (2013). *Drag Reduction of Turbulent Flows by Additives*. Springer Science & Business Media. <https://doi.org/10.1007/978-94-017-1295-8>
- Hall, M. G. (1972). VORTEX BREAKDOWN. *Annual Review of Fluid Mechanics*, 4(1), 195–318.
- Haller, G. (2005). An objective definition of a vortex. *Journal of Fluid Mechanics*, 525, 1–26. <https://doi.org/10.1017/S0022112004002526>
- Harder, K. J., Tiederman, W. G., & Hardert, K. J. (1991). Drag Reduction and Turbulent Structure in Two-Dimensional Channel Flows. *Source: Philosophical Transactions: Physical Sciences and Engineering*, 336(1640), 19–34.
- Hegedús, F., Hós, C., Pandula, Z., & Kullmann, L. (2010). Measurement on the cavitating vortex

- shedding behind rectangular obstacles. *IOP Conference Series: Earth and Environmental Science*, 12(1), 012066.
- Hickel, S. (2015). DNS and LES of two-phase flows with cavitation. *Direct and Large-Eddy Simulation*, IX, 595–604.
- Housiadas, K. D., & Beris, A. N. (2005). Direct numerical simulations of viscoelastic turbulent channel flows at high drag reduction. *Korea - Australia Rheology Journal*, 17(3), 131–140.
- Howard, R. J. A., & Pourquie, M. (2002). Large eddy simulation of an Ahmed reference model. *Journal of Turbulence*, 3.
- Hsiao, C., & Chahine, G. (2004). Prediction of tip vortex cavitation inception using coupled spherical and nonspherical bubble models and Navier–Stokes computations. *Journal of Marine Science and Technology*, 8(3), 99–108.
- Hsiao, C. T., Zhang, Q., Wu, X., & Chahine, G. L. (2010). Effects of Polymer Injection on Vortex Cavitation Inception. In *28th Symposium on Naval Hydrodynamics*.
- Hua, C., & Johnsen, E. (2013). Nonlinear oscillations following the Rayleigh collapse of a gas bubble in a linear viscoelastic (tissue-like) medium. *Physics of Fluids*, 25(8), 083101. <https://doi.org/10.1063/1.4817673>
- In, M., Bec, V., Aguerre-Chariol, O., & Zana, R. (1999). Quaternary Ammonium Bromide Surfactant Oligomers in Aqueous Solution: Self-Association and Microstructure†. *Langmuir*, 16(1), 141–148. <https://doi.org/10.1021/LA990645G>
- Issa, R. I. (1985). Solution of the Implicitly Discretised Fluid Flow Equations by Operator-Splitting. *JOURNAL OF COMPUTATIONAL PHYSICS*, 62, 40–65.
- Ivings, M., Causon, D., & Toro, E. (1998). On Riemann solvers for compressible liquids. *International Journal for Numerical Methods in Fluids*, 28(3), 395–418.
- Iyer, C. O., & Ceccio, S. L. (2002). The influence of developed cavitation on the flow of a turbulent shear layer. *Physics of Fluids*, 14(10), 3414–3431.
- Jamburidze, A., De Corato, M., Huerre, A., Pommella, A., & Garbin, V. (2017). High-frequency linear rheology of hydrogels probed by ultrasound-driven microbubble dynamics. *Soft Matter*, 13(21), 3946–3953.
- Japper-Jaafar, A., Escudier, M. P., & Poole, R. J. (2010). Laminar, transitional and turbulent annular flow of drag-reducing polymer solutions. *J. Non-Newtonian Fluid Mech*, 165, 1357–1372. <https://doi.org/10.1016/j.jnnfm.2010.07.001>
- Jasak, H., Weller, H. G., & Gosman, A. A. D. (1999). HIGH RESOLUTION NVD DIFFERENCING SCHEME FOR ARBITRARILY UNSTRUCTURED MESHES. *Int. J. Numer. Meth. Fluids*, 31, 431–449.
- Jiménez-Fernández, J., & Crespo, A. (2005). Bubble oscillation and inertial cavitation in viscoelastic fluids. *Ultrasonics*, 43, 643–651. <https://doi.org/10.1016/j.ultras.2005.03.010>
- Joseph, D. D. (1995). Cavitation in a flowing liquid. *Physical Review E*, 51(3), 1649–1650.
- Karathanassis, I. K., Trickett, K., Koukouvini, P., Wang, J., Barbour, R., & Gavaises, M. (2018). Illustrating the effect of viscoelastic additives on cavitation and turbulence with X-ray imaging. *Scientific Reports*, 8(1), 14968. <https://doi.org/10.1038/s41598-018-32996-w>
- Karathanassis, I., Koukouvini, P., Kontolatis, E., Li, Z., Wang, J., Mitroglou, N., & Gavaises, M. (2017). High-Speed Visualization of Vortical Cavitation Using Synchrotron Radiation. *Journal of Fluid Mechanics*.
- Karathanassis, I., Koukouvini, P., Lorenzi, M., Kontolatis, E., Li, Z., Wang, J., ... Gavaises, M. (2017). High-speed x-ray phase-contrast imaging of string cavitation in an enlarged diesel-injector orifice replica. In *Proc. 28th European Conf. Liquid Atomiz. Spray Systems*.
- Katz, J. (1984). Cavitation phenomena within regions of flow separation. *Journal of Fluid Mechanics*,

- Keller, S. L., Boltenhagen, P., Pine, D. J., & Zasadzinski, J. A. (1998). Direct observation of shear-induced structures in wormlike micellar solutions by freeze-fracture electron microscopy. *Physical Review Letters*, *80*, 2725–2728. <https://doi.org/10.1103/PhysRevLett.80.2725>
- Kim, B. K., & Telionis, D. P. (1989). The effect of polymer additives on laminar separation. *Physics of Fluids A: Fluid Dynamics*, *1*(2), 267–273.
- Kim, K., Adrian, R. J., Balachandar, S., & Sureshkumar, R. (2008). Dynamics of Hairpin Vortices and Polymer-Induced Turbulent Drag Reduction. *Physical Review Letters*, *100*, 134504. <https://doi.org/10.1103/PhysRevLett.100.134504>
- Kolev, N. I. (2005). *Multiphase Flow Dynamics*. Berlin: Springer.
- Koop, A. (2008). *Numerical simulation of unsteady three-dimensional sheet cavitation*. University of Twente.
- Koukouvinis, Naseri, H., Gavaises, M., Koukouvinis, P., Naseri, H., & Gavaises, M. (2016). Performance of turbulence and cavitation models in prediction of incipient and developed cavitation. *International Journal of Engine Research*, *18*(4), 333–350. <https://doi.org/10.1177/1468087416658604>
- Koukouvinis, P., & Gavaises, M. (2015). Simulation of throttle flow with two phase and single phase homogenous equilibrium model. *Journal of Physics: Conference Series*, *656*(1).
- Koukouvinis, P., Gavaises, M., Li, J., & Wang, L. (2016). Large Eddy Simulation of Diesel injector including cavitation effects and correlation to erosion damage. *Fuel*, *175*, 26–39. <https://doi.org/10.1016/j.fuel.2016.02.037>
- Koukouvinis, P., Mitroglou, N., Gavaises, M., Lorenzi, M., & Santini, M. (2017). Quantitative predictions of cavitation presence and erosion-prone locations in a high-pressure cavitation test rig. *Journal of Fluid Mechanics*, *819*, 21–57. <https://doi.org/10.1017/jfm.2017.156>
- Kubota, A., Kato, H., & Yamaguchi, H. (1990). Finite Difference Analysis of Unsteady Cavitation on a Two-Dimensional Hydrofoil. In *5th International Conference on Numerical Ship Hydrodynamics*.
- Kunz, R. F., Boger, D. a, Stinebring, D. R., Chyczewski, S., Lindau, J. W., Gibeling, H. J., ... Govindan, T. R. (2000). A preconditioned Navier - Stokes method for two-phase flows with application to cavitation prediction. *Computers & Fluids*, *29*, 849–875. [https://doi.org/10.1016/S0045-7930\(99\)00039-0](https://doi.org/10.1016/S0045-7930(99)00039-0)
- L'vov, V. S., Pomyalov, A., Procaccia, I., & Tiberkevich, V. (2004). Drag Reduction by Polymers in Wall Bounded Turbulence. *Physical Review Letters*, *92*(24), 244503. <https://doi.org/10.1103/PhysRevLett.92.244503>
- Laberteaux, K. R., & Ceccio, S. L. (2001). Partial cavity flows. Part 1. Cavities forming on models without spanwise variation. *Journal of Fluid Mechanics*, *431*, 1–41. <https://doi.org/10.1017/S0022112000002925>
- Lauder, B., Reece, G., & Rodi, W. (1975). Progress in the development of a Reynolds-stress turbulence closure. *Journal of Fluid Mechanics*, *68*(3), 537–566.
- Lesieur, M. (2012). *Turbulence in Fluids*. Springer Science & Business Media.
- Lesieur, M., Métails, O., & Comte, P. (2005). *Large-eddy simulations of turbulence*. Cambridge University Press.
- Li, C., Sureshkumar, R., & Khomami, B. (2006). Influence of rheological parameters on polymer induced turbulent drag reduction. *Journal of Non-Newtonian Fluid Mechanics*, *140*(1–3), 23–40. <https://doi.org/10.1016/j.jnnfm.2005.12.012>
- Li, F., Kawaguchi, Y., & Hishida, K. (2004). Investigation on the characteristics of turbulence transport for momentum and heat in a drag - reducing surfactant solution flow. *Physics of Fluids*, *16*(9), 3281–3295. <https://doi.org/10.1063/1.1769375>

- Lin, J., Yu, Z., & Shao, X. (2004). Coherent structures in the mixing layers of a non-Newtonian fluid. *Journal of Turbulence*, 5, 39. <https://doi.org/10.1088/1468-5248/5/1/039>
- Lind, S. J., & Phillips, T. N. (2012). The influence of viscoelasticity on the collapse of cavitation bubbles near a rigid boundary. *Theoretical and Computational Fluid Dynamics*, 26(1–4), 245–277. <https://doi.org/10.1007/s00162-011-0227-9>
- Lind, S. J., & Phillips, T. N. (2013). Bubble Collapse in Compressible Fluids using a Spectral Element Marker Particle Method. Part 2. Viscoelastic Fluids. *Int. J. Numer. Meth. Fluids*, 71(9), 1103–1130. <https://doi.org/10.1002/flid>
- Lindau, R. F., Kunz, J. W., Venkateswaran, S., & Boger, D. a. (2001). Application of Preconditioned , Multiple-Species , Navier-Stokes Models To Cavitating Flows. In *Cav2001* (pp. 1–14).
- Lodge, A. S. (1968). Constitutive equations from molecular network theories for polymer solutions. *Rheologica Acta*, 7(4), 379–392. <https://doi.org/10.1007/BF01984856>
- Lu, B., Li, X., Scriven, L. E., Davis, H. T., Talmon, Y., & Zakin, J. L. (1998). Effect of chemical structure on viscoelasticity and extensional viscosity of drag-reducing cationic surfactant solutions. *Langmuir*, 14(1), 8–16. <https://doi.org/10.1021/la970630n>
- Luchik, T. S., & Tiederman, W. G. (1988). Turbulent structure in low-concentration drag-reducing channel flows. *Journal of Fluid Mechanics*, 190, 241–263. <https://doi.org/10.1017/S0022112088001302>
- Lumley, J. L. (1973). Drag reduction in turbulent flow by polymer additives. *Journal of Polymer Science: Macromolecular Reviews*, 7(1), 263–290. <https://doi.org/10.1002/pol.1973.230070104>
- Martynov, S. (2005). *Numerical simulation of the cavitation process in diesel fuel injectors*. University of Brighton.
- Mauger, C., Méès, L., Michard, M., Azouzi, A., & Valette, S. (2012). Shadowgraph, Schlieren and interferometry in a 2D cavitating channel flow. *Experiments in Fluids*, 53, 1895–1913. <https://doi.org/10.1007/s00348-012-1404-3>
- Menter, F. (1993). Zonal two equation k-turbulence models for aerodynamic flows. *AIAA Paper*, 2906.
- Menter, F. (1994). Two-equation eddy-viscosity turbulence models for engineering applications. *AIAA Journal*, 32(8), 1598–1605.
- Min, T., Yoo, J. Y., Choi, H., & Joseph, D. D. (2003). Drag reduction by polymer additives in a turbulent channel flow. *Journal of Fluid Mechanics*, 486, 213–238. <https://doi.org/10.1017/S0022112003004610>
- Mitroglou, N., Gavaises, M., Nouri, J. M., & Arcoumanis, C. (2011). Cavitation Inside Enlarged And Real-Size Fully Transparent Injector Nozzles And Its Effect On Near Nozzle Spray Formation. In *DIPSI Workshop 2011 on Droplet Impact Phenomena & Spray Investigation*. Bergamo, Italy.
- Mitroglou, N., Lorenzi, M., Santini, M., & Gavaises, M. (2016). Application of X-ray micro-computed tomography on high-speed cavitating diesel fuel flows. *Experiments in Fluids*, 57(11), 175. <https://doi.org/10.1007/s00348-016-2256-z>
- Mitroglou, N., Stamboliyski, V., Karathanassis, I. K., Nikas, K. S., & Gavaises, M. (2017). Cloud cavitation vortex shedding inside an injector nozzle. *Experimental Thermal and Fluid Science*, (84), 179–189. <https://doi.org/10.1016/j.expthermflusci.2017.02.011>
- Mowla, D., & Naderi, A. (2006). Experimental study of drag reduction by a polymeric additive in slug two-phase flow of crude oil and air in horizontal pipes. *Chemical Engineering Science*, 61(5), 1549–1554. <https://doi.org/10.1016/J.CES.2005.09.006>
- Naseri, H., Trickett, K., Mitroglou, N., Karathanassis, I., Koukouvinis, P., Gavaises, M., ... Wang, J. (2018). Turbulence and Cavitation Suppression by Quaternary Ammonium Salt Additives. *Scientific Reports*, 8(1), 7636.

- Nicoud, F., & Ducros, F. (1999). Subgrid-scale stress modelling based on the square of the velocity gradient tensor. *Flow, Turbulence and Combustion*, 62(3), 183–200. <https://doi.org/10.1023/A:1009995426001>
- Norouzi, M., Varedi, S. R., & Zamani, M. (2016). Wake instability of viscoelastic flows past an unconfined inclined square cylinder. *Physics of Fluids*, 28(2), 023101.
- Nurick, W. H. (1976). Orifice Cavitation and Its Effect on Spray Mixing. *Journal of Fluids Engineering*, 98(4), 681. <https://doi.org/10.1115/1.3448452>
- Oda, R., Panizza, P., Schmutz, M., & Lequeux, F. (1997). Direct Evidence of the Shear-Induced Structure of Wormlike Micelles: Gemini Surfactant 12–2–12. *Langmuir*, 13(24), 6407–6412. <https://doi.org/10.1021/la9621170>
- Ohlendorf, D., Interthal, W., & Hoffmann, H. (1986). Surfactant systems for drag reduction: Physico-chemical properties and rheological behaviour. *Rheologica Acta*, 25(5), 468–486. <https://doi.org/10.1007/BF01774397>
- Okabayashi, K., & Kajishima, T. (2009). Investigation of turbulent modulation by cavitation for subgrid-scale modeling in LES. In *7th International Symposium on Cavitation CAV2009*.
- Oliveira, P. J. (2001). Method for time-dependent simulations of viscoelastic flows: vortex shedding behind cylinder. *Journal of Non-Newtonian Fluid Mechanics*, 101(1), 113–137. [https://doi.org/10.1016/S0377-0257\(01\)00146-X](https://doi.org/10.1016/S0377-0257(01)00146-X)
- Örley, F., Trummer, S., Hickel, S., Mihatsch, M. S., Schmidt, S. J., & Adams, N. A. (2015). Large-eddy simulation of cavitating nozzle flow and primary jet break-up. *Physics of Fluids*, 27(8), 086101. <https://doi.org/10.1063/1.4928701>
- Örley, Felix, Hickel, S., Schmidt, S. J., & Adams, N. A. (2017). Large-Eddy Simulation of turbulent, cavitating fuel flow inside a 9-hole Diesel injector including needle movement. *International Journal of Engine Research*, 18(3), 195–211. <https://doi.org/10.1177/1468087416643901>
- Owolabi, B. E., Dennis, D. J. C., & Poole, R. J. (2017). Turbulent drag reduction by polymer additives in parallel-shear flows. *J. Fluid Mech*, 827, R4. <https://doi.org/10.1017/jfm.2017.544>
- Pelz, P. F., Keil, T., Ludwig, G., Pelz, P. F., Keil, Á. T., Ludwig, Á. G., & Kim, K.-H. (2014). On the Kinematics of Sheet and Cloud Cavitation and Related Erosion. In Kim K., Chahine G., Franc J. P., & Karimi A. (Eds.), *Advanced Experimental and Numerical Techniques for Cavitation Erosion Prediction*. <https://doi.org/10.1007/978-94-017-8539>
- Pereira, A. A. S., Mompean, G., Thais, L., & Soares, E. E. J. (2017). Transient aspects of drag reducing plane Couette flows. *Journal of Non-Newtonian Fluid Mechanics*, 241, 60–69. <https://doi.org/10.1016/j.jnnfm.2017.01.008>
- Petitpas, F., Massoni, J., & Saurel, R. (2009). Diffuse Interface Model for High Speed Cavitating Underwater Systems. *International Journal of Multiphase Flow*, 35(8), 747–759.
- Plesset, M. S. (1949). The dynamics of cavitation bubbles. *Journal of Applied Mechanics*, 16, 277–282.
- Pope, S. (2000). *Turbulent flows*. Cambridge University Press.
- Pozrikidis, C. (2009). *Fluid dynamics: theory, computation, and numerical simulation*. Springer Science & Business Media.
- Procaccia, I., L'vov, V. S., & Benzi, R. (2008). Colloquium: Theory of drag reduction by polymers in wall-bounded turbulence. *Reviews of Modern Physics*, 80(1), 225–247. <https://doi.org/10.1103/RevModPhys.80.225>
- Ran, B., & Katz, J. (1994). Pressure fluctuations and their effect on cavitation inception within water jets. *Journal of Fluid Mechanics*, 262, 223. <https://doi.org/10.1017/S0022112094000492>
- Rayleigh, L. (1917). On the pressure developed in a liquid during the collapse of a spherical cavity. *Philosophical Magazine Series 6*, 34(200), 94–98. <https://doi.org/10.1080/14786440808635681>

- Reboud, J., Stutz, B., & Coutier-Delgosha, O. (1998). Two phase flow structure of cavitation: experiment and modeling of unsteady effects. In *3rd International Symposium on Cavitation CAV1998* (Vol. 26). Grenoble, France.
- Reid, B. A., Gavaises, M., Mitroglou, N., Hargrave, G. K., Garner, C. P., Long, E. J., & McDavid, R. M. (2014). On the formation of string cavitation inside fuel injectors. *Experiments in Fluids*, *55*(1). <https://doi.org/10.1007/s00348-013-1662-8>
- Richter, D., Iaccarino, G., & Shaqfeh, E. S. G. (2012). Effects of viscoelasticity in the high Reynolds number cylinder wake. *Journal of Fluid Mechanics*, *693*, 297–318.
- Roberts, W. W., Hall, T. L., Ives, K., Wolf, J. S., Fowlkes, J. B., & Cain, C. A. (2006). Pulsed Cavitation Ultrasound: A Noninvasive Technology for Controlled Tissue Ablation (Histotripsy) in the Rabbit Kidney. *The Journal of Urology*, *175*(2), 734–738. [https://doi.org/10.1016/S0022-5347\(05\)00141-2](https://doi.org/10.1016/S0022-5347(05)00141-2)
- Rose, G. D., & Foster, K. L. (1989). Drag reduction and rheological properties of cationic viscoelastic surfactant formulations. *Journal of Non-Newtonian Fluid Mechanics*, *31*, 59–85.
- Ryskin, G. (1987). Turbulent Drag Reduction by Polymers: A Quantitative Theory. *Physical Review Letters*, *59*(18), 2059–2062.
- Sato, K., & Saito, Y. (2002). Unstable Cavitation Behavior in a Circular-Cylindrical Orifice Flow. *JSME International Journal Series B*, *45*(3), 638–645. <https://doi.org/10.1299/jsmeb.45.638>
- Schmidt, D. P., Rutland, C. J., & Corradini, M. L. (1999a). A Fully Compressible, Two-Dimensional Model of Small, High-Speed, Cavitating Nozzles. *Atomization and Sprays*, *9*(3), 255–276.
- Schmidt, D. P., Rutland, C. J., & Corradini, M. L. (1999b). Cavitation in Two-Dimensional Asymmetric Nozzles. *SAE Technical Paper, No. 1999-0*.
- Schmidt, D., Rutland, C. J., & Corradini, M. L. (1997). A Numerical study of cavitating flow through various nozzle shapes. *Society of Automotive Engineers*, (412), 117–126. <https://doi.org/10.4271/971597>
- Schmidt, David P. (1997). *Cavitation in Diesel Fuel Injectors*. University of Wisconsin-Madison.
- Schmidt, S., Sezal, I., & Schnerr, G. (2006). Compressible Simulation of High-Speed Hydrodynamics with Phase Change. In *European Conference on Computational Fluid Dynamics ECCOMAS CFD 2006*.
- Schnerr, G. H., & Sauer, J. (2001). Physical and numerical modeling of unsteady cavitation dynamics. In *Fourth International Conference on Multiphase Flow*. New Orleans, USA.
- Schrage, R. W. (1953). *A Theoretical Study of Interphase Mass Transfer*. New York, Columbia University Press.
- Senocak, I., & Shyy, W. (2004). Interfacial dynamics-based modelling of turbulent cavitating flows, Part-2: Time-dependent computations. *International Journal for Numerical Methods in Fluids*, *44*(9), 997–1016. <https://doi.org/10.1002/fld.693>
- Seyer, F. A., & Metzner, A. B. (1969). Turbulence phenomena in drag reducing systems. *AIChE Journal*, *15*(3), 426–434.
- Sezal, I. H., Schmidt, S. J., & Schnerr, G. H. (2009). Shock and Wave Dynamics in Cavitating Compressible Liquid Flows in Injection Nozzles. *Shock Waves*, *19*(1), 49–58.
- Shih, T., Liou, W., Shabbir, A., Yang, Z., & Zhu, J. (1995). A new  $k-\epsilon$  eddy viscosity model for high reynolds number turbulent flows. *Computers & Fluids*, *24*(3), 227–238.
- Sibley, D. N. (2010). *Viscoelastic Flows of PTT Fluids*. University of Bath.
- Sijl, J., Dollet, B., Overvelde, M., Garbin, V., Rozendal, T., Dejong, N., ... De Jong, N. (2010). Subharmonic behavior of phospholipid-coated ultrasound contrast agent microbubbles. *Journal of the Acoustical Society of America*, *128*(5), 3239–3252. <https://doi.org/10.1121/1.3493443>
- Simpson, R. L. (1989). Turbulent boundary-layer separation. *Annual Review of Fluid Mechanics*,



21(1), 205–232.

- Singhal, A. K., Athavale, M. M., Li, H., & Jiang, Y. (2002). Mathematical Basis and Validation of the Full Cavitation Model. *Journal of Fluids Engineering*, 124(3), 617. <https://doi.org/10.1115/1.1486223>
- Soldati, A., & Banerjee, S. (1998). Turbulence modification by large-scale organized electrohydrodynamic flows. *Physics of Fluids*, 10(7), 1742–1756.
- Sou, A., Biçer, B., & Tomiyama, A. (2014). Numerical simulation of incipient cavitation flow in a nozzle of fuel injector. *Computers & Fluids*, 103, 42–48. <https://doi.org/10.1016/j.compfluid.2014.07.011>
- Sousa, P. C. P., Coelho, P. P. M., Oliveira, M. M. S. N., & Alves, M. A. (2011). Effect of the contraction ratio upon viscoelastic fluid flow in three-dimensional square–square contractions. *Chemical Engineering*, 66(5), 998–1009. <https://doi.org/10.1016/j.ces.2010.12.011>
- Speziale, C., Sarkar, S., & Gatski, T. B. (1991). Modelling the pressure–strain correlation of turbulence: an invariant dynamical systems approach. *Journal of Fluid Mechanics*, 227, 245–272.
- Sridhar, G., & Katz, J. (1999). Effect of entrained bubbles on the structure of vortex rings. *Journal of Fluid Mechanics*, 397, 171–202. <https://doi.org/10.1017/S0022112099006187>
- Srivastava, S. P., & Hancsok, J. (2014). *Fuels and Fuel-Additives*. John Wiley & Sons.
- Stinebring, D. R., Billet, M. L., Lindau, J. W., & Kunz, R. F. (2001). Developed cavitation-cavity dynamics. <https://doi.org/ADP010487>
- Stokes, J. R., W Graham, L. J., Lawson, N. J., & Boger, D. V. (2001). Swirling flow of viscoelastic fluids. Part 1. Interaction between inertia and elasticity. *J. Fluid Mech*, 429, 67–115. <https://doi.org/10.1017/S0022112000002883>
- Suh, H. K., Park, S. H., & Lee, C. S. (2008). Experimental investigation of nozzle cavitating flow characteristics for diesel and biodiesel fuels. *International Journal of Automotive Technology*, 9(2), 217–224.
- Suh, H., & Lee, C. S. C. (2008). Effect of cavitation in nozzle orifice on the diesel fuel atomization characteristics. *International Journal of Heat and Fluid Flow*, 29(4), 1001–1009. <https://doi.org/10.1016/j.ijheatfluidflow.2008.03.014>
- Sun, T., Jiang, Z., Strzalka, J., Ocola, L., & Wang, J. (2012). Three-dimensional coherent X-ray surface scattering imaging near total external reflection. *Nature Photonics*, 6(9), 586–590. <https://doi.org/10.1038/nphoton.2012.178>
- Sureshkumar, R., & Beris, A. N. (1995). Effect of artificial stress diffusivity on the stability of numerical calculations and the flow dynamics of time-dependent viscoelastic flows. *Journal of Non-Newtonian Fluid Mechanics*, 60, 53–80.
- Sureskumar, R., Beris, A. N., & Handler, A. H. (1997). Direct numerical simulation of the turbulent channel flow of a polymer solution. *Physics of Fluids*, 9(March), 743–755.
- Tabor, M., & de Gennes, P. G. (1986). A Cascade Theory of Drag Reduction. *Europhysics Letters*, 2(7), 519–522.
- Tanasawa, I., & Yang, W. (1970). Dynamic Behavior of a Gas Bubble in Viscoelastic Liquids. *Journal of Applied Physics*, 41(11), 4526–4531.
- Tennekes, H., & Lumley, J. L. (1972). *A first course in turbulence*. MIT Press.
- Thien, N. P., & Tanner, R. I. (1977). A new constitutive equation derived from network theory. *Journal of Non-Newtonian Fluid Mechanics*, 2(4), 353–365. [https://doi.org/10.1016/0377-0257\(77\)80021-9](https://doi.org/10.1016/0377-0257(77)80021-9)
- Toms, B. A. (1948). Some observations on the flow of linear polymer solutions through straight tubes at large Reynolds numbers. In *Proceedings of the 1st International Congress on Rheology*.

- Tsukahara, T., Motozawa, M., Tsurumi, D., & Kawaguchi, Y. (2013). PIV and DNS analyses of viscoelastic turbulent flows behind a rectangular orifice. *International Journal of Heat and Fluid Flow*, 41(41), 66–79. <https://doi.org/10.1016/j.ijheatfluidflow.2013.03.011>
- Valente, P. C., da Silva, C. B., & Pinho, F. T. (2016). Energy spectra in elasto-inertial turbulence. *Physics of Fluids*, 28(7), 075108. <https://doi.org/10.1063/1.4955102>
- Ventikos, Y., & Tzabiras, G. (2000). A numerical method for the simulation of steady and unsteady cavitating flows. *Computers & Fluids*, 29(1), 63–88.
- Versteeg, H., & Malalasekera, W. (2007). *An introduction to computational fluid dynamics: the finite volume method*.
- Virk, P. S. (1971). An elastic sublayer model for drag reduction by dilute solutions of linear macromolecules. *Journal of Fluid Mechanics*, 45(3), 417–440.
- Virk, P. S. (1975). Drag reduction fundamentals. *AIChE Journal*, 21(4), 625–656.
- Wallis, G. B. (1969). *One-Dimensional Two-Phase Flow*.
- Warholic, M. D., Heist, D. K., Katcher, M., & Hanratty, T. J. (2001). A study with particle-image velocimetry of the influence of drag-reducing polymers on the structure of turbulence. *Experiments in Fluids*, 31, 474–483.
- Warnez, M. T., & Johnsen, E. (2015). Numerical modeling of bubble dynamics in viscoelastic media with relaxation. *Physics of Fluids*, 27, 063103. <https://doi.org/10.1063/1.4922598>
- Washio, S. (2014). *Recent Developments in Cavitation Mechanisms: A Guide for Scientists and Engineers*. Elsevier Science.
- Wei, T., & Willmarth, W. (1992). Modifying turbulent structure with drag-reducing polymer additives in turbulent channel flows. *Journal of Fluid Mechanics*, 245, 619–641.
- White, C. M., & Mungal, M. G. (2008). Mechanics and prediction of turbulent drag reduction with polymer additives. *Annual Review of Fluid Mechanics*, 40, 235–256. <https://doi.org/10.1146/annurev.fluid.40.111406.102156>
- Wilcox, D. (2006). *Turbulence Modelling for CFD*. DCW Industries.
- Wilcox, DC. (1988). Reassessment of the scale-determining equation for advanced turbulence models. *AIAA Journal*, 26(11), 1299–1310.
- Winklhofer, E., Kull, E., Kelz, E., & Morozov, A. (2001). Comprehensive hydraulic and flow field documentation in model throttle experiments under cavitation conditions. In *ILASS-Europe 2001, 17 International Conference on Liquid Atomization and Spray Systems* (pp. 574 – 579). <https://doi.org/10.13140/2.1.1716.4161>
- Xi, L., & Graham, M. (2010). Turbulent drag reduction and multistage transitions in viscoelastic minimal flow units. *Journal of Fluid Mechanics*, 647, 421–452. <https://doi.org/10.1017/S0022112010000066>
- Xie, Y.-C., Huang, S.-D., Funfschilling, D., Li, X.-M., Ni, R., & Xia, K.-Q. (2015). Effects of polymer additives in the bulk of turbulent thermal convection. *J. Fluid Mech*, 784, R3. <https://doi.org/10.1017/jfm.2015.618>
- Yakhot, V., & Orszag, S. (1992). Development of turbulence models for shear flows by a double expansion technique. *Physics of Fluids A: ...*, 4(7), 1510–1520.
- Yamamoto, M. (1956). The Visco-elastic Properties of Network Structure I. General Formalism. *Journal of the Physical Society of Japan*, 11(4), 413–421. <https://doi.org/10.1143/JPSJ.11.413>
- Yang, J. (2002). Viscoelastic wormlike micelles and their applications. *Current Opinion in Colloid & Interface Science*, 7(5–6), 276–281. [https://doi.org/10.1016/S1359-0294\(02\)00071-7](https://doi.org/10.1016/S1359-0294(02)00071-7)
- Yang, W., & Lawson, M. (1974). Bubble pulsation and cavitation in viscoelastic fluids. *Journal of Applied Physics*, 45(2), 754–758.

- Yu, B., Li, F., & Kawaguchi, Y. (2004). Numerical and experimental investigation of turbulent characteristics in a drag-reducing flow with surfactant additives. *International Journal of Heat and Fluid Flow*, 25(6), 961–974. <https://doi.org/10.1016/j.ijheatfluidflow.2004.02.029>
- Zakin, J. L., Lu, B., & Bewersdorff, H.-W. (1998). Surfactant drag reduction. *Reviews in Chemical Engineering*, 14(4–5), 253–320. <https://doi.org/10.1515/REVCE.1998.14.4-5.253>
- Zwart, P. J., Gerber, A. G., & Belamri, T. (2004). A two-phase flow model for predicting cavitation dynamics. In *Proc. Of 5th International Conference on Multiphase Flow*.